Extensive Air Showers at Large Zenith Angles

Dissertation

zur Erlangung des Doktorgrades

an der Fakultät für Mathematik, Informatik und

Naturwissenschaften

Fachbereich Physik
der Universität Hamburg

vorgelegt von

Ali Baktash

Hamburg
2023

Gutachter der Dissertation:	Prof. Dr. Dieter Horns Dr. Abelardo Moralejo
Zusammensetzung der Prüfungskommission:	Prof. Dr. Dieter Horns Dr. Abelardo Moralejo Dr. Martin Tluczykont Prof. Dr. Marcus Brüggen Prof. Dr. Sven-Olaf Moch
Vorsitzender der Prüfungskommission:	Prof. Dr. Sven-Olaf Moch
Datum der Disputation:	29.01.2024
Vorsitzender des Fach-Promotionsausschusses PHYSIK:	Prof. Dr. Markus Drescher
Leiter des Fachbereichs PHYSIK:	Prof. Dr. Wolfgang J. Parak
Dekan der Fakultät MIN:	Prof. Dr.-Ing. Norbert Ritter

Abstract

The recent discovery by the LHAASO experiment of γ-ray emission in the PeV energy range indicates the existence of galactic sources capable of accelerating particles to multi-PeV energies, motivating further exploration of γ-ray sources above 100 TeV with Imaging Air Cherenkov Telescopes (IACTs). With increasing γ-ray energy, the sensitivity of IACTs mainly depends on the collection area A_{eff}. Despite achieving large collection areas, even up to 1 km^2, the expected photon rate above 100 TeV from the Crab Nebula is less than one photon per 100 hours, highlighting the challenges in detecting such high energy phenomena.

This thesis explores the possibilities of observing extensive air showers (EAS) at large zenith angles ($\geq 70^\circ$) with IACTs, in order to significantly increase the collection area compared to moderate zenith angle observations. In particular, the performance of H.E.S.S. CT5 is investigated. The study focuses on observations at a zenith angle of 80°, simulating γ-ray, proton, and helium induced air showers using `CORSIKA` and `sim_telarray`. The derived image parameters serve as inputs for evaluating the γ-hadron separation power, angular resolution, and energy resolution at a zenith angle of 80° using dedicated Random Forest Classifier and Random Forest Regressor techniques.

The investigation showcases the impressive performance of H.E.S.S. CT5, revealing an collection area of $A_{eff} \sim 5-6\,\mathrm{km}^2$ at 1 PeV after γ-hadron separation and direction cuts when operating as a stand-alone telescope at a zenith angle of 80°. It was found that H.E.S.S. CT5 achieves a quality factor Q on the order of $Q \sim 5$ at a zenith angle of 80°. The angular resolution is estimated at $\theta_{68\%} = 0.12^\circ$ for energies ≥ 10 TeV, improving to $\theta_{68\%} \leq 0.1^\circ$ for energies ≥ 100 TeV. Moreover, the energy resolution proves to be better than 18% at energies ≥ 10 TeV.

Monte Carlo simulations, such as `CORSIKA`, present a notable drawback in terms of increased computation time and storage size as the primary particle energy increases. This thesis introduces a 3.5-dimensional simulation of extended air showers and their subsequent emission of fluorescence and Cherenkov light. Utilizing parametrizations for electron-positron distributions, the simulation tool, termed `EASpy`, adopts a novel geometrical approach to determine the number of detected photons by an IACT. This approach significantly reduces computation time compared to traditional ray-tracing methods. Furthermore, `EASpy` can simulate the detector response, including the imaging of the simulated air shower.

Kurzfassung

Die kürzliche Entdeckung durch das LHAASO-Experiment von γ-Strahlenemission im PeV-Energiebereich weist auf die Existenz galaktischer Quellen hin, die in der Lage sind, Teilchen auf Multi-PeV-Energien zu beschleunigen. Dies motiviert eine vertiefte Erforschung von γ-Strahlenquellen über 100 TeV hinaus mit Imaging-Air-Cherenkov-Teleskopen (IACTs). Mit zunehmender γ-Strahlenenergie hängt die Sensitivität von IACTs hauptsächlich von der Sammelfläche A_{eff} ab. Trotz der Erreichung großer Sammelflächen, sogar bis zu 1 km^2, liegt die erwartete Photonenzahl oberhalb von 100 TeV vom Krebsnebel weniger als ein Photon pro 100 Stunden, was die Herausforderungen bei der Detektion solcher hochenergetischer Phänomene unterstreicht.

Diese Arbeit erforscht die Möglichkeiten der Beobachtung ausgedehnter Luftschauer (EAS) bei großen Zenitwinkeln ($\geq 70°$) mit IACTs, um die Sammelfläche im Vergleich zu Beobachtungen bei moderaten Zenitwinkeln signifikant zu erhöhen. Insbesondere wird die Leistung von H.E.S.S. CT5 untersucht. Die Studie konzentriert sich auf Beobachtungen bei einem Zenitwinkel von 80°, indem γ-Strahlen-, Protonen- und Helium-induzierte Luftschauer unter Verwendung von `CORSIKA` und `sim_telarray` simuliert werden. Die abgeleiteten Bildparameter dienen als Input für die Bewertung der γ-Hadron-Trennleistung, der Winkelauflösung und der Energieauflösung bei einem Zenitwinkel von 80° unter Verwendung spezieller Techniken des Random Forest Classifier und des Random Forest Regressor.

Die Untersuchung zeigt die beeindruckende Leistung von H.E.S.S. CT5 und enthüllt eine Sammelfläche von $A_{eff} \sim 5 - 6\,\text{km}^2$ bei 1 PeV nach γ-Hadron-Trennung und Richtungsschnitten, wenn es als eigenständiges Teleskop bei einem Zenitwinkel von 80° betrieben wird. Es wurde festgestellt, dass H.E.S.S. CT5 einen Qualitätsfaktor Q von der Größenordnung $Q \sim 5$ bei einem Zenitwinkel von 80° erreicht. Die Winkelauflösung wird auf $\theta_{68\%} = 0.12°$ für Energien ≥ 10 TeV geschätzt und verbessert sich auf $\theta_{68\%} \leq 0.1°$ für Energien ≥ 100 TeV. Darüber hinaus erweist sich die Energieauflösung besser als 18% bei Energien ≥ 10 TeV.

Monte-Carlo-Simulationen wie `CORSIKA` weisen einen signifikanten Nachteil in Bezug auf erhöhte Rechenzeit und Speicherplatz mit steigender Energie der Primärteilchen auf. Diese Arbeit stellt eine 3,5-dimensionale Simulation ausgedehnter Luftschauer und ihrer anschließenden Emission von Fluoreszenz- und Cherenkov-Licht vor. Unter Verwendung von Parametrisierungen für Elektron-Positron-Verteilungen übernimmt das Simulationswerkzeug namens `EASpy` einen neuartigen geometrischen Ansatz zur Bestimmung der Anzahl der detektierten Photonen durch ein IACT. Dieser Ansatz reduziert die Rechenzeit erheblich im Vergleich zu traditionellen ray-tracing Methoden. Darüber hinaus

kann `EASpy` die Reaktion des Detektors simulieren, einschließlich der Abbildung des simulierten Luftschauers.

Contents

Chapter 1

Observing the Very High Energy Universe

This chapter aims to serve as an introduction to the reader into the field of high energy cosmic rays and very high energy (VHE) γ-ray astronomy. The reader is introduced to the two most fundamental questions:

- What are the acceleration mechanisms?
- What astrophysical objects produce the energetic particles?

The two above mentioned questions are not the only fundamental questions physicists have asked themselves during the rich history of the very high energy universe. It is still very striking that from the time we had clear evidence of the existence of non-thermal high energy processes in our Universe until now we are not able to give a clear answer to these two questions.

In Sec. 1.1 a brief history of high energy cosmic ray physics is described (based on [1] with additional information) with a focus on the two above mentioned questions.

1.1 Evolution of cosmic ray physics

The history of observing the very high energy universe spans over a century of scientific progress and groundbreaking discoveries. The start of this journey marks Viktor Hess with his legendary balloon experiment and the discovery of cosmic rays in 1912 [2]. His measurements were based on the rate of discharge of an electroscope that flew aboard an atmospheric balloon, showing that the ionization level increases with altitude. This

discovery marked the initial awareness of high energy extra-terrestrial particles and he was awarded the Nobel Prize in 1936.

Since then numerous experiments have been conducted to understand the origin of cosmic rays. In 1928 Robert Millikan and Harvey Cameron reported on experiments in high-altitude California lakes. Similar to Viktor Hess they measured the ionization rate with electroscopes at various depth in two lakes with different altitudes (1500 m and 3600 m). They concluded that two meters of water absorbed as much of the radiation as two kilometers of air [3]. In hindsight, their report had more remarkable insights on 'cosmic rays':

"*...These facts, combined with the further observation made both before and at this time, that within the limits of our observational error the rays came in equally from all directions of the sky,... ...all this constitutes pretty unambiguous evidence that the high altitude rays do not originate in our atmosphere, very certainly not in the lower nine-tenths of it, and justifies the designation 'cosmic rays'...*"

The first hints that cosmic rays may be charged particles came also around this time. Jacob Clay observed a lower intensity of radiation at the equator than at the pole (so called "latitude effect") - a direct consequence of the interplay between the charged cosmic rays and the Earth‘s magnetic field. In 1933 Carl D. Anderson discovered the positron by using a cloud chamber in a magnetic field [4]:

"*To date, out of a group of 1300 photographs of cosmic-ray tracks 15 of these show positive particles penetrating the lead, none of which can be ascribed to particles with a mass as large as that of a proton, thus establishing the existence of positive particles of unit charge and of mass small compared to that of a proton.*"

For his discovery of antimatter - just a few years after Paul Dirac's prediction of antimatter in 1928 [5] [1] - Carl D. Anderson shared the Nobel prize with Viktor Hess in 1936. Later on, Carl D. Anderson and his student Seth Neddermeyer also discovered the muon in cosmic rays [7].

In 1933 Bruno Rossi showed that the cosmic ray flux contained a soft and hard component of charged particles. While the soft component could be easily absorbed by a few millimeters of lead, the hard component could traverse up to a meter of lead. He concluded that the hard component must consist of charged particles with maximum energies above 1 GeV [8]:

[1] It should be noted here that one of the first applications of Dirac's quantum theory - a theory to describe the *smallest* scales - was on an object as big as a star. In 1931 S. Chandrasekhar used the relativistic form of the Fermi-Dirac statistic to derive the maximum mass of white dwarfs [6].

"*Aus den gewonnenen Resultaten geht zunaechst hervor, dass ein bedeutender Bruchteil (etwa 50%) der am Beobachtungsort vorhandenen Korpuskularstrahlen eine Reichweite hat, die groesser ist als 1 m Blei, und man kann abschaetzen, dass ihre durchdringendste Komponente wenigstens 2,5 m Blei zu durchsetzen vermag; nach Heisenbergs Angaben ueber die Energieverluste sehr harter Korpuskularstrahlen in der Materie (a. a. 0.) wuerde man daraus schliessen, dass die maximale Energie der durchdringenden Korpuskularstrahlen den Wert von* $1,4 \cdot 10^{10}$ *e-Volt uebertrifft.* "

It was also Bruno Rossi who first observed 'extensive air showers' in 1933: When a cosmic ray with significant energy penetrates the atmosphere, it generates a cascade of secondary particles that can be observed on ground level. The foundation for this 'cascade theory' was delivered by H. Bethe and W. Heitler: They considered in detail the process of a charged particle passing through the electric field of an atomic nucleus. They found that the stopping of electrons with very high energies is mainly due to radiation and calculated the probability for a γ-ray to produce an electron-positron pair [9].

Pierre Auger and his collaborators explored the phenomena of 'extensive air showers' later in that same decade, yielding significant outcomes. They captured coinciding events on the ground even when the detectors were separated by distances of up to 300 m. Utilizing information about the density of particles on the ground and the total covered surface, they derived a total number of 10^6 particles for some of the showers. This estimation implied primary particle energies close to $\sim 10^{15}$ eV. Initially, these cascades were believed to be electromagnetic in nature, i.e., consisting of a succession of gamma-rays and electron-positron pairs. However, the observed coincidences at large distances on the ground exceeded what one would expect from an electromagnetic cascade. Pierre Auger and his collaborators suspected that the extensive lateral spread of the shower may be caused by nuclear collisions that created pions [10]:

"*As we have shown, these facts are in favor of a production of mesotrons in the showers, these mesotrons being able to penetrate the whole atmosphere so that with a small divergence angle they can hit the ground at large horizontal distances from the central beam of the shower, where the electrons and photons are concentrated.* "

The most profound remark in [10] can be found in the conclusion. Little did the authors know that even nearly 100 years later the acceleration processes are still not fully understood:

"*One of the consequences of the extension of the energy spectrum of cosmic rays up to* 10^{15} *eV is that it is actually impossible to imagine a single process able to give to a particle such an energy. It seems much more likely that the charged particles which*

constitute the primary cosmic radiation acquire their energy along electric fields of a very great extension. ”

A proposition of an acceleration mechanism for comic rays was delivered by Enrico Fermi in 1949. In his theory cosmic rays are accelerated in the magnetic fields of interstellar gas clouds (also called ”second-order Fermi acceleration”) [11]. Based on the original work of E. Fermi the notion of ”diffuse shock acceleration” (also called ”first-order Fermi acceleration”) was established [12, 13] and is still considered as the most likely mechanism to accelerate particles up to the highest energies, e.g., [14–16]. Diffuse shock acceleration is a process where charged particles gain energy by repeatedly crossing and interacting with shock waves in astrophysical environments. As particles bounce back and forth across the shock front, they gain energy with each encounter. Eventually the particle obtains enough energy to not be confined anymore and continues its path through the universe.

Closely linked to the acceleration mechanism of cosmic rays is the following question: What astrophysical objects produce cosmic rays?

Walter Baade and Fritz Zwicky were pioneering astrophysicists who tried to give an answer to this fundamental question. They suggested that supernovae, the explosive deaths of massive stars, could produce cosmic rays [17]. The base assumptions for their theory were:

- all cosmic rays are produced in supernovae,
- supernovae emit a fraction of the total released energy in cosmic rays,
- an estimated rate of one supernova per galaxy per thousand years.

With a value of $E_T = 10^{53}$ ergs to 10^{54} ergs for the total amount of energy emitted in the form of cosmic rays from supernovae, they obtained an intensity of cosmic rays reaching the earth of

$$\sigma = 0.8 - 8.0 \cdot 10^{-3}\,\mathrm{ergs\,cm^{-2}\,s^{-1}}.$$

This value was in surprisingly good agreement with observations of the intensity of cosmic rays at that time [18]. Today, the connection between supernovae and cosmic rays remains a fundamental aspect of astrophysics. Supernovae are considered one of the primary sources of low energy cosmic rays, while high energy cosmic rays likely have multiple sources.

The origin of the highest energy cosmic rays was further studied with the construction of numerous cosmic ray air shower detector arrays in the years from 1967 to 2008, like the Haverah Park cosmic ray detector [19] (covering an area of $12\,\mathrm{km}^2$), the Akeno Giant Air Shower Array (AGASA) [20] (covering an area of $100\,\mathrm{km}^2$) or the Pierre Auger Observatory [21] (covering an area of $3000\,\mathrm{km}^2$). These large detection areas are needed since the rate of cosmic rays reaching the Earth falls off rapidly with increasing energy (for a primary energy of $E = 10^{16}\,\mathrm{eV}$ the rate is only a few particles per square meter per year). While the Haverah Park experiment and AGASA used water Cherenkov detectors and Fluorescence detectors respectively, the Pierre Auger Observatory combined both detection methods in a hybrid approach. In 2008 the Pierre Auger Observatory reported on the arrival direction of cosmic rays at the highest energies ($E > 10^{18}\,\mathrm{eV}$) [22] using data with a total integrated exposure of $9000\,\mathrm{km}^2\,\mathrm{sr\,yr}$. The arrival directions seemed to be correlated with the position of nearby active galactic nuclei (AGN). This was one of the first observational hints that cosmic rays of the highest energies might have an extragalactic origin. A decade later, the Pierre Auger Collaboration reported again on large scale anisotropies in the arrival directions of cosmic rays above $4\,\mathrm{EeV}$ [23], [24]. They found a dipolar modulation in right ascension (R.A.) and concluded that the direction of the dipole indicates an extragalactic origin.

A summary of this brief journey - starting from an electroscope on a balloon and energies above a few GeV to $3000\,\mathrm{km}^2$ detector areas and energies above EeV - is given in Fig. 1.1. It shows the differential energy spectrum multiplied by $E^{2.6}$ as a function of energy E and displays three main features of the cosmic ray all-particle spectrum: 1) a steepening between $10^{15}\,\mathrm{eV}$ and $10^{16}\,\mathrm{eV}$ (also called "knee"), 2) another steepening around $10^{17}\,\mathrm{eV}$ (also called "2nd knee"), 3) a plateau around $10^{18.5}\,\mathrm{eV}$ (also called "ankle"). The sudden steepening of the spectrum around $10^{19.2}\,\mathrm{eV}$ is believed to be due to the Greisen-Zatsepin-Kuzmin (GZK) effect [25, 26]. The spectrum unmistakably indicates that the origin of the particles lies in non-thermal phenomena. The precise source of these high energy particles remains largely elusive. Despite nearly a century of dedicated research, the mechanism behind their acceleration and the specific astrophysical objects responsible for their production are still open questions [27–29].

However, a century of research gave definitely more insights into the composition of cosmic rays. Primary cosmic rays are composed mainly of protons (89%), helium (10%) and heavier nuclei ($\sim 1\%$). The fluxes of nuclei up to iron is shown in Fig. 1.2. One can clearly observe that the fractions of primary nuclei are nearly constant up to energies of $10^6\,\mathrm{GeV}$. One methodical approach to study the composition is to determine the atmospheric depth of the shower maximum X_{max} and comparing it to Monte Carlo simulations based on different interaction models [31].

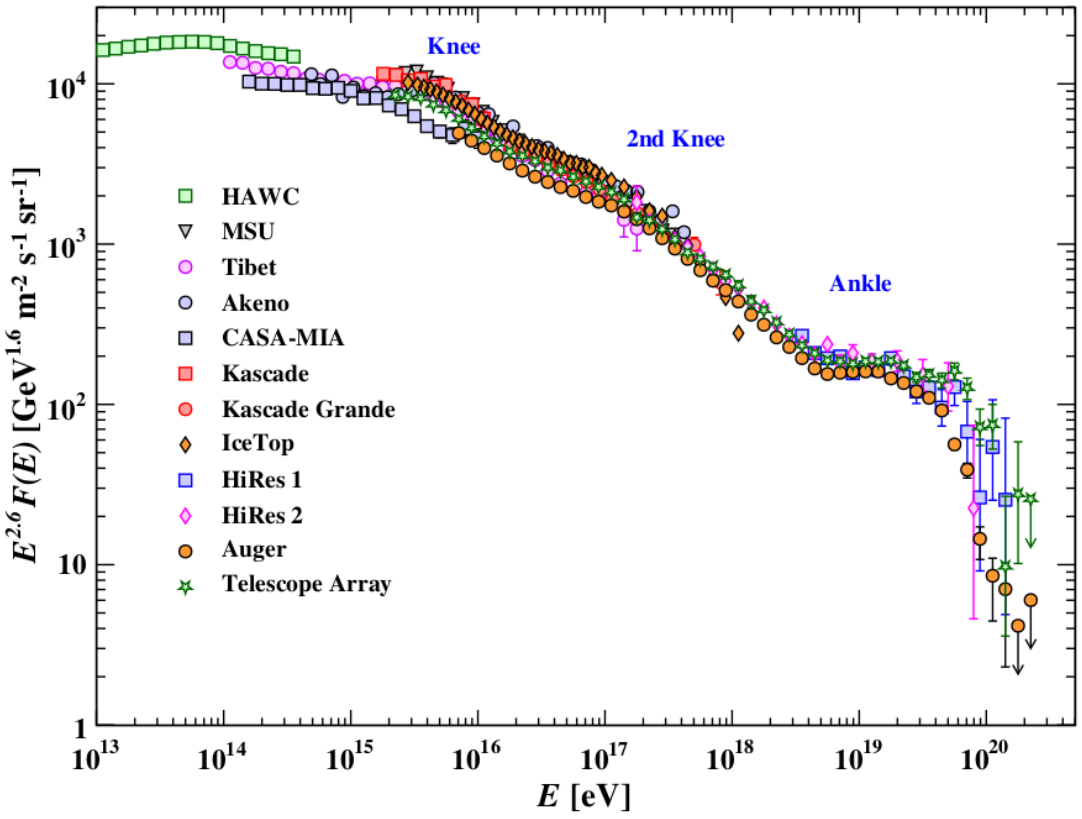

Figure 1.1: All-particle cosmic ray energy spectrum measured with various instruments. Taken from [30].

1.2 Very high energy γ-ray astronomy

Part of the reason why it is so hard to pin-point the astrophysical objects producing cosmic rays lies in the charged nature of cosmic rays. Any directional information is lost since they are deflected by weak magnetic fields in the Milky Way (a few μG, e.g., [32], [33]) or, in the case of extragalactic cosmic rays, by even weaker extragalactic magnetic fields [34]. Therefore, only neutral particles allow to trace back their trajectories in order to determine the location of the astrophysical object of their origin. This limitation reduces the possible candidates to three particles: neutrons, neutrinos and photons[2]. However, neutrons and neutrinos have some caveats: free neutrons are not stable and relatively short-lived, neutrinos are very difficult to detect due to the nature of weakly interacting particles. Therefore, photons, being stable and compared to neutrinos easier to detect, are the optimal candidates for deducing directional information.

In fact, it was quickly realized that phenomena generating non-thermal, extremely high energy charged particles could also result in the production of very high energy photons

[2]In the recent years the detection of gravitational waves have opened a new window on the Universe. For a general overview of 'Multi-messenger astrophysics', including gravitational waves, see [35]

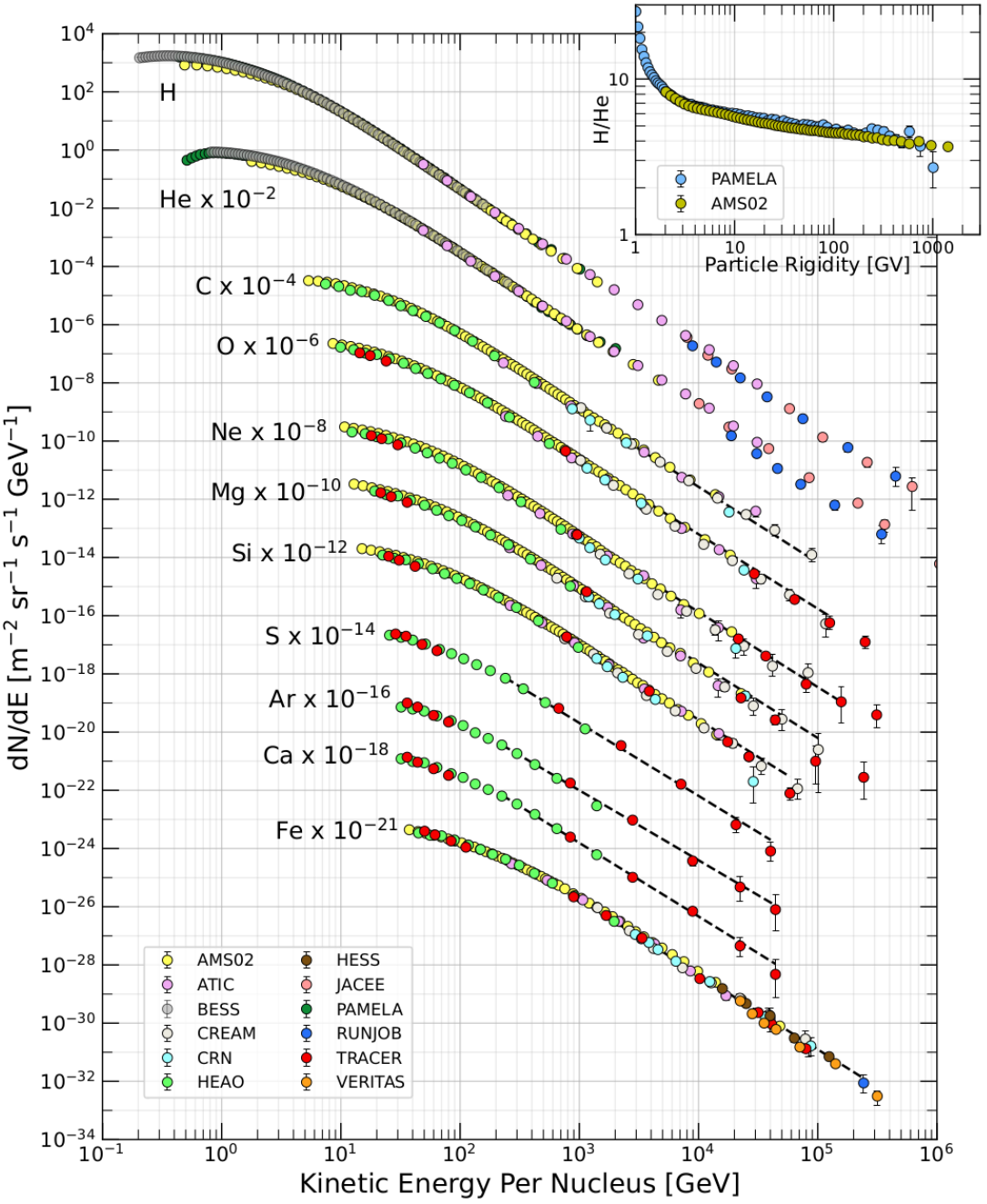

Figure 1.2: Fluxes of cosmic ray nuclei measured with various instruments. The inset figure on the upper right shows the fraction of H/He as a function of rigidity. Taken from [30].

- or VHE γ-rays - through the interaction of these particles with the interstellar medium (ISM), e.g., [36]. In the field of VHE γ-ray astronomy the two main production processes are:

Inverse Compton Scattering

Inverse Compton scattering describes the process of VHE electrons scattering with low energy photons of an ambient photon field γ_{rad}. In this scattering process the VHE electron transfers some if its kinetic energy to the photon:

$$e + \gamma_{\mathrm{rad}} \longrightarrow e + \gamma_{\mathrm{VHE}}$$

The total relevant cross section is given by [37]:

$$\sigma_{\mathrm{IC}} = \pi r_e^2 \frac{1}{x}\left[\left(1 - \frac{2(x+1)}{x^2}\right)\ln(2x+1) + \frac{1}{2} + \frac{4}{x} - \frac{1}{2(2x+1)^2}\right], \tag{1.1}$$

where $x = \frac{h\nu}{m_e c^2}$ and $r_e = \frac{e^2}{4\pi\epsilon_0 m_e c^2}$.

Two reasonable approximations which can be made are for non-relativistic energies ($x \ll 1$) and ultra-relativistic energies ($x \gg 1$). While the non-relativistic case is of no interest here the ultra-relativistic case has an important implication [37]:

$$\sigma_{\mathrm{IC}}^{\mathrm{K-N}} = \pi r_e^2 \frac{1}{x}\left(\ln(2x) + \frac{1}{2}\right), \tag{1.2}$$

meaning that at the highest energies inverse Compton scattering is suppressed. The ultra-relativistic regime is also called "Klein-Nishina" regime [38]. If inverse Compton scattering is the only production process of VHE γ-rays, then the Klein-Nishina effect will leave an imprint on the spectral energy distribution of observed astrophysical objects, namely a steepening of the spectral energy distribution at the highest energies. Consequently, based on the shape of the spectral energy distribution, one could imply that the nature of VHE γ-rays is purely due to leptonic processes.

The mean energy loss rate by inverse Compton scattering for a single electron is given by [37]:

$$-\left(\frac{dE}{dt}\right)_{\mathrm{IC}} = \frac{4}{3}\sigma_{\mathrm{T}} c u_{\mathrm{rad}} \beta^2 \gamma^2, \tag{1.3}$$

where σ_{T} is the Thomson cross section, c is the speed of light, u_{rad} is the energy density of the ambient photon field, $\beta = \frac{v}{c}$ and γ is the Lorentz factor. The two important characteristics of inverse Compton radiation are:

- The emission is proportional to γ^2, meaning that any (leptonic) emission process of lower order in γ can be neglected (e.g., Bremsstrahlung).
- The emission is proportional to the energy density of the ambient photon field. An important one in the field of VHE γ-ray astronomy is the Cosmic Microwave Background (CMB) radiation with $u_{\mathrm{CMB}} = 0.26\,\mathrm{eV/cm^3}$.

The maximum energy the scattered photon can obtain is given by [37]:

$$(\epsilon_\gamma)_{\mathrm{max}} = \frac{4}{3}\gamma^2 \epsilon_{\mathrm{rad}}, \tag{1.4}$$

where ϵ_{rad} is the energy of the photon of the ambient photon field. Using the average energy of a CMB photon $\epsilon_{\mathrm{CMB}} \sim 0.6\,\mathrm{meV}$, this means that a 1 TeV γ-ray is produced by an electron with an energy of $\sim 10\,\mathrm{TeV}$ which corresponds roughly to a Lorentz factor of $\gamma \sim 2 \times 10^7$.

Decay of neutral pions

Pions are created when accelerated protons interact with gas clouds in the ISM, e.g,:

$$\begin{aligned} p + p &\longrightarrow p + p + \pi^0 \\ p + p &\longrightarrow p + n + \pi^+ \\ p + p &\longrightarrow p + p + \pi^+ + \pi^- \end{aligned}$$

Neutral pions have short lifetimes ($\sim 10^{-16}\,\mathrm{s}$) and mainly decay into two photons:

$$\pi^0 \longrightarrow \gamma + \gamma$$

The reaction for the production of π^0 is only possible above a certain energy threshold $E_{\mathrm{thresh}} \sim 280\,\mathrm{MeV}$, assuming that one proton is at rest [37]. Using $m_\pi = 135\,\mathrm{MeV}$ for the rest mass of the neutral pion, the two produced photons will have an energy in the π^0 rest frame of:

$$\epsilon^*_\gamma = \frac{1}{2} m_\pi c^2 = 67.5\,\mathrm{MeV}. \tag{1.5}$$

An approximation for the fraction κ of energy of the incident proton released into the produced photons is $\kappa = 0.17$ [39]. This means that ultra-relativistic protons with kinetic energy E_p can produce VHE γ-rays via the production and subsequent decay of neutral pions, where the energy of the γ-ray is roughly

$$\epsilon_\gamma \sim 0.1 \times E_p. \tag{1.6}$$

The main feature of the pion decay process, compared to the leptonic case, is that it will exhibit a "pion bump" visible in the spectral energy distribution , e.g., [40, 41]. Note, that while the leptonic and hadronic case will produce a specific spectrum, also a combination of both processes could explain certain γ-ray observations.

An unambiguous evidence, independent of the shape of the spectral energy distribution, for hadronic acceleration processes in astrophysical sources would be the detection of neutrinos, since the charged pions are also not stable (lifetime of $\sim 10^{-8}\,\mathrm{s}$) and decay into muons and neutrinos:

$$\pi^+ \longrightarrow \mu^+ + \nu_\mu$$
$$\pi- \longrightarrow \mu^- + \bar{\nu}_\mu$$

Successively, the muons will also decay (lifetime of $\sim 10^{-6}\,\mathrm{s}$) into positrons, electrons and neutrinos:

$$\mu^+ \longrightarrow e^+ + \nu_e + \bar{\nu}_\mu$$
$$\mu^- \longrightarrow e^- + \bar{\nu}_e + \nu_\mu$$

1.3 Shock acceleration

Any theory describing an acceleration mechanism for cosmic rays must be able to reproduce the observed energy spectrum shown in Fig. 1.1. The observed spectrum can be modelled as a power-law, i.e., $\mathrm{d}N(E) \propto E^{-\Gamma}\mathrm{d}E$, where $\Gamma \sim 2.6$. Additionally, the acceleration process must be able to account for the highest observed energies of $E \sim 10^{20}\,\mathrm{eV}$.

As mentioned in Sec. 1.1, a first proposition to explain the acceleration process was delivered by Enrico Fermi in 1949. A brief introduction to his theory, based on the description in [37], together with key results is given in Sec. 1.3.1 and 1.3.2.

1.3.1 Second order Fermi acceleration

In Fermi's original version, charged particles are randomly deflected by magnetic perturbations. The energy E' of the particle after a single collision at incident angle θ (see Fig. 1.3) in the observer's frame is given by [37]:

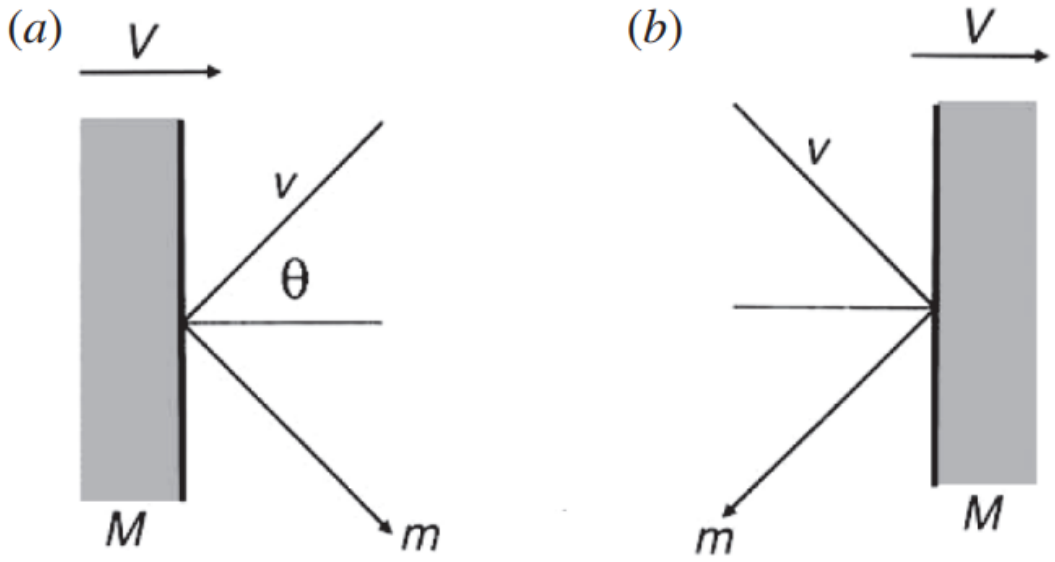

Figure 1.3: Second order Fermi acceleration. Collision between particle of mass m and a (interstellar) cloud of mass M. The angle between the initial direction of the particle and the normal to the surface is θ. Relative velocities between the particle (v) and the cloud (V) are a) $v + V\cos(\theta)$, b) $v - V\cos(\theta)$. Taken from [37].

$$E' = \gamma_V^2 E \left[1 + \frac{2Vv\cos(\theta)}{c^2} + \left(\frac{V}{c}\right)^2\right],$$

where γ_V is the Lorentz factor corresponding to the velocity V of the magnetic perturbation, v is the velocity of the particle and c is the speed of light. Assuming relativistic particles with $v \approx c$ and averaging over all incident angles, the average energy gain per collision is given by [37]:

$$\left\langle \frac{\Delta E}{E} \right\rangle = \frac{8}{3}\left(\frac{V}{c}\right)^2. \tag{1.7}$$

There are two key aspects regarding Eqn. 1.7:

- The average gain in energy is only second order in V/c. Assuming $V/c \sim 10^{-4}$ [37] for the velocities of interstellar clouds, the average energy gain per collision would be of the order of 10^{-8}. This means, that second order Fermi acceleration can only be efficient if a very high rate of collisions could compensate the low energy gain or if the speed of the interstellar cloud is much greater than in the typical ISM.
- Note, that the process would broaden the energy distribution of the accelerated particles even if all particles were injected with a single energy.

As mentioned in the beginning of this Section, the acceleration process must be able to reproduce the observed power-law energy spectrum. This can be derived from the diffusion-loss equation [37]:

$$\frac{\mathrm{d}N}{\mathrm{d}t} = D\nabla^2 N + \frac{\partial}{\partial E}[b(E)N(E)] - \frac{N}{\tau_{\mathrm{esc}}} + Q(E),$$

where $N(E)$ describes the number of particles depending on energy E, D is the diffusion coefficient, $b(E)$ is the energy loss term $b(E) = -\mathrm{d}E/\mathrm{d}t$, τ_{esc} is the characteristic time the particles remain inside the acceleration region and $Q(E)$ is the source term. Re-defining the energy loss term $b(E)$ as an energy gain term, $b(E) = -\alpha E$ where α describes the rate of energy gain, and assuming no diffusion and no sources, the steady-state solution can be found as [37]

$$N(E) = \text{constant} \times E^{-x}, \tag{1.8}$$

where $x = 1 + (\alpha\tau_{\mathrm{esc}})^{-1}$. Indeed, second order Fermi acceleration results in a power-law energy spectrum but it fails to explain why the power-law index should be roughly $x \sim 2.6$.

1.3.2 First order Fermi acceleration

The main restriction of second order Fermi acceleration comes from its low efficiency due to the $(V/c)^2$ scaling in Eqn. 1.7. However, it was realized that acceleration in the presence of strong shock waves may result in higher efficiency and the notion of "diffuse shock acceleration" was established [12, 13].

A strong shock, like in supernova remnants or active galactic nuclei, is characterized by a nearly discontinuous change in density, temperature, and pressure in a medium moving with supersonic speed. Let us call the region in front of the shock front "upstream" and the region behind the shock front "downstream", while the shock wave itself is

propagating with velocity U (see Fig. 1.4). In the rest frame of the shock the velocity of the gas in the upstream region is $v_1 = U$. The velocity of the gas in the downstream region can be derived from the continuity equation:

$$\rho_1 v_1 = \rho_2 v_2.$$

For a strong shock, the compression factor ρ_2/ρ_1 is given by the ratio of specific heat capacities $\kappa \approx \frac{f+2}{2}$ of the gas, where f denotes the thermally degrees of freedom [37]:

$$\frac{\rho_2}{\rho_1} = \frac{\kappa + 1}{\kappa - 1}.$$

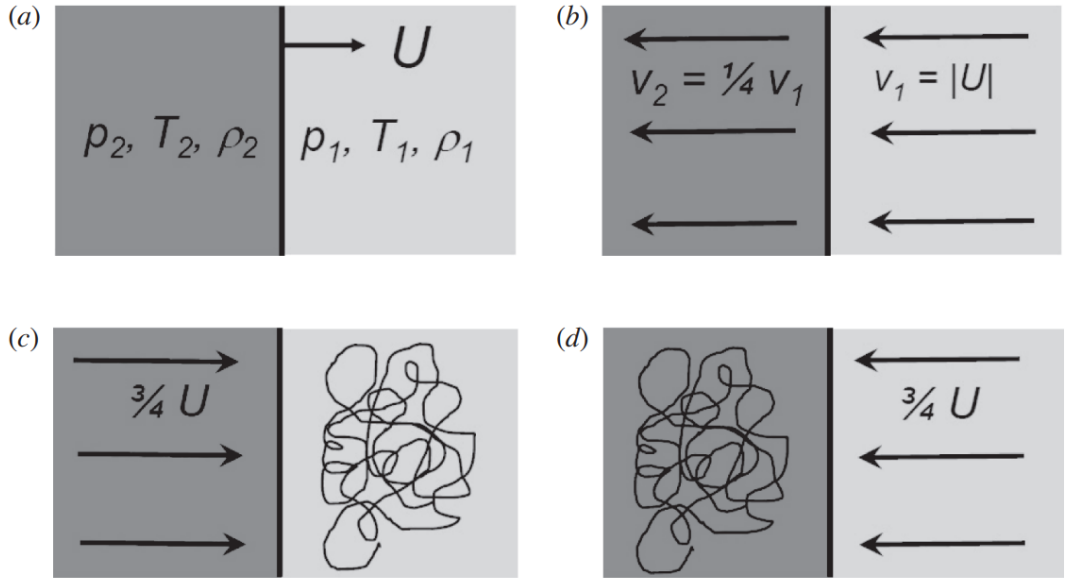

Figure 1.4: Schematic sketch describing the properties of diffuse shock acceleration. Taken from [37].

For a monoatmoic gas, with 3 degrees of freedom, $\kappa = \frac{5}{3}$, such that $\rho_2/\rho_1 = 4$. Therefore, the velocity of the gas in the downstream region is $v_2 = \frac{1}{4}v_1$ (see Fig. 1.4 (b)). For a test particle in the rest frame of the upstream region the gas in the downstream region is approaching with a velocity of $\frac{3}{4}U$. The same picture holds for a test particle in the rest frame of the downstream region - now the gas in the upstream region is approaching with a velocity of $\frac{3}{4}U$ (see Fig. 1.4 (c) and (d)). In both cases, the particles scatter randomly due to streaming instabilities or turbulent motions such that the resultant particle velocity distribution becomes isotropic on either side of the shock.

Similar to Sec. 1.3.1, one can calculate the average gain in energy for each crossing [37]:

$$\left\langle \frac{\Delta E}{E} \right\rangle = \frac{2}{3}\frac{V}{c}, \tag{1.9}$$

where $V = \frac{3}{4}U$ is the velocity of the gas approaching the particle in the rest frame of the upstream or downstream region. Note, that the gain in energy is now first order in V/c.

Let us now define P as the probability that the particle remains inside the accelerating region and β as the energy ratio of the particle after (E) and before (E_0) one cycle of crossing, i.e., $\beta = \frac{E}{E_0} = 1 + \frac{4}{3}\frac{V}{c}$. Equivalent to Eqn. 1.7, one can show that first order Fermi acceleration also reproduces a power-law differential energy spectrum [37]:

$$N(E)\mathrm{d}E \propto E^{-1+(\ln P/\ln \beta)}\mathrm{d}E. \tag{1.10}$$

The beauty of diffuse shock acceleration lies in the fact, that it naturally produces a power-law index Γ close to $\sim$2.6. For a strong shock the logarithm of the escape probability P and the efficiency β is $\frac{\ln P}{\ln \beta} = -1$ and therefore $\Gamma = 2$, which is close to the observed power-law index.

The maximum energy a particle can obtain is constraint by the time the particle remains within the acceleration region. This is directly connected to the gyroradius:

$$r_g = \frac{\gamma m c^2}{qeB},$$

where γ is the Lorentz factor, m is the mass and q is the charge of the particle, c is the speed of light and B is the magnetic field strength. The condition is that r_g has to be smaller than the physical size L of the accelerator. The maximum energy E_{max} a particle can acquire is given by:

$$E_{\mathrm{max}} = zeBUL, \tag{1.11}$$

where ze is the charge of the particle. The above criteria is also known as "Hillas criteria" [42]. Note, that Eqn. 1.11 scales with the atomic number z. Therefore, heavier ions can be accelerated to higher energies compared to less massive ions by the same accelerator.

Using Eqn. 1.11 and estimating B and L for a variety of astrophysical sources, one can deduce which sources are capable to accelerate particles to a specific maximum energy. This is shown in Fig. 1.5 for protons with energies of 100 EeV (red dotted line) and 1 ZeV (red solid line) and for iron with an energy of 100 EeV (green solid line). Sources which

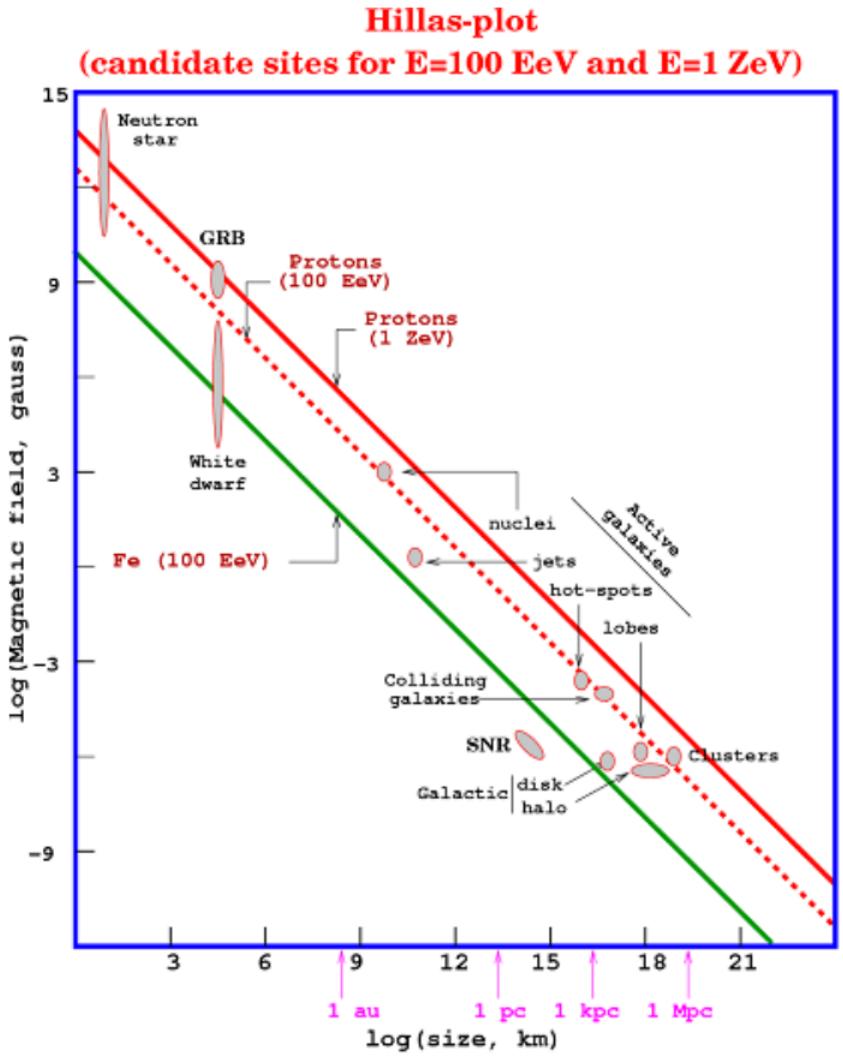

Figure 1.5: Magnetic field strength B as a function of physical size L for a variety of astrophysical sources. The red dotted line marks protons with energies of 100 EeV, the red solid line protons with energies of 1 ZeV and the green solid line iron with an energy of 100 EeV. All sources above the corresponding lines are capable to accelerate particles up to the respective energy. Taken from [43].

are able to accelerate particles up to these energies lie above the corresponding line. While supernova remnants (SNRs) can not account for the three mentioned examples, active galactic nuclei, clusters of galaxies, gamma-ray bursts (GRBs) and neutron stars seem to be able to produce and accelerate particles at these energies. A brief overview of the majority of the astrophysical sources in Fig. 1.5 is given in Section 1.4.

1.4 Source candidates

1.4.1 Supernova remnants

In general, (core-collapse) supernovae emerge when the nuclear fuel of a star is exhausted, such that nuclear fusion can not counteract the gravitational pressure anymore. The result is a spherical blast wave, ejecting outer shells of the stellar material into the interstellar medium. The kinetic energy of the ejected material is typically about 10^{51} erg [37]. The presence of molecular clouds in the vicinity of the supernova may act as target material for hadronic emission processes. In fact, there have been claims regarding hadronic accelerators beeing present at supernova remnants via the detection of the characteristic "pion bump", e.g., [44]. The stellar remnant of this violent event is either a neutron star or a black hole, depending on the mass of the object.

There exist two basic types of supernovae, Type I (absence of hydrogen lines in optical spectrum) and Type II (hydrogen lines present in optical spectrum). All supernovae types besides Type Ia are associated with the core-collapse of massive stars. Supernovae Type Ia result from the thermonuclear explosion of accreting white dwarfs and show remarkable similarities in their light curves. Therefore, they are used as "standard candles" for redshift-distance relations of objects with redshift $z \gtrsim 1$ [37].

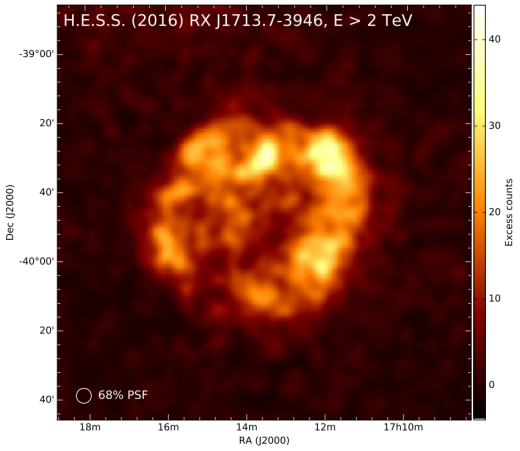

(a) Gamma-ray excess count image of RX J1713.7-3946 for events above an energy threshold of 2 TeV. The 68% containment radius of the point spread function (PSF) corresponds to 0.036°.

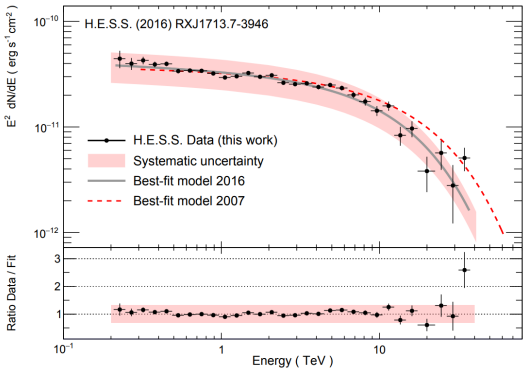

(b) Observed energy flux spectrum of RX J1713.7-3946 with H.E.S.S.. Best-fit model (gray solid line and dashed red line) is an exponential cut-off power-law model, i.e., $\mathrm{d}N/\mathrm{d}E = F_0 E^{-\Gamma} \exp(-E/E_{\mathrm{cut}})$.

Figure 1.6: H.E.S.S. observation of RX J1713.7-3946 [45].

One of the best-studied gamma-ray supernova is RX J1713.7-3946. It is one of a handful detected and spatially resolved gamma-ray supernova (see Fig. 1.6a). The observed energy spectrum with the High Energy Stereoscopic System (H.E.S.S.) extends up to energies of ∼30 TeV and shows a characteristic cut-off that sets in between 10 TeV to

20 TeV (see Fig. 1.6b). In an earlier report, the H.E.S.S. collaboration detected significant γ-ray emission beyond 30 TeV from RX J1713.7-3946, approaching nearly 100 TeV [46].

1.4.2 Pulsars and pulsar wind nebulae

Pulsars are neutron stars that rotate with periods ranging from 1.4 ms to 11 s and possess a very strong magnetic field ($\sim 10^{12}$ G) [47, 48]. The existence of neutron stars as a result of core-collapse supernovae was theoretically predicted in the 1940s [17, 49] and first detected in the form of a pulsar in 1967 [50]. Shortly thereafter, the first connections between pulsars and rapidly rotating neutron stars were established [51, 52].

The characteristic mass of a neutron star is approximately $M \approx 1 - 2\,M_{\odot}$, and via the relation

$$R_{\mathrm{NS}} \approx 4.5 \cdot \frac{\hbar^2}{G m_p^{8/3}} \cdot M^{-1/3} \tag{1.12}$$

the typical radius of a neutron star is $R_{\mathrm{NS}} \approx 1.2 \times 10^6$ cm [48]. Due to conservation of angular momentum and the significant reduction in size from $R_{\mathrm{Star}} \approx 10^{11}$ cm to $R_{\mathrm{NS}} \approx 10^6$ cm, the rotation of the neutron star accelerates to periods in the millisecond range during the collapse.

Pulsars have the rotation axis and magnetic field axis inclined at an angle to each other. As the pulsar rotates, the magnetic field axis undergoes a precession motion around the rotation axis. Electromagnetic radiation is then emitted from the magnetic poles, which is detectable by observers if they are within the generated radiation field. This results in the observer perceiving the radiation as pulsating.

For pulsars, the period P and its first time derivative $\dot{P}$ can be directly observed. Generally, $\dot{P} > 0$ is observed for isolated pulsars (no accretion). However, there are instances where the pulsar's rotation undergoes short term acceleration, resulting in an increase in the period over timescales of $\sim$ days to $\sim$ years until it returns to its original value. The cause of these period jumps (also known as 'glitches') has not been fully understood to date. A more detailed description and possible theories are discussed in [53, 54].
Using information about P and $\dot{P}$, the characteristic quantity $\dot{E}$ ('spin-down energy') can be defined as:

$$\dot{E} = \frac{dE_{\mathrm{rot}}}{dt} = I\Omega\dot{\Omega},$$

with $\Omega = \frac{2\pi}{P}$ and moment of inertia I. It is believed that this energy budget is used for the emission of electromagnetic radiation and particle acceleration [55]. Typically, the efficiency for converting spin-down energy into γ-ray emission is $\leq 10\%$ [56], with the majority of energy output carried away in the form of a pulsar wind.

The Crab Nebula has been detected by numerous instruments at TeV energies and beyond (e.g., [57–60]). In the very high energy regime ($\geq 100\,\mathrm{GeV}$), only two pulsars have been detected so far - the Crab pulsar [61] and Vela [62].

1.4.3 Active galactic nuclei

Most galaxies are known to host a supermassive black hole (SMBHs) at their centers, with masses exceeding million to billion times that of our Sun (mass $> 10^6$ $\mathrm{M}_\odot$) [63]. A small percentage ($\approx 3\%$) of these galaxies contain *active* SMBHs, and these active ones are predominantly found in large elliptical galaxies [64]. These black holes primarily increase in size through periods of efficient gas accretion, during which they become exceptionally bright and detectable as active galactic nuclei (AGN) [65].

When the core of a galaxy is in an active state, the supermassive black hole at its center draws in nearby matter, leading to the conversion of gravitational potential energy into kinetic energy and thermal radiation [65]. In certain instances, the energy release can give rise to two relativistic jets that extend outward in a bipolar and symmetrical fashion, reaching distances of several hundred kiloparsecs (kpc) from the galactic center [66]. The AGN, consisting of the accretion disk, torus, and corona, emits radiation across the entire electromagnetic spectrum, from radio to γ-ray wavelengths. These jets, comprising a plasma of relativistic particles, are propelled by magnetic fields [67]. The radio-emitting jets associated with an AGN can span considerable distances, often extending beyond the optical bulge of their host galaxies and reaching hundreds of kiloparsecs into the intergalactic medium.

AGN are among the most powerful known astrophysical objects, with luminosities in the range of $10^{42}\,\mathrm{erg/s}$ to 10^{48} erg/s [68]. They can release approximately 10% of the rest-mass energy of the material they accrete, and this energy release can have significant consequences for the surrounding environment, ultimately affecting the host galaxy. This phenomenon, known as AGN feedback, has the potential to alter the properties of the gas within the galaxy and influence the process of star formation [69]. In local galaxies, there exists a strong correlation between the mass of the black hole at the galaxy's center, the central velocity dispersion, and the mass of the galactic bulge. This correlation suggests the possibility of either co-evolution or feedback mechanisms at play, regulating the relationship between SMBHs and their host galaxies [70].

Well known AGN detected at energies of 1 TeV and beyond are Mrk 421 and Mrk 501 [71–73].

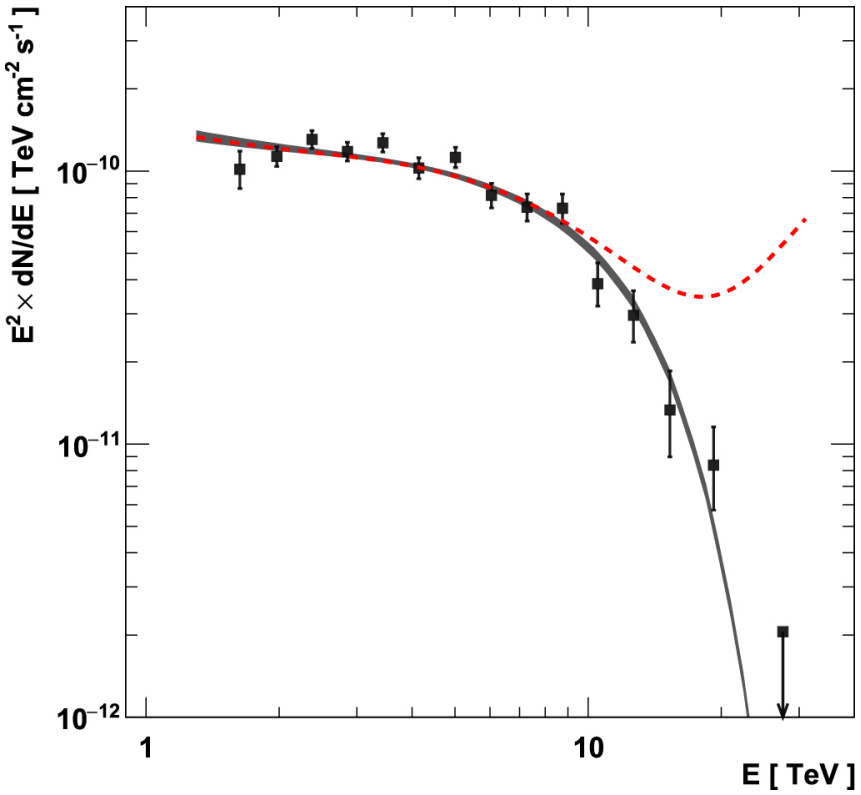

Figure 1.7: Energy spectrum observed with H.E.S.S. during a flaring state of Mrk 501 in 2014 [72]. Spectral points are indicated by filled squares, the solid line represents the best fit power law including attenuation on the extra galactic background light, the dashed red line is obtained by considering sub-luminal linear Lorentz invariance violation.

As an example, the energy spectrum of Mrk 501 during a flaring state in 2014 [72] is illustrated in Fig. 1.7. The report in [72] revealed multi-TeV variability of Mrk 501 on *minutes* timescales Δt, indicating that the emission region R can not be larger than $R \sim c \cdot \Delta t \sim 6 \times 10^{-7}$ pc, where c denotes the speed of light.

1.4.4 Gamma-ray bursts

Gamma-Ray Bursts (GRBs) are intense and brief flashes of γ-ray radiation, lasting for timescales of $\mathcal{O}(1\,\mathrm{s})$ to $\mathcal{O}(100\,\mathrm{s})$ [74]. Most GRBs feature a narrow beam of radiation, where the energy release in γ-rays is typically around $\mathcal{O}(10^{50}\,\mathrm{ergs})$, e.g., [75]. This relativistic beaming effect makes GRBs only detectable when the observer is aligned with the jet. In general, GRBs can be classified into two main stages: the prompt emission and the afterglow.

The prompt emission is the initial burst of γ-rays. The exact mechanism responsible for the prompt emission is not fully understood to date, but it is believed to arise from the dissipation of energy during the collapse of massive stars or the merger of compact objects, such as neutron stars or black holes [74]. However, some observations also suggest an association with supernovae, e.g., [76]. Additionally, it is believed that the prompt emission is driven by internal shocks, i.e., when different parts of the ejected material collide within the relativistic jet [74].

After the initial prompt stage, emission across a range of wavelengths - called afterglow -, from radio to γ-ray wavelengths, can be observed for a prolonged period of time $\mathcal{O}(100\,\mathrm{s})$. It is believed that the afterglow is caused by the interaction between the ejected material from the GRB and the surrounding interstellar medium (leading to so called "external shocks"), i.e., when the relativistic ejecta is slowed down by the surrounding matter. At later stages, the radiation processes become less efficient, leading to a transition into an adiabatic phase [74].

The by far brightest ever observed GRB is GRB221009A, located at a redshift of $z = 0.151$ [77]. With a bolometric fluence of $0.21\,\mathrm{erg\,cm^{-2}}$, almost three orders of magnitude higher than any previously reported GRB, it can be considered as a once in a lifetime event (recurrence rate at Earth of ~ 10000 years) [78]. To convey the exceptional nature of this event, a comparison of the differential flux between the Crab Nebula - one of the brightest steady galactic sources - and GRB221009A is presented in Fig. 1.8. Note, that GRB221009A is located almost 5 magnitudes of order farther away from the Earth than the Crab Nebula. Furthermore, the LHAASO collaboration reported on the detection of γ-ray emission from GRB221009A up to energies of roughly $\sim$10 TeV [79].

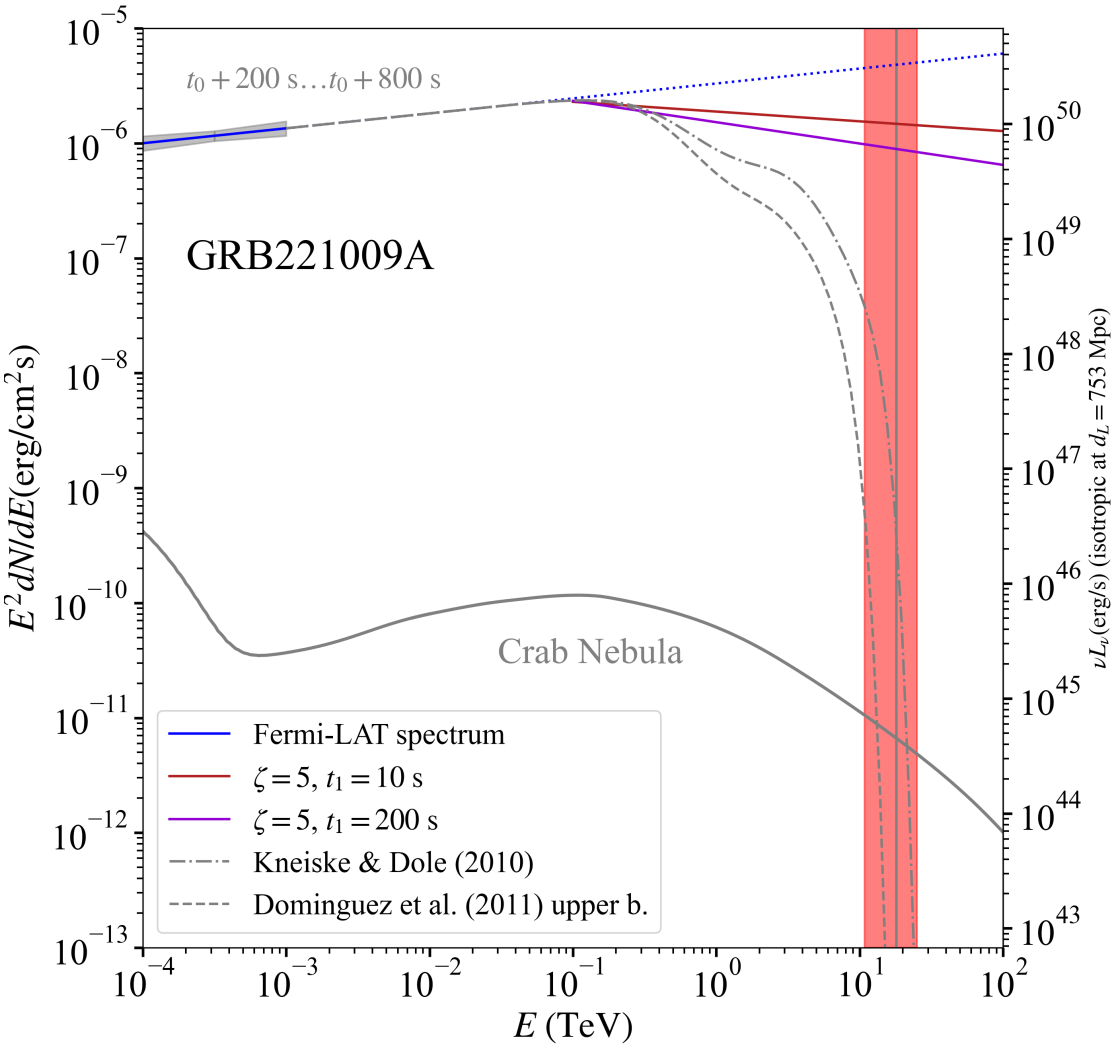

Figure 1.8: The gray shaded area indicates the estimated confidence region of the *Fermi*-LAT time averaged spectrum ($t_0 + 200$ s…$t_0 + 800$ s) of GRB221009A. The extrapolation to the highest energies is marked with a dotted line. The dash and dash-dotted lines are obtained by considering absorption on the extra galactic background light (EBL) using two specific EBL models. $\zeta = F_{VHE}/F_X$ describes two free parameters used in [77] for a time-dependent model of the flux of GRB2201009A, where F_X is the energy flux in the X-ray band and F_{VHE} in the very high energy regime. The vertical grey line marks an energy of 18 TeV, while the red shaded area corresponds to a relative energy resolution of 40 %. The SED of the Crab Nebula is taken from [80]. Figure is taken from [77].

Chapter 2

Extensive Air Showers

As mentioned in Section 1.1, a cascade of secondary particles is generated when a cosmic ray or γ-ray penetrates the atmosphere. This chapter aims to give a more in-depth description of the different cascade processes to the reader as well as general characteristics of extensive air showers. First of all, a brief overview of frequently used terms in the field of extensive air showers is given, followed by a description of hadron initiated showers and γ-ray (or lepton) initiated showers. The properties of Cherenkov light and fluorescence light are describe in Sec. 2.3 and Sec. 2.4, respectively.

The total number of produced particles in an extensive air shower at a specific level h in the atmosphere is called shower size $N(h)$. Commonly, it covers all produced charged particles, neglecting produced photons or neutrinos. The shower size N mainly depends on the energy E_0, the zenith angle θ, and the height of the first interaction h_1 in the atmosphere of the primary particle. Along the path of the primary particle, more and more mass in the atmosphere will be penetrated. This traversed mass density along the path of the primary particle is called slant depth X and it is measured in units of g/cm^2 from the top of the atmosphere. It is also common to express the shower size as a function of slant depth X, since h and X are directly related to each other:

$$X = \int \rho(h)\,\mathrm{d}s, \tag{2.1}$$

where $\rho(h)$ is the density at height h and $\mathrm{d}s$ is the traversed slant distance along the trajectory of the primary particle. The depth of the shower maximum $X_{\max}$ is reached, when the shower development has reached its maximum $N_{\max}$, i.e., $N_{\max} = N(X_{\max})$. A primary particle with higher energy will be able to penetrate more mass in the atmosphere, hence $X_{\max}$ will increase as the energy of the primary particle increases [81].

The shower axis (see Fig. 2.1 (a)) is determined by extending the initial momentum vector (i.e., the momentum vector before the first interaction) of the primary particle along the path of the cascade's progression. It is used as reference axis for the description of the longitudinal and lateral development of the air shower. The shower front has a disk-like structure and broadens slightly with increasing radial distance from the shower axis. In general, lower energy particles will be further away from the shower axis compared to higher energy particles. The number of particles as a function of arrival time for a hadron initiated shower is shown in Fig. 2.1 (b). The majority of the particles will arrive in a narrow time window of a few 10 ns, while the tail of the signal extends up to ∼200 ns.

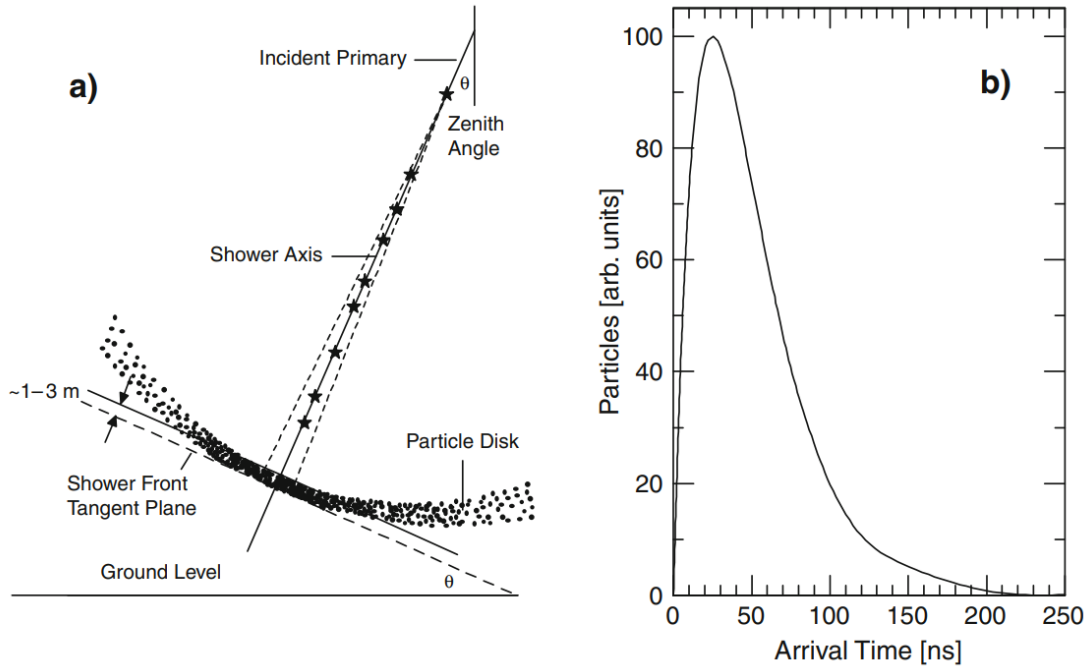

Figure 2.1: a) Schematic sketch of the shower axis and shower front of an air shower. b) Number of particles as a function of arrival time for a hadron initiated air shower. Taken from [81].

2.1 Electromagnetic showers

Electromagnetic showers are caused by either leptons or γ-rays. Here, especially γ-ray initiated air showers are of interest because they are not deflected by galactic (or extragalactic) magnetic fields and therefore carry information about the source of their origin.

The main cascade processes involved in the development of electromagnetic showers are electron-positron pair-production by photons and Bremsstrahlung by electrons in the

Coulomb field of a nucleus. Additionally, whenever a charged particle is propagating through a medium of atomic number Z it will suffer ionization losses. In the following description of the electromagnetic cascade these ionization losses are not further discussed. However, the critical energy E_{crit} where an electron loses equal amount of energy per unit radiation length X_0[1] by ionization and Bremsstrahlung should be mentioned here. In a gaseous medium, the critical energy is approximately given by [81]:

$$E_{\text{crit}} \approx \frac{710}{Z + 0.92}\,[\text{MeV}].$$

The effective atomic number Z_{eff} for air is $Z_{\text{eff}} = 7.6$, such that in air $E_{\text{crit}} \approx 83\,\text{MeV}$. The electromagnetic radiation length X_0 can be approximated as [82]:

$$\frac{1}{X_0} \approx 4\alpha r_e^2 \frac{N_A}{A} Z^2 \ln(183\, Z^{-1/3}), \tag{2.2}$$

where α is the fine-structure constant, r_e the classical radius of the electron, N_A is Avogadro's number and A is the mass number of the medium. Using Eqn. 2.2 yields $X_0 = 36.7\,\text{g}\,\text{cm}^{-2}$ for (dry) air. Energy losses of electrons and positrons due to ionization are causing a rapid extinction of the shower when the energy is below E_{crit}.

Above E_{crit} the main energy loss of an electron(positron) is by Bremsstrahlung in the Coulomb field of a nucleus. The average energy loss per slant depth X is given by [37]

$$-\left\langle \frac{\mathrm{d}E}{\mathrm{d}X} \right\rangle_{\text{br}} = \frac{E}{X_0}, \tag{2.3}$$

hence, the (relativistic)[2] Bremsstrahlung energy loss rate is proportional to the energy E of the electron. The opening angle of the emitted photons due to Bremsstrahlung is related to the Lorentz factor of the electron:

$$\langle \theta \rangle = \frac{1}{\gamma}.$$

Additionally, multiple scattering of the electrons leads also to a broadening of the shower.

The incident γ-ray and the emitted photons due to Bremsstrahlung can create a electron-positron pair in the field of a nucleus, if the photon energy is greater than $2m_e c^2$, where m_e is the electron mass. Overall, the succession of pair production and Bremsstrahlung leads to a cascade of secondary particles. A very simple model to illustrate the electromagnetic cascade process was developed by Heitler [83]. In his model he considered only

[1] Radiation length X_0 is defined as the distance at which the energy is reduced by a factor of 1/e.
[2] In the non-relativistic case the energy loss rate is proportional to $E^{1/2}$ [37]

pair production and Bremsstrahlung for the cascade process, while the energy is always distributed equally among the secondary particles at eacht step (see Fig. 2.2).

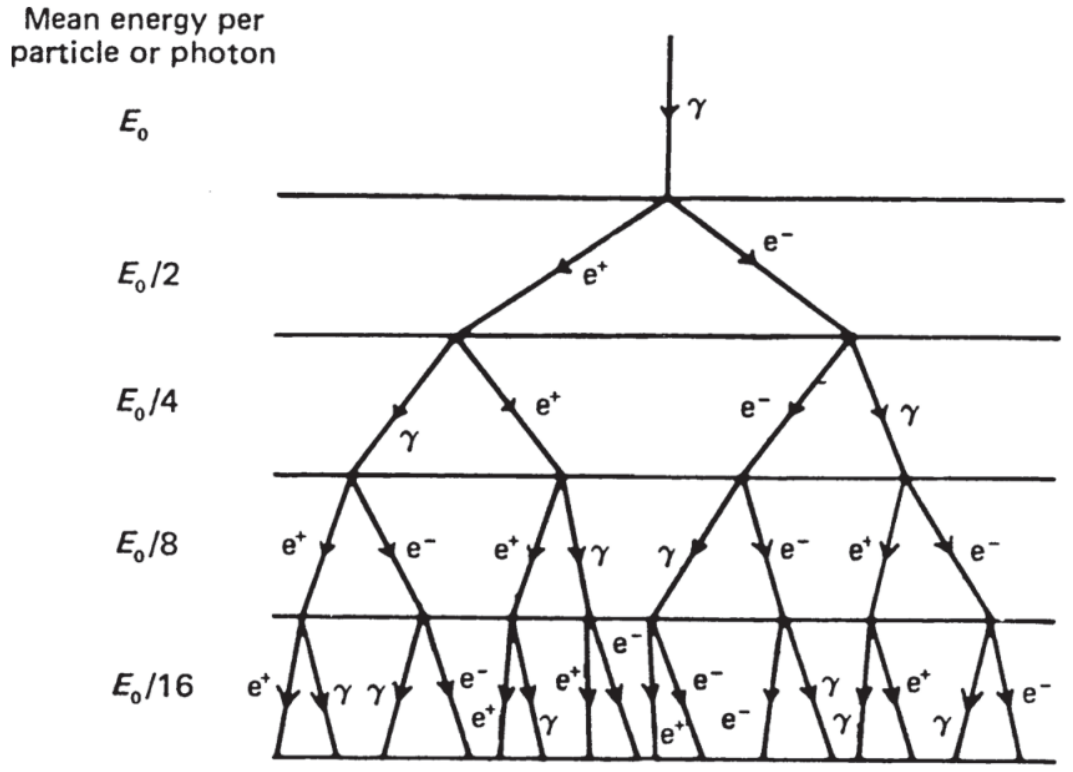

Figure 2.2: Heitler model for an electromagnetic shower. Taken from [37].

The branching in Fig. 2.2 takes place after one radiation length X_0, such that after $n = X/X_0$ steps the number of particles $N(X)$ is

$$N(X) = 2^{X/X_0}.$$

Since energy is split equally at each step, the energy $E(X)$ of each produced particle at slant depth X is given by:

$$E(X) = E_0/N(X),$$

where E_0 is the energy of the incident γ-ray. The shower will continue to develop until the critical energy is reached, i.e., $E(X) = E_{\text{crit}}$. Therefore, the number of particles at the shower maximum is

$$N_{\text{max}} = N(X_{\text{max}}) = \frac{E_0}{E_{\text{crit}}}$$

and the depth of the shower maximum can be expressed as

$$X_{\max} = X_0 \frac{\ln(E_0/E_{\text{crit}})}{\ln(2)}.$$

Hence, the number of particles at the shower maximum is directly proportional to the energy of the incident γ-ray, $N_{\max} \propto E_0$, and the corresponding depth is proportional to the logarithm of the energy, $X_{\max} \propto \ln(E_0)$.

2.2 Hadronic showers

Similar to electromagnetic cascades initiated by γ-rays, high energy cosmic ray protons (or heavier nuclei) initiate nucleonic cascades. During this process, short lived pions are produced which subsequently decay, causing an electromagnetic sub-shower due to the decay products (see Fig. 2.3). This fact already has an important implication, since any experiment sensitive to the detection of the electromagentic cascade initiated by γ-rays will eventually also capture electromagnetic sub-showers initiated by high energy cosmic rays. Indeed, the vast majority of extensive air showers are caused by high energy cosmic rays - therefore, hadronic showers are a significant background source for, e.g., Imaging Air Cherenkov Telescopes (IACTs, see Sec. 2.5).

One way to distinguish γ-ray induced showers from hadronic showers is by capturing the differences in the lateral development of the shower. While the lateral spread of the γ-ray induced shower is caused mostly by multiple Coulomb scattering of the electrons, the lateral spread of the hadronic shower is due to the transverse momentum of the produced secondary particles in the nucleonic cascade. As a result, the development of the γ-ray induced air shower is close to the shower axis whereas in the hadronic case the air shower shows a larger lateral extension [81].

This is also shown in Fig. 2.4a and Fig. 2.4b, where a 100 TeV γ-ray induced air shower is compared to a 100 TeV proton induced air shower. One can clearly observe a different spatial structure between the two showers. Not only are the particles strongly beamed in the forward direction in Fig. 2.4a compared to Fig. 2.4b, γ-ray induced air showers show also less fluctuations in their development.

The height of the first interaction h_1 of the primary in the atmosphere as well as the height where $N_{\max}$ is reached increases with increasing primary mass. Hence, the depth of the shower maximum $X_{\max}$ will decrease for heavier nuclei (the composition of cosmic rays is indicated in Fig. 1.2) induced showers compared to proton induced showers of the same energy [81].

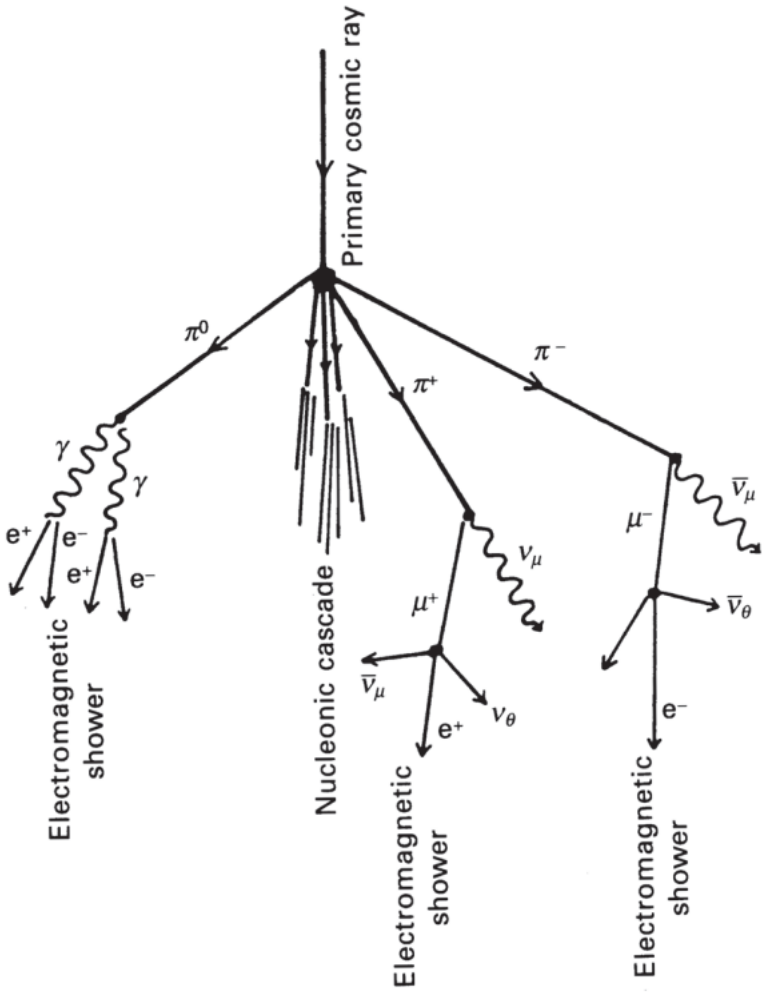

Figure 2.3: Schematic example of a hadron initiated air shower. Taken from [37].

2.3 Cherenkov light

When a charged particle moves with velocity v through a dielectric medium, it polarizes the molecules along its path, such that a dipole field in the vicinity of the charged particle is formed. If v is smaller than the speed of light in that medium (given by $c = c_0/n$, where n denotes the refractive index of the medium and c_0 the speed of light in vacuum), the polarization field is symmetric around the charged particle (see Fig. 2.5). Contrary, for $v > c_0/n$ the polarization field is asymmetric in the direction of motion of the charged particle. This asymmetry causes constructively interfering wavefronts, when the polarized molecules return to their ground state via the emission of electromagnetic radiation [85].

Since the emitted photons have a smaller velocity than the charged particle, the emission angle θ_{Ch} can be calculated as:

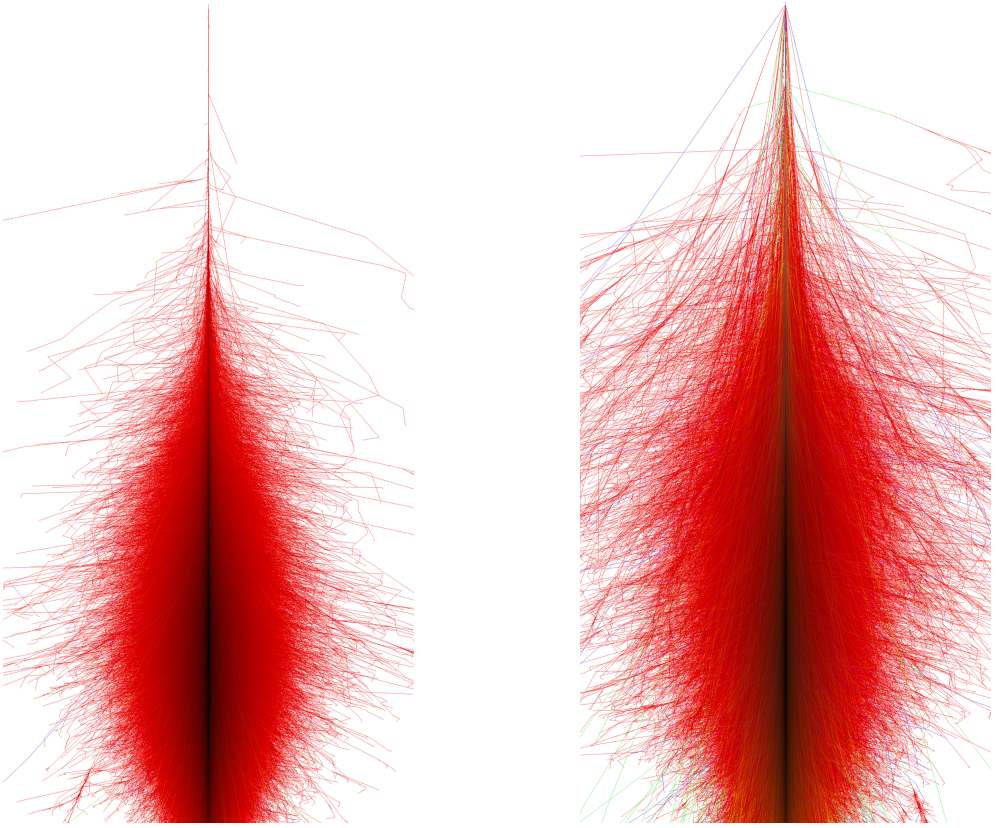

(a) 100 TeV γ-ray induced air shower. (b) 100 TeV proton induced air shower.

Figure 2.4: Simulated air showers for primary particle energy of 100 TeV. Red trajectories mark the path of electrons, positrons and gammas, green trajectories mark the path of muons and blue trajectories the path of hadrons. Horizontal axis spans ± 5 km measured from the shower axis. Height of first interaction is at 30 km in both cases. Taken from [84].

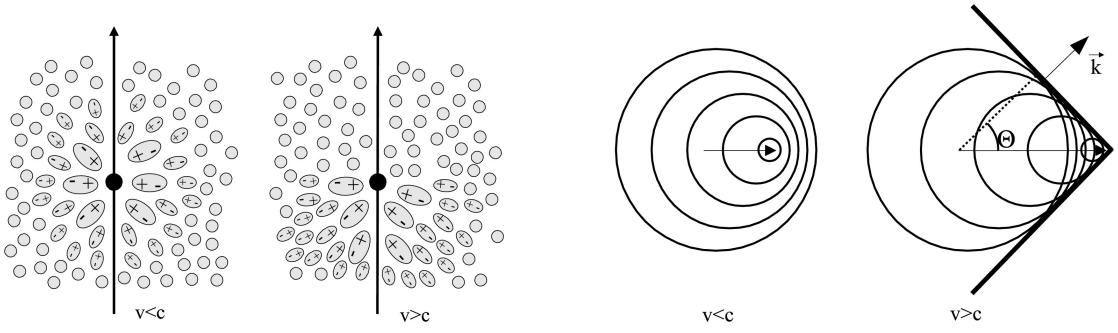

Figure 2.5: Left: Schematic sketch of the polarization of a dielectric medium (gray shaded areas) caused by a charged particle (black circle) with velocity $v < c$ and $v > c$, where c denotes the speed of light in the medium. Right: Cherenkov wavefront with opening angle θ. Taken from [85].

$$\cos(\theta_{\mathrm{Ch}}) = \frac{c_0}{vn}. \tag{2.4}$$

This effect is named after Pavel Cherenkov, for which he was awarded the Nobel prize together with I. Frank and I.Tamm in 1958. Note, that the Cherenkov opening angle in Eqn. 2.4 depends on the refractive index n. Therefore, θ_{Ch} is a function of altitude h in air, since the refractive index of the atmosphere changes depending on the density $\rho(h)$.

The number of photons N emitted per unit length $\mathrm{d}x$ travelled by the particle per unit of wavelength λ is given by the Frank-Tamm formula:

$$\frac{\mathrm{d}^2N}{\mathrm{d}x\mathrm{d}\lambda} = 2\pi\alpha Z^2\lambda^{-2}\left(1 - \frac{1}{\beta^2 n^2}\right). \tag{2.5}$$

Note, that in Eqn. 2.5 $\frac{\mathrm{d}^2N}{\mathrm{d}x\mathrm{d}\lambda} \propto \lambda^{-2}$, which means that the resulting spectrum of emitted Cherenkov photons follows a $1/\lambda^2$ distribution. Furthermore, Eqn. 2.5 also gives a condition for the emission of Cherenkov photons, since for $\left(1 - \frac{1}{\beta^2 n^2}\right) < 0$ the right hand side of the equation is not defined, i.e., the threshold for Cherenkov emission is reached. This condition can be translated into an energy threshold E_{Ch} by using $E = \gamma m_e c_0^2$ and $\gamma = (1-\beta^2)^{-1/2}$:

$$E_{\mathrm{Ch}} = \frac{m_e c_0^2}{\sqrt{1 - \frac{1}{n^2}}}, \tag{2.6}$$

yielding 21 MeV for electrons at sea level.

With respect to extensive air showers, the interplay of the altitude dependent Cherenkov angle θ_{Ch} and the emission height leads to a characteristic distribution of photons at the ground. This is also shown in Fig. 2.6 for an air shower at zenith angle $\theta = 0°$ ("vertical shower"). The Cherenkov light cone produced by a particle at 10 km height has a radius of about $\sim$ 130 m at ground. The overall distribution has a ring-like structure on the ground with a peak intensity at a radius R of 150 m around the core position. At distances $R > 150$ m the photon density on the ground steadily decreases, since the main bulk of the produced secondary particles will stay close to the shower axis [85].

Near the core of the shower, photons emitted at lower altitudes reach the detector before those emitted at higher altitudes. Conversely, at larger distances from the impact point, photons emitted at lower altitudes have a longer total path compared to those emitted at higher altitudes. As a result, the photons from lower altitudes arrive at the detector after the photons from higher altitudes. Overall, the shower has a duration of a few ns

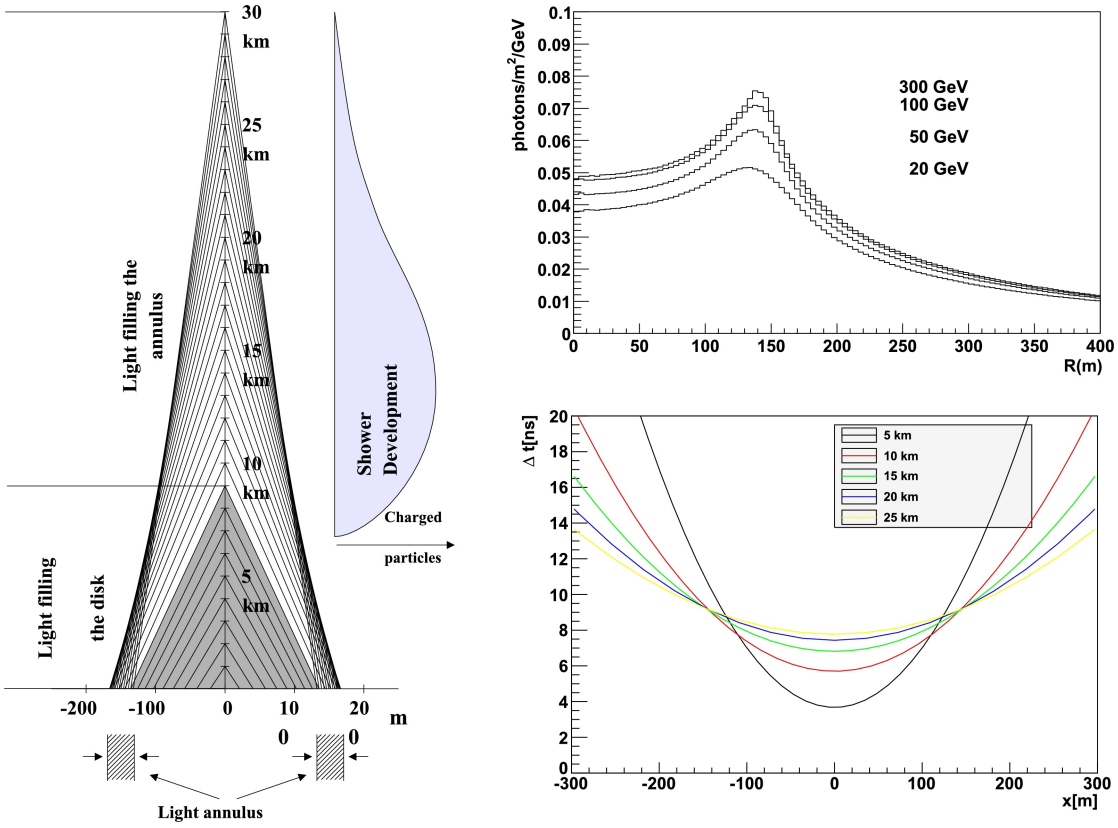

Figure 2.6: Left: Direction of Cherenkov light emitted by particles close to the shower axis for a vertical shower. Upper right: Photon density per unit of energy as a function of radial distance R to the shower core. Lower right: Arrival time of Cherenkov light as a function of lateral distance x for various emission heights. Taken from [85].

and the duration of the light pulse reaching the detector depends on the impact distance (see Fig. 2.6 lower right) [85].

Cherenkov photons undergo scattering and absorption processes while propagating through the atmosphere. These processes reduce the detectable light intensity at ground level and shift the spectrum of emitted photons. Particularly, due to Rayleigh and Mie scattering, shorter wavelength photons experience substantial scattering, while photons with wavelengths below 200–300 nm are predominantly absorbed. As a result, the peak of the emitted Cherenkov light distribution is shifted from UV wavelengths to the optical blue band [86].

2.4 Fluorescence light

Charged particles within an extensive air shower will excite or ionize molecules along their path through the atmosphere. The excited molecules will then return to their ground state by the emission of atmospheric fluorescence light. In the near-ultraviolet (UV) region, molecular nitrogen is primarily responsible for the emission of fluorescence

light. The two molecular systems of interest are the Second Positive system (2P) of N_2 and the First Negative system (1N) of N_2^+ (see Fig. 2.7) [87]. Together with the change of the vibrational and rotational states of the molecule, these transitions lead to several fluorescence emission bands [87]. The majority of the emitted fluorescence light falls within a wavelength range from 300 nm to 400 nm.

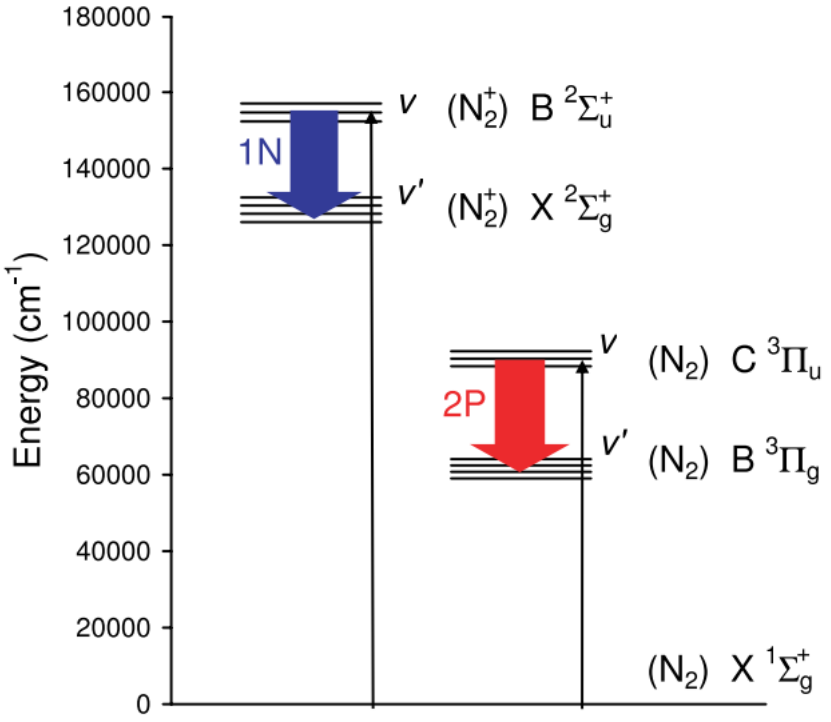

Figure 2.7: Schematic diagram of the (1N) and (2P) system of molecular Nitrogen. Nitrogen molecules are excited from ground state to an upper level v (thin black arrow) before relaxing to a lower level $v\prime$ (thick blue and red arrow). Taken from [87].

The excitation of the nitrogen molecules is caused mostly by electrons and positrons produced in the cascade process of an extensive air shower. The radiative lifetimes of the molecular states of the (1N) and (2P) system are of the order of $\mathcal{O}(10\,\text{ns})$, while the lifetime in the lower atmosphere reduces down to $\mathcal{O}(1\,\text{ns})$ [88]. This effect is caused by excited molecules returning to their ground state without emitting light through collisions with water vapor molecules (also called "collisional quenching" effect). Therefore, the emission of fluorescence light in air depends on several atmospheric parameters like pressure, temperature and humidity.

The parameter quantifying the emission of fluorescence light in air is the fluorescence yield Y_{air} - it represents the number of photons emitted per unit of energy deposited by electrons or positrons. The fluorescence yield in air is usually expressed in terms of the absolute yield of the 337 nm band in dry air at reference pressure p_0 and temperature T_0:

$$\frac{Y_{air}(\lambda, T, p, p_w)}{Y_{air}(337, T_0, p_0)} = \frac{I_\lambda(T_0, p_0)}{I_{337}(T_0, p_0)} \cdot \frac{1 + p_0/p'_{337}(T_0)}{1 + p/p'_\lambda(T, p_w)}, \tag{2.7}$$

where λ is the wavelength of the emitted fluorescence photon, p is the ambient atmospheric pressure, p_w is the water vapour partial pressure, T is the temperature, $I_\lambda(p_0, T_0)$ is the specific intensity and the function $p'_\lambda(T, p_w)$ takes into account temperature-dependent non-radiative de-excitation effects. Importantly, the fluorescence yield in air is found to be essentially independent of the energy and type of ionizing particle, indicating that the fluorescence emission is directly proportional to the energy deposited in nitrogen molecules [89].

Contrary to Cherenkov light, fluorescence light is emitted isotropically. Consequently, a large fraction of the emitted fluorescence photons will not propagate in the direction of a detector on the ground. However, the isotropic nature of fluorescence emission allows for efficient coverage of the sky using telescopes. As an (extreme) example: A telescope (sensitive to the detection of fluorescence and Cherenkov light) pointing at zenith will eventually be able to capture the fluorescence light emitted by an air shower coming from the horizon (i.e., at a zenith angle of 90°) but it will not be able to detect the Cherenkov light due to its directed emission.

Similar to Cherenkov light, fluorescence photons will also undergo scattering and absorption processes along their path through the atmosphere. The effects of these processes, especially for observations at large zenith angles, are discussed in Sec. 4.1.6.

2.5 Imaging air Cherenkov telescopes

The γ-ray production mechanisms discussed in Sec. 1.2 generally yield steeply falling power-law spectra, resulting in a very low photon flux at very high energies. The integrated flux of the Crab Nebula, one of the brightest steady galactic γ-ray sources, above energies of 1 TeV is $\sim 2 \times 10^{-11}\,\mathrm{cm^2\,s^{-1}}$ [90] which translates to only ∼7 photons per square meter per year. Hence, observing astrophysical sources at these energies require a very large collection area, which is not feasible with satellite-based experiments orbiting the earth. Imaging Air Cherenkov Telescopes (IACTs) achieve collection areas of the order of $\mathcal{O}(10^5\,\mathrm{m^2})$ by capturing the Cherenkov light produced in the cascade process of an extensive air shower (see Sec. 2.1 and Sec. 2.3).

These optical telescopes feature a large mirror (typically consisting of several mirror tiles) designed to focus the Cherenkov light onto a camera system (see Fig. 2.8). The

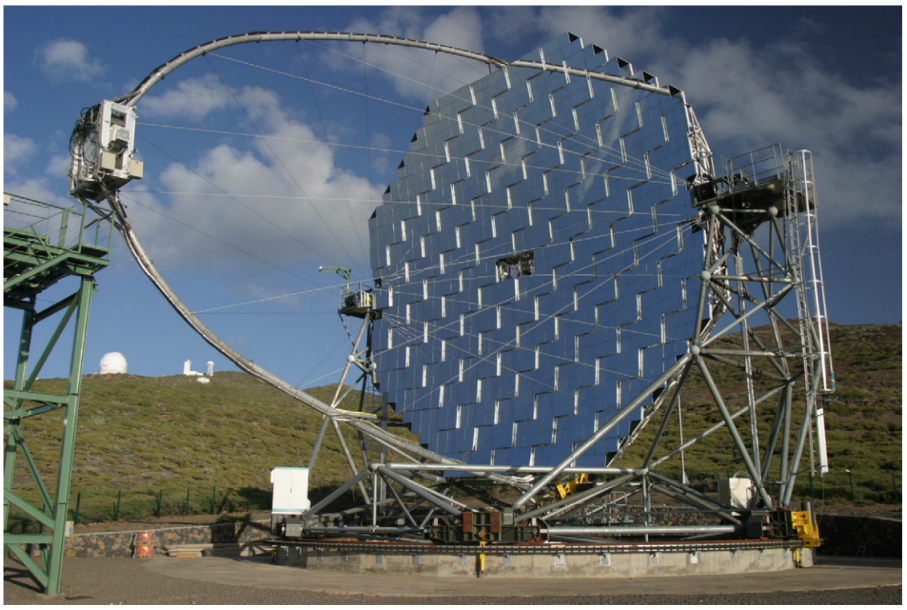

Figure 2.8: One of the two Cherenkov telescopes of the MAGIC experiment located on the Canary Island of La Palma. Taken from [91].

mirror area of operating Cherenkov telescopes ranges from, e.g., $\sim$115 m^2 (VERITAS) to $\sim$615 m^2 (H.E.S.S. II) using either a parabolic or Davies-Cotton optical design [92]. The mirror reflects and directs the incoming Cherenkov light, such that it reaches the camera at the focal plane of the optical system. The camera system, typically equipped with an array of photomultiplier tubes (PMTs) or Geiger-mode avalanche photodiodes (GAPDs), converts the Cherenkov light into an electrical signal. Modern camera systems can record both the intensity and arrival times of the incoming light, allowing for the spatial and temporal reconstruction of the air shower. The typical total field of view of the current generation of IACTs is around 3° to 5° on the sky, while the field of view of a single pixel is $\sim$0.1° (see, e.g., Tab. 2.1). Dedicated data analysis techniques are then applied to reconstruct the camera images and extract valuable information about the properties of the primary particle (e.g. the energy, direction, and type) by using the properties of the recorded image (e.g., its shape, intensity and orientation). The camera image of the observed Cherenkov light has generally a compact elliptical shape for γ-ray initiated air showers, where the ellipse is defined by the minor axis and major axis of the ellipse. The major axis of the ellipse indicates the shower axis projected onto the image plane, while the minor axis quantifies the lateral extension of the air shower.

The geometrical reconstruction of the air shower can be improved by using an array of telescopes. Indeed, almost all current experiments using the air Cherenkov technique have two or more telescopes typically placed $\sim$100 m apart from each other. This allows for the recording of several images of the same air shower, such that the intersection of the major axes of the ellipses defines the arrival direction of the shower. This approach

is also referred to as "stereoscopic imaging technique" (see Fig. 2.9). Additionally, the stereoscopic approach provides more effective suppression of the background light caused by hadronic showers. The first experiment proving the capabilities of stereoscopic IACT arrays was the HEGRA experiment [93], consisting of 4 telescopes[3] with a mirror area of only 8.5 m^2 per telescope and a pixel size of 0.25°. Using this array of telescopes, they were able to detect significant γ-ray emission from the Crab Nebula and Mkn 501 up to energies of ∼10 TeV [94]. The mirror area of Cherenkov telescopes has significantly increased over time, in order to extend the energy spectrum of observed sources to lower energies ($\leq$ 1 TeV). Since the amount of produced Cherenkov light scales with the energy of the primary γ-ray, larger optical systems were needed in order to optimize lower energy sensitivities.

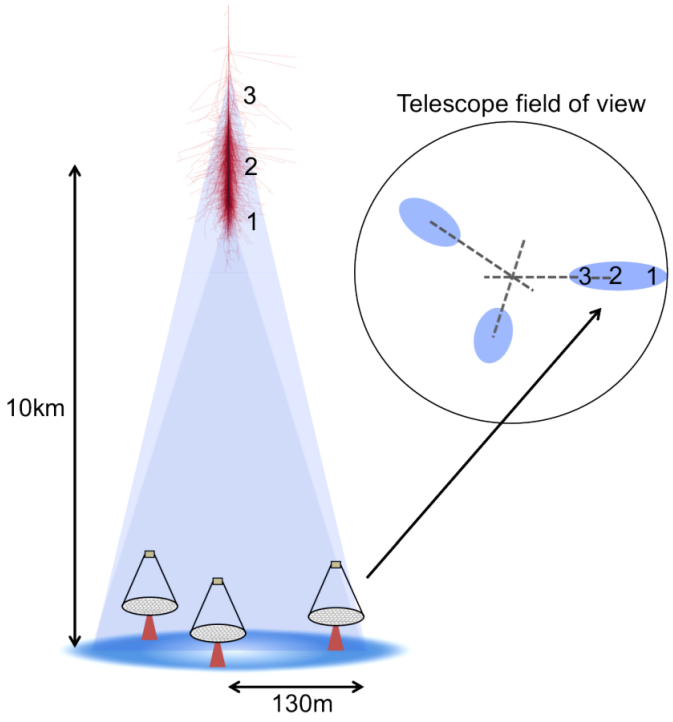

Figure 2.9: Schematic sketch of an IACT array observing the Cherenkov light produced by an extensive air shower. Each of the telescopes record an image of the shower (blue shaded ellipses), allowing to reconstruct the origin by intersecting the major axes of the ellipses. Taken from [95].

Commonly, the data analysis techniques mentioned earlier involve a moment analysis of the image. This analysis is used to derive several parameters that describe the elliptical shape of the recorded image. As mentioned in the beginning of this Chapter, the development of hadron initiated air showers differs from γ-ray initiated air showers, which consequently also impacts the shape of the recorded image for these two shower types. The parameters describing the shape of the image can then be used to define cuts with

[3]The final configuration of the HEGRA IACT array had 6 telescopes.

the aim to reduce the number of background events in the analysis. The first one who realized the potential of this approach was A.M. Hillas, after whom these parameters are named - "Hillas parameter" [96]:

"*It is shown that it should be possible to distinguish very effectively between background hadronic showers and TeV gamma-ray shower from a point source on the basis of the width, length and orientation of the Cerenkov light images of the shower, seen in the focal plane of a focusing mirror, even with a relatively coarse pixel size ... It is found that hadronic showers have longer and more fluctuating images (leading particle effect), and are wider (due largely to emission angles of pions), and are not systematically aligned with the source (if isotropic) ...*"

With respect to IACTs, it is very striking that even after nearly 40 years most of the modern γ-hadron seperation techniques use this rather simple set of parameters to improve their background rejection power. A brief overview of the Hillas parameters used in Chapter 3 is given in Sec. 2.5.1.

2.5.1 Image parameters

Besides the contribution from Cherenkov light, the recorded image will also contain a fluctuating signal caused by the night-sky background (NSB) light. Therefore, dedicated algorithms are applied with the aim to remove the contribution from NSB light, before calculating the Hillas parameters of the image ellipse. The number of pixels surviving this cleaning process is termed **npix**.

A summary of the basic Hillas parameters is given in Fig. 2.10. In the following, a brief description of these parameters is provided.

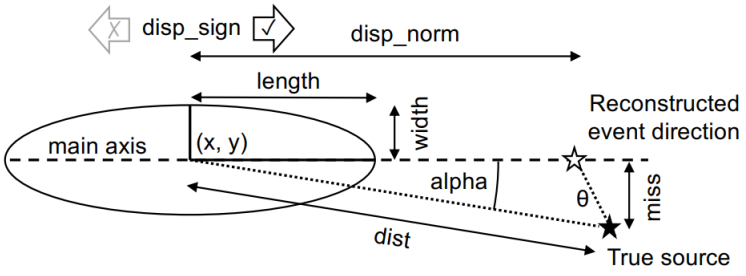

Figure 2.10: Basic Hillas parameters of an example image ellipse. Taken from [97].

- The **image size** A is the sum of all pixel amplitudes a_i which survived the cleaning process. Here, the subscript i denotes the pixel number.

$$A = \sum_i a_i.$$

- The **Center of Gravity (CoG)** of the image ellipse describes the first moment of the amplitude distribution a_i in the camera.

$$CoG_x = \frac{\sum_i a_i \times x_i}{A},$$
$$CoG_y = \frac{\sum_i a_i \times y_i}{A},$$

  where x_i and y_i denotes the position of the pixel i in the camera.

- The **length** of the ellipse describes the RMS angular size in the direction of the (semi-) major axis of the ellipse. In the rotated coordinate system $(x\prime, y\prime)$ (i.e., such that the CoG defines the origin of the coordinate system), the length parameter can be calculated using the second moments:

$$length = \sqrt{\frac{\sum_i a_i x\prime_i^2}{A}}.$$

- The **width** of the ellipse describes the RMS angular size in the direction of the (semi-) minor axis of the ellipse.

$$width = \sqrt{\frac{\sum_i a_i y\prime_i^2}{A}}.$$

- The parameter **disp_norm** denotes the angular distance between the CoG and the reconstructed source position in the camera, where **disp_sign** (either +1 or -1) gives the direction.

- The parameter $\boldsymbol{\alpha}$ denotes the angle which is enclosed by the major axis and the vector formed by the CoG and the true source position in the camera. The angular distance between the major axis and the true source position in the camera is denoted by the **miss** parameter, while the parameter $\boldsymbol{\theta}$ quantifies the angular distance between the true source position and the reconstructed source position. Ideally, all three parameters have values close to $\sim 0^\circ$ for γ-ray air showers originating from point-like sources.

- The angular distance between the CoG and the true source position in the camera is denoted by the **dist** parameter.

These image parameters are widely used in experiments, like the High Energy Stereoscopic System (see Sec. 2.5.2) and the upcoming Cherenkov Telescope Array (see Sec. 2.5.3).

2.5.2 H.E.S.S.

The High Energy Stereoscopic System (H.E.S.S.) consists of five IACTs located in the Khomas Highlands of Namibia at an altitude of 1800 m above sea level. The telescopes are arranged in a square, where four identical telescopes (CT1 - CT4) with a dish diameter of 12 m are placed at the corners of the square and one large telescope (CT5) with a dish diameter of 28 m is placed at the center of the square. The installation and construction of CT1-CT4 ("Phase I") started in Summer 2002 and was completed in December 2003, when all four IACTs were operational. "Phase II" of the H.E.S.S. project started with the inauguration of CT5 in September 2012, which improved the lower energy sensitivity of the H.E.S.S. project due to the unprecedented mirror area of $\sim 615\,\mathrm{m}^2$.

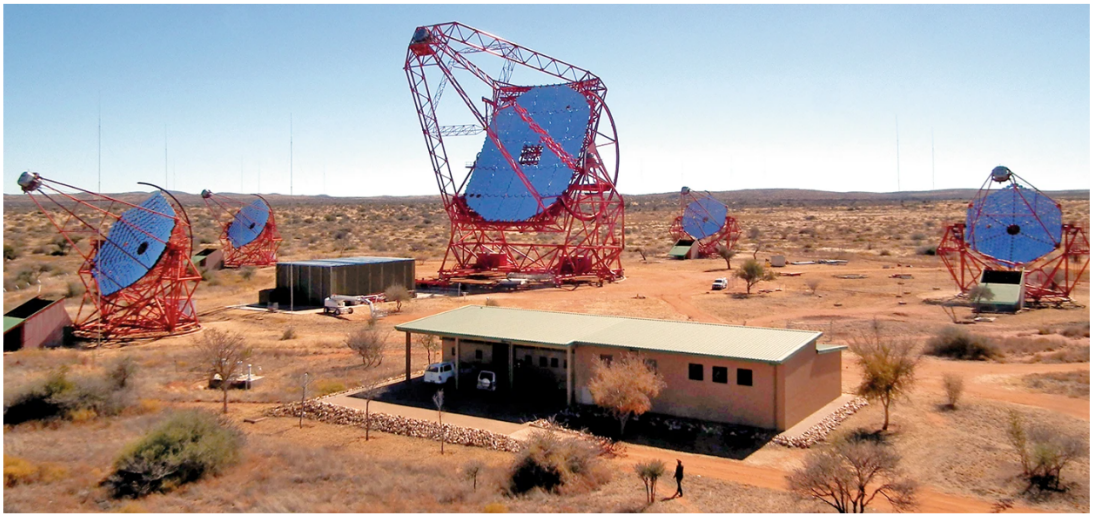

Figure 2.11: The IACT array of H.E.S.S. in Namibia. Taken from [98].

All five IACTs have a reflector dish that focuses incoming rays onto the camera at the focal plane of the optical system. For CT1-CT4, the hexagonal reflector dish consists of 382 round mirror segments with a diameter of 60 cm respectively. The shape of the reflector follows a Davis-Cotton optical design with a focal length of 15 m. CT5 has a circular dish consisting of 875 hexagonal mirror segments, which considerably reduces the gaps between the mirror tiles compared to round mirror tiles. The flat-to-flat size of the hexagonal mirrors measures 90 cm and they are arranged such that the shape of reflector has a parabolic form with a focal length of 36 m. The camera of CT1-CT4 (CT5) features 960 (2048) PMTs with a 1 GHz signal sampling rate and two gain channels for each pixel.

For convenience, a summary of the properties of CT1-CT5 is provided in Table 2.1.

	CT1-CT4	CT5
Optical design	Davies-Cotton	Parabolic
Focal length	15 m	36 m
Mirror area	108 m^2	614 m^2
Mirror facets	382 round facets	875 hexagonal facets
Number of pixels	960 (hexagonal)	2048 (hexagonal)
Pixel size	42 mm (= 0.16°)	42 mm (= 0.067°)
Field of view	5°	3.2°
Effective exposure time	16 ns	16 ns
Image recording rate	500 images/s	3600 images/s
Weight	60 tons	580 tons

Table 2.1: Specifications of the five IACTs of H.E.S.S. `https://www.mpi-hd.mpg.de/HESS/pages/about/HESS_I_II/`

2.5.3 CTA

The Cherenkov Telescope Array (CTA) is planned to include two arrays of IACTs located in the northern (on the Canary Island of La Palma in Spain) and southern (at Paranal in Chile) hemispheres. These IACTs will come with mirrors of three different sizes, each designed for specific energy ranges.

The northern hemisphere array will primarily focus on the low and mid energy ranges from 20 GeV to 5 TeV, while the southern hemisphere array will encompass the mid to high energy range from 150 GeV to 300 TeV. In the final form, these IACT arrays will include three types of telescopes: Small-Sized Telescopes (SSTs), Medium-Sized Telescopes (MSTs), and Large-Sized Telescopes (LSTs).

The SSTs, designed to have an optimized sensitivity in the energy range from 5 TeV to 300 TeV, will be stationed in the southern array. The optical system has a modified Schwarzschild-Couder dual-mirror optical design [99] with a primary reflector diameter of ∼4 m. The use of a dual-mirror system reduces the point spread function over a large field of view, allowing for more accurate imaging of air showers. Consequently, this leads to improved angular resolution for γ-ray observations. In total, there will be 37 SSTs distributed across several square kilometers in the southern hemisphere. A prototype of the SST (the ASTRI-Horn telescope) has successfully demonstrated the performance of this telescope type with the detection of the Crab Nebula at TeV energies [100].

The MSTs cover the core energy range from 150 GeV to 5 TeV of the CTA project. Currently, two optical designs for the MSTs are investigated and tested: a single reflector with a diameter of 12 m and a Schwarzschild-Couder dual-mirror optical design with a

	SST	MST	LST
Number of telescopes	37 (S)	14 (S), 9 (N)	4 (N)
Desired energy range	5 TeV - 300 TeV	150 GeV - 5 TeV	20 GeV - 150 GeV
Optical design	Schwarzschild-Clouder	Davies-Cotton	Parabolic
Focal length	2.15 m	16 m	28 m
(Effective) Mirror area	$>5\,\mathrm{m}^2$	$88\,\mathrm{m}^2$	$370\,\mathrm{m}^2$
Mirror facets	18 hexagonal	86 hexagonal	198 hexagonal
Number of pixels	2048	1764/1855[4]	1855
Pixel size	0.16°	0.17°	0.10°
Field of view	8.8°	7.5°/7.7°	4.3°
Weight	17.5 tons	89 tons	103 tons

Table 2.2: Specifications of the three telescope types of CTA `https://www.cta-observatory.org/project/technology/`. The acronyms "S" and "N" refer to "South" and "North" respectively.

primary mirror diameter of 9.7 m. Additionally, two versions of the camera for the single-mirror MST were developed - NectarCAM [101] and FlashCAM [102], while the dual-mirror MST uses silicon photomultipliers [103] (SiPMs, similar to the camera of the SST). The NectarCAM will be used on 9 MSTs of the northern array and FlashCAM for 14 MSTs of the southern array. Currently, the dual-mirror MSTs are planned for a future stage of the CTA project but a prototype has already successfully detected the Crab Nebula with a significance of $8.6\,\sigma$ using 21.6 h of observational data [104].

The LSTs, with their parabolic reflector of 23 m in diameter, are designed to cover the lowest energy range of the CTA project. By using reinforced carbon fiber and steel tubes, the telescope's resulting weight is only 103 tons. This allows the telescope to be repositioned to any point in the sky within 20 seconds, which is an important feature for transient observations, such as follow-up observations of GRB alerts. The construction of the first (LST-1) of the four LSTs in the northern hemisphere was completed in October 2018. Currently, LST-1 is in the commissioning phase and the construction of the remaining three telescopes is foreseen for mid 2024. The design of LST-1 has proved to reach the expected performance with the detection of the Crab Nebula and Pulsar, yielding an energy threshold at trigger level of around $\sim 20\,\mathrm{GeV}$ [105].

A summary of the properties of the three telescope types is provided in Tab. 2.2. The LST-1 during an observation in May 2021 is shown in Fig. 2.12.

2.6 Large zenith angle observations

At increasing primary energy, the sensitivity of IACTs to observe the produced Cherenkov and fluorescence light from an extended air shower depends mainly on the collection area

Figure 2.12: LST-1 located at the Canary Island of La Palma. Picture was taken by the author of this thesis during a shift in May 2021.

A_{eff}. As mentioned in Sec. 2.5, the integrated flux of the Crab Nebula above energies of 1 TeV is roughly ~ 7 photons per square meter per year. Above energies of 100 TeV, the expected photon rate reduces even further: for a collection area as large as $A_{\text{eff}} = 1\,\text{km}^2$ the photon rate is less than one photon per 100 h, while the current generation of IACTs reach an effective area of roughly $A_{\text{eff}} = 10^5\,\text{m}^2$ for TeV γ-ray observations at low zenith angles $\theta \leq 30°$ (see, e.g., Fig. 2.13).

As a result of the limited collection area of the current generation of IACTs, the γ-ray sky above energies of 100 TeV remains largely unexplored. The detection of VHE γ-ray sources with energies up to 1.4 PeV with the LHAASO experiment [107, 108] provides a strong motivation to explore possibilities to observe gamma-ray sources above 100 TeV with IACTs. Investigating the γ-ray sky at energies above 100 TeV will eventually provide more insights into the origin and acceleration mechanisms of these objects. In particular, the discovery in [107, 108] demonstrates the existence of galactic sources capable of accelerating particles to multi-PeV energies.

One way to increase A_{eff} is to distribute numerous telescopes over several square kilometers, like in the CTA project. Indeed, with the distribution of telescopes indicated in

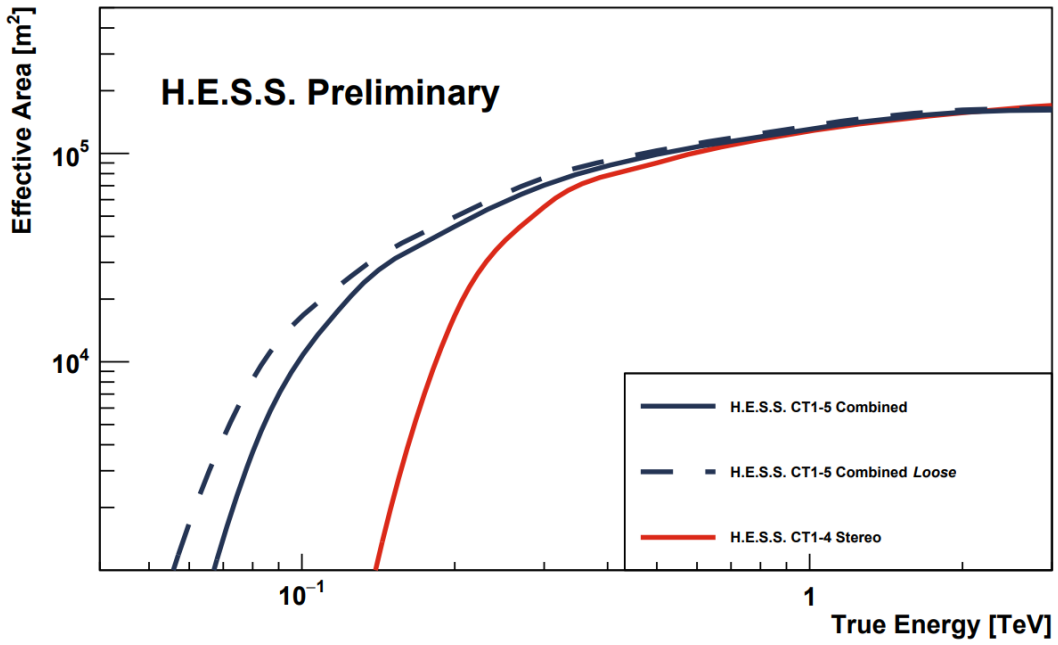

Figure 2.13: Effective area as a function of energy for CT1-CT4 (red line), and CT1-CT5 (blue lines). The dashed blue line denotes a different configuration for the cuts used in the gamma-hadron separation analysis pipeline. Taken from [106].

Tab. 2.2, the northern and southern array are expected to reach effective areas of the order of $\mathcal{O}(1\,\mathrm{km}^2)$ at 10 TeV after γ-hadron separation cuts (see Fig. 2.14).

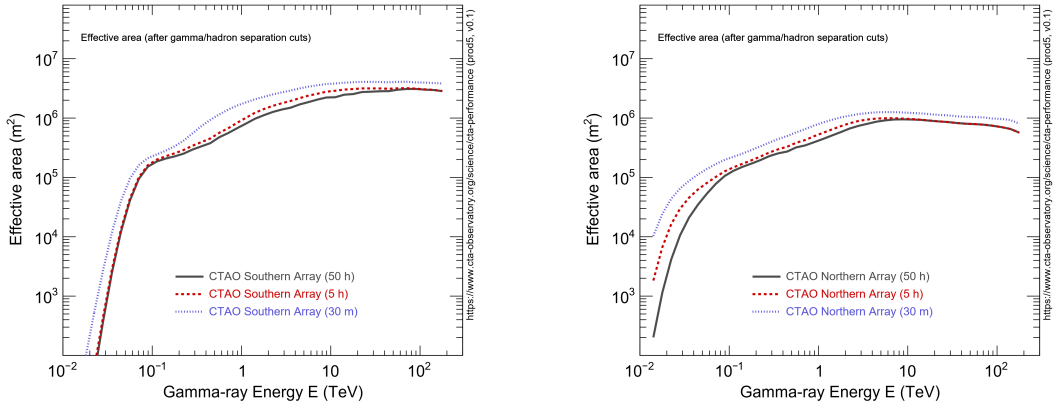

(a) Southern array

(b) Northern array

Figure 2.14: Effective area as a function of energy for the northern and southern array of the CTA project.

The downside of this approach is rather obvious: The cost-stamp for projects as big as CTA is several hundred million EUR. Furthermore, the construction of telescopes over an area of multiple square kilometers necessarily results in significant human interference with nature. Especially for IACTs, one of the conditions for choosing the location is an

environment with low light pollution - which consequently means that this environment was (more or less) untouched before.

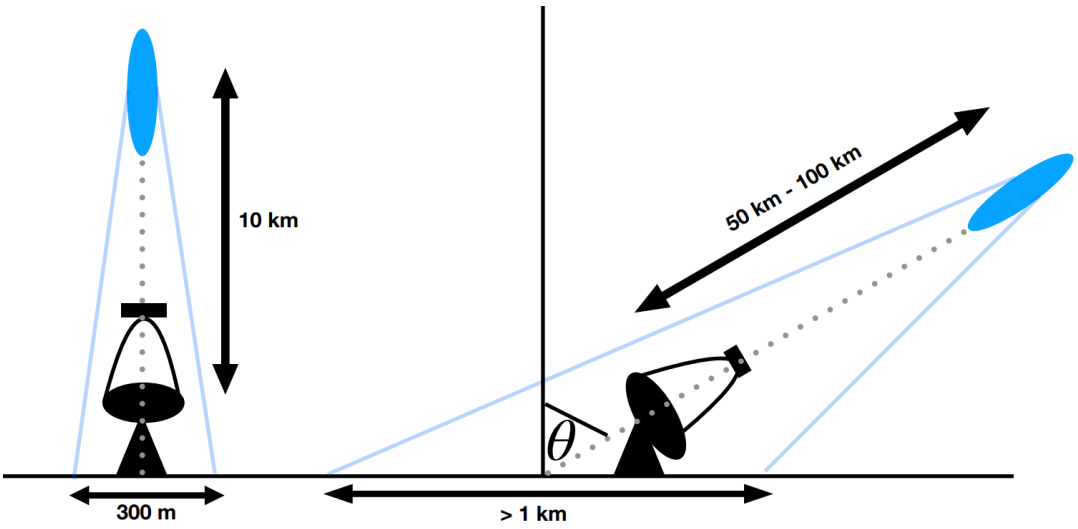

Figure 2.15: Schematic sketch of the properties of vertical showers (left) and inclined showers (right), where θ denotes the zenith angle. The gray dotted line marks the shower axis, the blue shaded area marks the air shower, the light blue solid lines indicate the Cherenkov light cone respectively.

A more budget-friendly approach is to perform large zenith angles (LZA) observations, which typically means zenith angles $\theta \geq 70°$. By observing at LZA, the distance to the shower is greatly increased (50 km to 100 km, while the distance to the shower for vertical showers is roughly $\sim 10\,\text{km}$), resulting in the expansion of the light pool on the ground (see Fig. 2.15). This expansion comes at the expense of increased column density of air due to a longer photon path to the observer.

This is also shown in Fig. 2.16, where the relative air mass (i.e., column density normalized to the vertical column density) is given as a function of zenith angle $\theta \geq 60°$. While the column density at a zenith angle of 60° is roughly twice as large as for a vertical path, it increases rapidly with increasing zenith angle, approaching nearly 10-times the value of the vertical column density at a zenith angle of $\theta = 85°$. As a consequence, the air shower will not only develop far away ($\gg 10\,\text{km}$) from the observer but also the emitted light from the air shower will undergo increased light attenuation. Both of the aforementioned consequences have an impact on the Cherenkov light intensity, i.e., the Cherenkov light intensity significantly diminishes for a shower at LZA in contrast to the intensity from an identical vertical shower. Therefore, the energy threshold of IACTs at LZA will increase compared to moderate zenith angle observations.

These characteristics of extensive air showers at large zenith angles lead to the following desired properties for an IACT performing LZA observations:

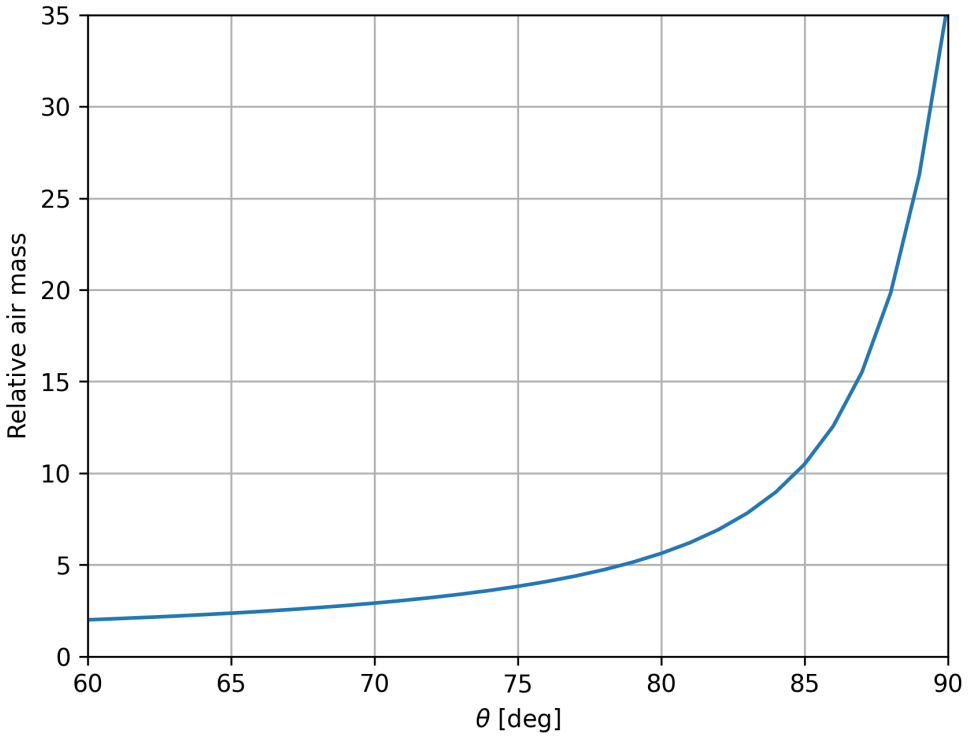

Figure 2.16: Relative air mass as a function of zenith angle θ.

- Given the significant reduction in Cherenkov light intensity during observations at LZA, the use of large reflector surfaces becomes essential. It's worth noting, that large optical systems have been constructed over the past few decades for a very similar reason: The Cherenkov light intensity scales with the energy of the primary γ-ray. Therefore, a large reflector surface enhances the sensitivity towards lower energies. In principle, telescopes designed for optimized sensitivity in the lower energy range ($\mathcal{O}(10\,\mathrm{GeV})$) should also be well-suited for LZA observations.
- The distance from the shower maximum to the observer is greatly increased for observations at LZA. Consequently, the angular size of the recorded image will get smaller compared to vertical showers. Therefore, a camera with a small pixel size ($\sim 0.1°$) is needed.

The MAGIC collaboration has successfully demonstrated that observations at a zenith angle range of 70° to 80° increase the collection area to be larger than a square km. With an observation time of $\sim 56\,\mathrm{h}$, they were able to detect γ-ray emission from the Crab Nebula up to energies of 100 TeV [109].

A case study at a zenith angle of 80° for the IACT with the largest mirror radius of $R = 14\,\mathrm{m}$ and smallest pixel size of $\sim 0.07°$ of currently operating IACTs is presented in Chapter 3.

Chapter 3

H.E.S.S. CT5 Performance Study at Large Zenith Angles

Commonly, simulations are used to study and optimize the performance of IACTs, such as testing and verifying event reconstruction and γ-hadron separation techniques or to simulate the instrument response function. In the field of IACTs, Monte Carlo simulations, e.g., CORSIKA [110], have proven to deliver reliable results when comparing simulated and observational data and therefore have become essential in order to optimize IACTs and reconstruction methods.

The widely adopted CORSIKA framework for simulating air showers has become the standard software in ground-based air shower detection. In particular, the fundamental Monte Carlo approach in CORSIKA has been employed in this field for over five decades [111]. The CORSIKA software package includes the simulation of hadronic and electromagnetic interactions using interaction models that have been validated through experimental data, e.g., high energy observations at the Large Hadron Collider (LHC) [112]. Especially, the IACT/ATMO extension package [113] for CORSIKA allows for flexible and detailed simulation of the geometry of IACT arrays, e.g., position of telescopes, mirror segments, shadowing effetcs, etc., as well as the usage of tabulated atmospheric profiles. Overall, the CORSIKA software package provides the framework for the emission of Cherenkov light by extended air showers and the subsequent collection of this light by IACTs. For this, the telescope is modeled as a sphere with radius R. Only the information (e.g., time information or momentum vector) of the photons intersecting the telescope's sphere is stored in a machine- and compiler-independent data format. For a more detailed description of the workflow of CORSIKA see [114].

The `sim_telarray` software package [113] uses the information on the Cherenkov light in order to simulate the detector response. It simulates the entire process, starting from the reflection of Cherenkov light on the mirror tiles, the electronic response of the received light, to the final recorded image. The software accounts for detailed aspects, such as the shadowing of the reflector surface caused by the camera or the camera mast, the formation of a trigger and the cleaning of images. All relevant information regarding the instrument parameters for the H.E.S.S. telescopes is provided in configured files (the configuration H.E.S.S. phase 2D3 is used for the analysis in this thesis). The Hillas parameter (see Sec. 2.5.1) can be written out to a log-file on a event-by-event basis for further analysis. For a more in-depth description of `sim_telarray` see [113].

3.1 Monte Carlo dataset

In the following, all relevant information regarding `CORSIKA` version, compiling options, and parameter settings used to simulate the air showers are provided:

`CORSIKA` version	7.690
compiling options	VOLUMEDET, IACT v1.56, ATMEXT, CURVED[1], VIEWCONE, SLANT, CERENKOV
interaction models	QGSJET-01D [115], GHEISHA 2002d [116], EGS4 [117]
atmosphere	all-year average profile at H.E.S.S. site

For the energy cut-off of the particle kinetic energy for hadrons, muons and electrons 0.3 GeV, 0.1 GeV and 0.02 GeV is used respectively. The lower and upper limit of the wavelength band for the Cherenkov radiation production covers a range 250 nm to 700 nm with a bunchsize of 5. The longitudinal development of particle numbers and energy deposit by ionization energy losses are sampled in steps of 20 g/cm^2. Explanations for the compiling options and keywords for the `CORSIKA` input card can be found in [114].

γ-ray data set:

The γ-ray data set is simulated for a point like source coming from the north (azimuth angle of 180°) at a zenith angle of $\theta = 80°$. Since the computation time (for the simulation of the extended air showers) scales with the energy of the primary particle, it becomes challenging to cover a wide energy range with sufficient statistics. Due to limited computation power and storage capacity, the γ-ray data set is simulated at

[1] By enabling the CURVED compiling option, the curvature of Earth's atmosphere is taken into account. The default is a plane-parallel atmosphere model, valid for zenith angles $\theta \leq 60°$.

discrete energies of 1 TeV, 10 TeV, 100 TeV and 1000 TeV. The computation time can be further reduced by re-using simulated air showers *n_scat*-times and scattering them over an rectangular area (perpendicular to the shower axis) with half-side lengths *x_scat* and *y_scat*. Note, that the actual shower development is identical for re-used showers. Especially at lower energies ($\leq$ 1 TeV), there is a risk that fluctuations during the shower development might not be accurately captured in the simulated data set. For higher energies of the primary particle these fluctuations are considerably smaller. Therefore, for the 100 TeV and 1000 TeV simulations the *n_scat* parameter is chosen to be larger compared to the 1 TeV and 10 TeV simulations (see Tab. 2.2). For each energy and the specifications provided in Tab. 3.1, 121 runs have been performed. For example, for an energy of 1 TeV, a total of $121 \times 20000 \times 5 = 12.1 \times 10^6$ showers are simulated.

	1 TeV	10 TeV	100 TeV	1000 TeV
n_shower	20000	1500	10	10
n_scat	5	10	100	100
x_scat	1000 m	2500 m	3000 m	4000 m
y_scat	1000 m	2500 m	3000 m	4000 m

Table 3.1: Specifications of the simulated γ-ray data set.

Background data set:

The background data set consists of simulated proton and helium induced air showers with discrete energies of 0.5 TeV, 1 TeV, 10 TeV, 100 TeV and 1000 TeV. As mentioned in Sec. 1.1, cosmic rays are isotropic on the sky, i.e., they show (for the energies discussed here) no apparent directional preference. Therefore, the background simulations are not performed for a single azimuth and zenith angle combination, but rather over a grid of azimuth and zenith angles (see Fig. 3.1).

	0.5 TeV	1 TeV	10 TeV	100 TeV	1000 TeV
n_shower	50000	20000	2000	200	20
n_scat	2	5	10	100	100
x_scat	800 m	1000 m	1500 m	3500 m	4000 m
y_scat	800 m	1000 m	1500 m	3500 m	4000 m

Table 3.2: Specifications of the simulated background data set.

For each azimuth and zenith angle combination indicated in Fig. 3.1, one run is performed with the specifications provided in Tab. 3.2 (respectively for proton and helium). For example, for the azimuth/zenith angle combination of 175°/75°, a total of $50000 \times 2 = 10^5$ showers are simulated for a proton (or helium) primary energy of 0.5 TeV.

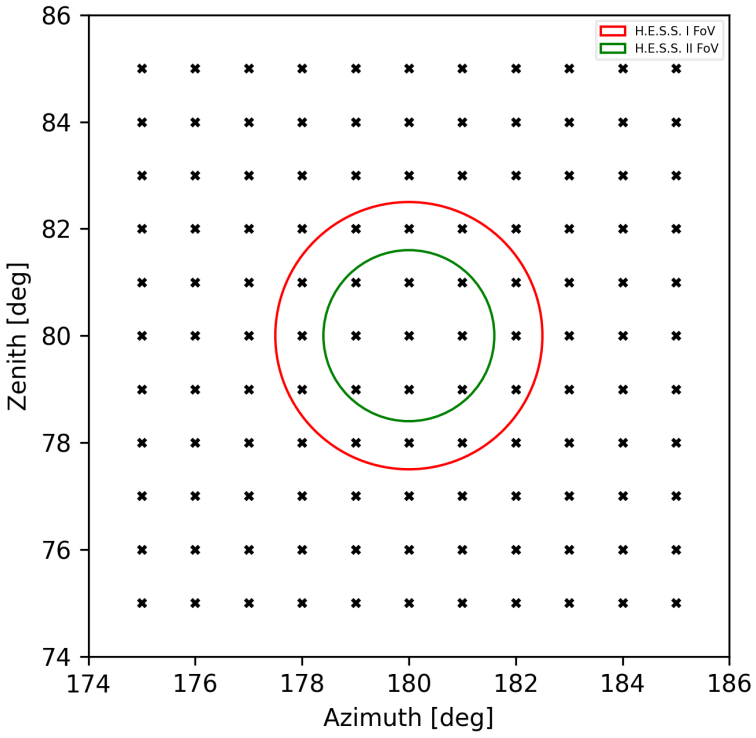

Figure 3.1: Grid over azimuth and zenith angles (black crosses) used for the simulation of the background data set. Additionally, the field of view (FoV) of CT1-CT4 (red circle) and the FoV of CT5 (green Circle) is indicated.

3.1.1 Background estimation

Unfortunately, there have been no observations of the H.E.S.S. telescopes at a zenith angle of $\theta = 80°$. Consequently, to estimate the background flux, the cosmic ray proton [118] and helium [119] energy spectrum measured by the DAMPE satellite are utilized. Both, the proton and helium spectrum, can be described by a smoothly broken power-law:

$$\Phi(E) = \Phi_0 \left(\frac{E}{\mathrm{TeV}}\right)^{-\gamma} \left[1 + \left(\frac{E}{E_B}\right)^{s}\right]^{\Delta\gamma/s}, \tag{3.1}$$

where Φ_0 is the flux normalization, γ indicates the slope of the spectrum for energies E much smaller than the break energy E_B, $E \ll E_B$ (note, that Eqn. 3.1 essentially becomes a simple power-law for $E_B \gg E$), $\Delta\gamma$ describes the change of the slope for energies $E \geq E_B$, and s quantifies the smoothness of the break. For convenience, the best-fitting parameters for both spectra are provided in Tab. 3.3. Strictly speaking, these best-fitting parameters were obtained in the energy range of 40 GeV to 100 TeV for the proton spectrum and 70 GeV to 80 TeV for the helium spectrum. For the analysis

in this thesis, Eqn. 3.1 is extrapolated up to energies of 1000 TeV using the best-fitting parameters indicated in Tab. 3.3.

	Proton		Helium	
Fit range	[0.1 - 6.3] TeV	[6.3 - 100] TeV	[0.32 - 5.0] TeV	[6.8 - 80.0] TeV
$\Phi_0/10^5$	$7.58^{+0.36}_{-0.31}$	$8.68^{+0.50}_{-0.45}$	$6.08^{+0.22}_{-0.25}$	$4.71^{+0.27}_{-0.25}$
γ	2.772 ± 0.002	2.60 ± 0.01	2.68 ± 0.02	2.41 ± 0.02
E_B	0.48 ± 0.01	$13.6^{+4.1}_{-4.8}$	$1.25^{+0.15}_{-0.12}$	$34.4^{+6.7}_{-9.8}$
$\Delta\gamma$	0.173 ± 0.007	-0.25 ± 0.07	$0.18^{+0.05}_{-0.02}$	$-0.51^{+0.18}_{-0.2}$
s	5.0 (fixed)	5.0 (fixed)	$3.6^{+2.3}_{-1.6}$	5.0 (fixed)

Table 3.3: Best-fitting parameters derived by DAMPE measurements for the cosmic ray proton and helium energy spectrum. Φ_0 is given in units of $1/\mathrm{GeV/s/m^2/sr}$ and E_B in units of TeV. Values taken from [118] (proton) and [119] (helium).

Let $P(\phi, \theta, E)$ define the trigger probability:

$$P(\phi, \theta, E) = \frac{n_{trig}}{n_{total}}, \tag{3.2}$$

where $n_{total} \equiv n_{total}(\phi, \theta, E)$ represents the total number of simulated proton (or helium) showers for the given azimuth/zenith angle combination ϕ/θ with energy E, and $n_{trig} \equiv n_{trig}(\phi, \theta, E)$ corresponds to the number of showers that trigger the telescope, $n_{trig} \leq n_{total}$. An effective solid angle $\Omega_{eff}(E)$ can be calculated by integrating over the solid angle Ω weighted by the trigger probability $P(\phi, \theta, E)$:

$$\Omega_{eff}(E) = \int_{175^\circ}^{185^\circ} \int_{75^\circ}^{85^\circ} P(\phi, \theta, E)\, \mathrm{d}\Omega. \tag{3.3}$$

The energy dependent background differential rate ($DR_{bkg}(E)$, in units of 1/TeV/s) can then be estimated by:

$$DR_{bkg}(E) = \Omega_{eff}(E) \times A_{sim}(E) \times \Phi(E), \tag{3.4}$$

where $\Phi(E)$ is given by Eqn. 3.1 and Tab. 3.3, and $A_{sim}(E)$ is the energy dependent simulated area $A_{sim}(E) = 2 \times x_{scat}(E) \cdot 2 \times y_{scat}(E)$ (see Tab. 3.2).

The trigger probabilities shown in Fig. 3.2 and Fig. 3.3 are derived for the H.E.S.S. CT5 telescope pointing at an azimuth angle of 180° and zenith angle of 80°. The average

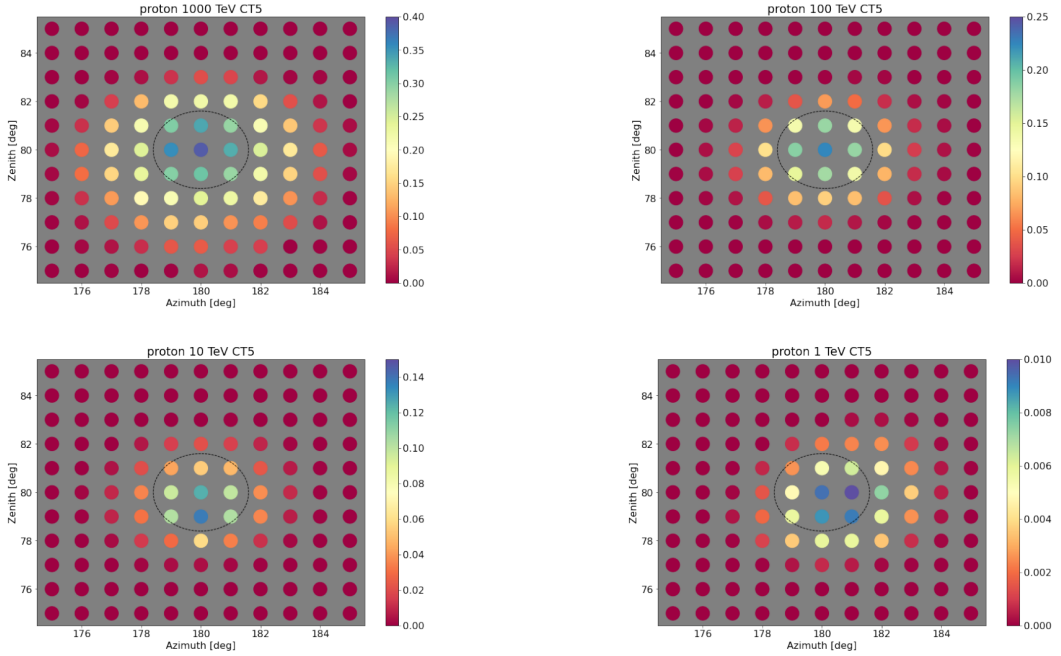

Figure 3.2: Proton trigger probabilities (color-bar on the right) for the simulated grid indicated in Fig 3.1 (here, denoted with filled circles). The dashed circle marks the FoV of H.E.S.S. CT5.

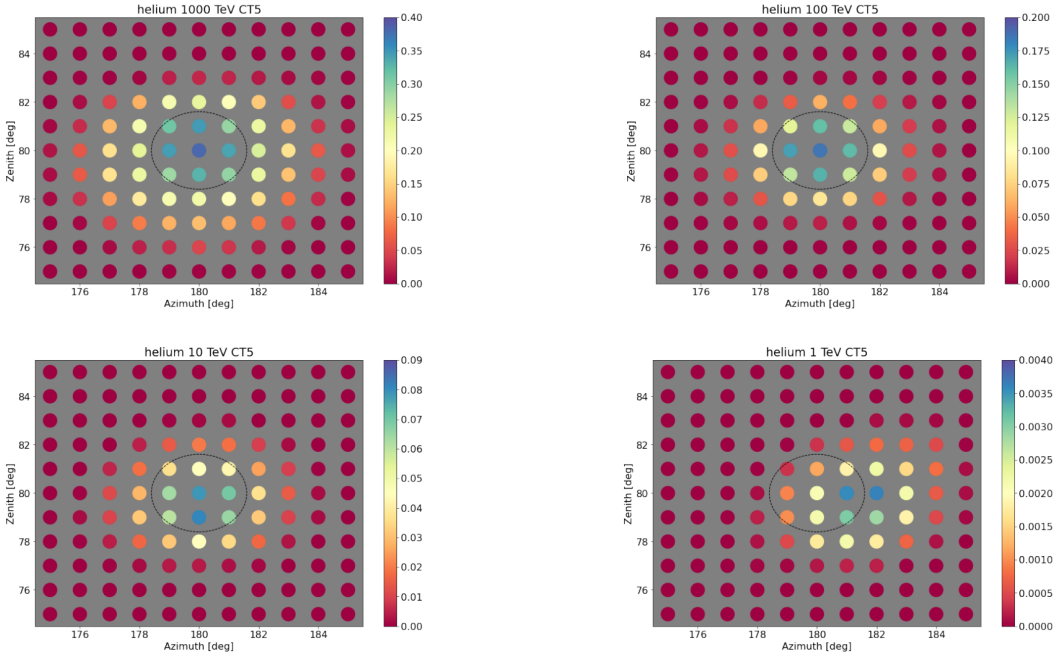

Figure 3.3: Helium trigger probabilities (color-bar on the right) for the simulated grid indicated in Fig. 3.1 (here, denoted with filled circles). The dashed circle marks the FoV of H.E.S.S. CT5.

night sky background for CT5 is set to 0.161 p.e./ns. The angular acceptance for proton and helium showers noticeably decreases at 100 TeV compared to 1000 TeV energies, as illustrated in the upper panels of Fig. 3.2 and Fig. 3.3. This reduction can be explained by considering that the depth of the shower maximum X_{max} depends on the energy of the primary particle. Higher energy primary particles penetrate deeper into the atmosphere, resulting in an increased X_{max} when compared to lower energy particles.

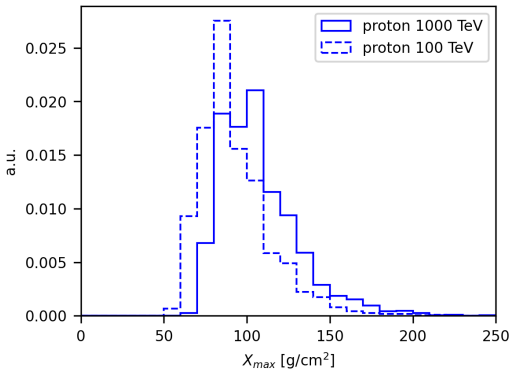

(a) Comparison between the normalized distribution of the depth of the shower maximum X_{max} for proton energies of 100 TeV and 1000 TeV.

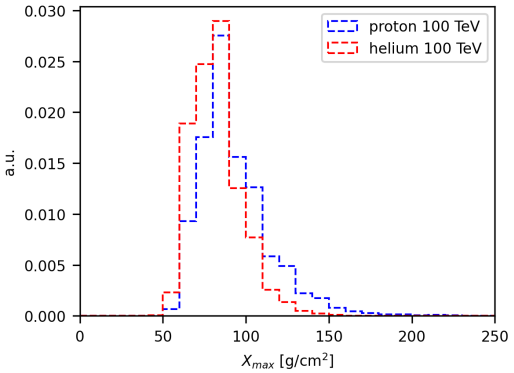

(b) Comparison between the normalized distribution of the depth of the shower maximum X_{max} for proton and helium air showers with energies of 100 TeV.

Figure 3.4: Comparison of X_{max} for (a) proton events of different energy and (b) proton and helium events of similar energy.

This relationship is also shown in Fig. 3.4a, which compares the X_{max} values for proton energies at 100 TeV and 1000 TeV. The peak of the distribution at 1000 TeV is roughly at $X_{max} \sim [100 - 110]\,\mathrm{g/cm^2}$, while for 100 TeV the peak of the distribution is located at $X_{max} \sim 90\,\mathrm{g/cm^2}$. Consequently, since X_{max} is reached earlier for proton energies of 100 TeV, the emitted light will undergo increased light attenuation compared to proton energies of 1000 TeV.

Additionally, when comparing maximum trigger probabilities for proton and helium showers at energies below 100 TeV, it is evident that helium showers tend to have lower trigger probabilities than proton showers. As discussed in Chapter 2, the depth of the shower maximum decreases for showers induced by heavier nuclei compared to proton induced showers at the same energy (see Fig. 3.4b). As a result, similar to the discussion above, the photon density on the ground for 100 TeV helium induced air showers is lower than that for 100 TeV proton induced air showers.

Especially at 1 TeV, there appears to be an azimuth angle dependence in the angular acceptance. This dependence is likely due to the interaction between the charged primary particle and Earth's magnetic field (the magnetic field at the H.E.S.S. site is characterized by the horizontal magnitude $H = 12.074\,\mathrm{T}$, the downward vertical component

$Z = -25.614\,\mathrm{T}$ and the magnetic field declination $D = -13.167°$). It is important to note that, within the discussed zenith angle range, the first interaction for a 1 TeV proton or helium shower must occur at lower altitudes to trigger the telescope (note the relatively low peak trigger probabilities of less than 1% at 1 TeV). Consequently, the charged primary particle travels a longer path in the magnetic field, leading to increased deflection before the cascade process begins.

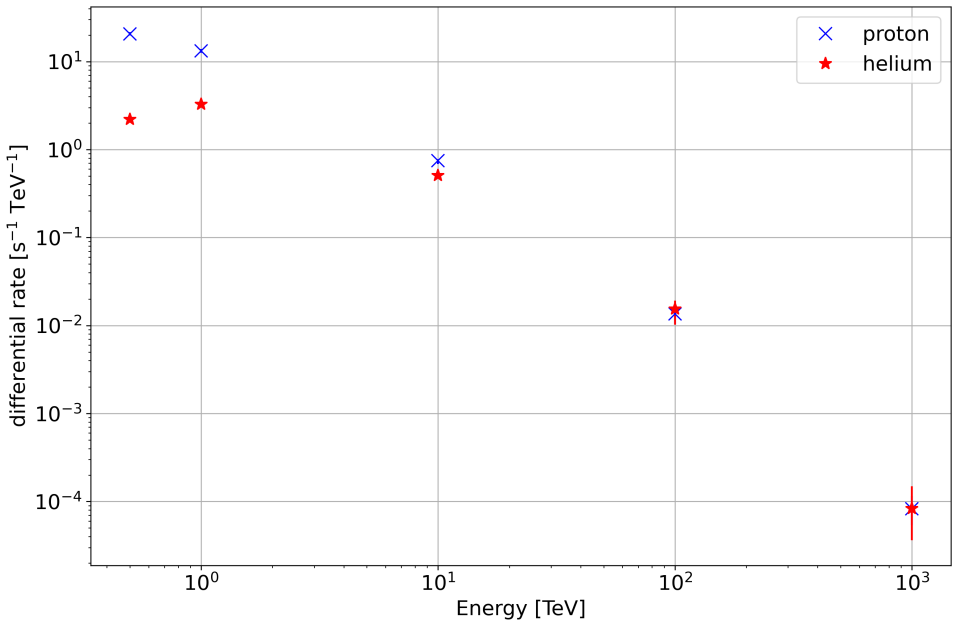

Figure 3.5: Estimated energy dependent differential rate for proton (blue crosses) and helium (red stars) for H.E.S.S. CT5 pointing at a zenith angle of $\theta = 80°$.

The estimated differential rates, calculated using Eqn. 3.4, are presented in Fig. 3.5 for proton and helium, respectively. The errors are determined by considering the uncertainties associated with the best-fitting parameters listed in Tab. 3.3. At 0.5 TeV, the differential rate for helium is approximately one order of magnitude lower than that for protons. However, at energies $\geq$100 TeV, the rates become similar and, as a result, cannot be neglected.

Furthermore, when looking at the peak trigger probabilities at 1 TeV of $\sim$1% for protons and $\sim$0.4% for helium, the high differential rates at the lower energy range in Fig. 3.5 might be surprising at first glance. Nevertheless, these low trigger probabilities get compensated by the high flux values (see Fig. 3.6) at the lower energy range for protons and helium, respectively.

The trigger rate, i.e., the differential rate integrated over the energy range from 0.5 TeV to 1000 TeV, evaluates to 112^{+6}_{-8} counts/s for protons and 49^{+2}_{-3} counts/s for helium. Note

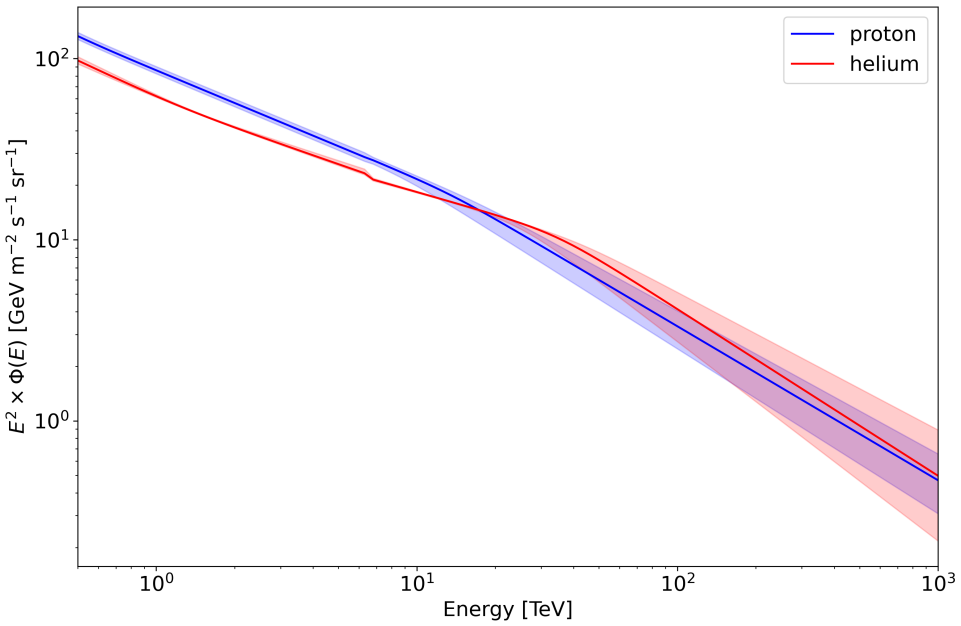

Figure 3.6: Cosmic ray proton and helium flux multiplied by E^2 as a function of energy E. The flux (solid lines) and the $1\,\sigma$ envelope (shaded area) are calculated with Eqn. 3.1 and Tab. 3.3.

that these values are derived at the "trigger level", i.e., no cuts are applied to the simulated proton and helium datasets.

3.2 Random Forest analysis

The analysis in this chapter is conducted using the Random Forest implementation from `scikit-learn` [120, 121]. Random Forest is an ensemble machine learning method that builds upon decision trees, making it suitable for a variety of tasks, including classification (e.g., γ-hadron separation) and regression (e.g., origin or energy reconstruction). The following brief introduction to Random Forests is based on the description given in [122].

A decision tree is a hierarchical structure that recursively splits the data into subsets based on specific feature conditions. For that, users need to provide a set of input parameters (e.g., Hillas parameters, as discussed in Sec. 2.5.1). These input parameters are used to create branches in the tree, and each branch can further split into more branches. This way several nodes are created, also called "leafs", while the number of branches within a single node is called "depth". The depth of a node is user configurable with the *max_depth* parameter. Two other important parameters are *min_samples_split*

and *min_samples_leaf*. These parameters control when a decision tree stops splitting its nodes. The parameter *min_samples_split* specifies the minimum number of samples needed to split an internal node. A node will stop to split further, if it has fewer samples than this value. The parameter *min_samples_leaf* specifies the minimum number of samples required for a node to be a leaf. Note that, excessively fine splitting (i.e., large *max_depth* value) can lead to over fitting. Therefore, these parameters do not only serve as a stopping criterion for the decision tree but also help to prevent over fitting by ensuring that nodes do not split too finely.

For each split, the `scikit-learn` implementation employs a loss function, particularly the Gini impurity for classification tasks. The Gini impurity measures how often a randomly chosen element would be incorrectly classified. When splitting a node m, the Gini impurity is calculated for the child nodes (i.e., the left and right branches of the tree). The data subsets in the left Q_m^{left} and right Q_m^{right} branches can be described by:

$$
\begin{aligned}
Q_m^{left}(\theta) &= \{(par, label) \,|\, par_j \leq par_m^{thr}\} \\
Q_m^{right}(\theta) &= Q_m \setminus Q_m^{left},
\end{aligned}
$$

where par is a set of provided parameters, $\theta = (j, par_m^{thr})$ is a candidate split condition for the parameter par_j with the node specific threshold condition par_m^{thr}, i.e., $par_j \leq par_m^{thr}$, and, *label* is the class specific label for the provided set of parameters (e.g., 0 for hadrons and 1 for photons).

The decision tree selects the feature condition θ^* that minimizes the weighted sum of the Gini impurity $G(Q_m, \theta)$ for the child nodes[2]:

$$
G(Q_m, \theta) = \frac{n_m^{left}}{n_m} H(Q_m^{left}(\theta)) + \frac{n_m^{right}}{n_m} H(Q_m^{right}(\theta)), \tag{3.5}
$$

$$
\theta^* = \text{argmin}_\theta \, G(Q_m, \theta), \tag{3.6}
$$

where the data at node m with $n_m, n_m^{left}, n_m^{right}$ samples is denoted by $Q_m, Q_m^{left}, Q_m^{right}$ respectively and H represents the task dependent loss function. This feature condition becomes the splitting criterion for that node.

For a dataset with multiple classes, a Gini impurity of 0 represents perfect purity (all data points in each of the child nodes belong to the same class), while a Gini impurity of 0.5 means equal proportions of different classes in each child node.

[2] `https://scikit-learn.org/stable/modules/tree.html#tree-mathematical-formulation`

For classification tasks, the loss function H in Eqn. 3.5 is given by:

$$\begin{aligned} H(Q_m) &= \sum_k p_{mk}(1 - p_{mk}) \\ &= f_\gamma(1 - f_\gamma) + f_{bkg}(1 - f_{bkg}), \\ p_{mk} &= \frac{1}{n_m} \sum_{label \in Q_m} I(label = k), \end{aligned}$$

where p_{mk} measures the fraction of class k in node m. Here, we have two classes, i.e., photon (γ) events and background (bkg) events. Hence, f_γ represents the fraction of photon events and f_{bkg} the fraction of background events at node m.

For regression tasks, the loss function H in Eqn. 3.5 makes use of the Mean Squared Error (MSE), in order to predict a value E^m_{rec} for node m:

$$MSE = \frac{1}{n_m} \sum_{E_{true} \in Q_m} (E_{true} - E^m_{rec})^2,$$

where the predicted value E^m_{rec} is given by the mean value $\bar{E}_m$, such that:

$$\begin{aligned} E^m_{rec} = \bar{E}_m &= \frac{1}{n_m} \sum_{E_{true} \in Q_m} E_{true} \\ H(Q_m) &= \frac{1}{n_m} \sum_{E_{true} \in Q_m} (E_{true} - \bar{E}_m)^2 \end{aligned}$$

The Random Forest algorithm uses the bootstrapping technique to generate subsets of the data. Multiple decision trees are then created, each trained on a random subset of the data. In addition to using random subsets of the data, Random Forest makes us of "feature randomness". For each tree in the forest, only a random subset of features is considered when making decisions [3].

After constructing a set of decision trees, they collectively contribute to the final prediction through a voting mechanism. In regression tasks, the predictions of all the trees are averaged. In the context of classification, the ensemble of decision trees yields a probability-like value, which indicates the fraction of trees voting for a particular class. With respect to γ-hadron separation, this probability-like value is termed *gammaness*

[3] `https://scikit-learn.org/stable/modules/generated/sklearn.ensemble.RandomForestRegressor.html`

with values closer to 1 indicating a preference for γ-ray events and values closer to 0 indicating a preference for background events.

3.2.1 Data preparation

Typically, only the images of air showers fully within the field of view of the camera are considered. This ensures the accurate calculation of the Hillas parameter, which describes the elliptical shape of the recorded image. Therefore, only events with a maximum distance of 1° between the CoG and the camera center are considered. For energies $E \sim 1\,\mathrm{PeV}$ and a zenith angle of 80°, air showers with an impact position far away ($\geq 1\,\mathrm{km}$) from the telescope position will still trigger the telescope. For on-axis observations, this leads to an increased number of air showers with distances $\geq 1°$ between the CoG of the image and the camera center compared to off-axis observations (see Fig. 3.7).

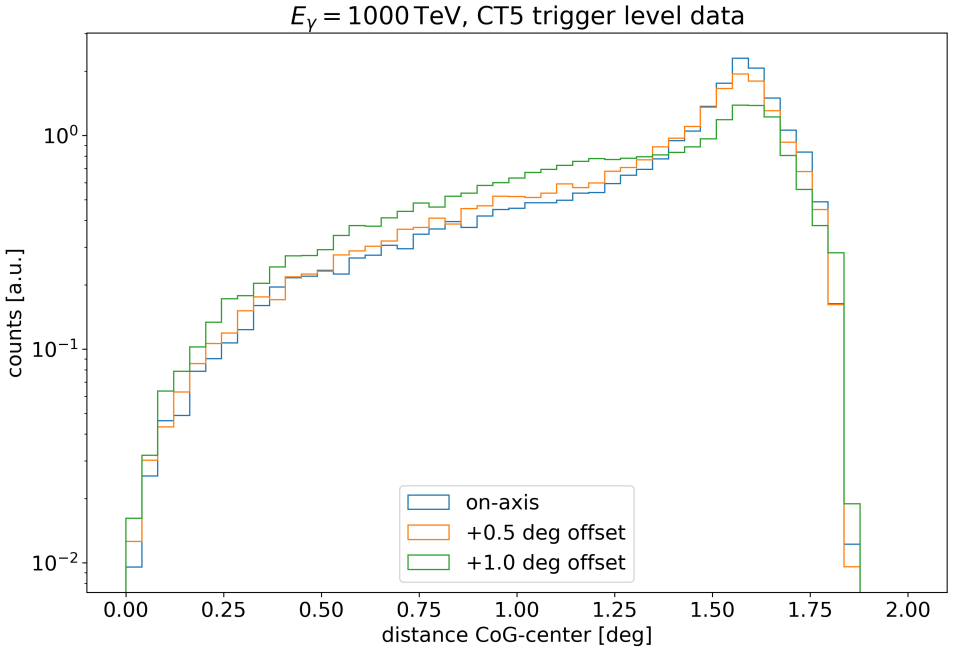

Figure 3.7: Normalized distribution of the angular distance between the Center of Gravity (CoG) of the recorded image and the camera center. Only γ-ray initiated air showers with energies of $E_\gamma = 1000\,\mathrm{TeV}$ triggering CT5 are considered. The γ-ray air showers are coming from the north (azimuth angle of 180°) at a zenith angle of 80°, while CT5 is pointing at an azimuth angle of 180° and zenith angle of 80° (blue histogram), 80.5° (orange histogram) and 81° (green histogram) respectively.

Therefore, the analysis in this Chapter is conducted for two observation modes for H.E.S.S. CT5: on-axis (i.e., CT5 is pointing at a zenith angle of 80°) and +1° offset (i.e., CT5 is pointing at a zenith angle of 81°, hereafter also called "off-axis" observation).

Additionally, an effective way to distinguish low energy ($\sim$ 1 TeV) background events from high energy ($\geq$ 100 TeV) γ-ray events, besides the Hillas parameter, was explored. It was found, that the trigger pattern of the five H.E.S.S. telescopes (the H.E.S.S. array layout is illustrated in Fig. 3.8) can be used as an additional parameter for the Random Forest classification. The produced secondary muons in the hadronic cascade (see Chapter 2) will form an observable pattern at the ground, and can be used as a veto to suppress the background events.

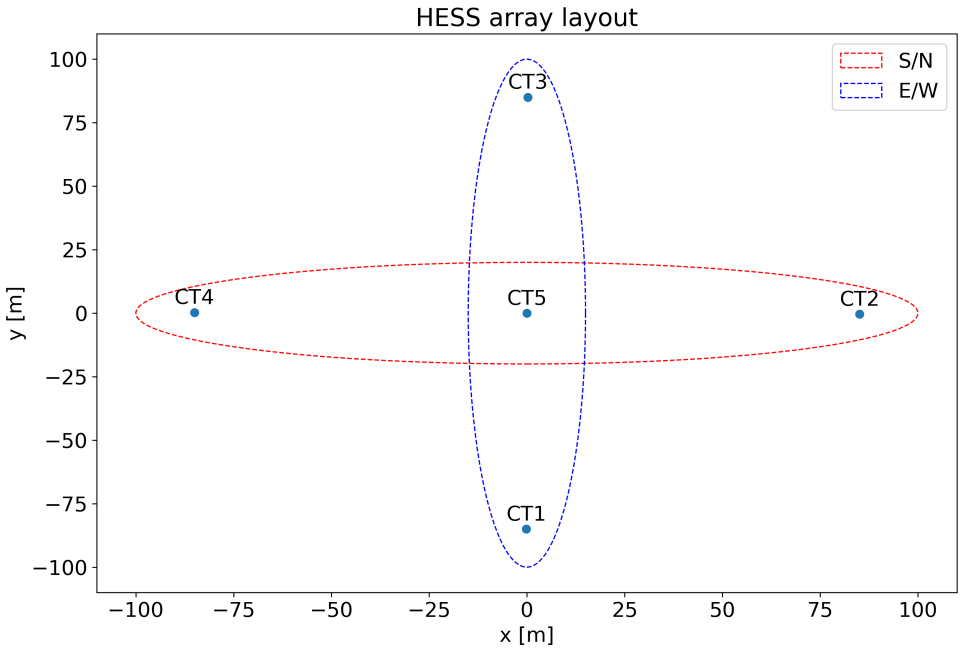

Figure 3.8: H.E.S.S. array layout together with the south/north (S/N, north is given by the positive x-axis) direction indicated in red and east/west (E/W, west is given by positive y-axis) direction indicated in blue.

This is also illustrated in Fig. 3.9, where the trigger pattern[4] is compared for background events with energies of 1 TeV and γ-ray events with energies of 100 TeV after an angular distance cut of 1° (CoG - camera center) for CT5 and 1.67° for CT1-CT4. Note that, while the trigger pattern in Fig. 3.9 is derived for on-axis observation, the distribution is similar for off-axis observations with an offset of 0.5° and 1°. It is evident, that the distribution of two-telescope triggers (e.g., ”15” - meaning that CT1 and CT5 have triggered for the specific event) shows no preferred pattern for background events. An increased number of background events with three-telescope triggers is found for the south/north telescopes (see Fig. 3.8) of the H.E.S.S. array. Four-telescope and five-telescope triggers are predominantly caused by high energy γ-rays rather than low energy background events.

[4]Here, only trigger events including CT5 are shown.

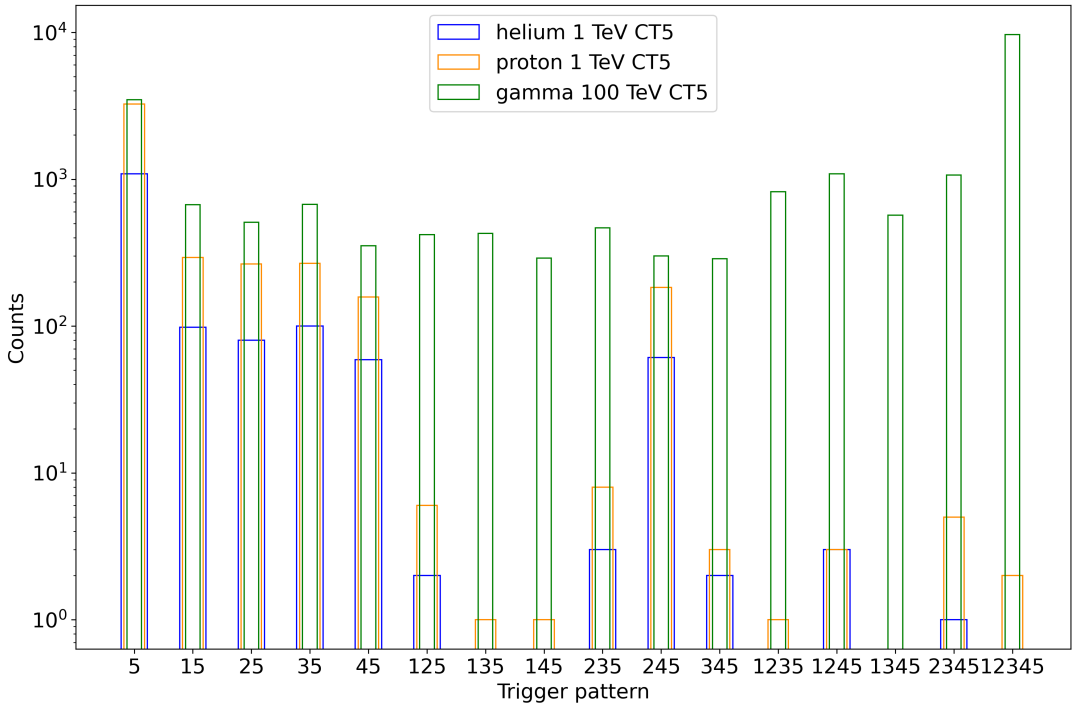

Figure 3.9: Trigger pattern of the five H.E.S.S. telescopes for proton and helium events with energies of 1 TeV and γ-ray events with energies of 100 TeV.

For the Random Forest classification in Sec. 3.3 the parameters *width*, *length*, *width*/*length*, *npix*, *dist* and the information of the trigger pattern (called *multi*) are used. Note that, since the *dist* parameter is included for the Random Forest classification, the analysis is source dependent.

3.3 γ-hadron separation

In order to evaluate the separation power of the Random Forest classifier, two separate Monte Carlo datasets for the background events and γ-ray events are simulated (see Sec. 3.1, i.e., 2×Tab. 3.1 and 2×Tab. 3.2). One dataset is used as a training sample set for the Random Forest classifier and the other one as a test dataset, i.e., the trained Random Forest classifier is applied to this dataset.

The performance of the γ-hadron separation can be quantified by using the quality factor Q, defined as:

$$Q = \frac{\epsilon_\gamma}{\sqrt{\epsilon_{bkg}}}, \tag{3.7}$$

where $\epsilon_\gamma = \frac{N_\gamma^{\text{after}}}{N_\gamma^{\text{before}}}$ denotes the fraction of γ-ray events and, similarly $\epsilon_{bkg} = \frac{N_{bkg}^{\text{after}}}{N_{bkg}^{\text{before}}}$ the fraction of background events surviving the γ-hadron separation. The quality factor Q is closely linked to the significance S of the instrument [122]:

$$S \approx \frac{N_{sig}}{\sqrt{N_{bkg}}} \propto Q \times \sqrt{t},$$

where N_{sig} signal events from a point source are recorded together with N_{bkg} isotropic background events during an observation time t. A more general description for the significance S is given in [123]:

$$S = \sqrt{2}\left[N_{on}\ln\left[\frac{1+\alpha}{\alpha}\left(\frac{N_{on}}{N_{on}+N_{off}}\right)\right] + N_{off}\ln\left[(1+\alpha)\left(\frac{N_{off}}{N_{on}+N_{off}}\right)\right]\right]^{1/2} \tag{3.8}$$

where N_{on} photons are observed from the source position during an observation time of t_{on} and N_{off} photons from the background measurement during an observation time of t_{off}, such that the number of observed photons from the source N_S is $N_S = N_{on} - \alpha N_{off}$ with $\alpha = t_{on}/t_{off}$.

The Random Forest is configured to build a total of $n\_estimators = 100$ trees, limiting each tree's maximum depth to $max\_depht = 20$ levels. For every split in the trees, a minimum of $min\_samples\_split = 4$ samples is necessary, and each leaf should contain a minimum of $min\_samples\_leaf = 2$ samples.

The training and test dataset as well as the performance of the Random Forest classifier is presented in Sec. 3.3.1 and Sec. 3.3.2 for on-axis and 1° offset observations, respectively.

3.3.1 On-axis observation

An overview of the number of events for the test dataset and training dataset is provided in Tab. 3.4 and Tab. 3.5. Both tables indicate the energy dependent number of events at a trigger level and after an angular distance cut of 1° between the CoG of the recorded image and the camera center. Note that, nearly $\sim 100\%$ of the γ-ray events survive the angular distance cut at 10 TeV. This indicates that the sweet-spot, in terms of statistics after an angular distance cut of 1° (CoG-Center), for on-axis observation is around $\mathcal{O}(10\,\text{TeV})$ for H.E.S.S. CT5 at a zenith angle of 80°.

The Random Forest classifier is trained and tested on the respective datasets with an angular distance cut of 1° (CoG-Center). The resulting efficiencies ϵ_γ and ϵ_{bkg} for the full energy range are shown in Fig. 3.10a. For a γ-efficiency of $\epsilon_\gamma \approx 0.5$ a *gammaness*

	Proton		Helium		γ	
Data level	Trigger	1° cut	Trigger	1° cut	Trigger	1° cut
0.5 TeV	5044	1756 (35%)	779	275 (35%)	-	-
1.0 TeV	12782	4441 (35%)	4408	1497 (34%)	1079	364 (34%)
10.0 TeV	25721	9663 (38%)	20478	7497 (37%)	52466	52382 (99%)
100.0 TeV	55714	17897 (32%)	51038	16877 (33%)	52147	21098 (40%)
1000.0 TeV	18385	4728 (26%)	17581	4492 (26%)	46157	10338 (22%)
Total	0.12×10^6	0.38×10^5	0.94×10^5	0.31×10^5	0.15×10^6	0.84×10^5

Table 3.4: Statistics for the test dataset. The number of events at trigger level and after an angular distance cut of 1° (CoG-Center) for CT5 are presented for proton, helium, and γ events, respectively.

	Proton		Helium		γ	
Data level	Trigger	1° cut	Trigger	1° cut	Trigger	1° cut
0.5 TeV	5028	1780 (35%)	765	241 (32%)	-	-
1.0 TeV	12897	4510 (35%)	4342	1541 (35%)	955	327 (34%)
10.0 TeV	25476	9323 (37%)	20191	7348 (36%)	52456	52375 (99%)
100.0 TeV	55077	17712 (32%)	50988	16940 (33%)	52062	21292 (41%)
1000.0 TeV	18685	4787 (26%)	17635	4387 (25%)	46231	10149 (22%)
Total	0.12×10^6	0.38×10^5	0.94×10^5	0.31×10^5	0.15×10^6	0.84×10^5

Table 3.5: Statistics for the training dataset. The number of events at trigger level and after an angular distance cut of 1° (CoG-Center) for CT5 are presented for proton, helium, and γ events, respectively.

cut of $gammaness \geq 0.9$ is needed. The corresponding background efficiency is roughly $\epsilon_{bkg} = 0.01$. The γ-hadron separation power in terms of the quality factor Q is presented in Fig. 3.10b. For a cut of $gammaness \geq 0.9$, the overall quality factor is $Q \sim 5.1$.

The number of background events as well as γ-ray events after the γ-hadron separation with a *gammaness* cut of $gammaness \geq 0.9$ is provided in Tab. 3.6. Noticeably, no γ-ray events at 1 TeV survive the γ-hadron separation, while the γ-efficiency at 1000 TeV is approximately $\epsilon_\gamma \sim 95\%$.

The feature importances of the provided input parameters are shown in Fig. 3.11. Clearly, the parameters *width* and $width/length$ (w/l) have less separation power compared to the four other parameters. Especially, the information of the trigger pattern (*multi*) proves to have a visible impact on the Random Forest classification. Rather

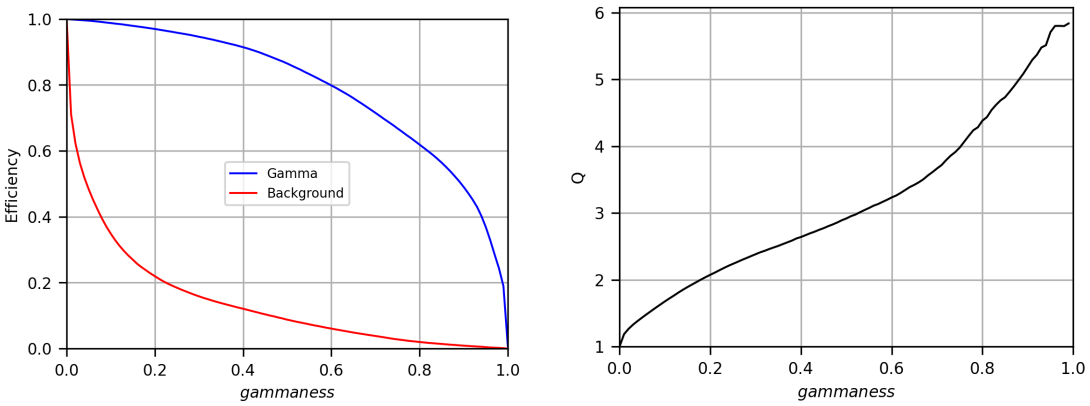

(a) Efficiency for γ-ray events and background events as a function of *gammaness* cut values.

(b) Quality factor Q (see Eqn. 3.7 for definition of Q) as a function of *gammaness* cut values.

Figure 3.10: γ-hadron separation power for the on-axis analysis.

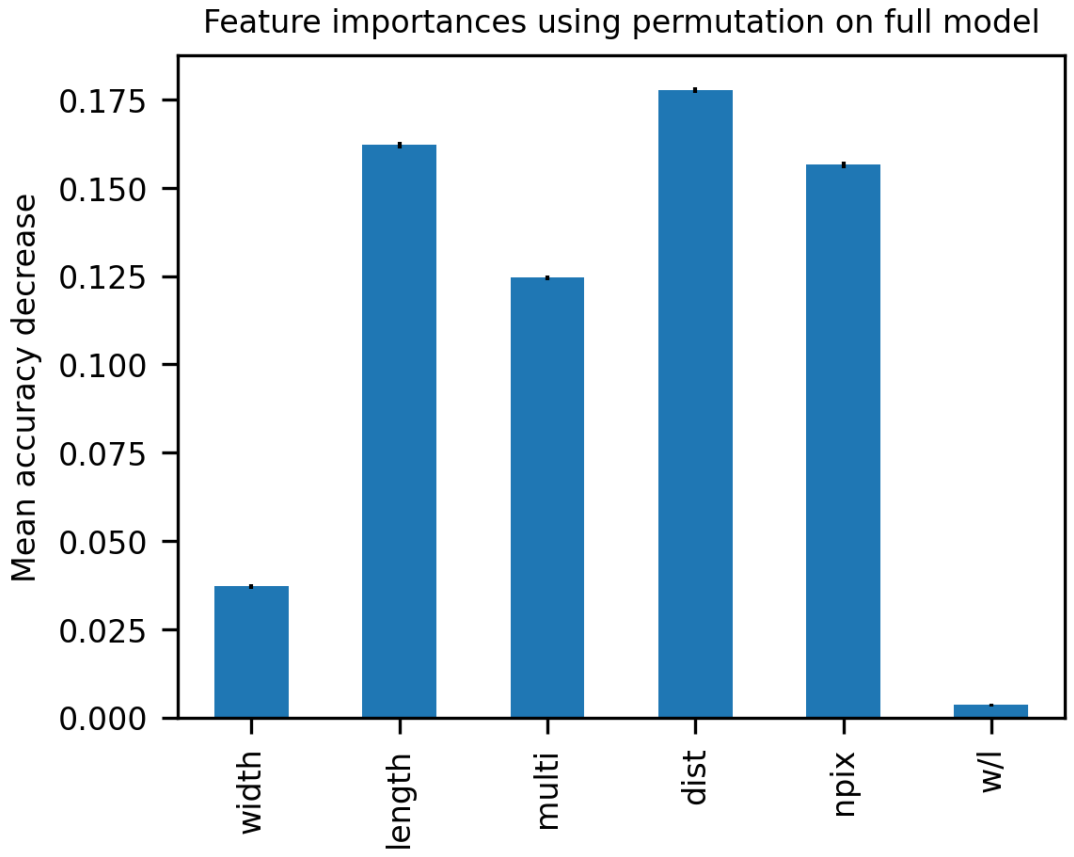

Figure 3.11: Feature importances for the Random Forest Classifier in the on-axis case.

	Proton	Helium	γ	Q
0.5 TeV	24	2	-	-
1.0 TeV	48	19	0	0
10.0 TeV	111	47	16150	3.2
100.0 TeV	295	62	16740	7.8
1000.0 TeV	49	15	9806	11.4
Total	5.27×10^2	1.45×10^2	4.27×10^4	5.1

Table 3.6: Number of events surviving the γ-hadron separation with a *gammaness* cut of $gammaness \geq 0.9$. Additionally, the quality factor Q is indicated for each simulated energy.

unexpected is the high importance for the number of pixels surviving the cleaning process *npix*. Most likely, this is caused by choosing discrete energies for the simulation of the γ-ray and background datasets. Hadronic showers typically have approximately one-third the number of charged particles when compared to electromagnetic showers of equivalent energy. As a result, this reduction in charged particles leads to fewer Cherenkov photons, eventually affecting *npix*. A Random Forest classification with the same input parameters as above except *npix* yields a quality factor of $Q = 3.4$ at a γ-efficiency of $\epsilon_\gamma = 0.5$. The corresponding cut on *gammaness* is $gammaness \geq 0.8$ and the background efficiency is $\epsilon_{bkg} = 0.02$.

3.3.2 1° offset observation

The number of events for the test dataset and training dataset for a 1° offset observation (i.e., CT5 is pointing at a zenith angle of 81°) is presented in Tab. 3.7 and Tab. 3.8, respectively. The fraction of γ-ray events that survive the angular distance cut of 1° at 10 TeV decreases from $\sim$ 100% for on-axis observation to $\sim$ 40%. In contrast, the fraction of surviving γ-ray events increases from $\sim$ 22% to $\sim$ 31% at 1000 TeV, while at 100 TeV it basically remains unchanged $\sim$ 40%. For the fraction of surviving background events, no noticeable change is observed.

Similar to Sec. 3.3.1, the datasets are used for training and testing under the constraint of an angular distance cut of 1° (CoG-Center). The corresponding results for the efficiencies ϵ_γ and ϵ_{bkg} are displayed in Fig. 3.12a across the complete simulated energy range. To achieve a γ-efficiency of $\epsilon_\gamma = 0.5$, a *gammaness* threshold of $gammaness \geq 0.93$ is

	Proton		Helium		γ	
Data level	Trigger	1° cut	Trigger	1° cut	Trigger	1° cut
0.5 TeV	3485	1279 (37%)	430	153 (36%)	-	-
1.0 TeV	9641	3331 (35%)	3107	1069 (34%)	721	376 (52%)
10.0 TeV	17928	6596 (37%)	15693	5700 (36%)	49166	19967 (41%)
100.0 TeV	50620	16929 (33%)	46795	16152 (35%)	38744	16547 (43%)
1000.0 TeV	17629	4683 (27%)	16622	4517 (27%)	45456	13941 (31%)
Total	9.93×10^4	3.28×10^4	8.26×10^4	2.76×10^4	1.34×10^5	5.08×10^4

Table 3.7: Statistics for the test dataset. The number of events at trigger level and after an angular distance cut of 1° (CoG-Center) for CT5 are presented for proton, helium, and γ events, respectively.

	Proton		Helium		γ	
Data level	Trigger	1° cut	Trigger	1° cut	Trigger	1° cut
0.5 TeV	3461	1210 (35%)	422	136 (32%)	-	-
1.0 TeV	9824	3364 (34%)	3165	1124 (36%)	661	354 (54%)
10.0 TeV	17561	6349 (36%)	15640	5705 (36%)	49148	19712 (40%)
100.0 TeV	50138	16913 (34%)	46803	16418 (35%)	38657	16299 (42%)
1000.0 TeV	17788	4722 (27%)	16703	4528 (27%)	45379	13958 (31%)
Total	9.88×10^4	3.26×10^4	8.27×10^4	2.79×10^4	1.34×10^5	5.03×10^4

Table 3.8: Statistics for the training dataset. The number of events at trigger level and after an angular distance cut of 1° (CoG-Center) for CT5 are presented for proton, helium, and γ events, respectively.

required, while the associated background efficiency is approximately $\epsilon_{bkg} \approx 0.01$. The evaluation of the γ-hadron separation power, quantified using the quality factor Q, is presented in Fig. 3.12b, where, with a *gammaness* cut of $gammaness \geq 0.93$, the overall quality factor reaches roughly $Q \sim 5.6$. Note that this value is consistent with the derived Q for the on-axis analysis (see Sec. 3.3.1).

The energy dependent quality factor Q, together with the number of γ and background events after a *gammaness* cut of $gammaness \geq 0.93$, is provided in Tab. 3.9. Identical to the on-axis analysis in Sec. 3.3.1, no γ-ray events at 1 TeV survive the γ-hadron separation. While the overall quality factor Q is indeed comparable to the result obtained in the on-axis analysis, it is worth noting that the energy dependent Q at 10 TeV, 100 TeV and 1000 TeV differ between the off-axis and on-axis analyses (see Tab. 3.6). Whereas Q increases from $Q_{\mathrm{on-axis}} = 3.2$ to $Q_{\mathrm{off-axis}} = 4.1$ at 10 TeV, it noticeably decreases at

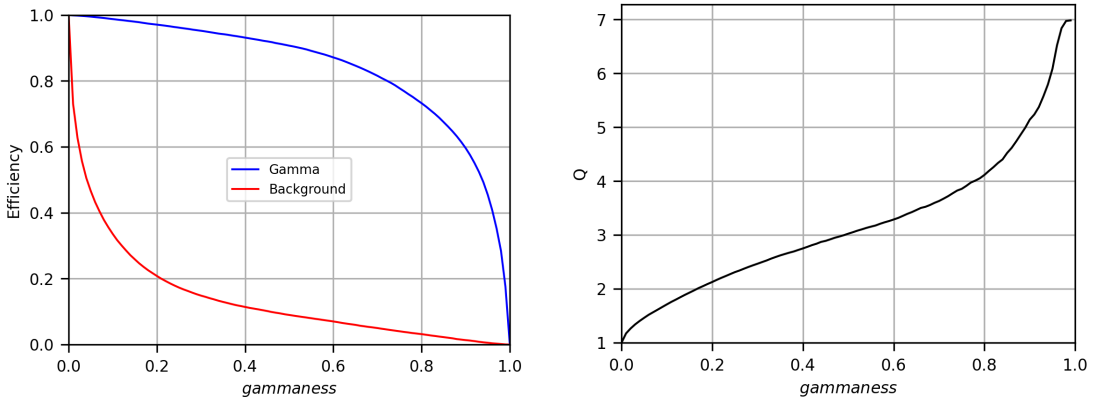

(a) Efficiency for γ-ray events and background events as a function of *gammaness* cut values.

(b) Quality factor Q (see Eqn. 3.7 for definition of Q) as a function of *gammaness* cut values.

Figure 3.12: γ-hadron separation power for the off-axis analysis.

	Proton	Helium	γ	Q
0.5 TeV	18	1	-	-
1.0 TeV	38	13	0	0
10.0 TeV	90	44	8455	4.1
100.0 TeV	169	61	6883	5.0
1000.0 TeV	65	38	11375	7.7
Total	3.80×10^2	1.57×10^2	2.67×10^4	5.6

Table 3.9: Number of events surviving the γ-hadron separation with a *gammaness* cut of *gammaness* ≥ 0.93. Additionally, the quality factor Q is indicated for each simulated energy.

100 TeV from $Q_{\mathrm{on-axis}} = 7.8$ to $Q_{\mathrm{off-axis}} = 5.0$ and at 1000 TeV from $Q_{\mathrm{on-axis}} = 11.4$ to $Q_{\mathrm{off-axis}} = 7.7$.

The feature importances of the provided input parameters for the off-axis analysis are illustrated in Fig. 3.13. In comparison to the on-axis analysis (see Fig. 3.11), the feature importance for the parameters *length*, *multi* and *npix* slightly decreases, while the feature importance for the parameters *width*, *dist* and *width*/*length* (w/l) clearly increases. Especially the increase of importance for the *width* parameter is striking, since it indicates that the *width* distribution of the γ and/or background events significantly changes for off-axis observations compared to on-axis observations.

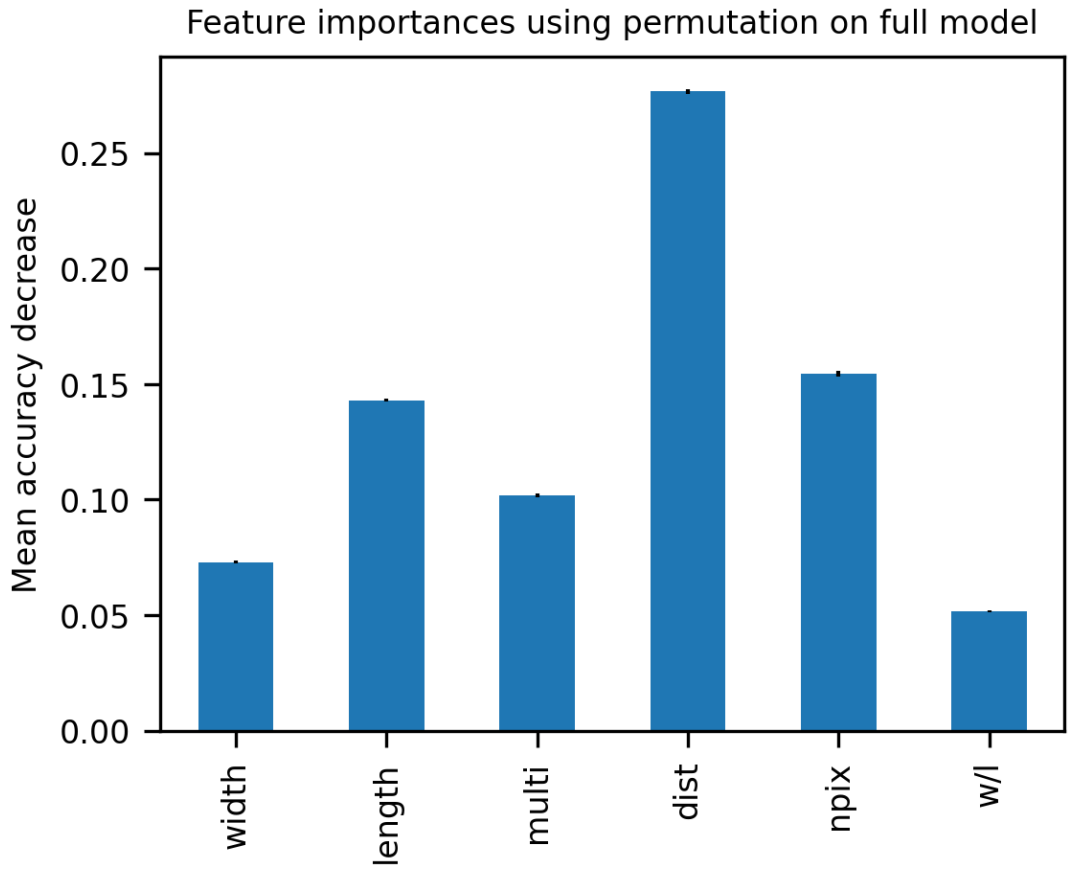

Figure 3.13: Feature importances of the Random Forest Classifier in the off-axis case.

3.3.3 Discussion

In order to cross-check the increased importance of the *width* parameter for off-axis observations compared to on-axis observations, the distribution of the *width* parameter for the complete simulated energy range is provided in Fig. 3.14. Evidently, the distribution of the *width* parameter for background events (proton+helium) is similar for on-axis and off-axis observations, while the distribution for γ-ray events is shifted towards higher *width* values for off-axis observations compared to on-axis observations. It is important to note, that the main bulge of the background and γ-ray events for on-axis observations lies in a very similar range of *width* values ($\sim 0.04^\circ$ to 0.065°), whereas the main bulge of the γ-ray events for off-axis observations lies within a narrower range of *width* values ($\sim 0.05^\circ$ to 0.06°). As a result, a cut on the *width* values for on-axis observations, with respect to γ-hadron separation, is less effective.

Noticeably, the *width* distribution in Fig. 3.14 shows a bipolar behaviour (i.e., two peaks can be observed), independent of the observation type and particle type. This bipolar behaviour is predominantly caused by the low energy ($\leq 10\,\mathrm{TeV}$) simulations, as indicated in Fig. 3.15a, where the distribution of the *width* values for γ-ray events

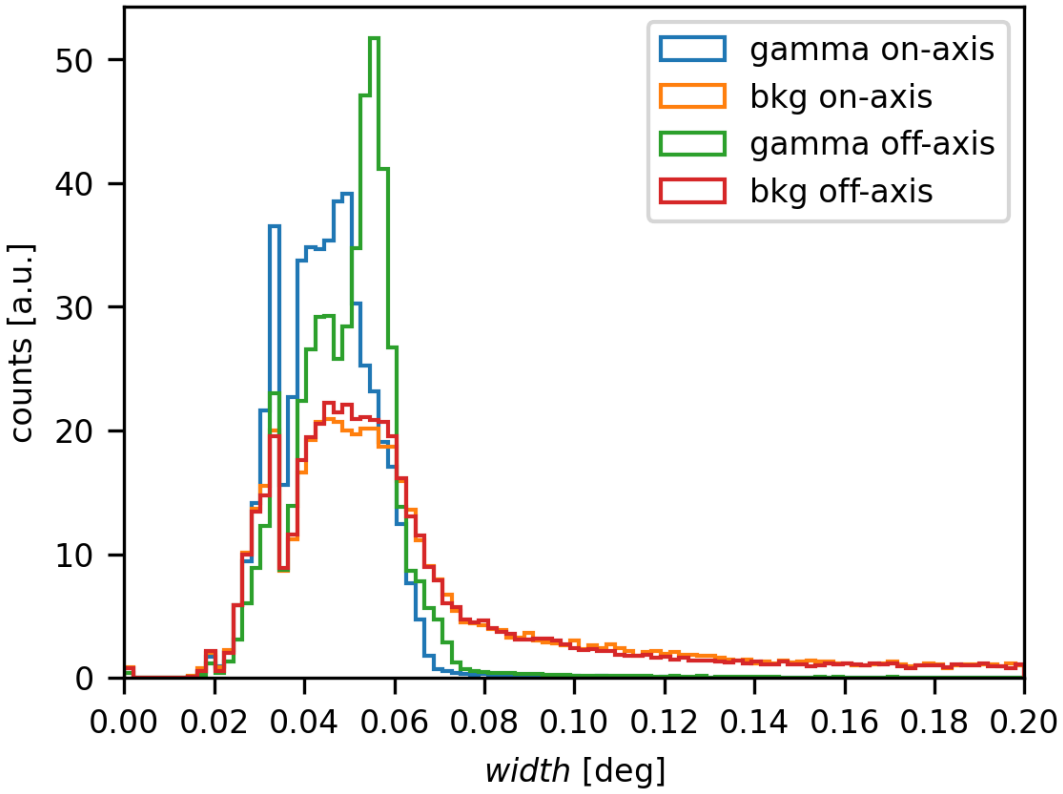

Figure 3.14: Normalized distribution of the *width* values across the complete simulated energy range, including an angular distance cut of 1° (CoG-Center), for γ-ray (blue/-green histogram: on-axis/off-axis) and background events (orange/red histogram: on-axis/off-axis). Here, off-axis observation indicates that H.E.S.S. CT5 is pointing at a zenith angle of 81°.

after an angular distance cut of 1° (CoG-Center) for on-axis observation is compared for energies of 10 TeV, 100 TeV and 1000 TeV [5]. Similarly, a bipolar behaviour of the *width* values for energies $\leq$ 10 TeV is observed for proton events after an angular distance cut of 1° (see Fig. 3.15b), where strikingly the distribution at 1 TeV and 10 TeV is essentially identical. Although not presented here, the distribution of the *width* values for helium events exhibit also a bipolar behaviour at energies $\leq$ 10 TeV together with an almost identical distribution of *width* values at 1 TeV and 10 TeV.

This can be explained by considering, that the detector has a finite resolution, which depends on the pixel size. In case of H.E.S.S. CT5, the pixel size is approximately $pixel_{res} \sim 0.067°$, as indicated in Tab. 2.1. Note that, the first peak in Fig. 3.15a and Fig. 3.15b at energies $\leq$ 10 TeV occurs roughly at a *width* value of $width \approx 0.03° \approx pixel_{res}/2$. Not only is the air shower fainter for primary energies of $\leq$ 10 TeV compared to primary energies of $\geq$ 10 TeV, but also the depth of the shower maximum X_{max} will decrease (see Sec.2.1 and Sec. 2.2) with decreasing primary energies. Therefore,

[5] The 1 TeV simulations are not included in Fig. 3.15a due to low statistics.

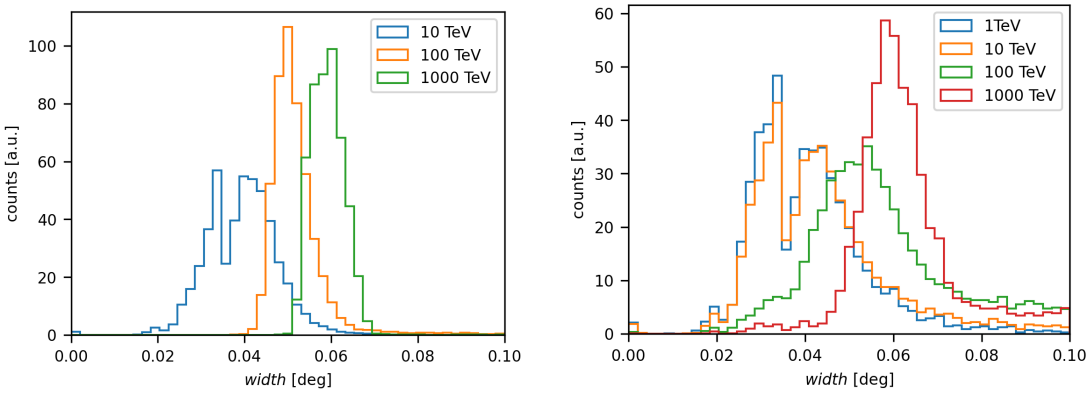

(a) Normalized distribution of *width* values for γ-ray events at energies of 10 TeV, 100 TeV and 1000 TeV for on-axis observation.

(b) Normalized distribution of *width* values for proton events at energies of 1 TeV, 10 TeV, 100 TeV and 1000 TeV for on-axis observation.

Figure 3.15: Comparison of *width* values for (a) γ-ray events and (b) proton events.

the distance of the shower maximum to the telescope increases with decreasing primary energy, and as a result, the air shower is observed under smaller angles. This also explains, why the *width* distribution in Fig. 3.15b for energies of 1 TeV and 10 TeV is almost identical - the air showers will appear so small, that the resolution of the detector is not sufficient to distinguish these two cases anymore.

An example camera image of H.E.S.S. CT5 for γ-ray events with energies of 10 TeV and 1000 TeV is presented in Fig. 3.16a and Fig. 3.16b, respectively. It is evident, that in the 10 TeV case the recorded camera image consists in total of only a few triggered pixels. Furthermore, along the shower development, just a single illuminated pixel in the perpendicular direction of the shower axis (yellow solid line) can be observed, while in the 1000 TeV case the lateral extension of the recorded image is significantly larger.

Consequently, since the *width* distribution changes depending on the observation type, the distribution of *width*/*length* will also be affected by the observation type. This is shown in Fig. 3.17a and Fig. 3.17b for γ-ray energies of $E_\gamma = 1000$ TeV, in terms of a two-dimensional histogram of *width*/*length* plotted against the *dist* parameter, for on-axis and off-axis observation respectively. Clearly, the distribution for the on-axis observation appears to be broader compared to the off-axis observation. A further investigation, in order to understand the difference in the distributions, remarkably revealed that for on-axis observations the impact position of the shower on the ground, in particularly, whether the impact position is *behind* (impact $x < 0$) or *in front* (impact $x > 0$)[6] of the telescope, plays a crucial role.

[6]For a definition of x see Fig. 3.8. CT5 is pointing in the direction of the positive x-axis.

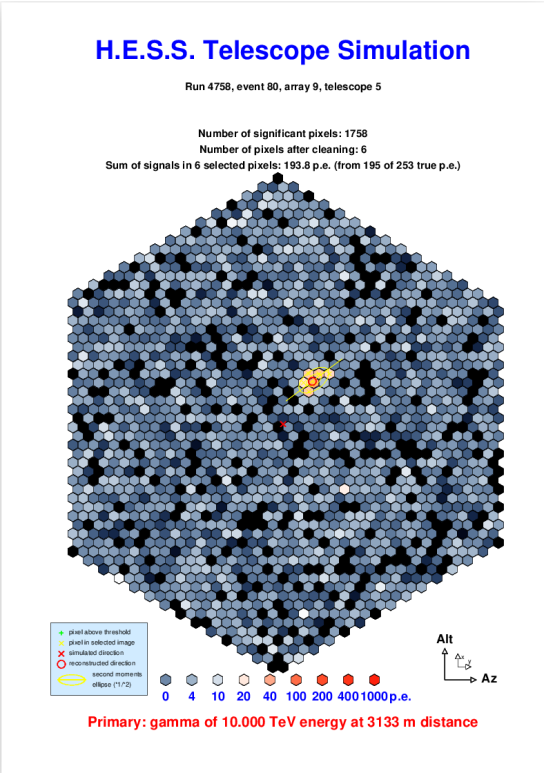

(a) Camera image of a 10 TeV γ-ray event, recorded with H.E.S.S. CT5. Telescope is pointing parallel to the shower axis at a zenith angle of 80°. The yellow ellipses indicate the first and second moment of the Hillas ellipse, calculated by using the pixels marked with a yellow cross.

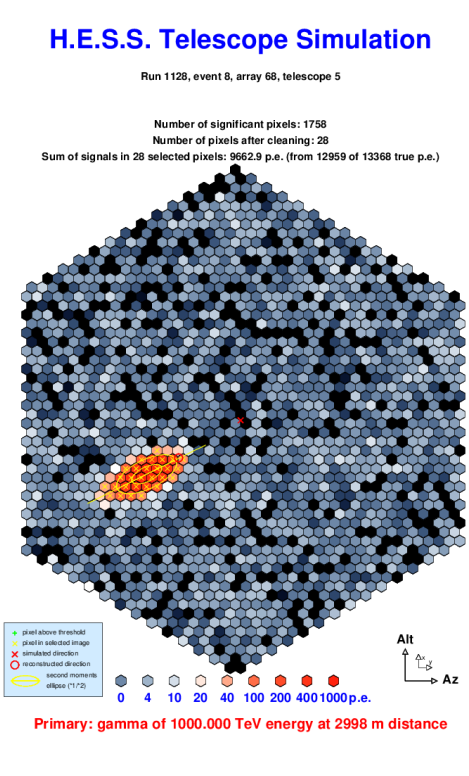

(b) Camera image of a 1000 TeV γ-ray event, recorded with H.E.S.S. CT5. Telescope is pointing parallel to the shower axis at a zenith angle of 80°. The yellow ellipses indicate the first and second moment of the Hillas ellipse, calculated by using the pixels marked with a yellow cross.

Figure 3.16: Comparison of a recorded (a) 10 TeV and (b) 1000 TeV γ-ray event with H.E.S.S. CT5.

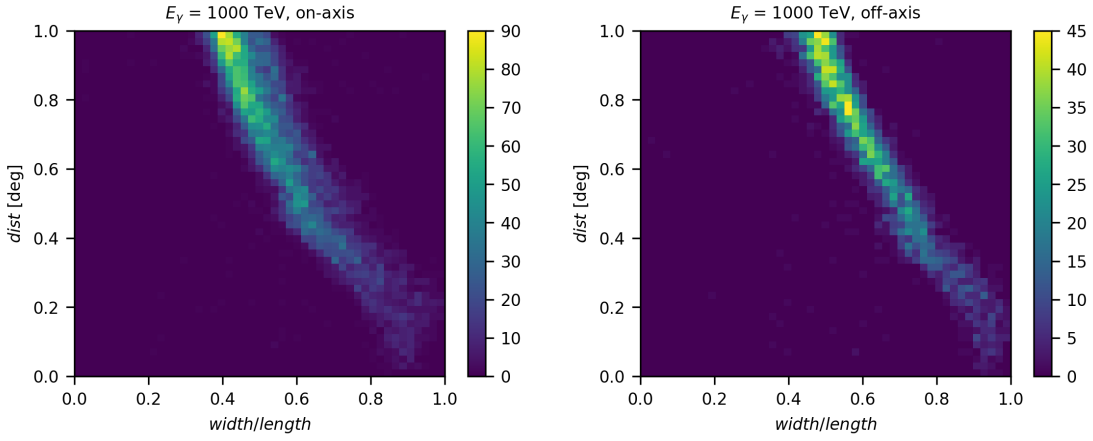

(a) Two-dimensional histogram of the *dist* parameter and *width/length* for γ-ray energies of 1000 TeV. H.E.S.S. CT5 is pointing at a zenith angle of 80°.

(b) Two-dimensional histogram of the *dist* parameter and *width/length* for γ-ray energies of 1000 TeV. H.E.S.S. CT5 is pointing at a zenith angle of 81°.

Figure 3.17: Comparison of *dist* as a function of *width/length* for (a) on-axis and (b) off-axis observations.

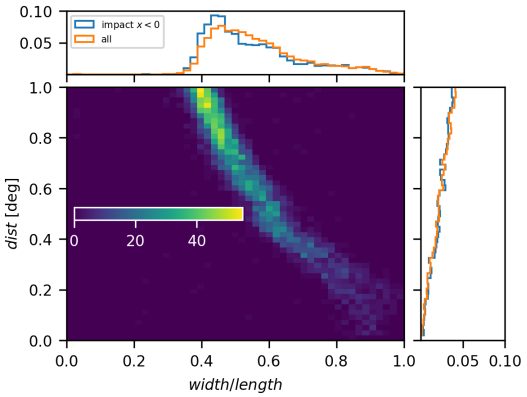

(a) Same as in Fig. 3.17a, but here only the γ-ray events with impact positions behind the telescope (impact $x < 0$) are considered. Additionally, the normalized projections of the x-axis and y-axis are shown in the top and right panel (blue histograms) respectively, together with the corresponding normalized projections of Fig. 3.17a (orange histograms).

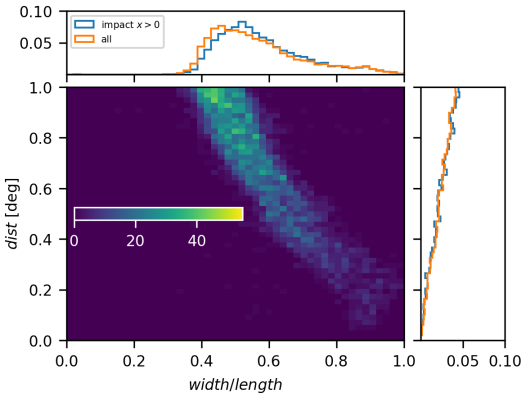

(b) Same as in Fig. 3.17a, but here only the γ-ray events with impact positions in front of the telescope (impact $x > 0$) are considered. Additionally, the normalized projections of the x-axis and y-axis are shown in the top and right panel (blue histograms) respectively, together with the corresponding normalized projections of Fig. 3.17a (orange histograms).

Figure 3.18: Influence of (a) impact $x < 0$ and (b) impact $x > 0$ on the *dist* distribution as a function of *width*/*length* for on-axis observation.

The effect of the impact position on the ground is illustrated in Fig. 3.18a and Fig. 3.18b, where the two-dimensional histogram presented in Fig. 3.17a is now shown for impact positions $x < 0$ and $x > 0$. Noticeably, the distribution for impact positions behind the telescope is comparable to the distribution of the off-axis observation (see Fig. 3.17b), while the distribution for impact positions in front the telescope still appears to be broader.

The corresponding *width* and *length* distributions are presented in Fig. 3.20a and Fig. 3.20b, respectively. Additionally, the *width* and *length* distributions for the off-axis observation are indicated for $x_{scat} > 1.4\,\text{km}$ and $x_{scat} < 1.4\,\text{km}$. Note that, x_{scat} and y_{scat} refer to the position of the scattered shower in a plane perpendicular to the shower axis (see Sec. 3.1). Therefore, the impact x position on the ground can be calculated with $x = x_{scat}/\cos(80°)$. The value of 1.4 km is chosen based on Fig. 3.19, where the triggered events are displayed for both observation types in terms of a two-dimensional histogram in the (x_{scat}, y_{scat}) plane. The overlapping region in Fig. 3.19 can roughly be described by considering the events with $x_{scat} > 0$ for on-axis observation and $x_{scat} < 1.4\,\text{km}$ for off-axis observation. This way, events with a similar core radius can be compared in terms of the *width* and *length* parameters for both observation types.

For the *width* distribution in Fig. 3.20a, two general remarks can be made: 1) The *width* distributions for the on-axis observation with $x_{scat} > 0$ and the off-axis observation

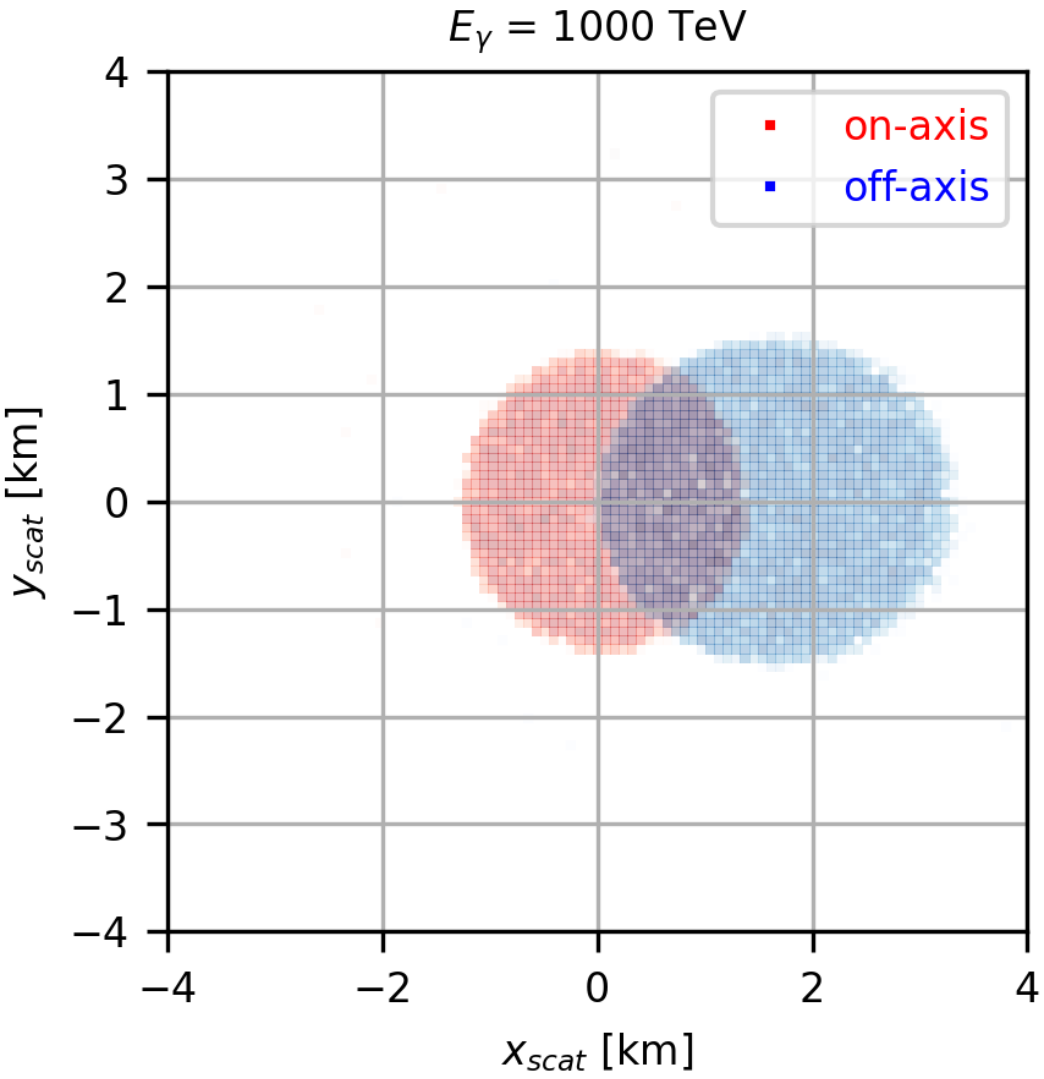

Figure 3.19: Two-dimensional histogram for triggered events after an angular distance cut of 1° for on-axis (red, CT5 is pointing at a zenith angle of 80°) and off-axis (blue, CT5 is pointing at a zenith angle of 81°) observation. The γ-ray primaries with energies of $E_\gamma = 1000\,\text{TeV}$ have a zenith angle of 80°. x_{scat} and y_{scat} indicate the position of the scattered shower in a plane perpendicular to the shower axis (see Sec. 3.1). Almost all bins (80 m × 80 m) have approximately 10 events.

(independent of x_{scat}) cover roughly the same range of *width* values, with the exception of a clearly visible tail for the off-axis observation with $x_{scat} < 1.4\,\text{km}$. This tail is caused by events with a small core distance R_{core} of the order of $R_{core} \sim \mathcal{O}(500)\,\text{m}$ (see Fig. 3.22). The shape of the recorded image for these events is almost circular, such that $width/length \approx 1$ (see Fig. 3.17b, lower right part of the distribution). 2) The *width* distribution for the on-axis observation with impact $x < 0$ is shifted towards higher values compared to the on-axis observation with impact $x > 0$.

The *length* distribution in Fig. 3.20b also shows unexpected behaviour: 1) Clearly, for

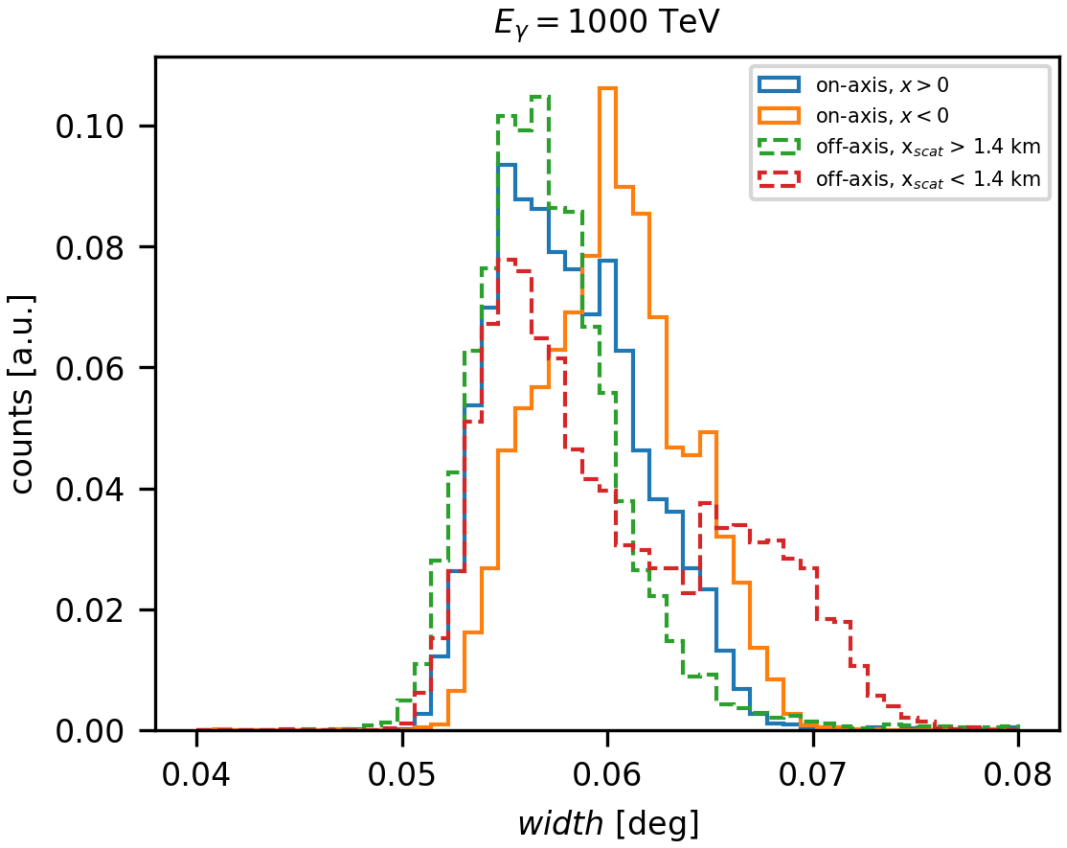

(a) *width* distribution of the events in Fig. 3.19.

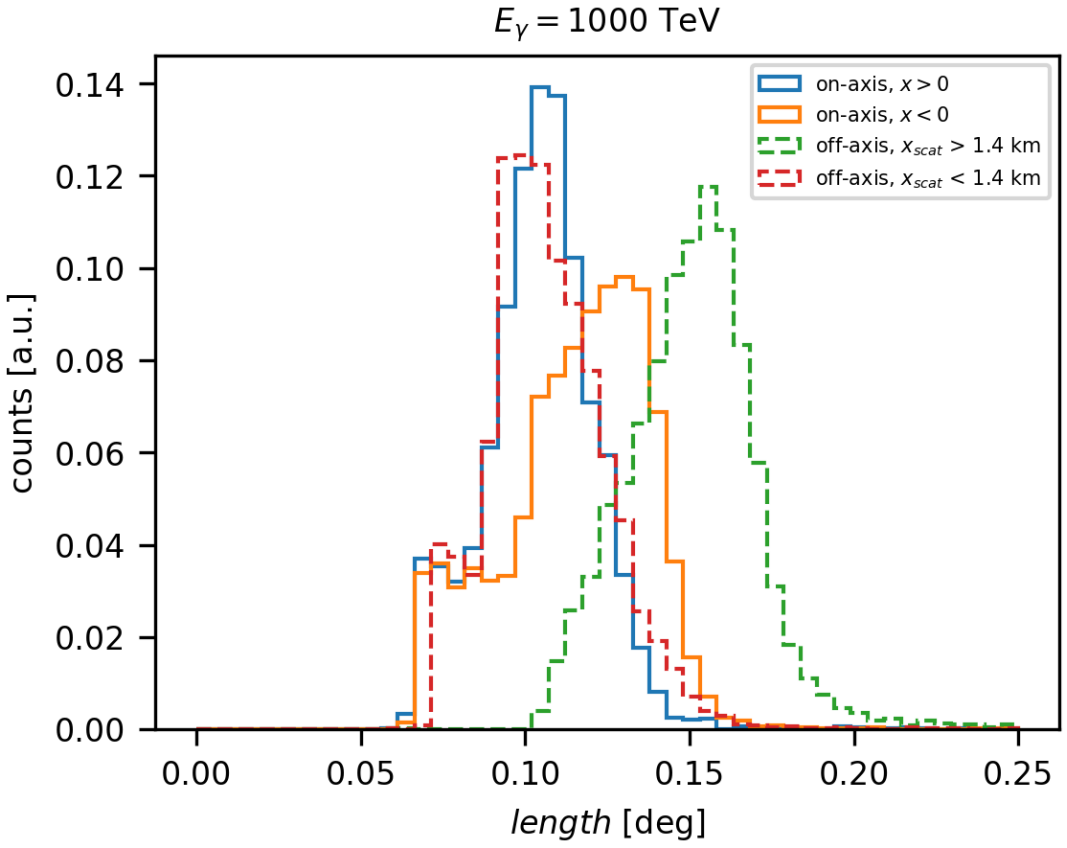

(b) *length* distribution of the events in Fig. 3.19.

Figure 3.20: Comparison of (a) *width* and (b) *length* for on-axis and off-axis observation.

on-axis observation the distribution is shifted towards larger values for impact $x < 0$ compared to $x > 0$. In the case of off-axis observation, a shift towards larger *length* values can be observed for $x_{scat} > 1.4\,\text{km}$ compared to $x_{scat} < 1.4\,\text{km}$ and, this shift is more pronounced than in the on-axis case (see also Fig. 3.21). 2) The distribution for the on-axis observation with impact $x > 0$ and the off-axis observation with $x_{scat} < 1.4\,\text{km}$ are comparable.

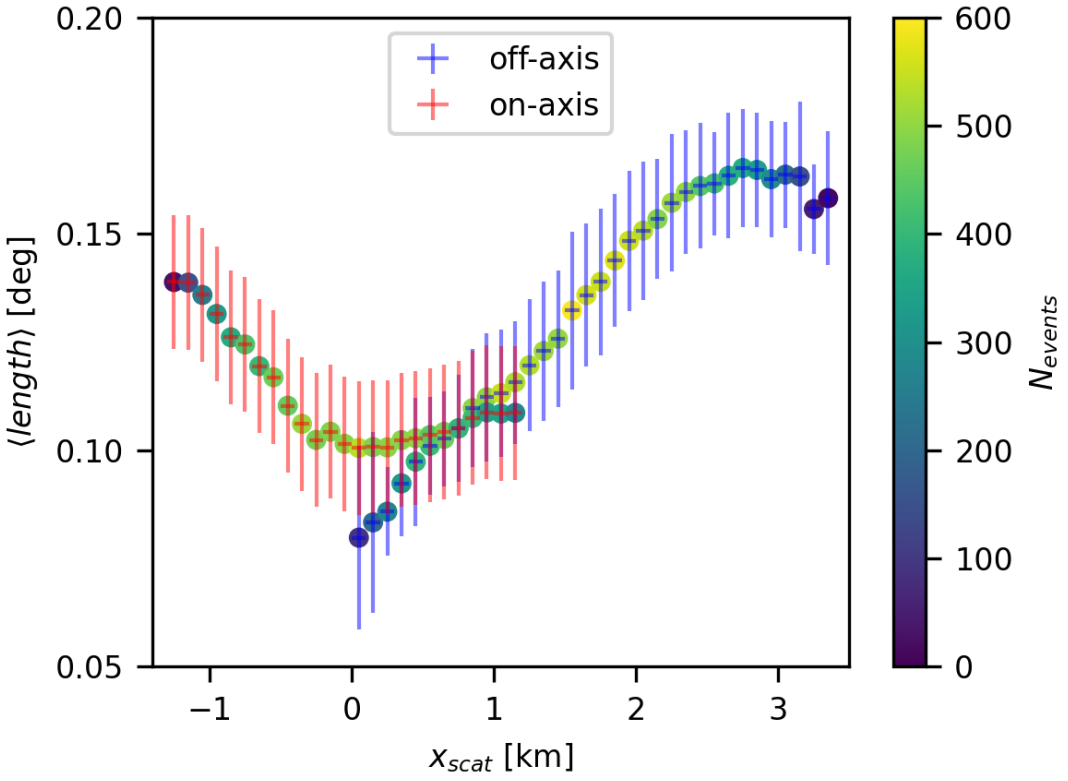

Figure 3.21: Mean *length* values $\langle length \rangle$ for on-axis (red) and off-axis (blue) observation considering 100 m x_{scat} slices (horizontal lines) of Fig. 3.19 together with the corresponding $1\,\sigma$ errors (vertical lines). The filled circles indicate the total number of events N_{events} within one x_{scat} slice (see right colorbar).

A clear explanation for the above mentioned remarks regarding Fig. 3.20a and Fig. 3.20b could not be found. However, especially the *length* distribution in Fig. 3.20b, independent of the observation type, indicates that different stages of the shower development are observed depending on the impact position on the ground for observations at large zenith angles. For on-axis observation with impact $x > 0$, the *width* and *length* distribution suggest that early stages of the shower development are captured while the light emitted at later stages is not collected by the telescope anymore due to a larger Cherenkov opening angle with decreasing height in the atmosphere (see Sec. 2.3). Since at early stages of the shower development the electrons and positrons are on average closer to the shower axis, the lateral extension of the shower will appear smaller in angular size. Conversely, for impact $x < 0$ also the light emitted at later stages of the

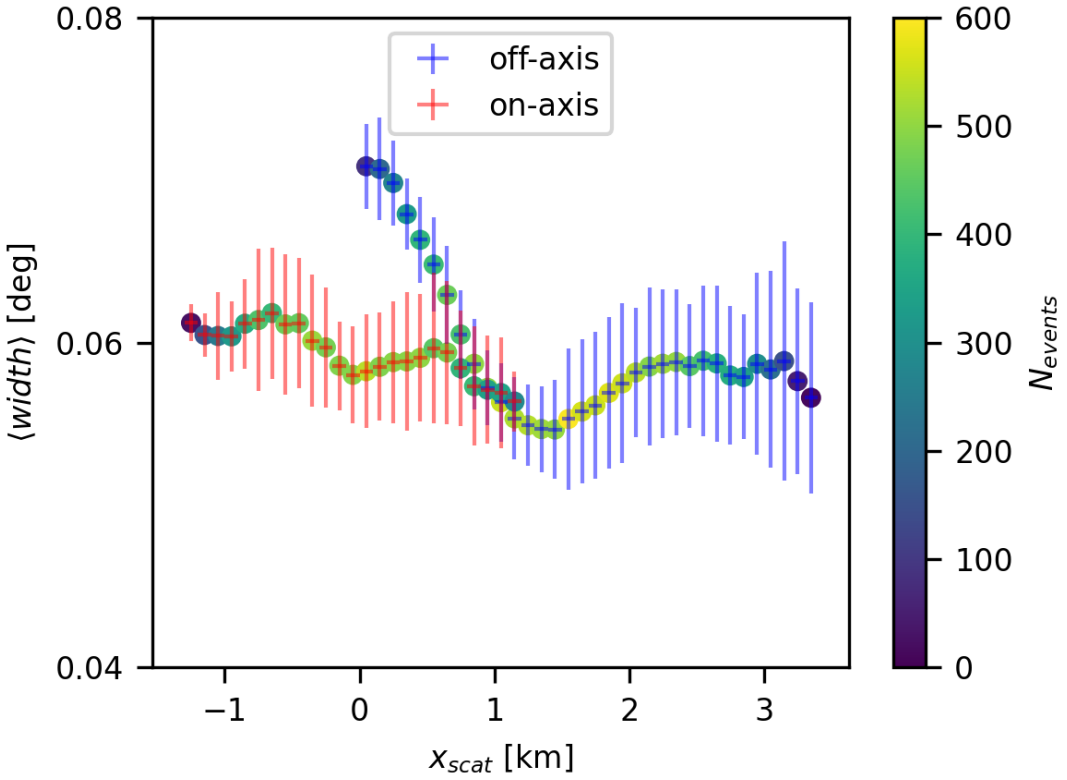

Figure 3.22: Mean *width* values $\langle width \rangle$ for on-axis (red) and off-axis (blue) observation considering 100 m x_{scat} slices (horizontal lines) of Fig. 3.19 together with the corresponding 1 σ errors (vertical lines). The filled circles indicate the total number of events N_{events} within one x_{scat} slice (see right colorbar).

shower development will reach the telescope and, therefore the *length* distribution will be shifted towards larger values. Additionally, as the development of the air shower advances, the air shower will broaden up due to multiple Coulomb scattering of electrons and positrons, and as a result the average lateral extension of the shower will appear larger in angular size.

The situation for the off-axis observation is more complex, since the telescope is not pointing parallel to the shower axis anymore and, the core distance increases greatly, i.e., $R_{core}^{\max} = x_{scat}^{max} / \cos(80°) \approx 20\,\text{km}$ (see Fig. 3.19)[7]. A possible explanation for the distributions might be, that the cone formed by the field of view of the telescope starts to intersect larger regions of the shower development with increasing x_{scat}, since the telescope is pointing with a 1° offset with respect to the shower axis.

[7]Note, that the maximum core radius in case of on-axis observation is approximately $R_{core}^{max} \sim 1/\cos(80°)\,\text{km} \sim 6\,\text{km}$

3.4 Origin reconstruction

In this section, the reconstructed source position in the camera is determined with the *disp* method [124].

As mentioned in Sec. 2.5, one can infer the projection of the shower axis onto the image plane from the orientation of the major axis. However, this information alone only specifies that the source position is located somewhere on the projection of the major axis. In order to determine where on the axis the origin lies, the angular distance *disp* of the CoG to the source location needs to be reconstructed. Still, since there is an ambiguity in which direction the origin is located (see Fig. 2.10), one also needs to deduce a sign (+1 or -1). In general, the recorded image of γ-ray events have a light distribution, which is skewed towards the source location in the image plane. Therefore, to solve the ambiguity issue, the sign of the *skew* parameter (third moment of the Hillas ellipse along the major axis) is used.

The *disp* parameter is reconstructed using the Radom Forest Regressor with the same configuration as explained in Sec. 3.3. The Random Forest Regressor is trained with the γ-ray training dataset, including a 1° cut (CoG-Center), presented in Tab. 3.5 and Tab. 3.8 for on-axis and off-axis observation, respectively. The parameters *size*, *width*, *length* and *width/length* are used as training parameters.

The reconstructed source position in the camera (x_{cam}, y_{cam}) is calculated with:

$$(x_{cam}, y_{cam}) = (\cos(\phi), \sin(\phi)) \cdot disp_{reco} \cdot \text{sign}(skew) + (CoG_x, CoG_y), \tag{3.9}$$

where ϕ denotes the orientation of the major axis.

3.4.1 On-axis observation

The trained Random Forest Regressor is applied to the on-axis dataset after γ-hadron separation, i.e., to the dataset indicated in Tab. 3.6.

The importance of the training parameters is provided in Fig. 3.23a, where clearly the *length* parameter appears to be the most important parameter. Conversely, the parameters *width* and *width/lenth*(w/l) show basically no importance at all. This is particularly surprising for the *width/length* parameter, considering that parametrizations for the *disp* parameter typically depend on this feature (see, e.g., [125]). The performance of the Random Forest Regressor is indicated in Fig. 3.23b in terms of a normalized histogram of the residuals $disp_{true} - disp_{reco}$ for the complete energy range, where $disp_{true}$

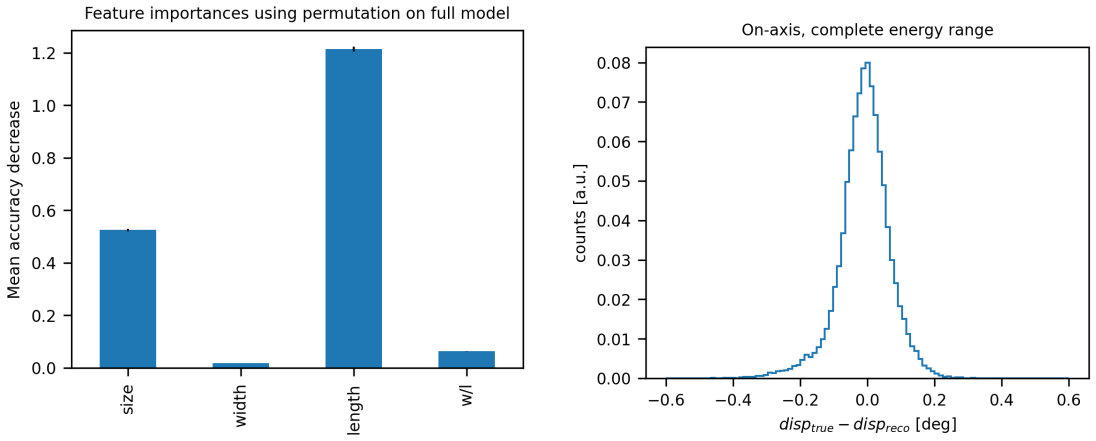

(a) Feature importances of the Random Forest Regressor for the *disp* parameter

(b) Normalized histogram of the residuals $disp_{true} - disp_{reco}$.

Figure 3.23: Performance of the *disp* reconstruction in the on-axis case.

denotes the true value of the *disp* parameter and $disp_{reco}$ the reconstructed value. The Full Width Half Maximum (FWHM) of the distribution appears to be approximately $\sim 0.1°$.

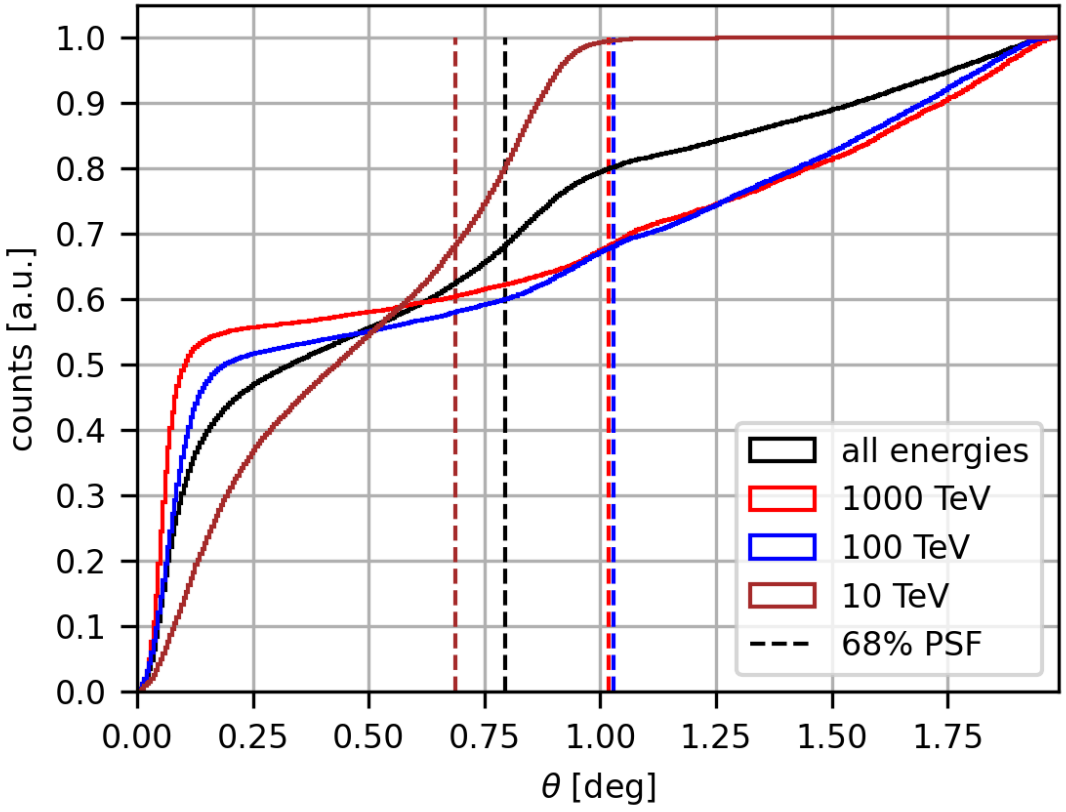

Figure 3.24: Cumulative distribution of the θ values for energies of 10 TeV, 100 TeV, 1000 TeV and the complete energy range, where the dashed lines indicate the 68%-percentile.

The energy dependent angular resolution (defined as the 68%-percentile) of the detector is illustrated in Fig. 3.24, in the form of a cumulative distribution of the θ values, where θ is the angular distance between the true source position and the reconstructed source position (see Fig. 2.10). Without a question, the distribution shows unexpected behaviour, resulting in a poor resolution across all energies. Since the reconstruction of the *disp* parameter shows promising performance, one has to conclude, that the sign assignement in Eqn. 3.9 does not give the correct direction for the majority of the events. Indeed, it was found that the angular resolution can be significantly improved, if the sign of the *skew* parameter sign(*skew*) is flipped for events with $CoG_x > 0$, i.e.,

$$\text{if}(CoG_x > 0):$$

$$(x_{cam}, y_{cam}) = (\cos(\phi), \sin(\phi)) \cdot disp_{reco} \cdot \text{sign}(skew) \cdot -1 + (CoG_x, CoG_y)$$

$$\text{else}:$$

$$(x_{cam}, y_{cam}) = (\cos(\phi), \sin(\phi)) \cdot disp_{reco} \cdot \text{sign}(skew) + (CoG_x, CoG_y)$$

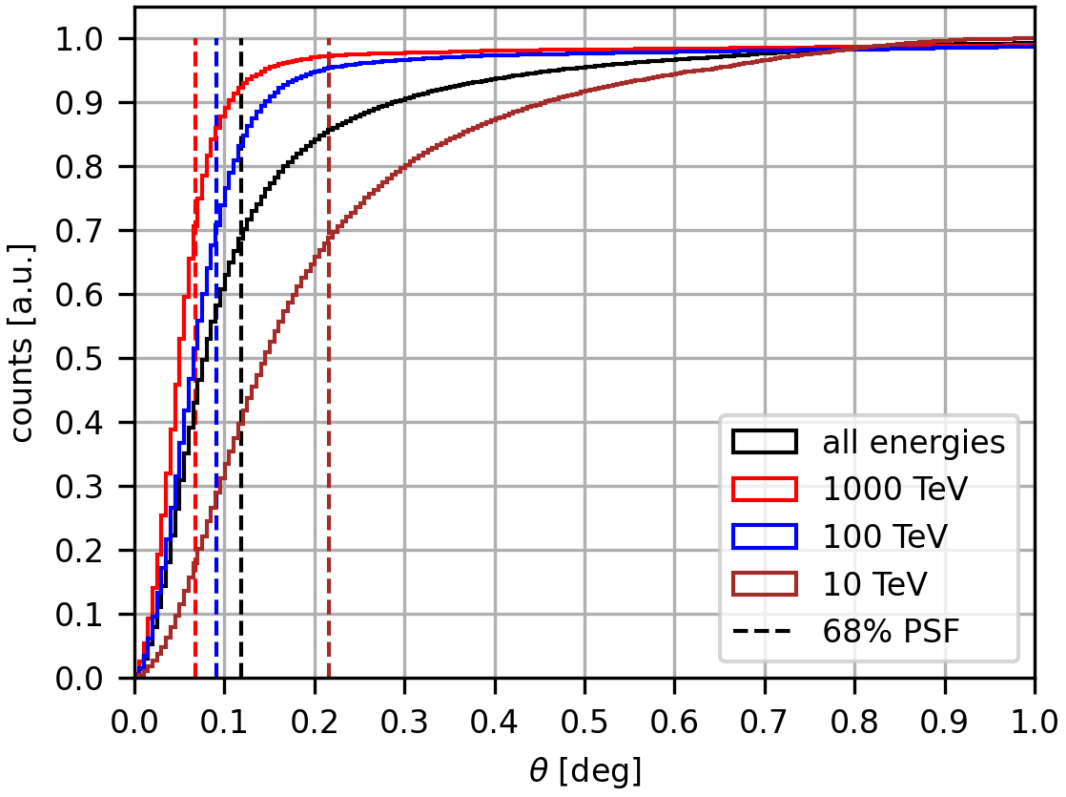

Figure 3.25: Cumulative distribution of the θ values for energies of 10 TeV, 100 TeV, 1000 TeV and the complete energy range, where the dashed lines indicate the 68%-percentile. Here, the reconstructed source position is calculated using Eqn. 3.9, where the sign of the *skew* parameter is multiplied with -1 for events with $CoG_x > 0$.

Note, that the CoG_x position in the camera depends on the impact x position of the air shower on the ground. The effect of impact $x > 0$ and $x < 0$ for on-axis observation is discussed in-depth in Sec. 3.3.3. The resulting angular resolution using the sign flip for events with $CoG_x > 0$ is presented in Fig. 3.25 and Tab. 3.10.

	10 TeV	100 TeV	1000 TeV	all energies
$\theta_{68\%}$	0.22°	0.09°	0.07°	0.12°

Table 3.10: Angular resolution in terms of the 68%-percentile value of θ, see Fig. 3.25.

Overall, an angular resolution of 0.12° is achieved, while the angular resolution for energies of 100 TeV and 1000 TeV is $< 0.1°$. The angular resolution significantly worsens for energies at 10 TeV with $\theta_{68\%} = 0.22°$.

3.4.2 1° offset observation

The trained Random Forest Regressor is applied to the off-axis dataset after γ-hadron separation, i.e., to the dataset indicated in Tab. 3.9.

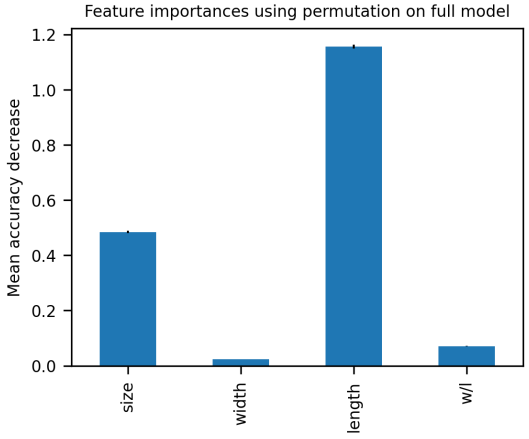

(a) Feature importances of the Random Forest Regressor for the *disp* parameter

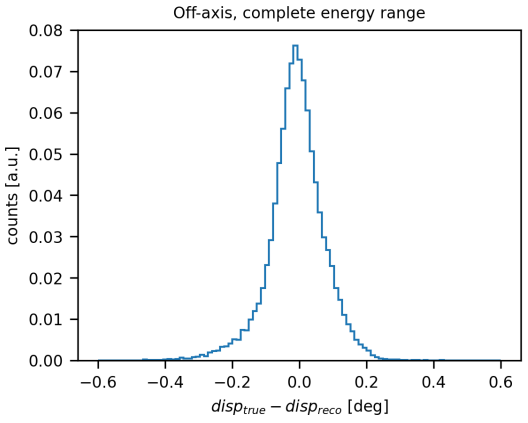

(b) Normalized histogram of the residuals $disp_{true} - disp_{reco}$.

Figure 3.26: Performance of the *disp* reconstruction in the off-axis case.

The importance of the training parameters as well as the performance of the Random Forest Regressor are provided in Fig. 3.26a and Fig. 3.26b, respectively. Notably, the *length* parameter is the most important parameter, similar to the results obtained for the on-axis observation (see Fig. 3.23a). Likewise, the histogram of the residuals $disp_{true} - disp_{reco}$ has a width comparable to that shown in Fig. 3.23b.

The energy dependent angular resolution of the detector is provided in Fig. 3.27 and Tab. 3.11.

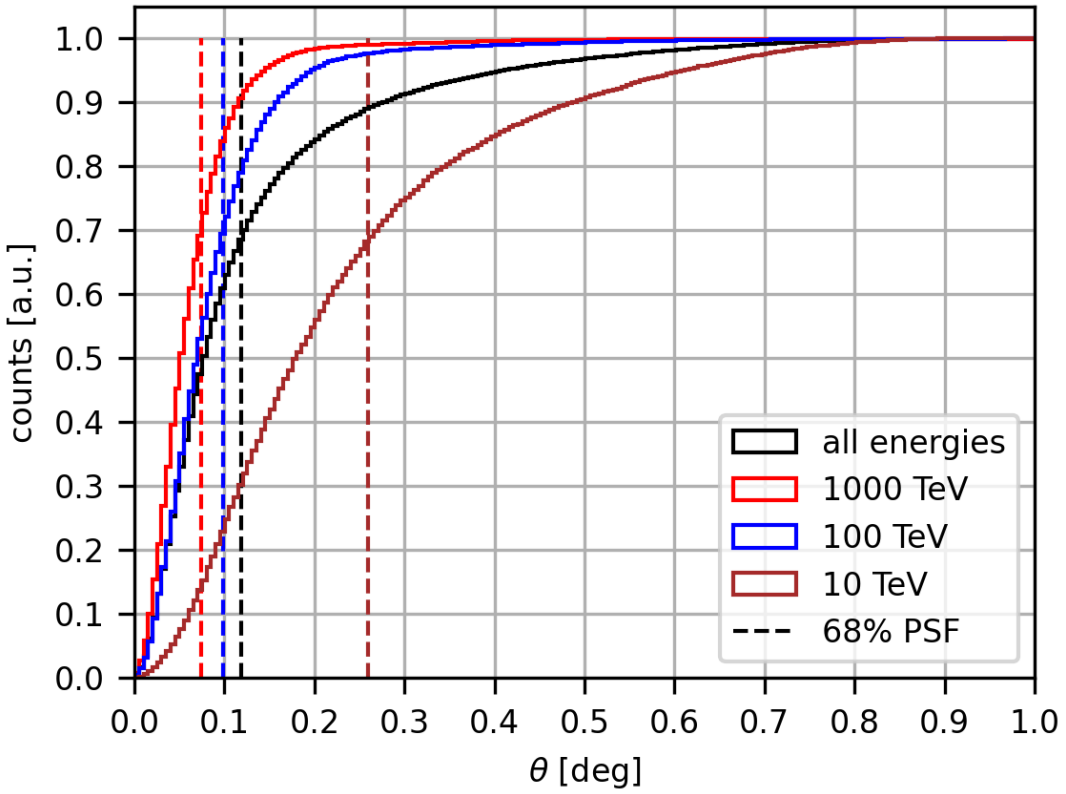

Figure 3.27: Cumulative distribution of the θ values for energies of 10 TeV, 100 TeV, 1000 TeV and the complete energy range, where the dashed lines indicate the 68%-percentile. The reconstructed source position is calculated with Eqn. 3.9.

	10 TeV	100 TeV	1000 TeV	all energies
$\theta_{68\%}$	0.26°	0.10°	0.07°	0.12°

Table 3.11: Angular resolution in terms of the 68%-percentile value of θ, see Fig. 3.27.

In general, the angular resolution for the off-axis observation seems to be consistent with the results derived in the on-axis observation, with an angular resolution of $\theta_{68\%} = 0.12°$ for the entire energy range.

It is important to emphasize, that for the off-axis observation the sign flip discussed in Sec. 3.4.1 is not applied, i.e., the source position in the camera is calculated with Eqn. 3.9, without any modifications. One has to conclude, that the reason for this is closely related to the fact that for off-axis observations, the telescope exclusively triggers for values of $x_{scat} > 0$ (see Fig. 3.19).

3.4.3 Discussion

The results presented in Sec. 3.4 for the angular resolution of H.E.S.S. CT5 at a zenith angle of 80° are compared to the angular resolution of the LHAASO experiment, particularly to LHAASO KM2A (see Fig. 3.28). For an in-depth description of the LHAASO experiment, the reader is directed to [108]. Scientific highlights of the LHAASO experiment include so far the detection of PeV emission from the Crab Nebula [59] and the observation of TeV emission from GRB 221009A in the afterglow phase [126].

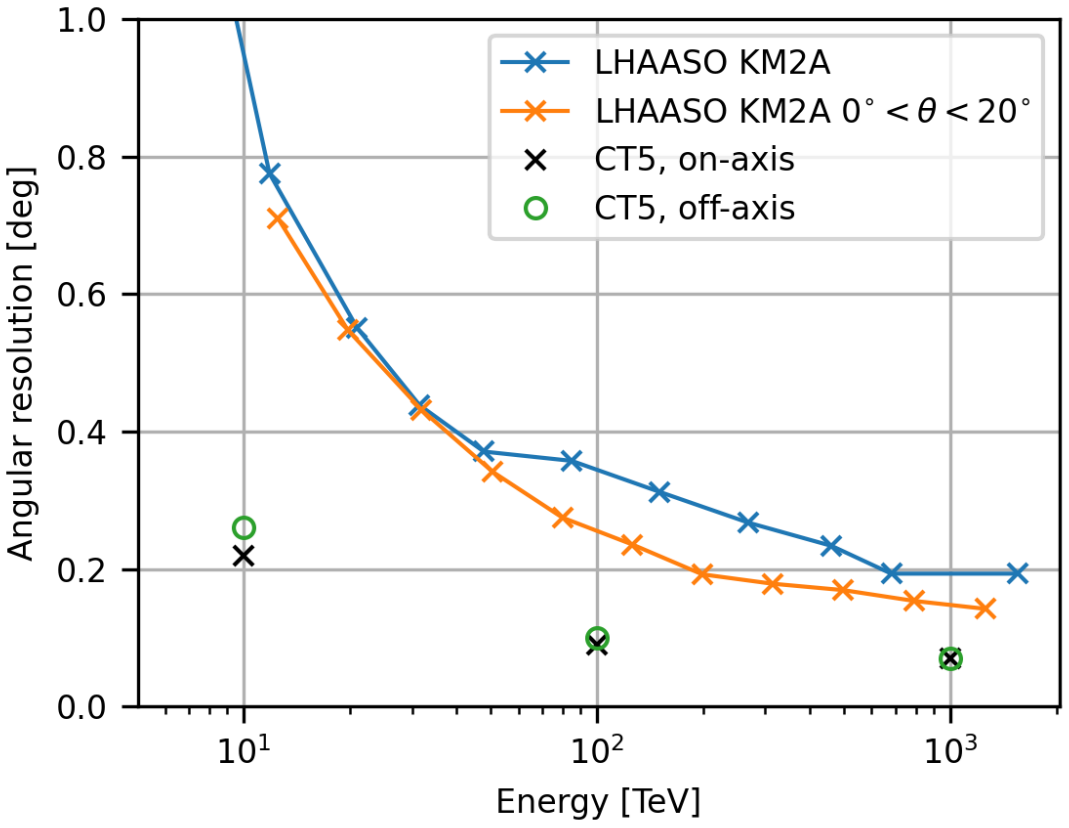

Figure 3.28: Comparison of the angular resolution between LHAASO KM2A and the results derived for H.E.S.S. CT5 at a zenith angle of 80°. The blue crosses are taken from [108] (zenith angle averaged) and the orange crosses from [127] for a zenith angle range of $0° < \theta < 20°$. The green circles and black crosses indicate the results obtained for off-axis and on-axis observation, respectively.

Evidently, based on the results derived in Sec. 3.4, H.E.S.S. CT5 at a zenith angle of 80° is able to compete with LHAASO KM2A with respect to the angular resolution at energies $\geq 10\,\mathrm{TeV}$. Especially at 10 TeV, the angular resolution of LHAASO KM2A is significantly worse compared to H.E.S.S. CT5, independent of the observation type (i.e., on-axis/off-axis). Note, that in Fig. 3.28 the angular resolution of a single stand-alone telescope is compared to a kilometer squared detector array.

3.5 Energy reconstruction

The energy E_{true} of the γ-ray events is reconstructed, termed E_{reco}, using the Random Forest Regressor with the same configuration as explained in Sec. 3.3. Here, the Random Forest Regressor is trained with a γ-ray dataset simulated at a zenith angle of 80° and continuous in energy, rather than with discrete energies, in order to avoid introducing bias effects during the training.

The energy coverage of the respective datasets, at trigger level and after a 1° distance cut (CoG-Center), are presented in Sec. 3.5.1 and Sec. 3.5.2 for on-axis and off-axis observation, respectively. For both observation types, the Random Forest Regressor is trained with the respective datasets including a 1° distance cut (CoG-Center).

The parameters *size*, *width*, *length*, *dist*, *npix*, *skew*, CoG_x, CoG_y and *width*/*length*(w/l) are used as training parameters.

3.5.1 On-axis observation

The trained Random Forest Regressor is applied to the γ-ray test dataset indicated in Tab. 3.4 including a 1° distance cut (CoG-Center).

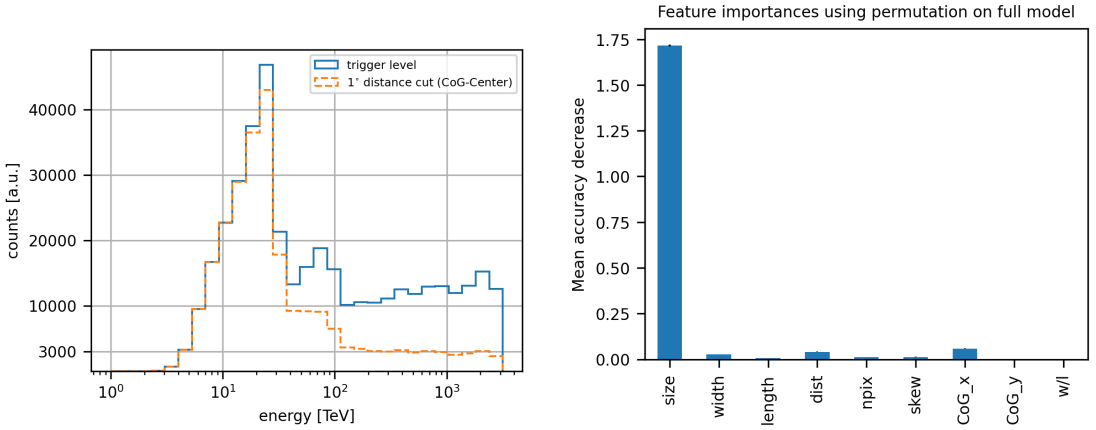

(a) Energy coverage of the simulated γ-ray dataset used for the Random Forest Regressor.

(b) Feature importances of the Random Forest Regressor for the reconstructed energy E_{reco}.

Figure 3.29: (a) energy coverage of the training dataset and (b) feature importances for the energy reconstruction in the on-axis case.

The energy coverage of the training sample set is presented in Fig. 3.29a. A significantly increased fraction of surviving γ-ray events after a distance cut of 1° can be observed for energies $\leq 30\,\text{TeV}$. In Sec. 3.3.1, the sweet-spot in terms of statistics after an angular distance cut of 1° for on-axis observation was estimated to be roughly $\mathcal{O}(10\,\text{TeV})$. Apparently, this sweet-spot extends up to maximum γ-ray energies of $E_\gamma \sim 30\,\text{TeV}$.

As expected, the *size* parameter is by far the most important parameter for the energy reconstruction (see Fig. 3.29b). Note, that the CoG_x parameter seems to be the second most important parameter, which is quite surprising. The feature importance of the CoG_x parameter was further investigated by looking at the two-dimensional distribution of the *size* parameter plotted against the CoG_x parameter for the γ-ray test dataset. The resulting distribution is illustrated in Fig. 3.30.

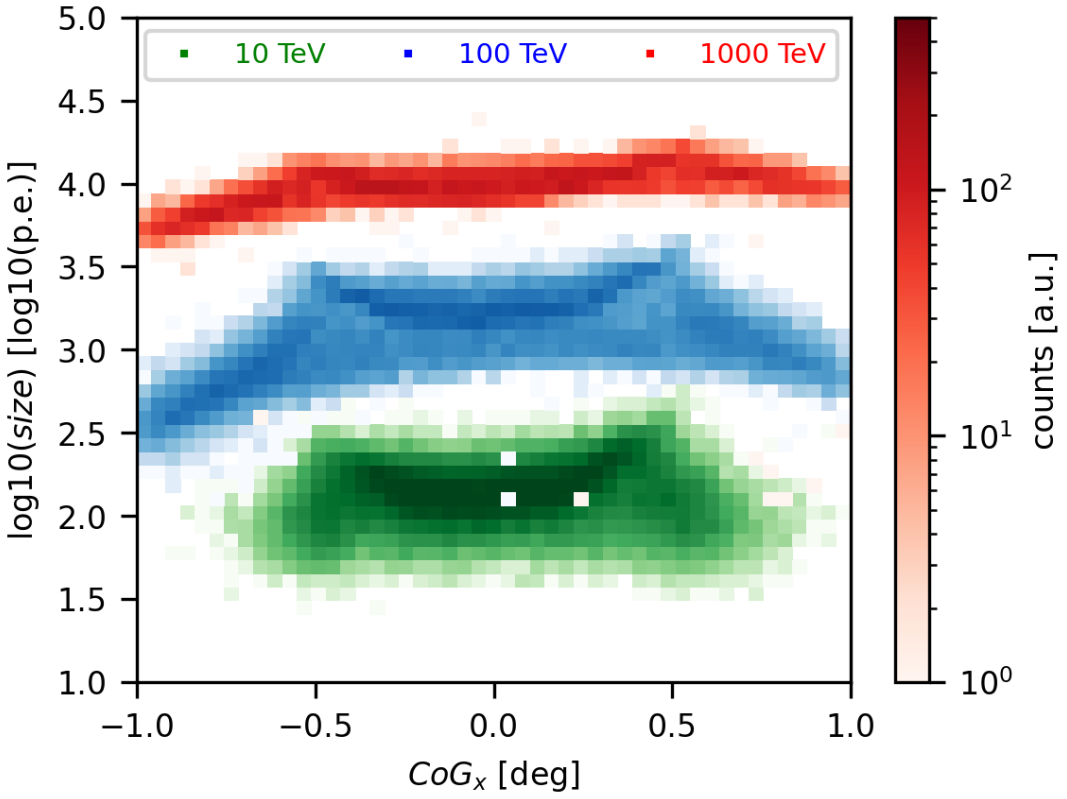

Figure 3.30: Two-dimensional histogram of the *size* parameter plotted against CoG_x for the γ-ray test dataset indicated in Tab. 3.4 including a 1° distance cut (CoG-Center). The gradient-counts assignement (see colorbar on the right) is valid for all energies.

Two general characteristics can be observed: 1) With increasing primary γ-ray energy, the distribution gets elongated along the CoG_x-axis. This is expected, since γ-ray events with lower energy will not be able to trigger the telescope, if the impact position of the shower is too far away from the telescope position. Consequently, this will result in a smaller range of CoG_x values for triggered γ-ray events. 2) With increasing primary γ-ray energy, the distributions get narrower along the *size*-axis. This is also expected, since the shower fluctuations are typically smaller at higher primary particle energies than at lower primary particle energies[8]. The distributions are shifted towards higher

[8]Note, that this could also be caused by a high n_{scat} value, since the shower development is identical for re-used showers. However, the 100 TeV and 1000 TeV dataset are simulated with the same $n_{scat} = 100$ value (see Tab. 3.1) and, clearly the 100 TeV distribution appears to be wider along the *size*-axis.

size values with increasing energy, since the number of produced Cherenkov photons increases with increasing primary energy.

A modest dependence of the *size* parameter, across all energies, can be observed for events with $CoG_x < -0.5°$ and $CoG_x > 0.5°$, justifying the modest feature importance of the CoG_x parameter.

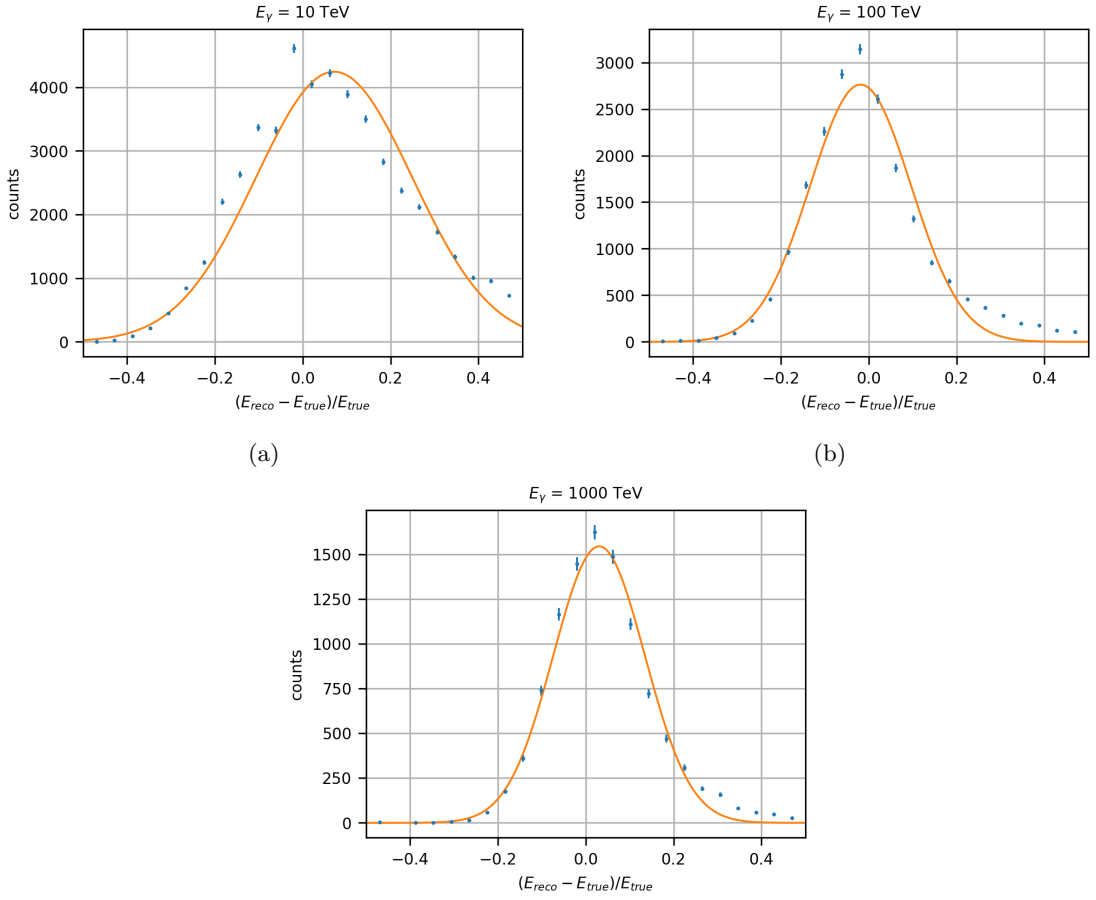

Figure 3.31: Residuals of $\frac{E_{reco}-E_{true}}{E_{true}}$ (blue points) together with a Gaussian fit to the residuals (orange line) for energies of a) 10 TeV b) 100 TeV and c) 1000 TeV. The 1 σ error bars are calculated by assuming Poissonian statistics.

	10 TeV	100 TeV	1000 TeV
σ_E	~ 0.18	~ 0.12	~ 0.10

Table 3.12: Estimated energy resolution based on the Gaussian fits in Fig. 3.31.

The energy resolution is estimated by fitting a Gaussian to the residuals $\frac{E_{reco}-E_{true}}{E_{true}}$ (see Fig. 3.31). The estimated values are provided in Tab. 3.12.

3.5.2 1° offset observation

The trained Random Forest Regressor is applied to the γ-ray test dataset indicated in Tab. 3.7 including a 1° distance cut (CoG-Center).

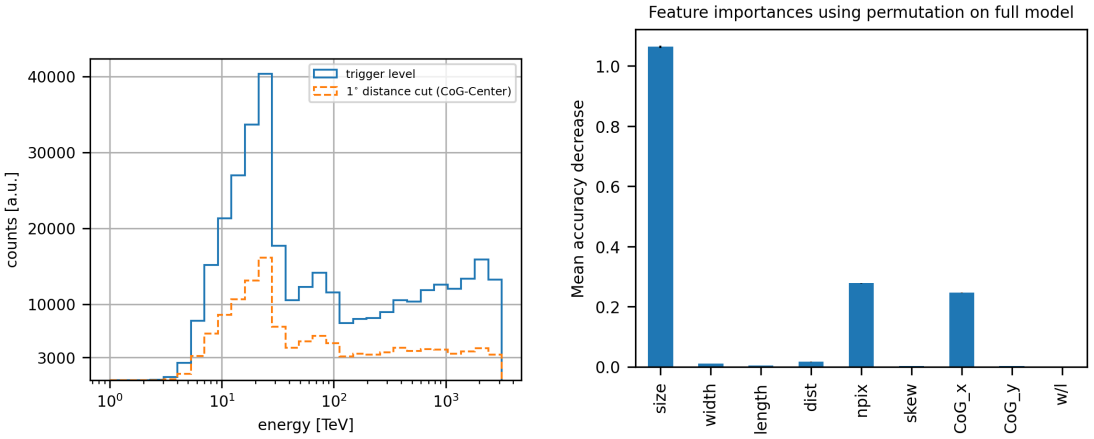

(a) Energy coverage of the simulated γ-ray dataset used for the Random Forest Regressor.

(b) Feature importances of the Random Forest Regressor for the reconstructed energy E_{reco}.

Figure 3.32: (a) energy coverage of the training dataset and (b) feature importances for the energy reconstruction in the off-axis case.

As already discussed in Sec. 3.2.1, higher statistics at the highest energies can be achieved with off-axis observation after a distance cut of 1° compared to on-axis observation (compare Fig. 3.32a with Fig. 3.29a), albeit at the cost of significant lower statistics for energies of the order of $\mathcal{O}(10\,\text{TeV})$.

The importance of the provided parameters for the Random Forest Regressor is illustrated in Fig. 3.32b. Similar to the on-axis case, the *size* parameter stands out as the most important parameter. However, upon comparing Fig. 3.29b with Fig. 3.32b, it is evident that the *npix* and CoG_x parameters appear to be more important in the off-axis case.

Equivalent to the on-axis investigation regarding the feature importance of the CoG_x parameter, a two-dimensional histogram of the *size* parameter plotted against CoG_x for the γ-ray test dataset is presented in Fig. 3.33. Notably, the shape of the distributions is considerably different from those in Fig. 3.30. A clear correlation between the *size* parameter and CoG_x can be observed for energies of 100 TeV and 1000 TeV, i.e., an increasing *size* value with increasing CoG_x position up to $CoG_x \sim 0.7°$, where the distribution starts to decrease towards lower *size* values. Most likely, this dependence between *size* and CoG_x causes the increased feature importance of the CoG_x parameter in the off-axis case.

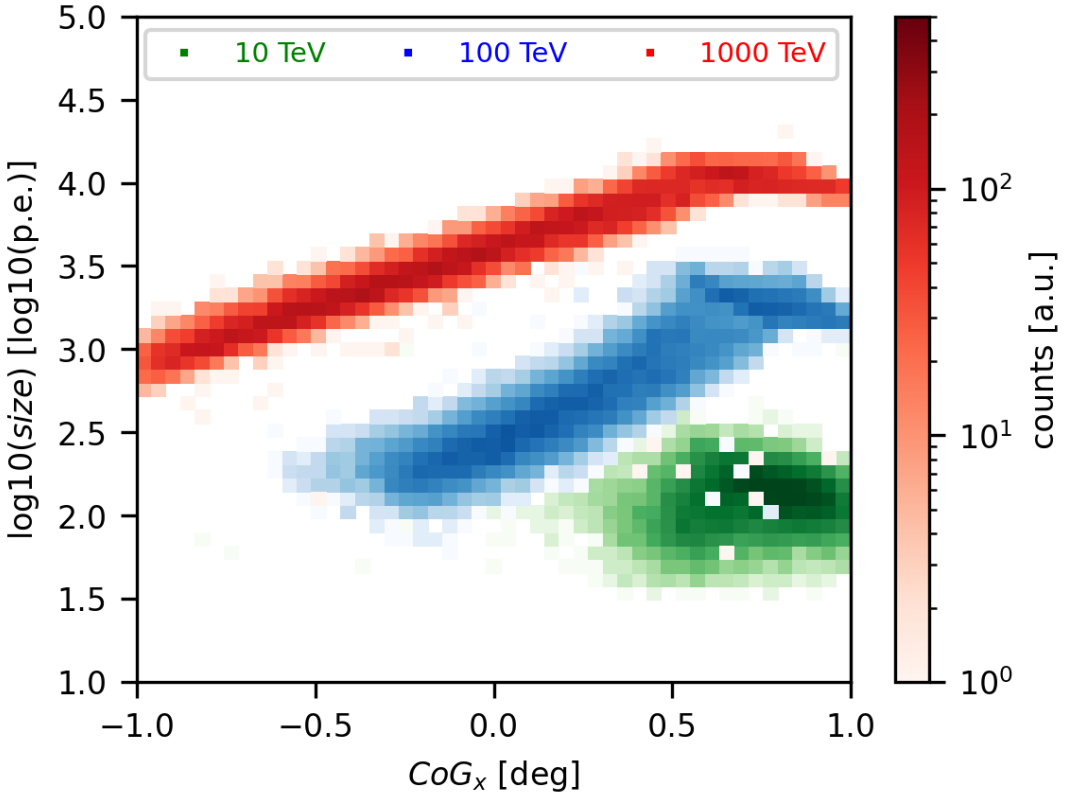

Figure 3.33: Two-dimensional histogram of the *size* parameter plotted against CoG_x for the γ-ray test dataset indicated in Tab. 3.7 including a 1° distance cut (CoG-Center). The gradient-counts assignement (see colorbar on the right) is valid for all energies.

	10 TeV	100 TeV	1000 TeV
σ_E	~ 0.17	~ 0.14	~ 0.12

Table 3.13: Estimated energy resolution based on the Gaussian fits in Fig. 3.34.

The energy resolution is estimated by fitting a Gaussian to the residuals $\frac{E_{reco}-E_{true}}{E_{true}}$ (see Fig. 3.34). The estimated values are provided in Tab. 3.13.

3.6 Effective area

The energy dependent effective area $A_{eff}(E_\gamma)$ is calculated as:

$$A_{eff}(E_\gamma) = \frac{N^{\text{after}}}{N^{\text{sim}}} \times A_{sim}(E_\gamma), \tag{3.10}$$

where $N^{\text{sim}} \equiv N^{\text{sim}}(E_\gamma)$ is the energy dependent total number of simulated γ-ray events and $A_{sim}(E_\gamma) = 2 \times x_{scat}(E_\gamma) \cdot 2 \times y_{scat}(E_\gamma)$ the energy dependent simulated area (see

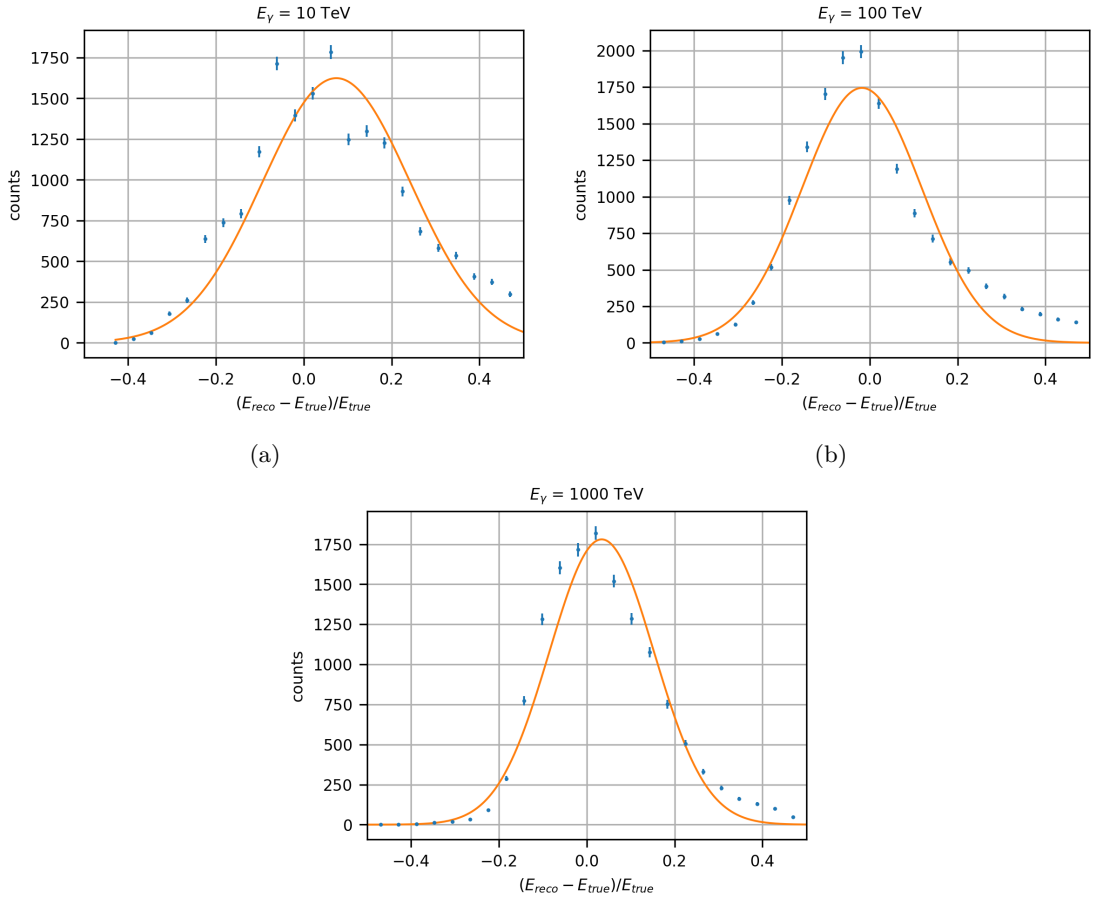

Figure 3.34: Residuals of $\frac{E_{reco}-E_{true}}{E_{true}}$ (blue points) together with a Gaussian fit to the residuals (orange line) for energies of a) 10 TeV b) 100 TeV and c) 1000 TeV. The $1\,\sigma$ error bars are calculated by assuming Poissonian statistics.

Tab. 3.1). The number of events at trigger level or after applying a succession of cuts, i.e., distance (CoG-Center), *gammaness* and direction cuts, is denoted by N^{after}.

The effective area of H.E.S.S. CT5 at trigger level and after various cuts, based on the results presented in Sec. 3.3 and Sec. 3.4, is provided in Fig. 3.35 and Fig. 3.36 for on-axis and off-axis observation, respectively. In both figures, the effective area after a $\theta < 0.18°$ cut is calculated by applying the θ cut on the respective datasets after γ-hadron separation (see Tab. 3.6 and Tab. 3.9).

For on-axis observation and after a distance cut of 1°, the peak effective area reaches approximately $A_{eff} \sim 6\,\text{km}^2$ at 100 TeV. Beyond 100 TeV, the effective area appears to decrease, reaching around $A_{eff} \sim 5\,\text{km}^2$ at 1000 TeV (see Fig. 3.35). In the case of off-axis observation and with a distance cut of 1°, the peak in the effective area is likely located at energies $\geq$ 1000 TeV. This assumption is based on the absence of a decline

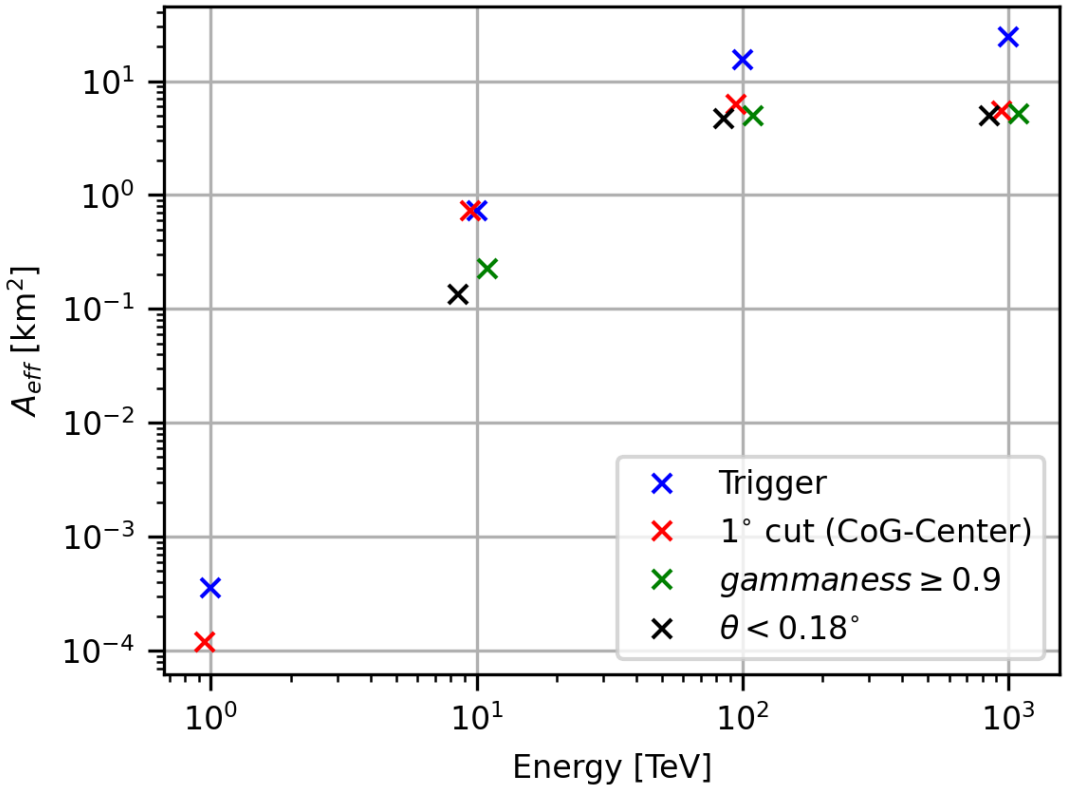

Figure 3.35: Effective area A_{eff} for H.E.S.S. CT5 ponting at a zenith angle of 80° at trigger level (blue), after a 1° distance cut (CoG-Center) (red), after γ-hadron separation with a *gammaness* > 0.9 cut (green) and after a *theta* $< 0.18°$ cut (black). The effective areas are calculated for discrete energies of 1 TeV, 10 TeV, 100 TeV and 1000 TeV. Here, the crosses are slightly shifted around the respective energies for visibility.

	10 TeV	100 TeV	1000 TeV
		[km^2]	
On-axis 80°	0.14	4.65	5.01
Off-axis 81°	0.06	1.92	5.88

Table 3.14: Effective area A_{eff} of H.E.S.S. CT5 after a $\theta < 0.18°$ cut for on-axis observation (see Fig. 3.35) and off-axis observation (see Fig. 3.36).

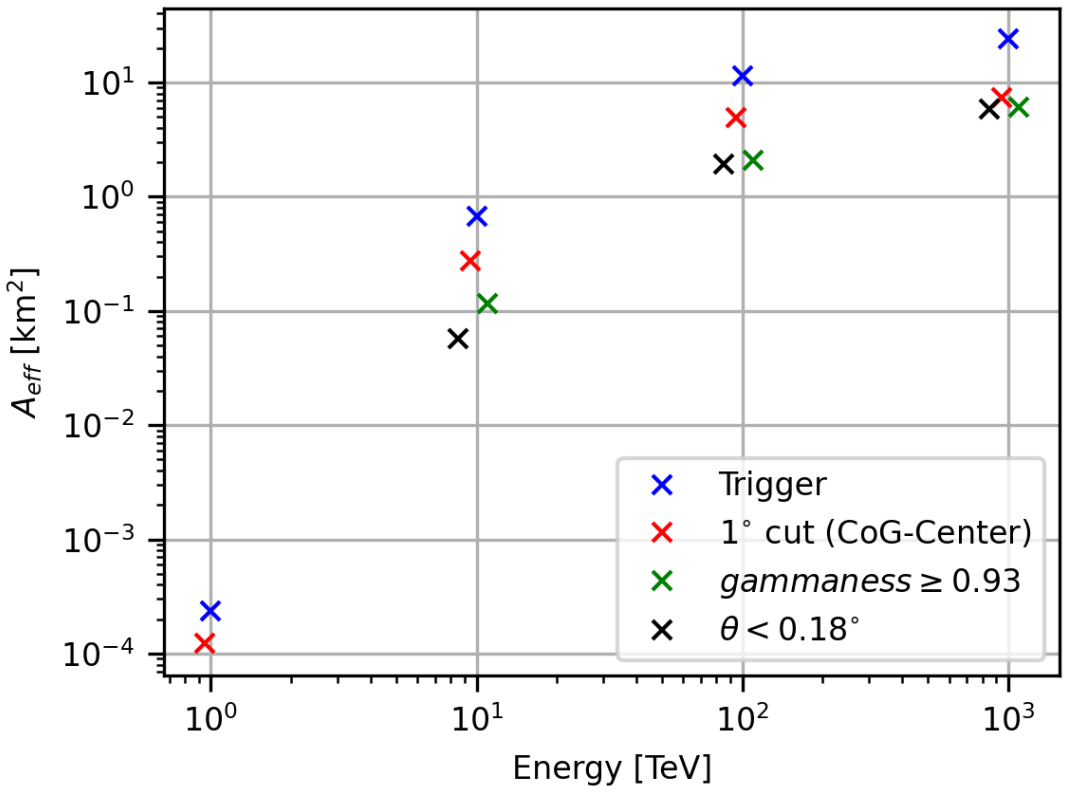

Figure 3.36: Effective area A_{eff} for H.E.S.S. CT5 pointing at a zenith angle of 81° at trigger level (blue), after a 1° distance cut (CoG-Center) (red), after γ-hadron separation with a *gammaness* > 0.93 cut (green) and after a *theta* $< 0.18°$ cut (black). The effective areas are calculated for discrete energies of 1 TeV, 10 TeV, 100 TeV and 1000 TeV. Here, the crosses are slightly shifted around the respective energies for visibility.

in A_{eff} with increasing energy, as shown in Fig. 3.36 (at 100 TeV: $A_{eff} \sim 5\,\mathrm{km}^2$ and at 1000 TeV: $A_{eff} \sim 7\,\mathrm{km}^2$).

After γ-hadron separation, the effective area at 1000 TeV for off-axis observation is approximately 1 km^2 larger than for on-axis observation ($\sim 5\,\mathrm{km}^2$ vs. $\sim 6\,\mathrm{km}^2$). However, for on-axis observation, the effective area after γ-hadron separation at 100 TeV is roughly $A_{eff} \sim 5\,\mathrm{km}^2$, while the corresponding effective area for off-axis observation is less than half of this value ($A_{eff} \sim 2\,\mathrm{km}^2$). The same aforementioned trend can be observed for the effective area at 10 TeV after γ-hadron separation, when comparing on-axis and off-axis results. Note, that the derived effective areas after γ-hadron separation for both observation types can compete with those of the CTA southern and northern arrays (see Fig. 2.14) at energies $\mathcal{O}(100\,\mathrm{TeV})$ and beyond.

The effective areas for on-axis and off-axis observations after a $\theta < 0.18°$ cut are provided in Tab. 3.14 and are compared in Fig. 3.37 with those of the CTA southern array (after

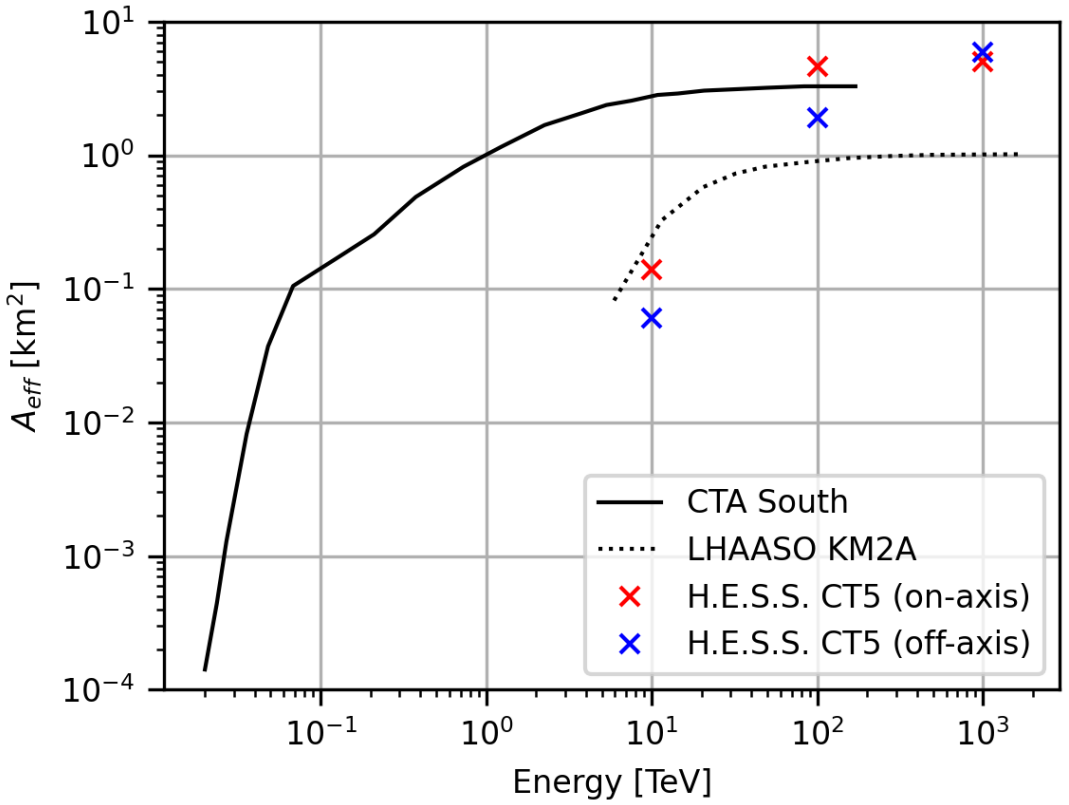

Figure 3.37: Effective areas of H.E.S.S. CT5 after a $\theta < 0.18°$ cut for on-axis (red crosses) and off-axis (blue crosses) observations. The solid black line indicates the energy dependent effective area of the CTA southern "alpha configuration" array after γ-hadron separation and direction cuts (see `https://www.cta-observatory.org/science/ctao-performance/`). The dotted black line marks the achieved collections areas of LHAASO KM2A [108].

γ-hadron separation and direction cuts, see `https://www.cta-observatory.org/science/ctao-performance/`) and LHAASO KM2A [108].

The comparison impressively illustrates the performance of a stand-alone telescope at a zenith angle of 80° in terms of the collection area A_{eff}. Based on the results presented in Fig. 3.37, H.E.S.S. CT5 would be able to achieve comparable effective areas at energies $\geq$ 100 TeV to those of the CTA southern "alpha configuration" array, while the performance of the CTA southern array remains superior at lower energies. The decline in A_{eff} by more than one magnitude of order for H.E.S.S. CT5, when going from energies of $\mathcal{O}$(100 TeV) to $\mathcal{O}$(10 TeV), reflects the biggest drawback of observations at large zenith angles, namely an increased distance from the shower maximum to the telescope position, causing a decrease in photon density at the observation level (see Sec. 2.6).

Nevertheless, when comparing the achieved effective areas of H.E.S.S. CT5 at energies of $\geq$ 10 TeV (on-axis) to those of LHAASO KM2A, one may conclude that a single stand-alone telescope, performing large zenith angle observations, reaches competitive

collection areas and even exceeds the performance of a kilometer squared array at energies $\geq 100\,\mathrm{TeV}$.

3.7 Sensitivity study

While the results presented in the previous sections demonstrate promising performance for H.E.S.S. CT5 when observing at large zenith angles, it is important to note that these results were exclusively obtained for a zenith angle of 80°. This represents an obvious limitation when considering the potential observation time of a source.

In order to quantify this limitation in observation time, the visibility of the detected sources with LHAASO KM2A [128] is calculated for the H.E.S.S. site (see Sec. 2.5.2) in the zenith angle range of $79° < \theta < 81°$. For each of the 75 LHAASO KM2A sources, the visibility is calculated for the entire 2024 observation season using the H.E.S.S. visibility tool (`https://www.mpi-hd.mpg.de/hfm/~bernlohr/HESS/Visibility.html` - restricted access) written by K. Bernlöhr[9]. Out of these 75 sources, 43 sources have been detected with a significance of $4\,\sigma$ above energies of 100 TeV [128].

Additionally, the expected event rate ER (in units of events/hour) for H.E.S.S. CT5 is calculated with:

$$ER = \int_{E_{\mathrm{min}}}^{1\,\mathrm{PeV}} \frac{\mathrm{d}N}{\mathrm{d}E} \cdot A_{eff}\,\mathrm{d}E, \tag{3.11}$$

where $\mathrm{d}N/\mathrm{d}E$ is the differential flux of the respective LHAASO source and A_{eff} is the derived effective area after γ-hadron separation and directions cuts for H.E.S.S. CT5 performing on-axis observations (see Fig. 3.35). The differential flux $\mathrm{d}N/\mathrm{d}E$ is modeled in [128] as a power-law, i.e.,

$$\frac{\mathrm{d}N}{\mathrm{d}E} = N_0 \left(\frac{E}{E_0}\right)^{-\Gamma}, \tag{3.12}$$

where N_0 is the normalization in units of $10^{-16}\,\mathrm{cm^{-2}\,s^{-1}\,TeV^{-1}}$, $E_0 = 50\,\mathrm{TeV}$ is the reference energy and Γ is the photon spectral index.

For all 75 LHAASO KM2A sources, the expected event rates with $E_{\mathrm{min}} = 10\,\mathrm{TeV}$ and $E_{\mathrm{min}} = 100\,\mathrm{TeV}$ (see Eqn. 3.11) for H.E.S.S. CT5, as well as the visibility at the H.E.S.S.

[9] `https://www.mpi-hd.mpg.de/hfm/~bernlohr/index.html.en`

site for the 2024 season, are provided in Tab. B.1. For convenience, the source location and the spectral parameters are also included.

Note, that the assumption here is that the derived effective area at a zenith angle of 80° is a sufficient average for the zenith angle range $79° < \theta < 81°$.

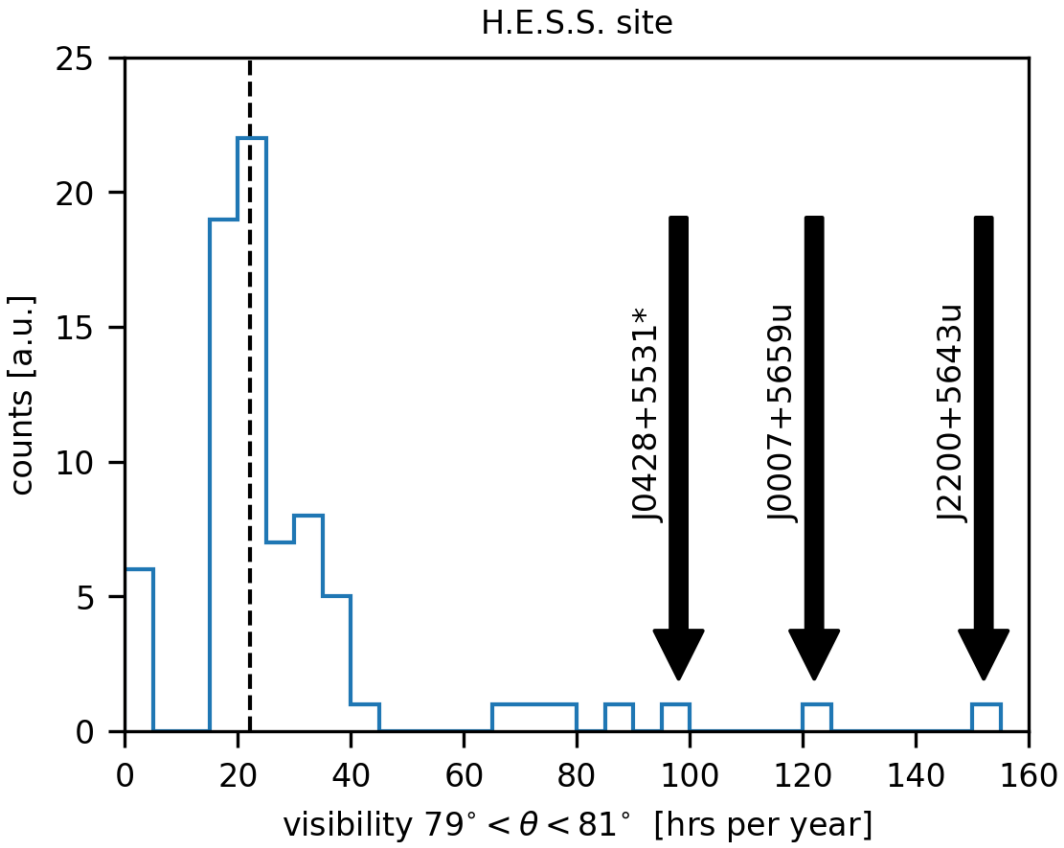

Figure 3.38: Visibility for the LHAASO KM2A sources [128] at the H.E.S.S. site for a zenith angle range of $79° < \theta < 81°$. The visibility of each source is calculated for the entire 2024 observation season. The three arrows mark the sources with visibility $\gtrsim 100$ hours per year. The dashed line indicates the visibility of the Crab Nebula.

A histogram illustrating the visibility of the LHAASO KM2A sources is provided in Fig. 3.38. Clearly, the majority of the sources can only be observed for a maximum observation time of roughly 20 hrs to 30 hrs per year. In particular, the Crab Nebula has a visibility of approximately ~ 22 hrs per year. However, for three of the LHAASO KM2A sources a maximum observation time of $\gtrsim 100$ hrs per year can be achieved.

The distribution of the expected number of photons per year, i.e., $ER\times$visbility, at energies above 10 TeV and above 100 TeV is provided in Fig. 3.39a and Fig. 3.39b, respectively. Notably, for two LHAASO KM2A sources a maximum of $ER\times$visibility $\gtrsim 400$ photons per year at energies above 10 TeV can be achieved, while for four LHAASO KM2A sources a maximum of $ER\times$visibility $\gtrsim 10$ photons per year at energies above

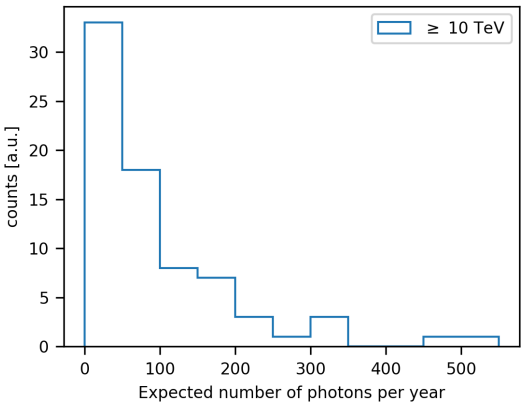

(a) Histogram for the expected number of photons per year, i.e., $ER\times$visibility, for the LHAASO KM2A sources at energies above 10 TeV.

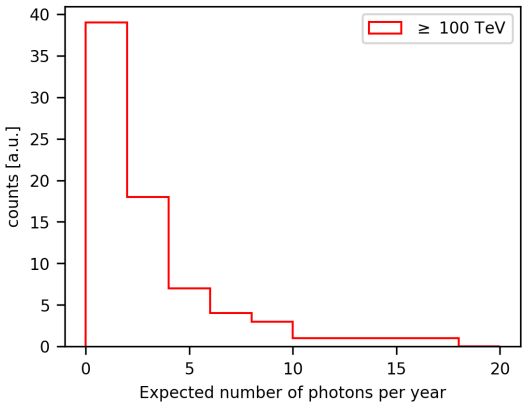

(b) Histogram for the expected number of photons per year, i.e., $ER\times$visibility, for the LHAASO KM2A sources at energies above 100 TeV.

Figure 3.39: Expected number of photons per year for the LHAASO KM2A sources.

100 TeV can be expected. The only source full filling $ER\times$visibility $\gtrsim 400$ at ≥ 10 TeV and $ER\times$visibility $\gtrsim 10$ at ≥ 100 TeV is J2200+5643 (see Fig. 3.40). Note, that from the three sources highlighted in Fig. 3.38 only J2200+5643 is represented in Fig. 3.40. For J0428+5531 the expected number of photons per year at energies above 10 TeV is $\sim$ 100 photons per year and at energies above 100 TeV $\sim$ 3 photons per year and, similarly for J0007+5659 $\sim$ 60 photons per year at $\geq$ 10 TeV and $\sim$ 3 photons per year at $\geq$ 100 TeV (see Tab. B.1). Both sources have a relatively low differential flux at 50 TeV of $\mathrm{d}N/\mathrm{d}E \leq 5 \times 10^{-17}\,\mathrm{cm}^{-2}\,\mathrm{s}^{-1}\,\mathrm{TeV}^{-1}$ paired with a photon spectral index of $\Gamma \geq 3.1$. The increase in effective area A_{eff} at energies ≥ 10 TeV is not sufficient to compensate the quickly dropping flux, and as a result, roughly $\sim$ 100 photons per year can be expected from these sources at energies ≥ 10 TeV.

In order to qualitatively evaluate the expected number of photons per year, the maximum significance (see Eqn. 3.8)[10] that can be reached during the entire 2024 observation season is calculated exemplary for J0428+5531, Crab Nebula (J0534+2200) and J1814-1636 in Fig. 3.41. For each of the sources the expected number of photons per year at energies ≥ 10 TeV is taken as the expectation value of a Poisson distribution. The expectation value for the number of background events at energies ≥ 10 TeV is estimated with the procedure discussed in Sec. 3.1.1 (here, the statistics of the background events after γ-hadron separation and direction cuts for on-axis observation are used). The integrated background rate BR at energies above 10 TeV (see Eqn. 3.4) yields in total (proton+helium) ≈ 0.05 counts per second after γ-hadron separation and direction cuts. For each expectation value, 10000 Poisson distributed values are simulated and presented in the form of a histogram for the resulting significance in Fig. 3.41.

[10] Here, a single on and off region is assumed, such that $\alpha = t_{on}/t_{off} = 1$.

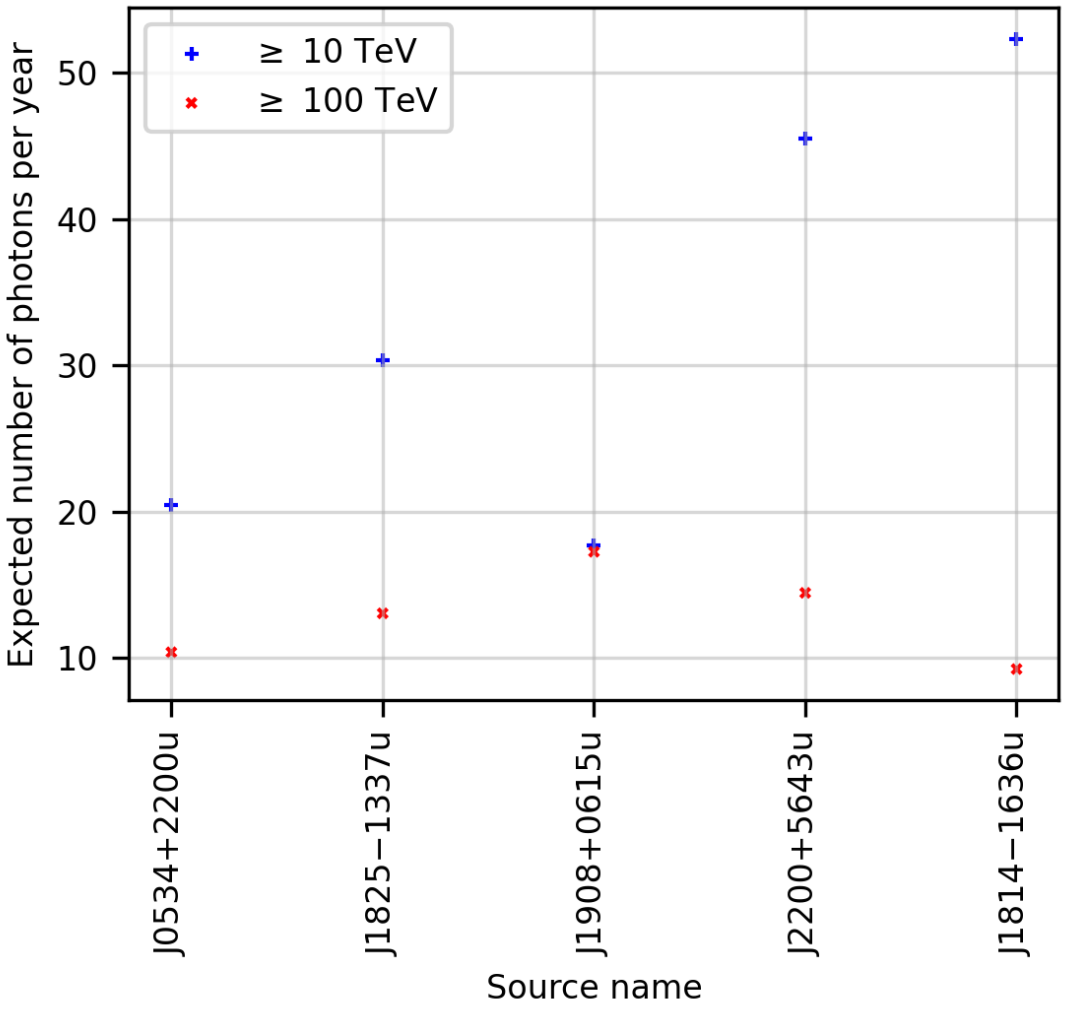

Figure 3.40: LHAASO KM2A sources with expected number of photons per year greater than 400, i.e, $ER\times$visibility $\gtrsim 400$, at energies above 10 TeV and/or $ER\times$visibility $\gtrsim 10$ at energies above 100 TeV. Here, the values for the ≥ 10 TeV case are scaled down by a factor of 10. The only source full filling both properties at energies above 10 TeV and 100 TeV is J2200+5643.

The distribution of the mean value of the significance for all LHAASO KM2A sources is provided in Fig. 3.42.

Notably, for five sources a maximum significance of $\geq 3\,\sigma$ can be achieved using the entire respective observation window of the 2024 season (see Fig. 3.38), while only J1814-1636 would exceed the canonical $5\,\sigma$ threshold. When considering that, e.g., bad weather conditions might reduce the possible observation time within one year, the results in Fig. 3.42 might appear underwhelming. However, the reader should consider that these results were obtained for a single stand-alone telescope, and the zenith angle range of $79° < \theta < 81°$ represents a rather narrow window. Most likely, a dedicated study for the performance of the *entire* H.E.S.S. array in the zenith angle range of 70° to 80° would improve the results presented in Fig. 3.42. Especially, a divergent pointing of

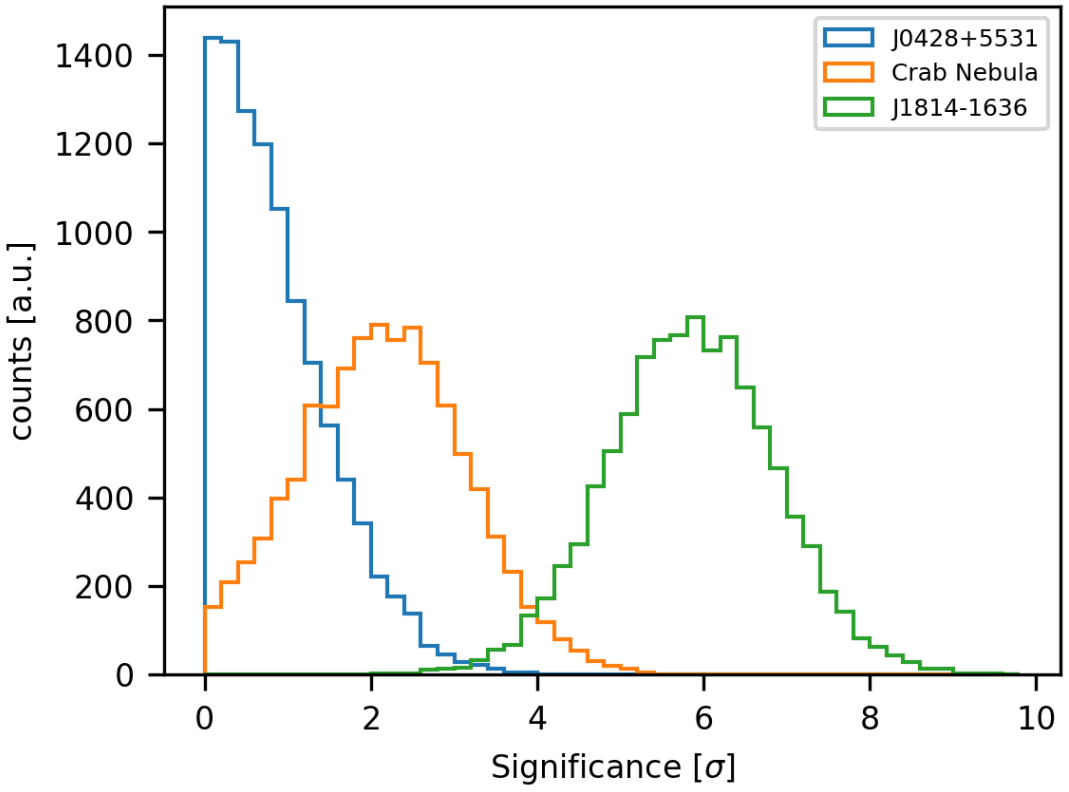

Figure 3.41: Distribution of the significance calculated with Eqn. 3.8 for 10000 realizations for J0428+5531, Crab Nebula (J0534+2200) and J1814-1636.

H.E.S.S. CT1-CT5 could significantly increase the total collection area A_{eff} at energies $\geq 100\,\mathrm{TeV}$ (see Appendix C).

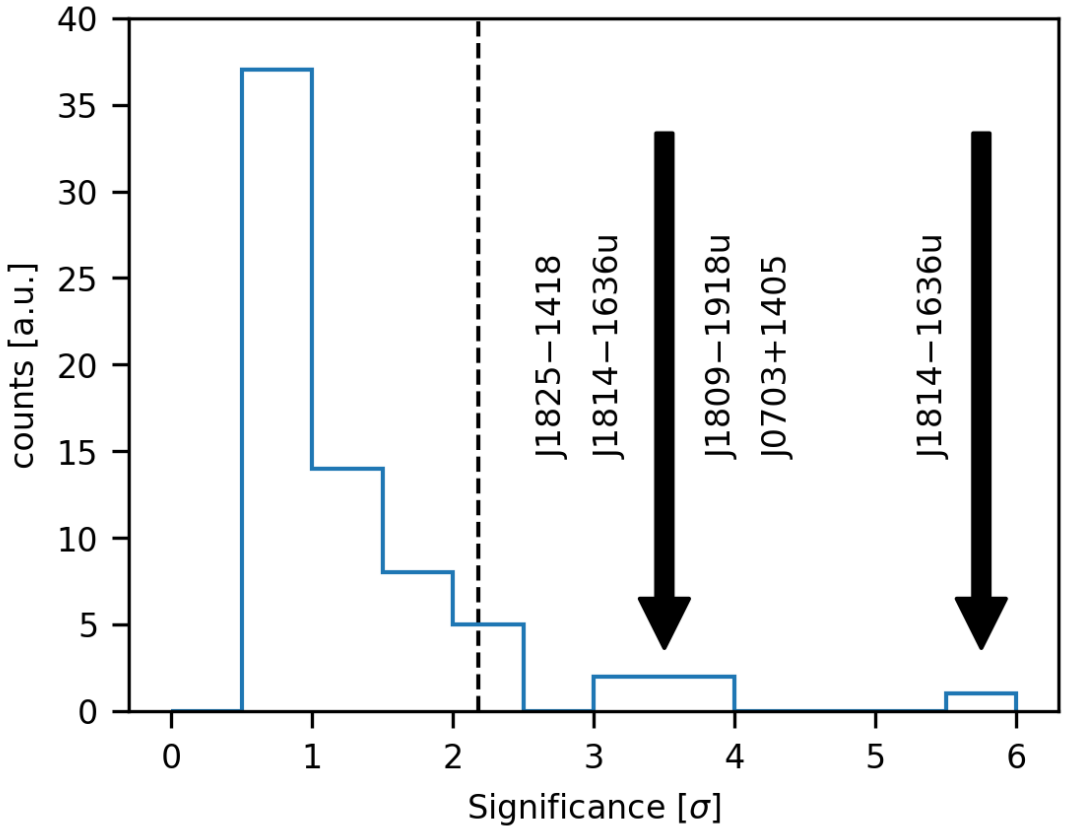

Figure 3.42: Distribution of the mean significance for all LHAASO KM2A sources. The dashed line indicates the mean significance of the Crab Nebula.

Chapter 4

EASpy

This Chapter is based on [129], where the author of this thesis developed the complete simulation tool and contributed all the figures and a first draft of the paper.

Until now, the IACT arrays in operation and those planned have been fine-tuned for observations at small zenith angles. To optimize their configuration at larger zenith angles, a significant effort is required to simulate a considerable number of air showers at high energies (see Chapter. 3). This involves their detection using various telescope layouts, camera sizes, mirror diameters, etc.. In the realm of performance studies, Monte Carlo simulations, such as `CORSIKA` [114], play a crucial role in optimizing IACTs and reconstruction methods. Since large zenith angle observations with IACTs provides an opportunity to collect the Cherenkov light from γ-ray air showers with primary energies above 100 TeV (see Sec.2.3), fluorescence emission (see Sec. 2.4) might have an impact on the recorded image at these primary energies. Although `CORSIKA` cannot simulate fluorescence light, community efforts have been made to implement fluorescence emission into `CORSIKA` [130, 131]. One notable drawback of these Monte Carlo simulations is the increased computation time associated with higher primary particle energies, along with an increase in storage size. Both former mentioned drawbacks are the reason why the Monte Carlo datasets presented in Sec. 3.1 were conducted at discrete energies rather than continuous energies.

A simplified approach to enhance the time efficiency of simulations involves using parametrizations that characterize the distribution of charged particles within an extensive air shower (EAS), bypassing the simulation of the entire shower development and the tracking of each generated particle. For the longitudinal number of charged particles in an EAS, common analytical functions include the Greisen [132] or Gaisser-Hillas [133] function.

Additionally, the Nishimura-Kamata-Greisen function [134] is frequently used for the lateral distribution. The aforementioned functions, together with parametrizations of fluorescence and Cherenkov light emission [135], have been implemented in `ShowerModel` [136, 137] to simulate the light emission in EAS and its detection by IACTs. While parametrizations tend to miss the fluctuations in the shower development, this is less of an issue at higher primary particle energies. Here, the fluctuations are noticeably smaller than at lower primary particle energies.

In this Chapter, `EASpy`[1] is presented, a 3.5-dimensional simulation of extensive air showers. This simulation relies on parametrizations for electron-positron distributions, capturing the subsequent emission of fluorescence and Cherenkov light analytically, all while considering the curvature of Earth's atmosphere. Similar to `ShowerModel`, the simulation tool is designed to compute detector responses in a fast pace while simultaneously achieving a high level of accuracy and flexibility. Here, the primary focus is on γ-ray initiated air showers to establish the method and compare the results obtained using `EASpy` with `CORSIKA` and `sim_telarray`, independent of specific hadronic interaction models.

One reason why ShowerModel is unsuitable for observations at large zenith angles (LZA) is that it does not take into account the curvature of Earth's atmosphere, which can not be neglected within the zenith angle range considered in this study (see Sec. 2.6). In Tab. 4.1, an overview of key properties for `CORSIKA/sim_telarray`, `ShowerModel`, and `EASpy` is presented. While the simplified approach for the light collection (see Sec. 4.1.8) remains independent of pixel shape, `EASpy` considers gaps between pixels, particularly in the case of round pixels. Additionally, a study [130] demonstrated significant differences in the lateral (transversal) spread of resulting fluorescence light images for core distances less than 8 km between one-dimensional and three-dimensional simulations. Another motivation behind this work was to avoid using parametrizations for Cherenkov and fluorescence light emission. In principle, the distribution of charged particles alone should be sufficient for an analytical treatment of both emission types.

In Section 4.1, the reader is introduced to the basic concepts of `EASpy` including the production of Cherenkov and fluorescence light from an EAS and the consequent collection of this light by an IACT. The simulation of the detector response is outlined in Section 4.1.8 together with a comparison of shower images obtained with `EASpy` and a full air shower simulation in Section 4.2. In Section 4.3, the characteristics of the Cherenkov and fluorescence photon ground distribution at LZA are discussed.

[1] https://github.com/4liBaktash/EASpy

	CORSIKA/sim_telarray	ShowerModel	EASpy
Simulation method	Full MC	parameterized	parameterized
Dimension (space+time)	3+1	1+1	2.5+1
Atmosphere	(sliding) plane parallel	plane parallel	spherical
Particle content	$e^{\pm}$, $\mu^{\pm}$, ν, hadrons	$e^{\pm}$	$e^{\pm}$
Fluorescence	no	yes (param.)	yes (particle based)
Cherenkov	yes (particle based)	yes (param.)	yes (particle based)
Cherenkov-light collection	ray-tracing	parametrized	geometrical approach
Zenith angle	$0° - 90°$	$0° - 70°$	$70° - 90°$
Imaging: PSF	yes	no	yes
Imaging: Pixel shape	hex./square/circ.	square	hex./square/circ.

Table 4.1: Comparison of properties between CORSIKA/sim_telarray, ShowerModel, EASpy.

4.1 EASpy framework

In this section the general framework of EASpy is presented. The consideration of the curvature of Earth's atmosphere and its consequent impact for observations at large zenith angles with respect to the atmospheric transmission is explained in Sec. 4.1.1 and Sec. 4.1.2. The parametrization used in this work for the electron-positron distributions is highlighted in Sec. 4.1.3 and Sec. 4.1.4. As mentioned in Sec. 2.4, the number of emitted fluorescence photons is proportional to the deposited energy by electrons and positrons in the atmosphere. In Sec. 4.1.5 the reader is introduced to how these ionization energy losses are treated within the EASpy framework. Finally, the implementation of fluorescence light (Sec. 4.1.6), Cherenkov light (Sec. 4.1.7) and the subsequent detector response (Sec. 4.1.8) is covered.

4.1.1 Spherical atmosphere

Since the fluorescence and Cherenkov light yields depend on atmospheric parameters, e.g., air density, temperature, pressure (see Sec. 2.3 and Sec. 2.4), the choice of an appropriate atmosphere model is crucial. Typically, at zenith angles $\leq 70°$ a plane-parallel atmosphere is assumed, indicating that the air mass scales with the secant of the zenith angle. However, at zenith angles $\geq 70°$, the curvature of the atmosphere becomes significant and can not be neglected anymore. In such cases, relying on a plane-parallel atmosphere approximation introduces substantial errors, particularly for the slant depth X and the atmospheric transmission. To achieve a more precise model, the atmosphere is segmented into a sequence of evenly spaced spherical shells, each separated by 6 m. In EASpy, this separation is user-configurable. However, a large value for the separation will introduce considerable inaccuracies due to the method of how the atmospheric parameters for each shell are calculated (see Eqn. 4.1). The computation of the slant distance traveled and the height of each spherical shell is performed in

a coordinate system where the origin is positioned at the midpoint of the Earth, as illustrated in Fig. 4.1a.

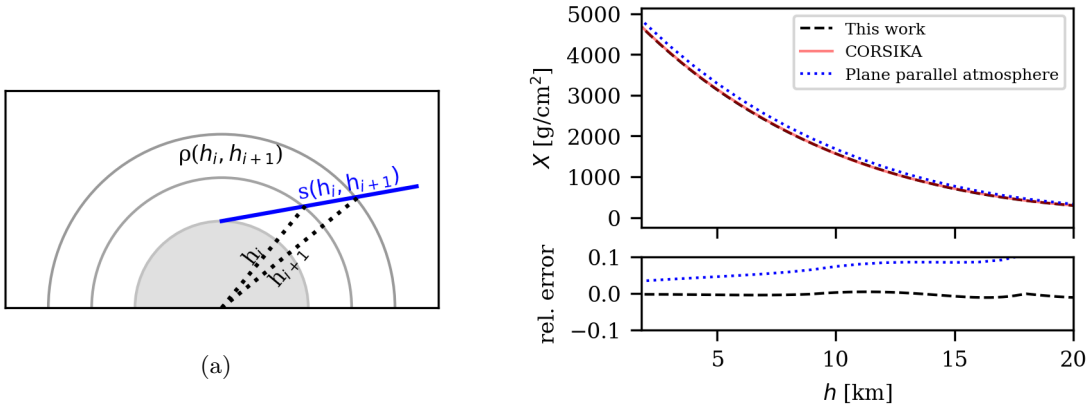

(a) (b)

Figure 4.1: (a) Schematic sketch of the spherical atmosphere model in `EASpy`. Gray shaded area denotes the Earth, the blue line marks the path of the primary particle and the dashed lines the height of the bin edges (h_i and h_{i+1}) for one spherical shell measured from the midpoint of the earth. The traversed slant distance for one spherical shell is then $s(h_i, h_{i+1})$. (b) Upper panel: Slant depth X as a function of height h at a zenith angle of 80°. Lower panel: Relative error for plane parallel atmosphere and this work compared to `CORSIKA`.

With provided measurements for the air density at various heights at zenith = 0°, the spherical symmetry of the model can be used for calculating the height dependent slant depth at LZA:

$$X(h_i, h_{i+1}) = \int_{h_i}^{h_{i+1}} \rho(h)\ \mathrm{d}s = \overline{\rho(h_i, h_{i+1})}\, s(h_i, h_{i+1}), \tag{4.1}$$

where $X(h_i, h_{i+1})$ is the traversed slant depth for one spherical shell with bin edges at heights h_i and h_{i+1}, $\overline{\rho(h_i, h_{i+1})}$ is the (linearly) averaged air density and $s(h_i, h_{i+1})$ is the slant distance for the primary particle path between the bin edges[2]. This method enables the calculation of atmospheric parameters along the trajectory of the primary particle. Within this approximation, the air shower can be treated to be symmetric in azimuth. A comparison between `CORSIKA` (compiled with the "CURVED" option), a plane parallel atmosphere, and the methodology proposed in this work is presented in Fig. 4.1b for the height-dependent slant depth at a zenith angle of 80°. The results from `CORSIKA` and `EASpy` demonstrate good agreement, whereas for a plane parallel atmosphere model, the relative error in comparison to `CORSIKA` is approximately 5% at the observation level, increasing with altitude.

[2] with $\rho \propto \exp(-h/h_0)$ and $h_0 \gg \Delta h$, the linear approximation for ρ in a shell is sufficiently accurate

4.1.2 Atmospheric transmission

The atmospheric transmission for Cherenkov and fluorescence light generated by air showers at large zenith angles is smaller than at small zenith angles, due to the increased traversed mass density with increasing zenith angle (see Fig. 2.16). The position of the shower maximum is observed at a distance of 50 km to 100 km, and as a result, more light will be scattered and absorbed in the atmosphere. In this work, the transmission is calculated with the `MODTRAN` [138] program. `MODTRAN` considers Rayleigh- and Mie-scattering, along with absorption processes with a moderate spectral resolution. The program provides various pre-defined atmospheric conditions, and for the work presented in this Chapter, the tropical atmosphere with a desert-type haze (aerosol) condition is selected.

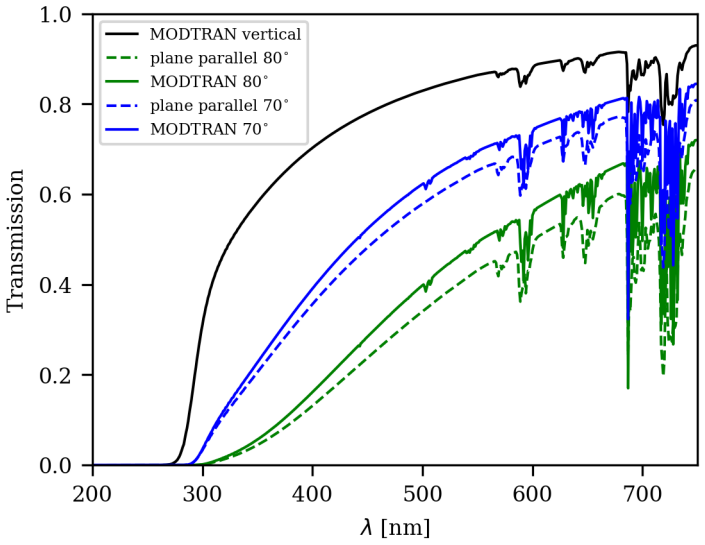

Figure 4.2: Transmission from 15 km to 1.8 km height as a function of wavelength λ for a vertical path, 70° and 80° zenith angle. Transmission profiles calculated with `MODTRAN` are for tropical atmospheric profile and desert haze.

In a model assuming a plane parallel atmosphere, the transmission T would be calculated for a vertical path, assuming that $\tau \propto \sec(\theta)$, where τ is the optical depth with $T = \exp(-\tau)$. Compared to a spherical atmosphere, this approach would overestimate the mass overburden, leading to an underestimation of the transmission. In Fig. 4.2, one can observe that a plane parallel atmosphere model would underestimate the transmission by $\sim 10\%$, with the transmission for a wavelength of ~ 500 nm reduced by a factor of 2 for a path with a zenith angle of 80° compared to a vertical path. Moreover, as expected, the difference between a plane parallel atmosphere approximation and `MODTRAN` is less for a path with a zenith angle of 70° compared to 80°.

`EASpy` provides a choice between using the plane-parallel atmosphere approximation or to use tabulated files describing the transmission for different values of zenith angle. The `EASpy` package will include a few selected zenith angle dependent look-up tables for the transmission T.

4.1.3 Parametrizing the electromagnetic shower component

To accurately simulate fluorescence and Cherenkov light in air showers, an accurate description of the distribution of charged particles is essential. Of particular interest is the distribution of electrons and positrons, as these particles are the most abundant charged particles in air showers. `EASpy` makes use of a multi-dimensional parametrization for the electron-positron distributions for particle energy, angular spectrum and lateral distance proposed by [139].

In the following, a brief introduction to the terminology is provided. For a full description of the functional form describing the distributions, the reader is refered to [139]. The Ansatz for the parametrization of the differential particle number n in a logarithmic interval $[\ln\epsilon, \ln\epsilon + \mathrm{d}\ln\epsilon]$ of kinetic energy ϵ of electrons and positrons in MeV follow from Eqn. 6 in Ref. [139]

$$n(t) \coloneqq \frac{1}{N(t)}\frac{\partial N(t)}{\partial \ln\epsilon} = \frac{1}{N(t)}N(t;\ln\epsilon), \tag{4.2}$$

for the particle number n_Ω in a differential interval of solid angle $[\Omega, \Omega + \mathrm{d}\Omega]$ given in Eqn. 8 in Ref. [139]

$$n_\Omega(t) \coloneqq \frac{1}{N(t;\ln\epsilon)}\frac{\partial^2 N(t)}{\partial \ln\epsilon \partial\Omega}, \tag{4.3}$$

and for the particle number n_x in a differential logarithmic interval of radial distance to the shower axis $[\ln x,\ \ln x + \mathrm{d}\ln x]$, where $x \equiv \frac{r}{r_\mathrm{M}}$ and r_M is the Molière radius

$$n_x(t) \coloneqq \frac{1}{N(t;\ln\epsilon)}\frac{\partial^2 N(t)}{\partial \ln\epsilon \partial \ln x}. \tag{4.4}$$

Here, $N(t)$ denotes the total number of electrons and positrons in the air shower crossing a plane perpendicular to the trajectory of the primary particle at relative evolution stage t. Hence, the distributions are fully described in terms of t:

$$t = \frac{X - X_\mathrm{max}}{X_0}, \tag{4.5}$$

where the maximum number of particles $N_\mathrm{max} = N(X_\mathrm{max}) = N(t=0)$ is reached at slant depth X_max and $X_0 \simeq 36.7$ g cm^{-2} is the radiation length of electrons and positrons

in air. Furthermore, the sign of t indicates whether the shower development is at a stage before (negative sign) or after (positive sign) the shower maximum, while the absolute value of $|t|$ quantifies the distance to the shower maximum in terms of radiation length X_0.

Note, that $n(t)$, $n_\Omega(t)$ and $n_x(t)$ are probability density functions given by Eqn. 6, 8 and 14 in Ref. [139]. The number of particles in the range of $[\ln\epsilon, \ln\epsilon + \mathrm{d}\ln\epsilon]$ and $[\ln x, \ln x + \mathrm{d}\ln x]$ at relative evolution stage t is calculated with:

$$N(t, \bar{\epsilon}, \bar{x}) = N(t) \iint n_x(t)\ \mathrm{d}\ln\epsilon\ \mathrm{d}\ln x. \tag{4.6}$$

The values for $\bar{x}$ and $\bar{\epsilon}$ are chosen to be the arithmetic and geometric averages of the intervals $[\ln\epsilon, \ln\epsilon + \mathrm{d}\ln\epsilon]$ and $[\ln x, \ln x + \mathrm{d}\ln x]$ respectively. In order to keep the notation simple, in the following ϵ and x are used instead of $\bar{\epsilon}$ and $\bar{x}$.

4.1.4 Electron-positron distributions

With a given shower profile $N(t)$ representing the total number of particles at the shower evolution stage t, the number of particles in differential intervals for distance r and energy ϵ, denoted as $N(t, \epsilon, r/r_M)$, is determined using Eqn. 4.6. Therefore the air shower is assumed to have a cylindrical symmetry and is binned as follows: within a fixed energy range of $[\ln\epsilon, \ln\epsilon + \mathrm{d}\ln\epsilon]$, the air shower is binned along the shower axis with a bin width of $\mathrm{d}s$ (see Eqn. 4.1) and perpendicular to the shower axis with a radial bin width of $\mathrm{d}r$. The resulting cylindrical shells are then divided into N_ϕ equally spaced bins (referred to as "voxels") over 2π around the shower axis (as illustrated in Fig. 4.3). For each of these voxels, the energy-dependent number of particles is determined by $N(t, \epsilon, r/r_M)/N_\phi$. The values of N_ϕ and dr are user-configurable but should be treated carefully, considering the imaging method employed in `EASpy` (see Sec. 4.1.8). For the results presented in Sec. 4.2, a value of $N_\phi = 300$ is used together with a radial bin width of $\mathrm{d}r = 5\,\mathrm{m}$ up to a maximum lateral distance of 1 km.

An overview of the shower development is provided in Fig. 4.4a, where the distribution of electrons and positrons (integrated over the energy range of $\epsilon_{\min} = 1\,\mathrm{MeV}$ to $\epsilon_{\max} = 10\,\mathrm{GeV}$) is projected onto the xz plane for a photon initiated air shower with zenith angle of 80°. The shower axis and the shower maximum (approximately at $x \simeq 85\,\mathrm{km}$ and $z \simeq 14\,\mathrm{km}$) are clearly observable.

The lateral distribution of shower particles surrounding the shower axis contributes to the production of Cherenkov light when their energy exceeds the Cherenkov energy

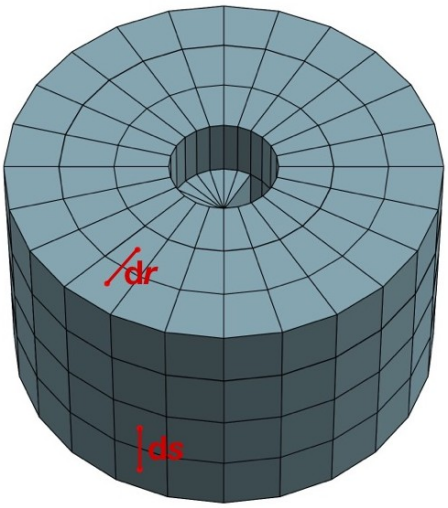

Figure 4.3: Schematic sketch of the shower binning in `EASpy`. The bin width along the shower axis is denoted as ds and the bin width in the radial direction as dr.

threshold (see Eqn. 2.6) of $E_{Ch} \approx 50\,\mathrm{MeV}$ at the position near the shower maximum. In Fig. 4.4b, the lateral distribution is compared for particles emitting Cherenkov light ($\epsilon > E_{Ch}$) with those that exclusively produce fluorescence light($\epsilon < E_{Ch}$). A substantial fraction (80%) of the Cherenkov light emitting particles is confined within 75 m in the radial direction of the air shower, while particles emitting fluorescence light are spread over a wider range: 80% of these particles are located within 400 m to the shower axis.

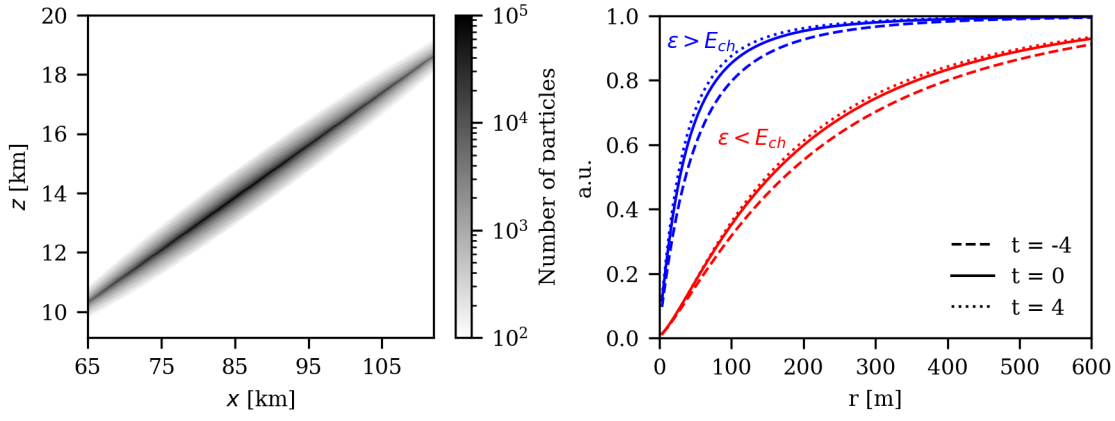

(a) (b)

Figure 4.4: (a) Electron and positron distribution projected on the xz plane (i.e., integrated over y-coordinate) for a γ-ray initiated air shower with primary energy of $E_\gamma = 975\,\mathrm{TeV}$ at a zenith angle of 80°. (b) Normalized cumulative distribution of particle numbers as a function of lateral distance to the shower axis r at $t = -4, 0, 4$ for the same air shower as in (a). E_{Ch} denotes the Cherenkov energy threshold and ϵ the energy of the electrons(positrons). The maximum distance to the shower axis is set to 1 km.

4.1.5 Ionization energy deposit

Electrons and positrons deposit energy differently in collisions with air molecules when passing through the atmosphere [140], due to the ambiguity between the electrons of the air shower and the atomic electrons. The stopping power for electrons can be calculated with the Møller cross section and for positrons with the Bhabha cross section [141]. Therefore, the stopping powers for electrons and positrons are implemented in `EASpy` as:

$$\left\langle -\frac{\mathrm{d}E}{\mathrm{d}X} \right\rangle = \frac{1}{2} K \frac{Z}{A} \frac{1}{\beta^2} \times [F(\gamma, \beta, I) - \delta], \tag{4.7}$$

where $K = 4\pi N_A r_e^2 m_e c^2$ in units of $\mathrm{mol}^{-1}\,\mathrm{cm}^2$, Z and A are the mean atomic number and mean atomic mass (in units of $\mathrm{g\,mol}^{-1}$) of air, I is the mean excitation energy in units of eV, $\gamma = \sqrt{\frac{1}{1-\beta^2}}$ and δ is a density correction factor. The functional form of $F(\gamma, \beta, I)$ depends on whether electrons or positrons are considered. Both stopping power formulas including the parameter values used in this work can be found in [141, 142].

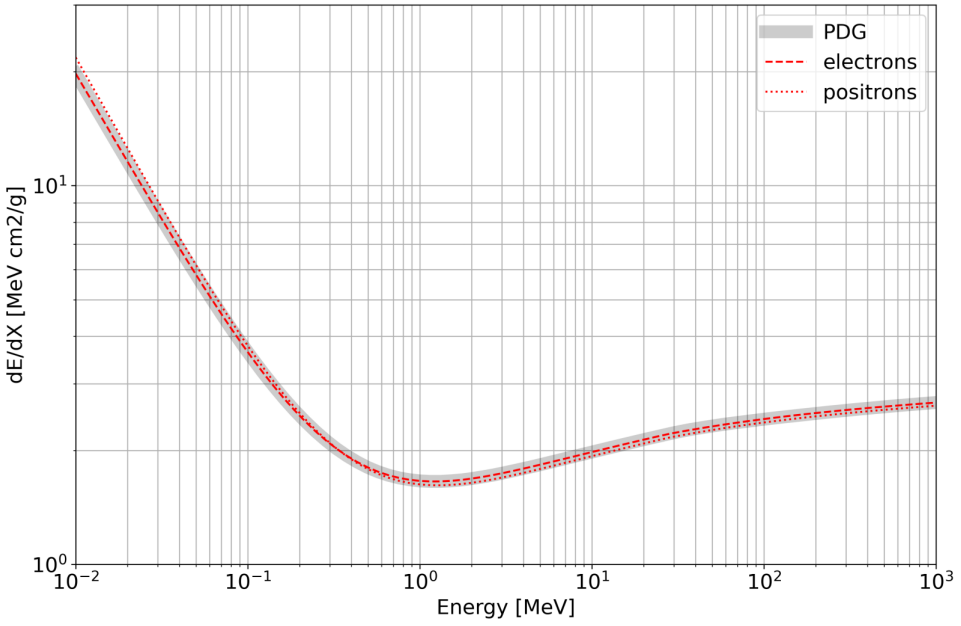

Figure 4.5: Stopping powers for electrons (dashed red line) and positrons (dotted red line) in dry air calculated with `EASpy`. The gray shaded area marks the stopping powers for electrons obtained with the `ESTAR` program: `https://physics.nist.gov/PhysRefData/Star/Text/ESTAR.html`.

The stopping powers calculated with EASpy for electrons and positrons in dry air is presented in Fig. 4.5. It is evident, that for energies $\leq 1\,\mathrm{MeV}$ the energy losses become significantly larger compared to $\geq 1\,\mathrm{MeV}$. As the energy increases, the term $\frac{1}{\beta^2}$ in Eqn. 4.7 approaches unity and as a result $\mathrm{d}E/\mathrm{d}x$ scales with the logarithm of the energy (due to a logarithmic dependence in $F(\gamma, \beta, I)$, see Eqn. 4.7).

The resulting ionization energy losses are assumed to be deposited at the midpoints of each voxel. It is important to note that in the framework of EASpy, the assumed cylindrical symmetry of the particle distribution defines the symmetry of the energy deposit. While this is an approximation, as the atmospheric conditions around the shower axis (for fixed t and r) may deviate slightly for different azimuth angles at large zenith angles, it is sufficient to capture the main features of the air shower relevant for the resulting image. This is demonstrated through a comparison of EASpy generated images with a full simulation (sim_telarray), as shown in Sec. 4.2.

The accuracy of the parametrization for the energy spectrum, as given in Eqn. 4.2, can be readily estimated by calculating the energy deposit using the stopping powers for electrons and positrons and then comparing the results with those obtained from CORSIKA. In Fig. 4.6, a comparison is presented between the results obtained using EASpy and those from CORSIKA for the energy deposit per slant depth $\frac{\mathrm{d}E}{\mathrm{d}X}$ for γ-ray initiated air showers in the energy range of 900 TeV to 1000 TeV at a zenith angle of 70° and 80°. The number of individual air showers is ~ 850 per zenith angle. The relative error is calculated as

$$\text{rel. error} = \frac{(\mathrm{d}E/\mathrm{d}X)_{\texttt{EASpy}} - (\mathrm{d}E/\mathrm{d}X)_{\texttt{CORSIKA}}}{(\mathrm{d}E/\mathrm{d}X)_{\texttt{CORSIKA}}}.$$

In the early shower stages, the relative difference is approximately 5-10%, whereas in the later stages, the correspondence is better than 5% for both zenith angles. The comparison indicates that discrepancies from CORSIKA results predominantly depend on the zenith angle, with a slightly improved correspondence at zenith angles around 70° in contrast to those closer to 80°. A negligible dependence on the primary particle energy was found.

The "spikes" in Fig. 4.6 are associated with how CORSIKA handles the atmosphere: The "CURVED" option uses a "sliding plane atmosphere" instead of a fully spherical atmosphere model. Every time the horizontal displacement of a particle exceeds a limit of 6 km to 20 km (depending on altitude), a transition to a new, locally plane atmosphere is performed [114]. Apparently, these "spikes" occur as a result of this treatment, each time when the transition is performed.

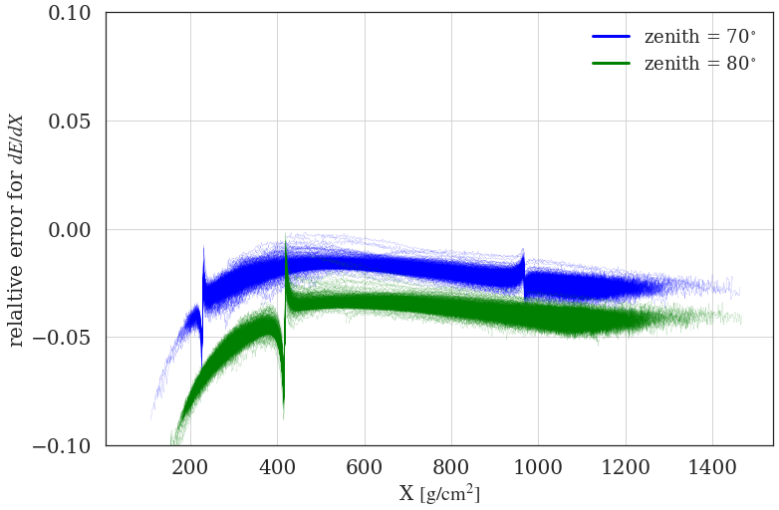

Figure 4.6: Relative error for the energy deposit per slant depth $\frac{\mathrm{d}E}{\mathrm{d}X}$ as a function of slant depth X for γ-ray initiated air showers with zenith angles of 70° and 80°.

4.1.6 Implementation of fluorescence light

A fraction of the ionization energy deposited in the atmosphere (see Sec. 4.1.5) results in the excitation of nitrogen atoms, followed by the emission of fluorescence light with a typical life time of the excited state of the order of $\mathcal{O}(10\,\mathrm{ns})$ (see Sec. 2.4). The number of produced fluorescence photons N^{fl} in a voxel at position (t, r, ϕ) can be calculated with:

$$N^{fl}(t,r,\phi) = \frac{\Delta X(t)}{N_\phi} \int_{\epsilon_{\min}}^{\epsilon_{\max}} N(t,\epsilon,r/r_M)\frac{\mathrm{d}E}{\mathrm{d}X}(\epsilon)\mathrm{d}\epsilon \cdot \int_{\lambda_{\min}}^{\lambda_{\max}} Y_{air}(\lambda,T,p,p_w)\mathrm{d}\lambda, \tag{4.8}$$

where $\Delta X(t)$ is the traversed slant depth depending on relative evolution stage t and $Y_{air}(\lambda, T, p, p_w)$ is the fluorescence yield in air depending on wavelength λ (in nm), ambient atmospheric pressure $p = p(t)$, water vapour partial pressure $p_w = p_w(t)$ and temperature $T = T(t)$. This way, the number of emitted fluorescence photons is directly proportional to the rate of ionization energy loss $\frac{\mathrm{d}E}{\mathrm{d}X}$. The fluorescence yield in air Y_{air} is typically expressed in terms of the absolute yield of the 337 nm band in dry air at reference pressure p_0 and temperature T_0 (see Eqn. 2.7). Given that the absolute yield $Y_{air}(337, T_0, p_0)$ is provided for a dry atmosphere, it is assumed that the reference water vapor pressure $p_{w,0} = 0$. Likewise, the values $I_\lambda(T_0, p_0)$, $I_{337}(T_0, p_0)$ and $p'_{337}(T_0)$ are specified for a dry atmosphere.

Highlighting the relative intensity I_λ/I_{337} (see Fig. 4.7), it is evident that the majority of fluorescence lines are located at wavelengths $\lambda \lesssim 400\,\mathrm{nm}$. For an in-depth discussion of the temperature, humidity, and pressure dependence of the fluorescence yield in air,

as well as the function $p'_\lambda(T, p_w)$, the reader is directed to [143, 144]. The parameters used for the fluorescence yield in air can be found in Appendix A. Note, that `EASpy` computes atmospheric parameters exclusively along the shower axis. Thus, at relative evolution stage t, all voxels in a plane perpendicular to the shower axis share the same values for the atmospheric parameters.

Assuming isotropic fluorescence emission, only a small fraction of the fluorescence photons are expected to be observed by the telescopes. Rather than distributing the photons randomly over 4π and keeping track of each photon trajectory, the number of fluorescence photons, N^{fl}_{sphere}, reaching the telescope's sphere is determined by its angular size as seen from the position of an individual voxel. In this context, the telescope is modelled as a sphere with radius set to the radius of the reflector surface. Consequently, the fraction N^{fl}_{sphere}/N^{fl} of the emitted fluorescence photons hitting the telescope's sphere depends only on the ratio of its radius R and distance d to the voxel position:

$$\begin{aligned} \frac{N^{fl}_{sphere}}{N^{fl}} &= \frac{\Delta\Omega(d, R)}{4\pi} \\ &= \frac{1 - \sqrt{1 - R^2/d^2}}{2} \approx \frac{R^2}{4d^2}. \end{aligned} \tag{4.9}$$

At a zenith angle of $70°(80°)$ and a radius $R = 14\,\mathrm{m}$, the resultant fraction is approximately $\approx 10^{-8}(10^{-9})$. This substantial decrease when going from 70° to 80° is due to the rapid increase in the distance from the telescope position to the shower maximum as the zenith angle of the air shower increases.

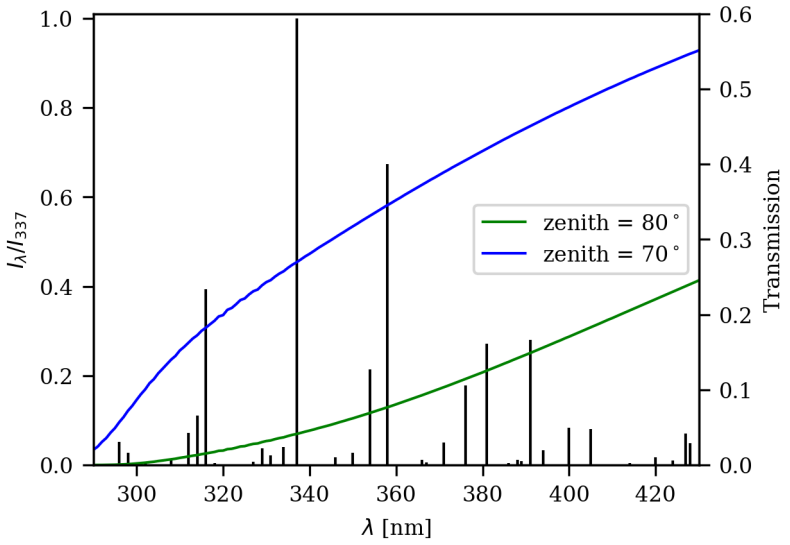

Figure 4.7: Black lines denote the wavelength dependent intensity relative to the 337 nm band I_λ/I_{337} (left axis). The blue (70° zenith angle) and green(80° zenith angle) lines describe the transmission T from the position of the shower maximum down to the observation level (right axis).

In addition to the geometric dilution of the fluorescence light, the atmospheric transmission decreases with an increasing zenith angle, corresponding to an increasing slant depth (see Fig. 2.16). In Fig. 4.7, the relative transmissivity for zenith angles of 70° and 80° is compared. The starting height is set as the average height of the shower maximum for air showers with $E_\gamma \sim 1\,\mathrm{PeV}$ (70°: $\sim 10\,\mathrm{km}$ and 80°: $\sim 14\,\mathrm{km}$). The observation level is positioned at a height of $\sim 1.8\,\mathrm{km}$ asl. A large fraction of the produced fluorescence photons will have a wavelength $\lambda \lesssim 400\,\mathrm{nm}$. At a zenith angle of 80° approximately 4% of the emitted light with wavelength $\lambda = 337\,\mathrm{nm}$ reaches the observation level, whereas at 70°, the observable light increases to around 27% of the emitted light.

4.1.7 Implementation of Cherenkov light

The total number of Cherenkov photons N^{Ch} produced in the wavelength range from λ_1 to λ_2 in a voxel at position (t, r, ϕ) is given by

$$N^{Ch}(t, r, \phi) = \frac{\Delta X(t)}{N_\phi} \frac{2\pi}{\alpha \rho(t)} \frac{\lambda_2 - \lambda_1}{\lambda_1 \lambda_2} \int_{E_{Ch}}^{\epsilon_{\max}} \left(1 - \frac{1}{n^2(t)\beta(\epsilon)^2}\right) N(t, \epsilon, r/r_M)\, \mathrm{d}\epsilon \qquad (4.10)$$

where E_{Ch} is the Cherenkov energy-threshold, α the fine-structure constant, $\beta = v/c$, and $n(t)$ the refractive index[3]. Note, that the produced Cherenkov photons are assumed to be emitted at the midpoint of the corresponding voxel positions. At each voxel and energy bin, the mean angle to the shower axis $\langle \theta_p \rangle$ is calculated using n_Ω (see Eqn. 4.3 and [139]).

Typically, it is assumed that the Cherenkov emission angle θ_{Ch} is smaller than $\langle \theta_p \rangle$. However, at sufficiently high energies, the Cherenkov angle becomes dominant and can no longer be ignored. This is illustrated in Fig. 4.8, where a comparison is made between the two angles. The average angle $\langle \theta_p \rangle$ reaches values comparable to the Cherenkov angle θ_{Ch} at energies of $\epsilon = 400\,\mathrm{MeV} \ldots 500\,\mathrm{MeV}$. Considering that most electrons will emit Cherenkov light close to the threshold, it may seem reasonable to neglect the Cherenkov angle. Nevertheless, even at energies close to threshold, the additional broadening of the angular distribution of the emitted light due to the Cherenkov angle leads to a considerable change of the order of $\mathcal{O}(100\,\mathrm{m})$ on the impact position at the detector level.

[3] We replace the height dependence of refractive index n and specific density ρ with its dependence on t

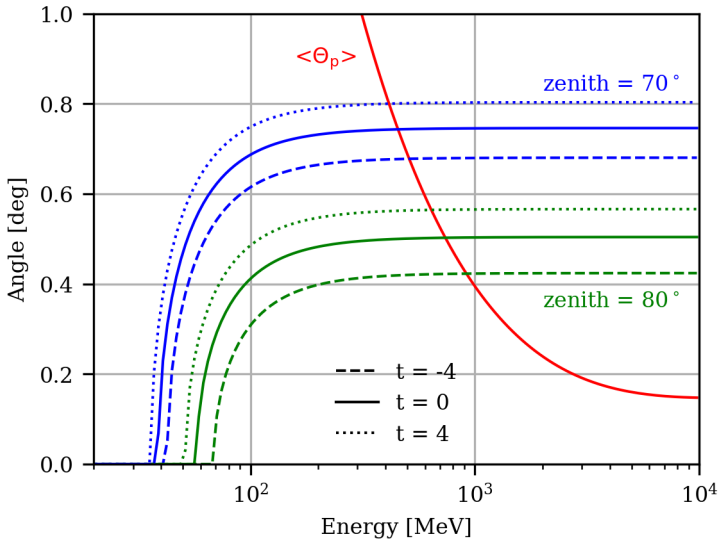

Figure 4.8: The red line marks the mean angle to the shower axis $\langle\theta_p\rangle$ of electrons as a function of energy. Blue (70° zenith angle) and green (80° zenith angle) lines indicate the Cherenkov emission angle for different stages of shower evolution ($t = -4, 0, 4$) marked by dashed, solid, and dotted lines.

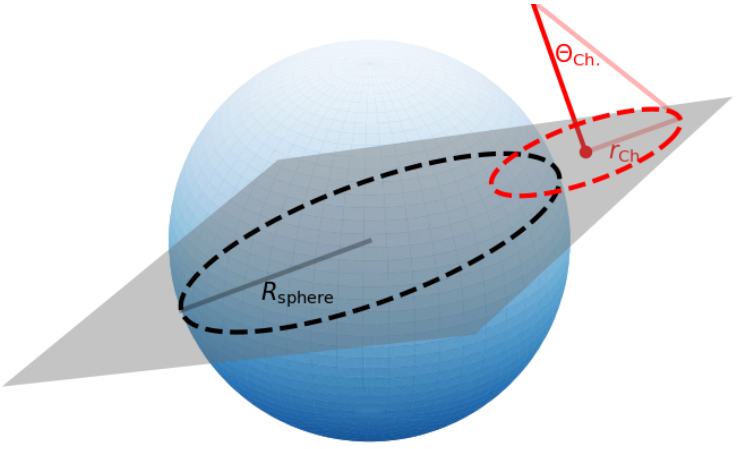

Figure 4.9: Thick red line is parallel to the momentum vector of the electrons, θ_{Ch} denotes the Cherenkov angle and r_{Ch} is the radius of the Cherenkov circle in the intersecting plane (perpendicular to the momentum vector, in grey). The intersection of the plane with the telescope's sphere with radius R_{sphere} results in a circle with radius R_{sphere}.

Finally, the calculation of the number of Cherenkov photons intersecting the telescope's sphere, denoted as N^{Ch}_{sphere}, is performed as follows: For each voxel position and energy bin, the number of produced Cherenkov photons is evaluated with Eqn. 4.10. Using the momentum vector of the emitting electrons, a plane perpendicular to its direction is constructed, intersecting the midpoint of the telescope's sphere. This plane is subsequently intersected by both the Cherenkov cone and the telescope's sphere, forming two circles (see Fig. 4.9). Given that the two circles overlap, the two intersection points determine an arc of length L along the Cherenkov cone that lies inside the sphere. The fraction of photons intersecting the sphere's surface is equivalent to the fraction of the arc length:

$$\frac{N^{Ch}_{sphere}}{N^{Ch}} = \frac{L}{2\pi r_{Ch}}. \tag{4.11}$$

This approach does not require any approximations and, in comparison to methods like ray-tracing, reduces the required computation time.

It is important to note that in the `EASpy` framework, particles always move away from the shower axis. This approximation breaks down for low energy electrons ($\epsilon \sim$ MeV), as demonstrated in [139]. However, given the higher Cherenkov energy threshold E_{Ch} at large zenith angles, these low energy electrons do not contribute to the Cherenkov photon production and can thus be neglected. Conversely, high energy electrons ($\epsilon \gtrsim 50\,\text{MeV}$) originate closer to the shower axis, where the majority of particles move away from the shower axis.

4.1.8 Imaging of simulated air showers

Up to this point, the description has covered the computation of the total number of fluorescence and Cherenkov photons for each voxel position, along with the determination of how many of these photons (termed N^{fl}_{sphere} and N^{Ch}_{sphere}) intersect the telescope sphere. Note that, with the approach described in Sec. 4.1.6 and Sec. 4.1.7, information about the directional vector of individual photons is not stored. Therefore, the detector response (i.e., the generation of a camera image) has to be treated in a simplified manner. This is achieved by recognizing that the shower maximum is at a substantial distance d of 50 km to 100 km which is much larger than the radius of the sphere (e.g., for the largest Cherenkov telescope $R = 14\,\text{m}$). Hence, it is reasonable to assume that all photons from a distant voxel intersect the sphere along its diameter. This assumption is justified for large distances d, by approximating the maximum angle difference $\Delta\alpha$ for a tangentially (to the sphere) intersecting photon:

$$\Delta\alpha = \arctan\left(\frac{R}{d}\right) \approx R/d. \tag{4.12}$$

For the large zenith angles considered here, $d \gtrsim 50\,\mathrm{km}$, the resultant maximum angle difference is $\Delta\alpha \lesssim 0.016°$. This potential additional widening of the angular distribution of photons intersecting the telescope sphere is less than the typical angular field of view for individual pixels (see. Sec.2.5), making it negligible (the smallest pixel size of currently operating IACTs covers a patch in the sky with a diameter of 0.07° [145]). Consequently, this approach allows for a substantial reduction in computation time (> three orders of magnitude) when compared to a ray-tracing method. However, it is important to note that this approximation introduces a systematic underestimate of the image *width* for the shower tail, even at large zenith angles where the tail is observed at distances ranging from 10 km to 20 km. For IACT configurations involving a very large telescope paired with a highly granular camera, the paraxial approximation becomes unreliable. Conversely, at smaller zenith angles, the accuracy of images generated using the paraxial approximation is limited to small sized telescopes ($\Delta\alpha \propto 1/d$, where $d \sim 10\,\mathrm{km}$ for moderate zenith angles, see Eqn. 4.12). Each combination of telescope radius, zenith angle, and pixel size requires individual consideration due to this limitation.

Finally, the generation of realistic camera images is explained in the following. Since camera images are based on the number of photo-electrons detected in the individual pixels, a coarse simulation of the detection process is implemented in `EASpy`, which includes:

- the combined wavelength-dependent quantum efficiency of the photo-cathode and collection efficiency for photo-electrons,
- the wavelength-dependent mirror reflectivity of the mirror facets, and
- the wavelength-dependent transmittance of the camera protective cover.

Furthermore, `EASpy` takes into account shadowing effects of the camera support structure and the light guide efficiency of the PMT. For this, the user can provide a single value for all wavelengths.

To consider the previously mentioned wavelength dependent effects in addition to atmospheric transmission, the efficiency P_j for detecting a photon (fluorescence or Cherenkov) after traversing the atmosphere is pre-computed for each voxel with index j at a specific height $h(j)$ above ground. The calculation of P_j involves integrating the product of emissivity $\Lambda^{Ch,fl}(\lambda)$, detection efficiency $\eta(\lambda)$, and transmission $T(\lambda, h)$. The resulting value is normalized, yielding:

$$P_j = \frac{\int_{\lambda_1}^{\lambda_2} \Lambda^{Ch,fl} \cdot T(\lambda, h)\eta(\lambda)\ \mathrm{d}\lambda}{\int_{\lambda_1}^{\lambda_2} \Lambda^{Ch,fl}\ \mathrm{d}\lambda}. \tag{4.13}$$

The wavelength distribution for the fluorescence photons is determined by the wavelength dependent intensity relative to the 337 nm band (see Fig. 4.7), while Cherenkov photons follow a $1/\lambda^2$ distribution (see Eqn. 2.5).

The camera's point spread function is defined by external lookup-tables with the 68% containment radius as a function of off-axis angle and zenith angle. For the simulation of the night sky background (NSB), the user can provide an average background rate in units of photo-electrons per nanosecond and per pixel. However, the detector simulation does not consider certain electronics-related effects like trigger formation, non-linearities, and digitization effects during read-out. While this could be theoretically implemented into the `EASpy` framework, other existing packages like `simtel_array` [146] can be used to obtain a more specific and accurate simulation of the detector response. For this, the information of the photons intersecting the telescope sphere would need to be stored in the `eventio` format in the future. Note, that with the paraxial approximation one can deduce the momentum vector of the photons. Although a parametrization for the delay time distribution of the electrons-positrons is given in [139], it is not yet implemented in `EASpy`. So far, `EASpy` considers only the time lag along the shower axis, neglecting delay times in the radial direction of the shower.

Finally, the simulated detector response, illustrated in Fig. 4.10, highlights the detected Cherenkov (upper panel) and fluorescence light (lower panel) emitted by an γ-ray air-shower with an energy of $E_\gamma = 780$ TeV at a zenith angle of 80°. The resulting image of the detected Cherenkov light resembles, as expected from observations of air Cherenkov light with Cherenkov telescopes (see Sec. 2.5), an ellipse, characterized by the major axis (so-called *length*) and minor axis (so-called *width*). Note, that the *length* appears to be roughly three times as large as the *width*. The image of the detected fluorescence light is comparable to the Cherenkov light image, albeit with a peak intensity reduced by a factor of ≈ 3000. Furthermore, the fluorescence light image appears to have a similar length but noticeably greater width than the Cherenkov light image. This is primarily a consequence of Cherenkov emission having an energy threshold E_{Ch}, and most particles with $\epsilon > E_{Ch}$ being very close to the shower axis (see Fig. 4.4b). Conversely, fluorescence emission scales with deposited energy, and electrons further away from the shower axis with $\epsilon < E_{Ch}$ also contribute to fluorescence photon production. Additionally, fluorescence emission is isotropic (see Sec. 2.4), while Cherenkov emission

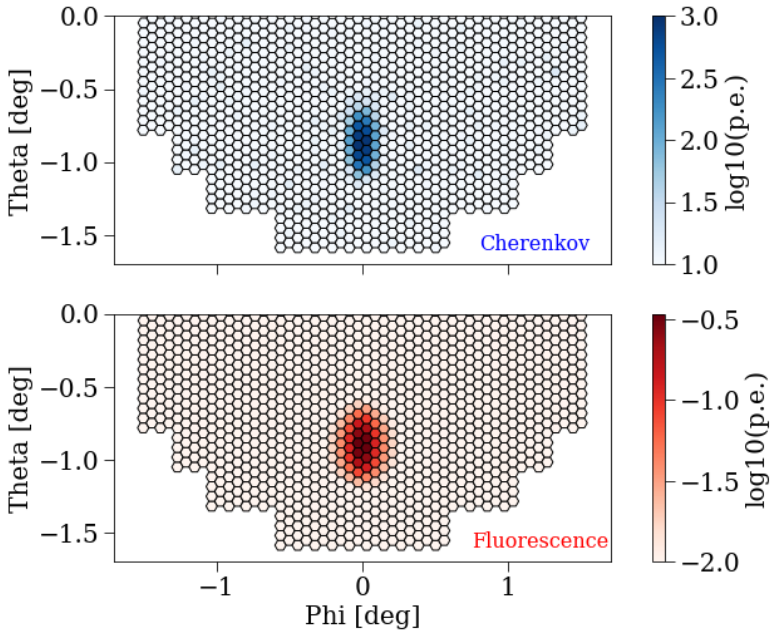

Figure 4.10: Example camera image formed by Cherenkov (upper panel) and fluorescence light (lower panel) produced by a γ-ray air shower with $E_\gamma = 780$ TeV at a zenith angle of 80°. Note, the logarithmic scales differ between the two images.

has an opening angle θ_{Ch} (see Eqn. 2.4) that limits the visibility of the shower for an IACT.

4.2 Verification with a full simulation

In Fig. 4.11, an example shower image generated with `EASpy` is compared side-by-side with the shower image as calculated with a complete air shower simulation and ray-tracing for Cherenkov light using the `sim_telarray` program. To make the comparison meaningful, the limited dynamical range and saturation of pixel amplitudes, similar to `sim_telarray`, is included for the `EASpy` generated image.

Note, that the underlying shower profile is identical for both images. Remarkably, the images appear quite similar despite the introduced simplifications and the utilization of a coarse detector simulation. The position of the image in the camera and the captured light in the pixels demonstrate a strong agreement. The approximate *length* matches in both images, with the *width* appearing slightly larger for the `EASpy` generated image. This discrepancy can be explained by assuming a perfectly symmetric point spread function (PSF) of the telescope optics. However, the PSF generally elongates along the radial direction, resulting in a smaller apparent width of the recorded image.

To provide a more quantitative comparison, a larger set of simulated air showers (see Fig. 4.12a) is taken into account. The detector response for each of these simulated air

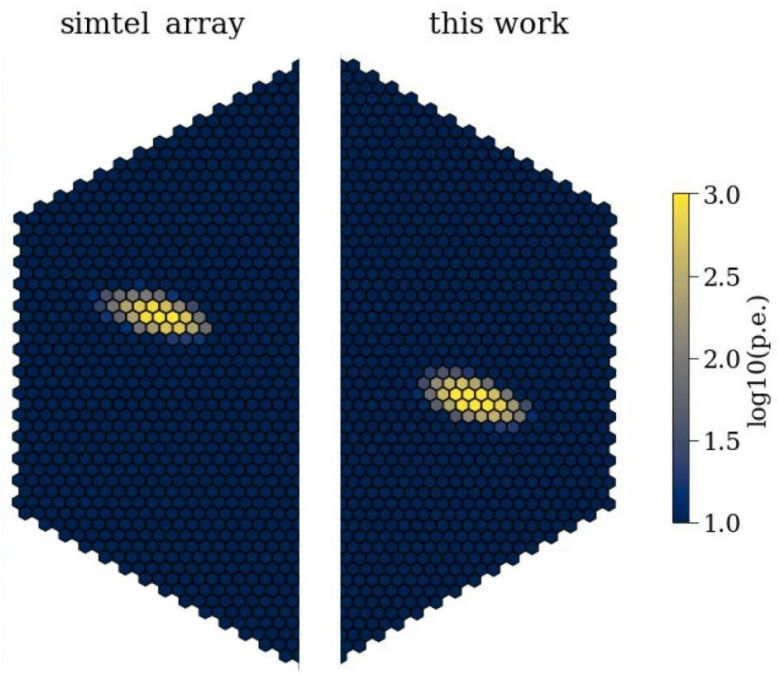

Figure 4.11: Side-by-side comparison of the camera image for a γ-ray shower with zenith angle of 80° obtained with `sim_telarray` (left) and `EASpy` (right). The `sim_telarray` camera image is rotated by 180°.

showers is carried out with `EASpy` and `sim_telarray`. The corresponding distributions of *width* and *length* of the images for on-axis observations at zenith angles of 70° and 80° are then compared in Sec. 4.2.1 and Sec. 4.2.2, respectively.

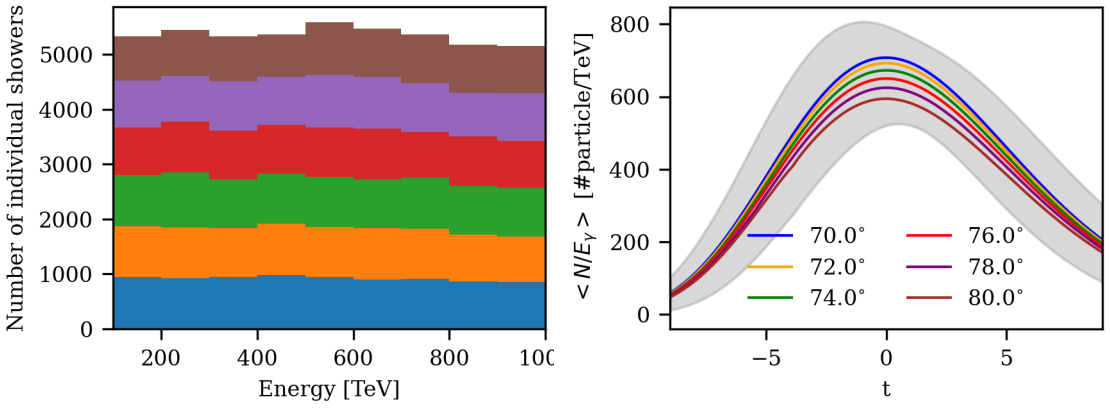

(a) (b)

Figure 4.12: (a) Histogram of simulated showers with bin width of 100 TeV for each zenith angle. (b) Mean number of particles per primary gamma energy for each zenith angle bin. The gray shaded area denotes the envelope of the 1 σ error bands of zenith angle bins.

The mean shower profile $N(t)$ per energy E_γ of the primary γ-ray for each simulated zenith angle bin is presented in Fig. 4.12b (see Eqn. 4.5 for definition of relative evolution stage t). While the mean shower profiles converge at very early ($t \leq$ -4) and late stages

($t \geq 4$), an unexpected deviation occurs around the shower maximum ($t \sim 0$). This behavior is not seen when normalizing the shower profiles to the number of particles at the shower maximum $N/N_{\max}$, with $N_{\max} = N(t = 0)$. Consequently, Fig. 4.12b indicates that at large zenith angles ($\geq 70°$), an increasing fraction of the primary γ-ray energy E_γ is missing in the electromagnetic cascade (in the form of electrons and positrons) with increasing zenith angle.

In the following, all relevant information regarding `CORSIKA` version, compiling options, and parameter settings used to simulate the air showers are provided:

`CORSIKA` version	7.7402
compiling options	VOLUMEDET, IACT, ATMEXT, CURVED, VIEWCONE, SLANT, CERENKOV
interaction models	QGSJET-01D [115], GHEISHA 2002d [116], EGS4 [117]
atmosphere	all-year average profile at H.E.S.S. site

For the energy cut-off of the particle kinetic energy for hadrons, muons and electrons 0.3 GeV, 0.1 GeV and 0.001 GeV are used respectively. The lower and upper limit of the wavelength band for the Cherenkov radiation production covers a range 250 nm to 700 nm with a bunchsize of 5. The longitudinal development of particle numbers and energy deposit by ionization energy losses are sampled in steps of 2 g/cm^2. Explanations for the compiling options and keywords for the `CORSIKA` input card can be found in [114].

4.2.1 Width distribution

In Fig. 4.13a, a comparison is made between the image *width* obtained with the full simulation (termed w_s) and the results from `EASpy` (termed w) at zenith angles of 70° and 80°. The two-dimensional histogram at a zenith angle of 70° demonstrates a clear and linear correlation between w_s and w. Both, the average values and individual distributions, appear to be very similar. The 68%-ile boundary around the centroid of the distribution is marked by blue (70°) and green (80°) ellipses. The orientation and position of these ellipses match well between the two methods for each zenith angle. Observable differences are likely a result of different cleaning procedures between the two methods. As expected, the *width* observed at 80° is systematically smaller than the *width* observed at 70° due to the increased distance to the shower maximum.

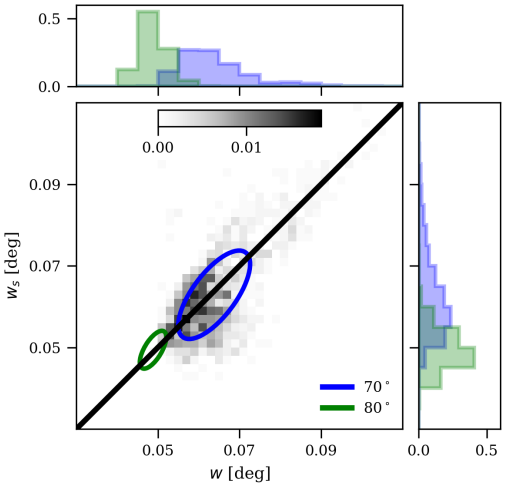

(a) Comparison of *width* parameter for showers with zenith angle 70°(80°) between `sim_telarray` (w_s along y-axis) and `EASpy` (w along x-axis). The 2D histogram is plotted only for 70° for visibility. The blue(green) ellipse describes the 68% enclosure around the mean value. Top and right panel shows the projection of the w and w_s-axis respectively. The black line marks the identity $w = w_s$.

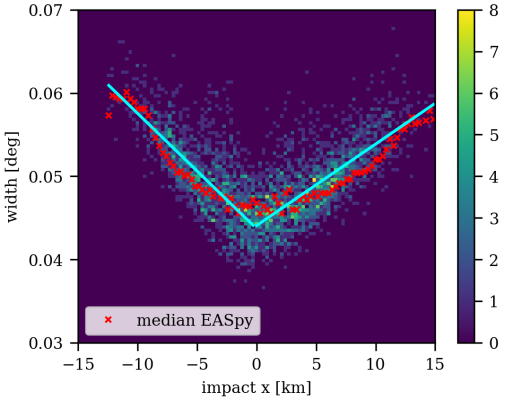

(b) Comparison of *width* parameter as a function of impact x-position for showers with zenith angle 80° between `sim_telarray` and `EASpy`. The 2D histogram shows only the values generated with `sim_telarray`, the red crosses mark the median values obtained with the `EASpy`, and the solid lines are derived by fitting a linear function to the median values of `sim_telarray` for $x \gtrsim 0$ and $x \lesssim 0$ respectively.

Figure 4.13: Comparison of *width* parameter between `EASpy` and `sim_telarray`.

The remarkable agreement between the *width* predicted using the simplified approach in `EASpy` and the full simulation encourages a further comparison of image parameters at different distances from the telescope to the shower impact position. In Fig. 4.13b, the *width* values for shower impact positions at a zenith angle of 80° along the x-coordinate in the observation plane are compared. The telescope is positioned at $x = y = 0$, and the shower moves from right to left. The two-dimensional histogram illustrates the distribution of w_s, while the median values of the w distribution for slices in x are indicated by red crosses. For easier comparison, the cyan line from a linear fit to the w_s distribution is superimposed.

Consistently observed in both simulations is the trend that as the distance d_{impact} between the telescope position and the shower impact position increases, the *width* value also increases. At first glance, this might seem counterintuitive, as one would expect the shower to appear smaller with increasing d_{impact}. However, from a geometrical point-of-view, the telescope will only capture photons at a larger angle relative to the shower axis as the distance d_{impact} increases. Consequently, the light observed at these distances originates from electrons with a large $\langle \theta_p \rangle$ (average angle between the momentum vector of the electron and the shower axis, see Sec. 4.1.7), which on average also have a greater distance from the shower axis.

The absolute value of the slope of the solid lines in Fig. 4.13b appears smaller for $x \gtrsim 0$ in comparison to $x \lesssim 0$. This can be explained by noting that for $x \gtrsim 0$ the shower maximum is farther from the telescope position than for $x \lesssim 0$. As a result, the shower is observed under smaller angles for $x \gtrsim 0$. Considering these explanations, it is noteworthy that the parametrization of the shower angle and its dependence on the radial distance to the shower axis proves to be sufficiently accurate to capture the interesting property of the *width* increasing with increasing distance to the observer.

4.2.2 Length distribution

In Fig. 4.14a, the distribution of the image *length* is presented for the two considered zenith angles of 70° in blue and 80° in green. In general, the distributions for both zenith angles show good agreement when considering the simplified approach. The slight tilt in the orientation of the blue ellipse is a result of a tail of images reconstructed with $l_s \gtrsim 0.18°$ for the `sim_telarray` distribution. The noticeable tilt of the green ellipse highlights the larger values of l_s found for $l \lesssim 0.11°$. This slight deviation can be explained by considering the differences in the image cleaning procedure. In `sim_telarray`, pixels with amplitudes below a threshold relative to the brightest pixel are removed, while in `EASpy` no imaging cleaning is applied (for a comparison of uncleaned images, see Fig. 4.16). Similar to the *width* distribution, the average value of the *length* decreases for larger zenith angle distances.

Equivalent to the discussion of the *width* parameter in Sec. 4.2.1, a comparison is made regarding the apparent *length* of images recorded at various positions of the shower core in the observer plane.

The result is provided in Fig. 4.14b for a zenith angle of 80°. As in Fig. 4.13b, the red crosses indicate the median values obtained with `EASpy`, while the superimposed solid lines represent the median values of `sim_telarray`.

The conclusions are comparable to those drawn from Fig. 4.13b: when d_{impact} is large, the telescope only registers photons with a large angle to the shower axis, resulting in an increase in the resulting *length* parameter. This pattern holds as long as the entire shower remains within the camera's field of view. However, once the shower images are truncated at the camera edges, the *length* values start to decrease (see in Fig. 4.14b for $x \lesssim -9\,\text{km}$ and $x \gtrsim 10\,\text{km}$). The consistent agreement between l and l_s demonstrates the validity of the simplified approach concerning the longitudinal development of the air shower.

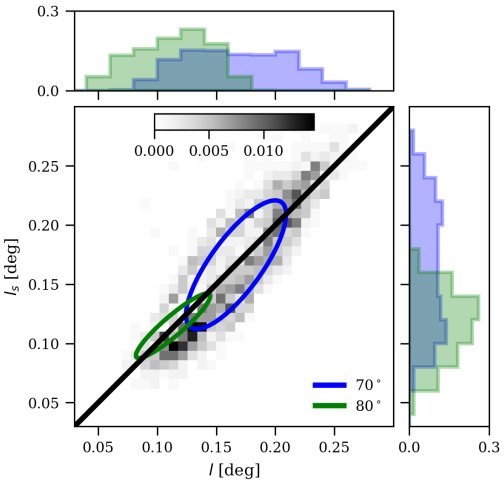

(a) Comparison of *length* parameter for showers with zenith angle 70°(80°) between `sim_telarray` (l along y-axis) and `EASpy` (l_s along x-axis). The 2D histogram is plotted only for 70° for visibility. The blue(green) ellipse describes the 68% enclosure around the mean value. Top and right panel show the projections of the l and l_s-axes respectively. The black line marks the identity $l = l_s$.

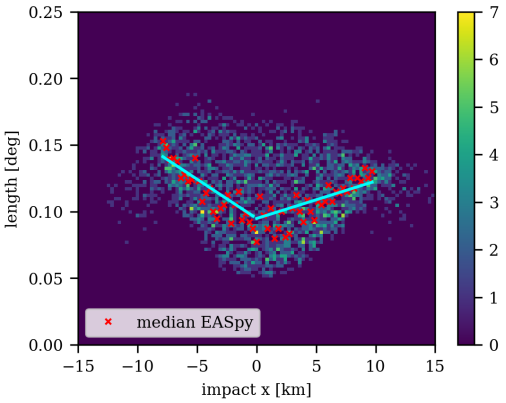

(b) Comparison of *length* parameter as a function of impact x-position for showers with zenith angle 80° between `sim_telarray` and `EASpy`. The 2D histogram shows only the values generated with `sim_telarray`, the red crosses mark the median values obtained with the `EASpy`, and the solid lines are derived by fitting a linear function to the median values of `sim_telarray` for $x \gtrsim 0$ and $x \lesssim 0$ respectively.

Figure 4.14: Comparison of *length* parameter between `EASpy` and `sim_telarray`.

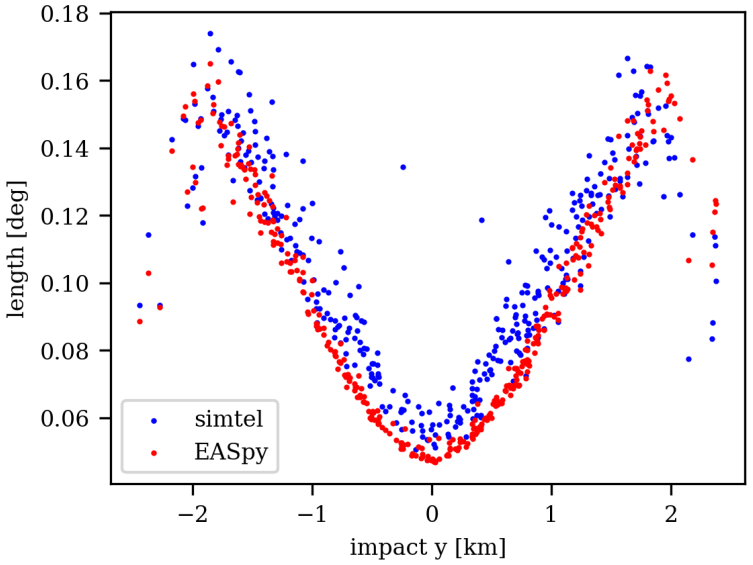

Figure 4.15: *length* values obtained with `EASpy` and `sim_telarray` for x positions of $-1\,\mathrm{km} < x < 1\,\mathrm{km}$.

A notable contrast between Fig. 4.13b and Fig. 4.14b is the more uniform spread of *length* values at any given x: in Fig. 4.13b, the difference between the maximum and minimum *width* values for $x \approx 0$ is approximately 0.01°, while the corresponding difference for the *length* values in Fig.4.14b is roughly 10 times higher ($\sim 0.1°$). Upon further investigation, this spread is related to a systematic increase in *length* with an increasing distance along the y-axis for a fixed x value (see Fig. 4.15). The evident explanation is the longitudinal development of the shower captured in the *length* parameter, in contrast to the *width* parameter which is primarily sensitive to the shower maximum.

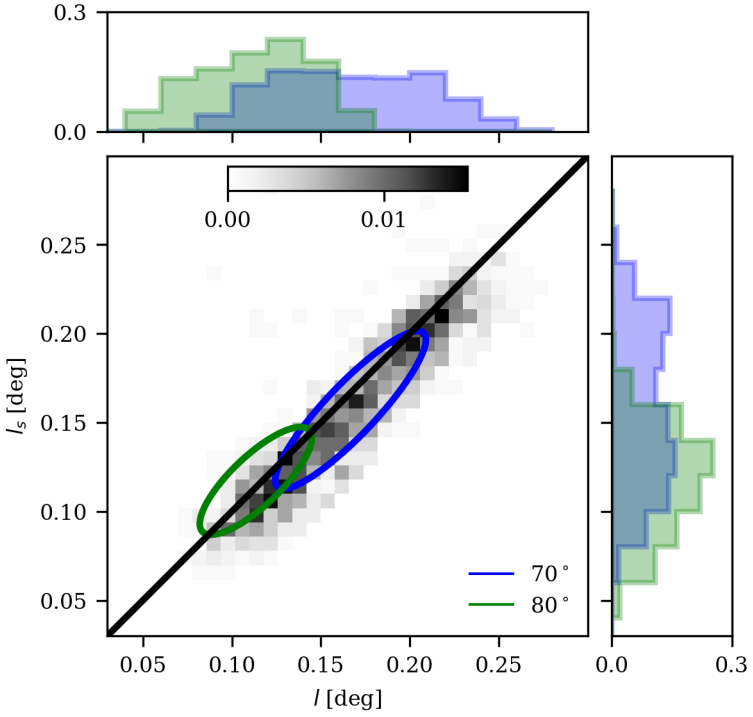

Figure 4.16: Same as in Fig. 4.14a but here using the uncleaned images from `sim_telarray`.

4.3 Photon ground distribution

Until now, the focus was on the Cherenkov light images recorded by a telescope observing the shower with its optical axis aligned parallel to the shower axis. In addition to Cherenkov light, fluorescence light is emitted isotropically and can be observed from various angles relative to the shower axis. In this case, the apparent brightness scales inversely with the square of the distance to the shower maximum. At small zenith angles, the maximum photon density of fluorescence coincides with that of Cherenkov light.

At larger zenith angles, there is a noticeable displacement between these positions. This displacement is evident in Fig. 4.17, where the photon density of fluorescence and

Cherenkov light on the ground (with ground level at a height of 1.8 km) is presented on a grid covering an area of 16 000 km^2 for an air shower with $E_\gamma = 10$ PeV at 80° zenith angle. To address atmospheric absorption for Cherenkov (fluorescence) photons, an averaged absorption is calculated from the shower maximum position to the ground level for a photon path with a zenith angle of 80° (0°), and this factor is applied to all Cherenkov (fluorescence) photons. The two peak positions are displaced by approximately 80 km. The peak position of the air fluorescence light pool aligns closely with the projected position of the shower maximum, while peak of the Cherenkov light pool is near to but not identical to the shower core position on the ground.

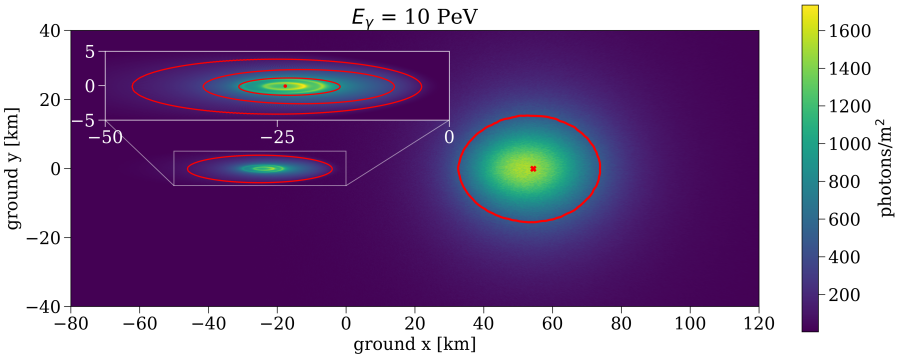

Figure 4.17: Cherenkov and fluorescence photon ground distribution for an air shower with zenith angle 80°. The fluorescence photon density is up-scaled by a factor of 5 to match the Cherenkov photon density. The red lines mark an iso-contour at a level of 100 photons/m^2 (here the fluorescence density is not up-scaled). Red cross marks the position of the shower maximum. Inset axis: Zoomed-in version of Cherenkov photon ground distribution. The dot marks the position of the impact, red lines indicate the iso-contours at a level of 100 photons/m^2, 350 photons/m^2 and 700 photons/m^2.

Indicated by the red ellipses are iso-contours corresponding to a photon surface density of 100 photons/m^2. It is noteworthy that, at larger zenith angles, there is clearly no observable contamination of Cherenkov light with fluorescence light. This effect was explored in [131] for a zenith angle of 30°, where the authors demonstrated that approximately 45% of the light recorded at PeV energies by a wide-angle detector at distances of about 1 km from the impact position would be due to atmospheric fluorescence emission.

The iso-contour for the fluorescence photon surface density has a circular shape, reflecting the isotropic nature of fluorescence emission. In contrast, the iso-contour for the Cherenkov case has a significant elongation in the x-direction compared to the y-direction by orders of magnitude. The inset-axis in Fig. 4.17 provides a zoomed-in version of the Cherenkov photon ground distribution, featuring three iso-contours (at 100, 350, and 700 photons/m^2) highlighting its complex structure. In proximity to the impact position, the two ring-like structures are directly linked to the minimum and maximum Cherenkov angle θ_{Ch} resulting from the superposition of Cherenkov light emission

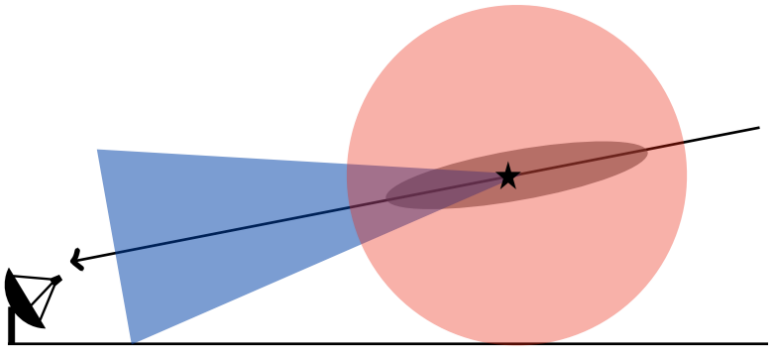

Figure 4.18: Sketch of the geometry properties for Cherenkov and fluorescence emission. The black star marks the shower maximum, the blue shaded area the Cherenkov emission cone and the red shaded area denotes isotropic fluorescence emission. The black line describes the shower axis and the arrow the direction of propagation of the shower.

throughout the entire shower development. Beyond the outer ring feature, the photon density experiences a rapid decline as this emission is primarily generated by electrons from the later stages of the shower development with a substantial angle relative to the shower axes. This decline is more pronounced for light reaching the ground on the far side of the impact position (to the left in Fig. 4.17), explained by the geometrical effect of projecting the photon density onto the ground (see Fig. 4.18).

Chapter 5

Summary and Outlook

The γ-ray sky provides a unique window into the most energetic events in the universe. By exploring the γ-ray sky, scientists can uncover answers to fundamental questions about the nature of cosmic phenomena and the underlying physics that govern these high energy processes. Despite nearly a century of dedicated research, the acceleration mechanism and the specific astrophysical objects responsible for the production of very high energy particles remain open questions. However, the discovery by the LHAASO experiment [107], [128] of γ-ray emission in the PeV energy range demonstrates the existence of galactic sources capable of accelerating particles to multi-PeV energies. This finding provides strong motivation to explore possibilities for observing γ-ray sources above energies of 100 TeV with Imaging Air Cherenkov Telescopes (IACTs).

High energy particles produce a cascade of secondary particles when they enter the atmosphere. The produced Cherenkov light from these 'extensive air showers' can be captured by IACTs in order to, e.g., deduce the direction or energy of the primary particle. With increasing energy of the primary particle, the sensitivity of IACTs to observe the produced Cherenkov light depends mainly on the collection area A_{eff}. The current generation of IACT arrays has been optimized for observations at moderate zenith angles ($\sim 30°$), where a collection area of the order of $\mathcal{O}(10^5)\,\mathrm{m}^2$ can be achieved. Nevertheless, even for a collection area as large as $A_{eff} = 1\,\mathrm{km}^2$, the expected photon rate above energies of 100 TeV from the Crab Nebula is less than one photon per 100 hours.

Performing observations at large zenith angles ($\geq 70°$) with IACTs can significantly increase the collection area to values of $A_{eff} > 1\,\mathrm{km}^2$. Even so, this increase in A_{eff} comes at the expense of increased column density of air due to a longer photon path to the telescope. While at moderate zenith angles the distance of the shower maximum, i.e., when the shower development has reached its maximum, to the telescope position is

$\sim 10\,\mathrm{km}$, this distance becomes 5 to 10 times as large at zenith angles $\geq 70°$. As a result, the Cherenkov photon density at ground level significantly diminishes for air showers at large zenith angles in contrast to the intensity from identical vertical air showers. Therefore, the desired properties of IACTs performing large zenith angle observations include a large reflector surface and a small pixel size.

In this thesis, the performance of H.E.S.S. CT5 - having the largest reflector surface of $R = 14\,\mathrm{m}$ in radius and at the same time the smallest pixel size of $\sim 0.07°$ of currently operating IACTs - at a zenith angle of 80° is explored. For this, γ-ray induced air showers, as well as proton and helium induced air showers, are simulated with `CORSIKA`. The detector response of H.E.S.S. CT5 to these air showers is simulated with the `sim_telarray` program, using the H.E.S.S. 'phase2D3' configuration. The derived image parameters are then employed to deduce the γ-hadron separation power, angular resolution, and energy resolution of H.E.S.S. CT5 at a zenith angle of 80° through the application of dedicated Random Forest Classifier and Random Forest Regressor.

This investigation revealed that for H.E.S.S. CT5 a quality factor Q of the order of $Q \sim 5$ can be achieved at a zenith angle of 80°. Furthermore, the angular resolution across energies $\geq 10\,\mathrm{TeV}$ is estimated to be $\theta_{68\%} = 0.12°$, while the angular resolution for energies of $\geq 100\,\mathrm{TeV}$ is $\theta_{68\%} \leq 0.1°$. Based on these results, H.E.S.S. CT5 performing large zenith angle observations is able to compete with LHAASO KM2A with respect to the angular resolution at energies $\geq 10\,\mathrm{TeV}$. The energy resolution proofed to be better than 18% at energies $\geq 10\,\mathrm{TeV}$.

An impressive collection area of the order of $A_{eff} \sim 5 - 6\,\mathrm{km}^2$ at 1 PeV after γ-hadron separation and direction cuts demonstrates the performance of a stand-alone telescope at a zenith angle of 80°. When comparing the achieved collection areas of H.E.S.S. CT5 at energies of $\geq 10\,\mathrm{TeV}$ to those of LHAASO KM2A, one may conclude that a single stand-alone telescope, performing large zenith angle observations, reaches competitive collection areas and even exceeds the performance of a kilometer squared array.

However, a zenith angle of 80° represents an obvious limitation when considering the possible observation time for a source. In order to quantify this restriction in observation time, the visibility in the zenith angle range of $79° < \theta < 81°$ at the H.E.S.S. site is calculated for 75 sources detected with LHAASO KM2A [128]. While the majority of the LHAASO KM2A sources have a visibility of ~ 25 hours per year at the H.E.S.S. site, a visibility of ≥ 100 hours per year can be achieved for three LHAASO KM2A sources. Furthermore, the sensitivity study of H.E.S.S. CT5 performing observations at a zenith angle of 80° revealed that for one of the LHAASO KM2A sources a significance of $\geq 5\,\sigma$ at energies of $\geq 10\,\mathrm{TeV}$ can be achieved using the 2024 observation window at the H.E.S.S. site.

One significant downside of Monte Carlo simulations, e.g., `CORSIKA`, is the increased computation time with higher primary particle energies, along with an increase in storage size. For a 1 PeV γ-ray induced air shower the computation time can be as high as 18 hours if the produced secondary electrons and positrons are tracked in the simulation up to energies of 1 MeV. If one is interested in studying the impact of fluorescence light at these primary γ-ray energies, low energy electrons and positrons can not be neglected, since the amount of produced fluorescence light scales with the deposited energy in the atmosphere.

In this thesis, a 3.5-dimensional simulation (comprising 2.5 spatial dimensions and 1 time dimension) of extensive air showers is presented. The simulation is based on parametrizations for electron-positron distributions [139] and their subsequent emission of fluorescence and Cherenkov light. The simulation tool, termed `EASpy` [129], employs a novel method in which the number of detected photons with an IACT is determined using a geometrical approach. This way, the resulting computation time can be reduced considerably in comparison to a ray-tracing approach. Additionally, `EASpy` is capable of simulating the detector response, i.e., the imaging of the simulated air shower.

In order to verify the proposed approach, the *width* and *length* parameters of Cherenkov air shower images at a zenith angle of 70° and 80° are compared between `EASpy` and a full simulation, i.e., `sim_telarray`. The comparison demonstrates excellent agreement for these imaging parameters. The proposed approach may motivate upcoming simulation tools since the computation time of `EASpy` does not scale with the energy of the primary particle.

Furthermore, the `EASpy` framework provides insights into the generation of air shower images and the distribution of light in the detector plane. This thesis outlines an effect not previously noted: with increasing impact distance, air shower images at large zenith angles exhibit a wider and longer appearance. This observed effect is linked to the interplay between the Cherenkov angle and the average angle of shower particles with respect to the shower axis. The effect is confirmed in the detailed simulations using `CORISKA/sim_telarray`. The distribution of light on the ground, as calculated by `EASpy`, reveals a distinct separation between the Cherenkov and fluorescence light pools. This aspect remains unexplored within the standard `CORSIKA` framework, presenting potential opportunities for future observational studies.

Appendix A

Fluorescence Parameters

In Table A.1 all necessary parameter values in order to evaluate $Y_{air}(\lambda, T, p, p_w)$ in Eq. 4.8 are provided. The parameter values are taken from [143], [144] and `ShowerModel`.

λ	$\frac{I_\lambda(T_0,p_0)}{I_{337}(T_0,p_0)}$	$PP0$	PPw	a
nm	$\times 10^{-2}$	hPa	hPa	-
296	5.16	18.50	0.00	0.00
298	2.77	17.30	0.00	0.00
302	0.41	21.00	0.00	0.00
308	1.44	21.00	0.00	0.00
312	7.24	18.70	0.00	0.00
314	11.05	12.27	1.20	-0.13
316	39.33	11.88	1.10	-0.19
318	0.46	21.00	0.00	0.00
327	0.80	19.00	0.00	0.00
329	3.80	20.70	0.00	0.00
331	2.15	16.90	0.00	0.00
334	4.02	15.50	0.00	0.00
337	100.0	15.89	1.28	-0.35
346	1.74	21.00	0.00	0.00
350	2.79	15.20	1.50	-0.38
354	21.35	12.70	1.27	-0.22
358	67.41	15.39	1.30	-0.35
366	1.13	21.00	0.00	0.00
367	0.54	19.00	0.00	0.00
371	4.97	14.80	1.30	-0.24
376	17.87	12.82	1.10	-0.17

381	27.20	16.51	1.40	-0.34
386	0.5	19.00	0.00	0.00
388	1.17	7.60	0.00	0.00
389	0.83	3.90	0.00	0.00
391	28.00	2.94	0.33	-0.79
394	3.36	13.70	1.20	-0.20
400	8.38	13.60	1.10	-0.20
405	8.07	17.80	1.50	-0.37
414	0.49	19.0	0.00	0.00
420	1.75	13.80	0.00	0.00
424	1.04	3.90	0.00	0.00
427	7.08	6.38	0.00	0.00
428	4.94	2.89	0.60	-0.54

Table A.1: Parameters for Fluorescence model. Reference atmospheric conditions for dry air are $p_0 = 800.0$ hPa and $T_0 = 293.0$ K. Reference yield of the 337 nm band is $Y_{air}(337, T_0, p_0) = 7.04$ photons/MeV. The table describes from left to right: wavelength λ in units of nm, relative intensity of each wavelength at reference atmospheric conditions, quenching pressure of dry air $PP0$ and quenching pressure of water vapor PPw in units of hPa and a parameter a which takes into account the temperature dependence.

Appendix B

Event Rates and Visibility for LHAASO Sources

The expected event rates for energies above 10 TeV and 100 TeV as well as the visibility at the H.E.S.S. site for all detected LHAASO KM2A sources [128] are provided in Tab. B.1. For convenience, the table also lists the spectral parameters and the position of the sources. The reader is redirected to [128] for the meaning of the suffix 'u' and '*' in the source name, e.g., 1LHAASO J0343+5254u*, and in the component, e.g., KM2A*.

Source name	Component	α	δ	N_0	Γ	$\geq 10\,\mathrm{TeV}$	$\geq 100\,\mathrm{TeV}$	visibility
1LHAASO J0007+5659u	KM2A	1.86	57.00	0.33±0.05	3.10±0.20	0.5	0.0	123.15
1LHAASO J0007+7303u	KM2A	1.91	73.07	3.41±0.27	3.40±0.12	5.9	0.2	0.0
1LHAASO J0056+6346u	KM2A	14.10	63.77	1.47±0.10	3.33±0.10	2.4	0.1	0.0
1LHAASO J0206+4302u	KM2A	31.70	43.05	0.24±0.03	2.62±0.16	0.3	0.0	38.7
1LHAASO J0212+4254u	KM2A	33.01	42.91	0.12±0.03	2.45±0.23	0.1	0.0	37.8
1LHAASO J0216+4237u	KM2A	34.10	42.63	0.18±0.03	2.58±0.17	0.2	0.0	36.8
1LHAASO J0249+6022	KM2A	42.39	60.37	0.93±0.09	3.82±0.18	2.3	0.0	0.0
1LHAASO J0339+5307	KM2A	54.79	53.13	0.58±0.06	3.64±0.16	1.2	0.0	75.4
1LHAASO J0343+5254u*	KM2A	55.79	52.91	1.07±0.07	3.53±0.10	2.0	0.1	72.1
1LHAASO J0359+5406	KM2A	59.78	54.10	0.85±0.06	3.84±0.15	2.1	0.0	88.4
1LHAASO J0428+5531*	KM2A	66.63	54.63	0.54±0.06	3.45±0.19	1.0	0.0	99.15
1LHAASO J0534+3533	KM2A	83.53	35.56	0.19±0.03	4.89±0.53	1.4	0.0	27.25
1LHAASO J0534+2200u	KM2A	83.61	22.04	6.23±0.10	3.19±0.03	9.3	0.5	22.05
1LHAASO J0542+2311u	KM2A	85.71	23.20	2.93±0.12	3.74±0.09	6.7	0.1	22.0
1LHAASO J0622+3754	KM2A	95.50	37.90	1.42±0.07	3.68±0.10	3.1	0.1	30.1
1LHAASO J0631+1040	KM2A	97.77	10.67	0.54±0.06	3.33±0.16	0.9	0.0	19.0
1LHAASO J0634+1741u	KM2A	98.57	17.69	4.42±0.15	3.69±0.06	9.7	0.2	20.2
1LHAASO J0635+0619	KM2A	98.76	6.33	0.94±0.10	3.67±0.18	2.0	0.0	18.45
1LHAASO J0703+1405	KM2A	105.83	14.10	6.30±0.23	3.98±0.08	18.0	0.2	19.4
1LHAASO J1740+0948u	KM2A	265.03	9.81	0.41±0.04	3.13±0.15	0.6	0.0	20.5
1LHAASO J1809-1918u	KM2A	272.38	-19.30	9.46±1.27	3.51±0.26	17.8	0.5	19.25
1LHAASO J1813-1245	KM2A	273.36	-12.75	1.42±0.27	3.66±0.34	3.0	0.1	18.8
1LHAASO J1814-1719u*	KM2A	273.27	-17.89	4.20±0.75	3.49±0.31	7.8	0.2	19.35
1LHAASO J1814-1636u	KM2A	273.72	-16.62	11.90±1.30	3.74±0.20	27.2	0.5	19.25
1LHAASO J1825-1418	KM2A	276.25	-14.00	7.26±0.98	3.53±0.18	13.9	0.4	18.95
1LHAASO J1825-1256u	KM2A	276.44	-12.94	5.08±0.42	3.33±0.13	8.3	0.3	18.95
1LHAASO J1825-1337u	KM2A	276.45	-13.63	10.10±0.61	3.28±0.09	16.0	0.7	19.0
1LHAASO J1831-1007u*	KM2A	277.81	-9.83	2.56±0.27	3.30±0.14	4.1	0.2	18.9
1LHAASO J1831-1028	KM2A	277.84	-10.48	5.39±0.60	3.53±0.15	10.3	0.3	19.0
1LHAASO J1834-0831	KM2A	278.44	-8.38	1.55±0.21	3.63±0.21	3.2	0.1	19.0
1LHAASO J1837-0654u	KM2A	279.31	-6.86	3.06±0.21	3.70±0.12	6.7	0.1	19.15
1LHAASO J1839-0548u	KM2A	279.79	-5.81	3.03±0.20	3.24±0.09	4.7	0.2	19.3
1LHAASO J1841-0519	KM2A*	280.21	-5.23	2.10±0.25	3.85±0.20	5.3	0.1	19.35
1LHAASO J1843-0335u	KM2A	280.91	-3.60	6.19±0.20	3.44±0.06	11.0	0.3	19.7
1LHAASO J1848-0153u	KM2A*	282.02	-1.78	3.29±0.17	3.69±0.10	7.2	0.1	19.95
1LHAASO J1848-0001u	KM2A	282.19	-0.02	1.64±0.10	2.75±0.07	1.9	0.2	20.1
1LHAASO J1850-0004u*	KM2A	282.89	-0.07	1.86±0.12	3.15±0.09	2.7	0.1	20.05
1LHAASO J1852+0050u*	KM2A*	283.10	0.84	3.22±0.22	3.64±0.12	6.7	0.1	20.5
1LHAASO J1857+0203u	KM2A	284.38	2.06	1.78±0.10	3.31±0.10	2.9	0.1	20.55
1LHAASO J1858+0330	KM2A*	284.59	3.51	1.56±0.10	3.78±0.15	3.7	0.1	20.8
1LHAASO J1908+0615u	KM2A	287.05	6.26	6.86±0.16	2.82±0.03	8.4	0.8	21.2
1LHAASO J1910+0516*	KM2A	287.55	5.28	0.57±0.08	3.15±0.18	0.8	0.0	20.7
1LHAASO J1912+1014u	KM2A*	288.38	10.50	1.52±0.10	3.26±0.11	2.4	0.1	21.6
1LHAASO J1913+0501	KM2A	288.28	5.03	0.45±0.06	3.30±0.18	0.7	0.0	20.6
1LHAASO J1914+1150u	KM2A*	288.73	11.84	0.79±0.06	3.41±0.13	1.4	0.0	21.95
1LHAASO J1919+1556	KM2A	289.78	15.93	0.24±0.04	4.71±0.53	1.5	0.0	22.6
1LHAASO J1922+1403	KM2A	290.73	14.11	0.45±0.04	3.79±0.20	1.1	0.0	22.0
1LHAASO J1924+1609	KM2A*	290.53	15.71	1.35±0.17	3.61±0.22	2.8	0.1	22.65
1LHAASO J1928+1813u	KM2A	292.07	18.23	2.48±0.16	3.24±0.08	3.8	0.2	23.05
1LHAASO J1928+1746u	KM2A	292.17	17.89	0.72±0.07	3.10±0.12	1.0	0.1	22.85
1LHAASO J1929+1846u*	KM2A	292.04	18.97	0.64±0.06	3.11±0.12	0.9	0.1	23.25
1LHAASO J1931+1653	KM2A	292.79	16.90	0.22±0.04	3.15±0.25	0.3	0.0	22.65
1LHAASO J1937+2128	KM2A*	294.32	21.48	1.87±0.17	3.40±0.15	3.2	0.1	24.15
1LHAASO J1945+2424*	KM2A	297.42	23.97	0.40±0.05	3.93±0.30	1.1	0.0	25.05
1LHAASO J1951+2608	KM2A*	297.94	26.15	1.13±0.12	3.43±0.17	2.0	0.1	26.4
1LHAASO J1954+2836u	KM2A	298.55	28.60	0.42±0.05	2.92±0.14	0.5	0.0	28.3
1LHAASO J1956+2921	KM2A	298.84	28.92	1.62±0.14	3.42±0.12	2.8	0.1	28.55
1LHAASO J1959+2846u	KM2A	299.78	28.78	0.84±0.07	2.90±0.10	1.1	0.1	28.4
1LHAASO J1959+1129u	KM2A	299.82	11.49	0.27±0.04	2.69±0.17	0.3	0.0	19.7
1LHAASO J2002+3244u	KM2A	300.60	32.64	0.15±0.03	2.70±0.22	0.2	0.0	30.75
1LHAASO J2005+3415*	KM2A	301.81	33.87	0.56±0.05	3.79±0.21	1.3	0.0	31.15
1LHAASO J2005+3050	KM2A	301.45	30.85	0.46±0.05	3.62±0.21	0.9	0.0	29.7
1LHAASO J2018+3643u	KM2A	304.65	36.72	3.93±0.11	3.46±0.05	7.1	0.2	32.25
1LHAASO J2020+4034	KM2A	305.20	40.43	0.35±0.05	3.56±0.23	0.7	0.0	34.4
1LHAASO J2020+3649u	KM2A	305.23	36.82	2.29±0.09	3.31±0.06	3.7	0.2	32.3
1LHAASO J2027+3657	KM2A	306.88	36.95	0.50±0.06	3.21±0.17	0.8	0.0	32.25
1LHAASO J2028+3352	KM2A	307.21	33.88	1.61±0.19	3.38±0.19	2.7	0.1	30.1
1LHAASO J2031+4052u*	KM2A	308.14	40.88	0.08±0.02	2.13±0.27	0.1	0.0	35.4
1LHAASO J2031+4127u	KM2A	307.95	41.46	2.56±0.08	3.45±0.06	4.6	0.1	36.0
1LHAASO J2047+4434	KM2A*	311.92	44.58	0.46±0.06	3.17±0.20	0.7	0.0	42.85
1LHAASO J2108+5153u	KM2A	317.10	51.90	1.38±0.07	2.97±0.07	1.8	0.1	65.4
1LHAASO J2200+5643u	KM2A	330.08	56.73	1.70±0.10	3.44±0.10	3.0	0.1	150.4
1LHAASO J2228+6100u	KM2A	337.01	61.00	4.76±0.14	2.95±0.04	6.2	0.5	0.0
1LHAASO J2229+5927u	KM2A*	337.88	59.55	4.43±0.36	3.53±0.11	8.5	0.2	0.0
1LHAASO J2238+5900	KM2A	339.54	59.00	2.03±0.12	3.55±0.09	3.9	0.1	0.0

Table B.1: α and δ J2000 RA. and Dec. in deg, N_0 in units of $10^{-16}\,\mathrm{cm^{-2}\,s^{-1}\,TeV^{-1}}$, event rates in events/hour, visibility in hour per year.

Appendix C

H.E.S.S. Large Zenith Angle Observations Outlook

C.1 H.E.S.S. CT1-5 divergent pointing

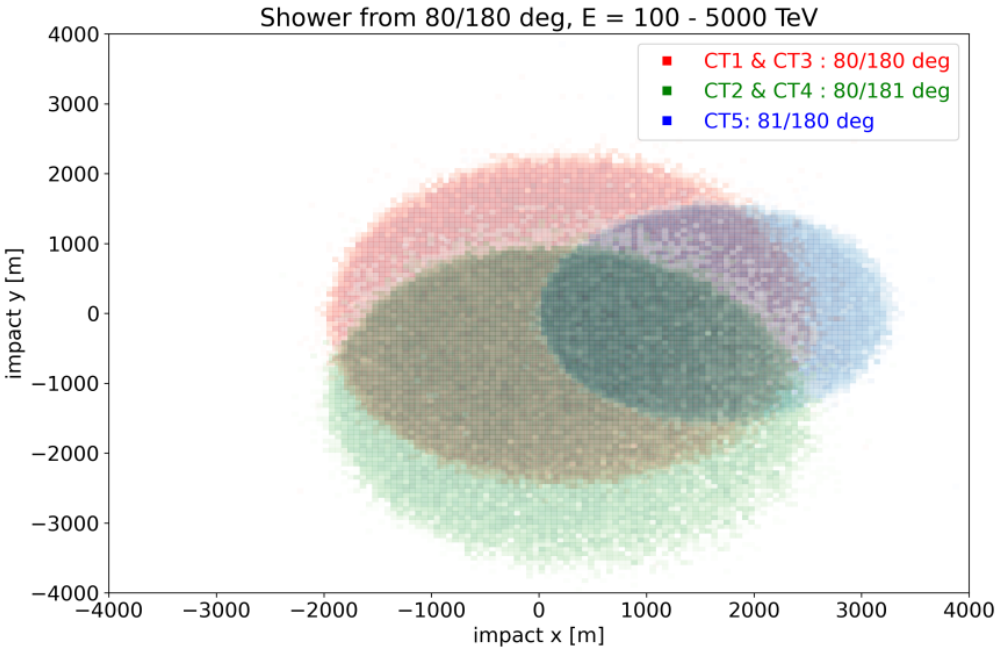

Figure C.1: Two-dimensional histogram for triggered events in the plane perpendicular to the shower axis after a distance cut (CoG-Center) of 1.67° for CT1-CT4 and 1° for CT5. The direction of the shower and the pointing of the telescopes are indicated as zenith/azimuth.

In Fig. C.1 the achievable effective area is indicated after a distance cut (CoG-Center) of 1° for CT5 and 1.67° for CT1-4 for γ-ray energies in the range of 100 TeV and 5000 TeV.

Here, a divergent pointing approach is illustrated, where CT1 and CT3 are pointing parallel to the air shower, while CT2 and CT4 are pointing with a 1° offset in azimuth and CT5 with a 1° offset in zenith with respect to the direction of the air shower. Note the significantly larger area enclosed by CT1-4 compared to CT5.

C.2 H.E.S.S. CT1-5 effective area at 70° and 80° zenith angle

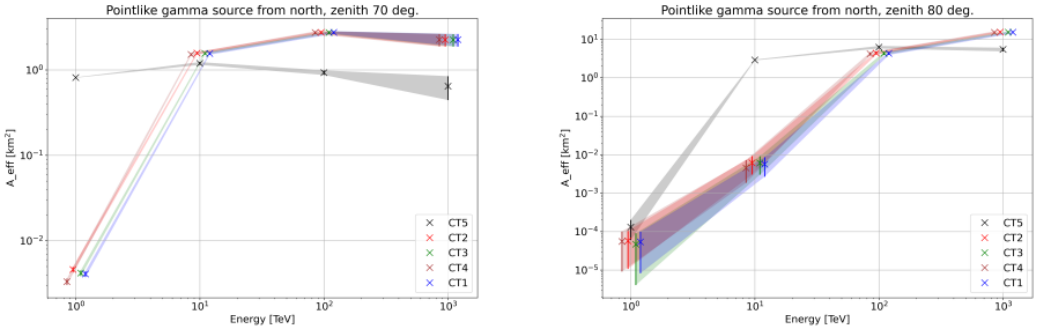

Figure C.2: Effective area A_{eff} after a distance cut (CoG-Center) of 1.67° for CT1-CT4 and 1° for CT5 for on-axis observation at a zenith angle of 70° (left panel) and 80° (right panel).

The effective area at a zenith angle of 70° and 80° for CT1-5 after distance cuts (CoG-Center) is presented in Fig. C.2. Remarkably, even after a distance cut, an effective area $A_{eff} > 10\,\mathrm{km}^2$ can be achieved for CT1-4 at 1 PeV and a zenith angle of 80°. Note, how the location of the peak effective area for CT5 shifts from 100 TeV at 80° zenith angle to 10 TeV at 70° zenith angle. Additionally, an effective area close to $\sim 1\,\mathrm{km}^2$ can be achieved for CT5 at 1 TeV and a zenith angle of 70°.

C.3 H.E.S.S. CT5 exposure map in the zenith angle range of $70° - 81°$

The one year exposure map at 100 TeV for CT5 in the zenith angle range from 70° to 81° together with the positions of the LHAASO sources in [107] is shown in Fig. C.3. The source with the highest possible exposure of $\sim 10^{3.5}$ hr km^2 is LHAASO J2108+5157, which makes it a promising candidate to observe under very large zenith angles with H.E.S.S. CT5.

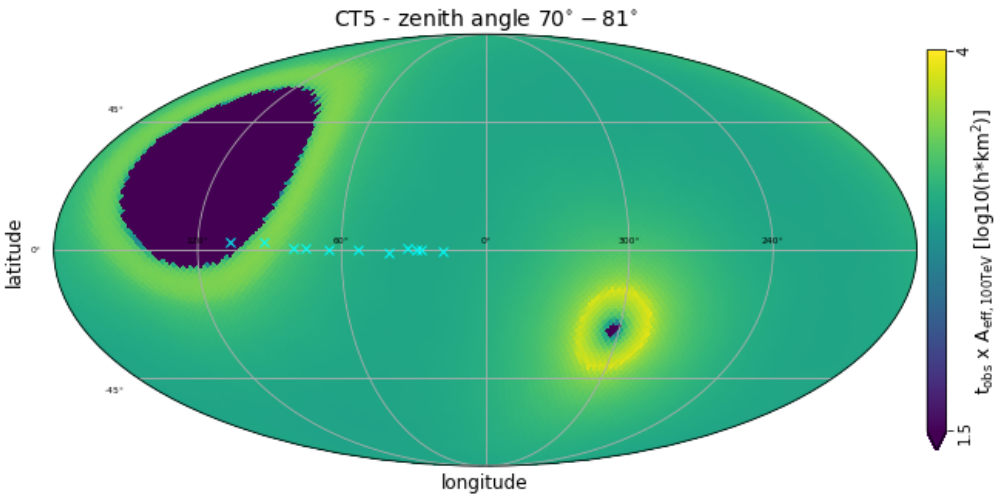

Figure C.3: One year exposure map at 100 TeV for CT5 in the zenith angle range of 70° to 81°. The cyan crosses mark the position of the sources listed in [107].

List of Figures

List of Tables

Abbreviations

VHE	Very High Energy
EAS	Extensive Air Shower
AGASA	Akeno Giant Air Shower Array
AGN	Active Galactic Nuclei
R.A.	Right Ascension
ISM	Interstellar Medium
IC	Inverse Compton
CMB	Cosmic Microwave Background
SNR	Supernova Remnant
GRB	Gamma-Ray Burst
H.E.S.S.	High Energy Stereoscopic System
CTA	Cherenkov Telescope Array
PWN	Pulsar Wind Nebula
SMBH	Supermassive Black Hole
IACT	Imaging Air Cherenkov Telescope
LZA	Large Zenith Angle
UV	Ultraviolet
PMT	Photomultiplier Tube
GAPD	Geiger-Mode Avalanche Photodiode
CoG	Center of Gravity
SST	Small-Sized Telescope
MST	Medium-Sized Telescope
LST	Large-Sized Telescope
LHAASO	Large High Altitude Air Shower Observatory
KM2A	Kilometer Squared Array
MC	Monte Carlo
PSF	Point Spread Function
QE	Quantum Efficiency

References

[1] P. Carlson. "A century of cosmic rays". In: *Physics Today* 65.2 (Feb. 2012), pp. 30–36. ISSN: 0031-9228. DOI: 10.1063/PT.3.1437. eprint: https://pubs.aip.org/physicstoday/article-pdf/65/2/30/10095294/30_1_online.pdf. URL: https://doi.org/10.1063/PT.3.1437.

[2] V. F. Hess. "Über Beobachtungen der durchdringenden Strahlung bei sieben Freiballonfahrten". In: *Phys. Z.* 13 (1912), pp. 1084–1091.

[3] R. A. MILLIKAN and G. H. CAMERON. "New Results on Cosmic Rays". In: *Nature* 121.3036 (Jan. 1928), pp. 19–26. ISSN: 1476-4687. DOI: 10.1038/121019a0. URL: https://doi.org/10.1038/121019a0.

[4] C. D. Anderson. "The Positive Electron". In: *Phys. Rev.* 43 (6 Mar. 1933), pp. 491–494. DOI: 10.1103/PhysRev.43.491. URL: https://link.aps.org/doi/10.1103/PhysRev.43.491.

[5] P. A. M. Dirac. "The quantum theory of the electron". In: *Proceedings of the Royal Society of London. Series A, Containing Papers of a Mathematical and Physical Character* 117.778 (Feb. 1928), pp. 610–624. DOI: 10.1098/rspa.1928.0023. URL: https://doi.org/10.1098%2Frspa.1928.0023.

[6] S. Chandrasekhar. "The Maximum Mass of Ideal White Dwarfs". In: ApJ 74 (July 1931), p. 81. DOI: 10.1086/143324.

[7] S. H. Neddermeyer and C. D. Anderson. "Note on the Nature of Cosmic-Ray Particles". In: *Phys. Rev.* 51 (10 May 1937), pp. 884–886. DOI: 10.1103/PhysRev.51.884. URL: https://link.aps.org/doi/10.1103/PhysRev.51.884.

[8] B. Rossi. "Über die Eigenschaften der durchdringenden Korpuskularstrahlung im Meeresniveau". In: *Zeitschrift fur Physik* 82.3-4 (Mar. 1933), pp. 151–178. DOI: 10.1007/BF01341486.

[9] H. Bethe and W. Heitler. "On the Stopping of Fast Particles and on the Creation of Positive Electrons". In: *Proceedings of the Royal Society of London Series A* 146.856 (Aug. 1934), pp. 83–112. DOI: 10.1098/rspa.1934.0140.

[10] P. Auger, P. Ehrenfest, R. Maze, J. Daudin, and R. A. Fréon. "Extensive Cosmic-Ray Showers". In: *Reviews of Modern Physics* 11.3-4 (July 1939), pp. 288–291. DOI: 10.1103/RevModPhys.11.288.

[11] E. Fermi. "On the Origin of the Cosmic Radiation". In: *Phys. Rev.* 75 (8 Apr. 1949), pp. 1169–1174. DOI: 10.1103/PhysRev.75.1169. URL: https://link.aps.org/doi/10.1103/PhysRev.75.1169.

[12] A. R. Bell. "The acceleration of cosmic rays in shock fronts - I." In: MNRAS 182 (Jan. 1978), pp. 147–156. DOI: 10.1093/mnras/182.2.147.

[13] R. D. Blandford and J. P. Ostriker. "Particle acceleration by astrophysical shocks." In: ApJ 221 (Apr. 1978), pp. L29–L32. DOI: 10.1086/182658.

[14] T. Inoue, R. Yamazaki, S.-i. Inutsuka, and Y. Fukui. "Toward Understanding the Cosmic-Ray Acceleration at Young Supernova Remnants Interacting with Interstellar Clouds: Possible Applications to RX J1713.7-3946". In: ApJ 744.1, 71 (Jan. 2012), p. 71. DOI: 10.1088/0004-637X/744/1/71. arXiv: 1106.3080 [astro-ph.HE].

[15] V. N. Zirakashvili and F. A. Aharonian. "Nonthermal Radiation of Young Supernova Remnants: The Case of RX J1713.7-3946". In: ApJ 708.2 (Jan. 2010), pp. 965–980. DOI: 10.1088/0004-637X/708/2/965. arXiv: 0909.2285 [astro-ph.HE].

[16] R. Indebetouw, M. Matsuura, E. Dwek, et al. "Dust Production and Particle Acceleration in Supernova 1987A Revealed with ALMA". In: ApJ 782.1, L2 (Feb. 2014), p. L2. DOI: 10.1088/2041-8205/782/1/L2. arXiv: 1312.4086 [astro-ph.SR].

[17] W. Baade and F. Zwicky. "Cosmic Rays from Super-novae". In: *Proceedings of the National Academy of Science* 20.5 (May 1934), pp. 259–263. DOI: 10.1073/pnas.20.5.259.

[18] I. S. Bowen, R. A. Millikan, and H. V. Neher. "New High-Altitude Study of Cosmic-Ray Bands and a New Determination of Their Total Energy Content". In: *Phys. Rev.* 44 (4 Aug. 1933), pp. 246–252. DOI: 10.1103/PhysRev.44.246. URL: https://link.aps.org/doi/10.1103/PhysRev.44.246.

[19] R. M. Tennent. "The Haverah Park extensive air shower array". In: *Proceedings of the Physical Society* 92.3 (Nov. 1967), p. 622. DOI: 10.1088/0370-1328/92/3/315. URL: https://dx.doi.org/10.1088/0370-1328/92/3/315.

[20] N. Chiba, K. Hashimoto, N. Hayashida, et al. "Akeno Giant Air Shower Array (AGASA) covering 100 km2 area". In: *Nuclear Instruments and Methods in Physics Research Section A: Accelerators, Spectrometers, Detectors and Associated Equipment* 311.1 (1992), pp. 338–349. ISSN: 0168-9002. DOI: https://doi.org/10.1016/0168-9002(92)90882-5. URL: https://www.sciencedirect.com/science/article/pii/0168900292908825.

[21] J. A. et al. "Properties and performance of the prototype instrument for the Pierre Auger Observatory". In: *Nuclear Instruments and Methods in Physics Research Section A: Accelerators, Spectrometers, Detectors and Associated Equipment* 523.1 (2004), pp. 50–95. ISSN: 0168-9002. DOI: https://doi.org/10.1016/j.nima.2003.12.012. URL: https://www.sciencedirect.com/science/article/pii/S0168900203033497.

[22] J. A. et al. "Correlation of the highest-energy cosmic rays with the positions of nearby active galactic nuclei". In: *Astroparticle Physics* 29.3 (Apr. 2008), pp. 188–204. DOI: 10.1016/j.astropartphys.2008.01.002. URL: https://doi.org/10.1016%2Fj.astropartphys.2008.01.002.

[23] A. A. et al. "Observation of a large-scale anisotropy in the arrival directions of cosmic rays above 8 × 10¡sup¿18¡/sup¿ eV". In: *Science* 357.6357 (2017), pp. 1266–1270. DOI: 10.1126/science.aan4338. eprint: https://www.science.org/doi/pdf/10.1126/science.aan4338. URL: https://www.science.org/doi/abs/10.1126/science.aan4338.

[24] A. A. et al. "Large-scale Cosmic-Ray Anisotropies above 4 EeV Measured by the Pierre Auger Observatory". In: *The Astrophysical Journal* 868.1 (Nov. 2018), p. 4. DOI: 10.3847/1538-4357/aae689. URL: https://dx.doi.org/10.3847/1538-4357/aae689.

[25] K. Greisen. "End to the Cosmic-Ray Spectrum?" In: *Phys. Rev. Lett.* 16 (17 Apr. 1966), pp. 748–750. DOI: 10.1103/PhysRevLett.16.748. URL: https://link.aps.org/doi/10.1103/PhysRevLett.16.748.

[26] G. T. Zatsepin and V. A. Kuz'min. "Upper Limit of the Spectrum of Cosmic Rays". In: *Soviet Journal of Experimental and Theoretical Physics Letters* 4 (Aug. 1966), p. 78.

[27] V. L. Ginzburg and S. I. Syrovatskii. *The Origin of Cosmic Rays*. 1964.

[28] N. Tomassetti. "Origin of the Cosmic-Ray Spectral Hardening". In: ApJ 752.1, L13 (June 2012), p. L13. DOI: 10.1088/2041-8205/752/1/L13. arXiv: 1204.4492 [astro-ph.HE].

[29] P. Blasi. "The origin of galactic cosmic rays". In: *The Astronomy and Astrophysics Review* 21.1 (Nov. 2013). DOI: 10.1007/s00159-013-0070-7. URL: https://doi.org/10.1007%2Fs00159-013-0070-7.

[30] R. L. Workman et al. "Review of Particle Physics". In: *PTEP* 2022 (2022), p. 083C01. DOI: 10.1093/ptep/ptac097.

[31] A. e. a. Aab. "Depth of maximum of air-shower profiles at the Pierre Auger Observatory. I. Measurements at energies above $10^{17.8}$ eV". In: *Phys. Rev. D* 90 (12 Dec. 2014), p. 122005. DOI: 10.1103/PhysRevD.90.122005. URL: https://link.aps.org/doi/10.1103/PhysRevD.90.122005.

[32] L. F. Burlaga, N. F. Ness, D. A. Gurnett, and W. S. Kurth. "Evidence for a Shock in Interstellar Plasma: Voyager 1". In: ApJ 778.1, L3 (Nov. 2013), p. L3. DOI: 10.1088/2041-8205/778/1/L3.

[33] J. L. Han, R. N. Manchester, A. G. Lyne, G. J. Qiao, and W. van Straten. "Pulsar Rotation Measures and the Large-Scale Structure of the Galactic Magnetic Field". In: ApJ 642.2 (May 2006), pp. 868–881. DOI: 10.1086/501444. arXiv: astro-ph/0601357 [astro-ph].

[34] Taylor, A. M., Vovk, I., and Neronov, A. "Extragalactic magnetic fields constraints from simultaneous GeV-TeV observations of blazars". In: *A&A* 529 (2011), A144. DOI: 10.1051/0004-6361/201116441. URL: https://doi.org/10.1051/0004-6361/201116441.

[35] P. Mészáros, D. B. Fox, C. Hanna, and K. Murase. "Multi-messenger astrophysics". In: *Nature Reviews Physics* 1.10 (Oct. 2019), pp. 585–599. ISSN: 2522-5820. DOI: 10.1038/s42254-019-0101-z. URL: https://doi.org/10.1038/s42254-019-0101-z.

[36] E. Feenberg and H. Primakoff. "Interaction of Cosmic-Ray Primaries with Sunlight and Starlight". In: *Phys. Rev.* 73 (5 Mar. 1948), pp. 449–469. DOI: 10.1103/PhysRev.73.449. URL: https://link.aps.org/doi/10.1103/PhysRev.73.449.

[37] M. S. Longair. "Interactions of high energy photons". In: *High Energy Astrophysics*. 3rd ed. Cambridge University Press, 2011, pp. 228–278. DOI: 10.1017/CBO9780511778346.010.

[38] O. KLEIN and Y. NISHINA. "The Scattering of Light by Free Electrons according to Dirac's New Relativistic Dynamics". In: *Nature* 122.3072 (Sept. 1928), pp. 398–399. ISSN: 1476-4687. DOI: 10.1038/122398b0. URL: https://doi.org/10.1038/122398b0.

[39] F. A. Aharonian and A. M. Atoyan. "Broad-band diffuse gamma ray emission of the galactic disk". In: A&A 362 (Oct. 2000), pp. 937–952. DOI: 10.48550/arXiv.astro-ph/0009009. arXiv: astro-ph/0009009 [astro-ph].

[40] S. R. Kelner, F. A. Aharonian, and V. V. Bugayov. "Energy spectra of gamma rays, electrons, and neutrinos produced at proton-proton interactions in the very high energy regime". In: *Phys. Rev. D* 74 (3 Aug. 2006), p. 034018. DOI: 10.1103/PhysRevD.74.034018. URL: https://link.aps.org/doi/10.1103/PhysRevD.74.034018.

[41] M. A. et al. "Detection of the Characteristic Pion-Decay Signature in Supernova Remnants". In: *Science* 339.6121 (Feb. 2013), pp. 807–811. DOI: 10.1126/science.1231160. URL: https://doi.org/10.1126%2Fscience.1231160.

[42] A. M. Hillas. "The Origin of Ultra-High-Energy Cosmic Rays". In: *Annual Review of Astronomy and Astrophysics* 22.1 (1984), pp. 425–444. DOI: 10.1146/annurev.aa.22.090184.002233. eprint: https://doi.org/10.1146/annurev.aa.22.090184.002233. URL: https://doi.org/10.1146/annurev.aa.22.090184.002233.

[43] F. Fraschetti. "On the acceleration of ultra-high-energy cosmic rays". In: *Philosophical Transactions of the Royal Society A: Mathematical, Physical and Engineering Sciences* 366.1884 (Sept. 2008), pp. 4417–4428. DOI: 10.1098/rsta.2008.0204. URL: https://doi.org/10.1098%2Frsta.2008.0204.

[44] H. Collaboration. "The supernova remnant W49B as seen with H.E.S.S. and Fermi-LAT". In: *Astronomy &amp Astrophysics* 612 (Apr. 2018), A5. DOI: 10.1051/0004-6361/201527843. URL: https://doi.org/10.1051%2F0004-6361%2F201527843.

[45] H. Collaboration. "H.E.S.S. observations of RX J1713.7-3946 with improved angular and spectral resolution: Evidence for gamma-ray emission extending beyond the X-ray emitting shell". In: *Astronomy &amp Astrophysics* 612 (Apr. 2018), A6. DOI: 10.1051/0004-6361/201629790. URL: https://doi.org/10.1051%2F0004-6361%2F201629790.

[46] H. Collaboration. "Primary particle acceleration above 100 TeV in the shell-type supernova remnant RX J1713.7-3946 with deep HESS observations". In: *Astronomy &amp Astrophysics* 464.1 (Nov. 2006), pp. 235–243. DOI: 10.1051/0004-6361:20066381. URL: https://doi.org/10.1051%2F0004-6361%3A20066381.

[47] R. N. Manchester, G. B. Hobbs, A. Teoh, and M. Hobbs. "The ATNF Pulsar Catalogue". In: (2004). DOI: 10.1086/428488. eprint: arXiv:astro-ph/0412641.

[48] P. Meszaros. *High-Energy Radiation from Magnetized Neutron Stars*. The University of Chicago Press, 1992.

[49] W. Baade and F. Zwicky. "On Super-novae". In: *Proceedings of the National Academy of Science* 20.5 (May 1934), pp. 254–259. DOI: 10.1073/pnas.20.5.254.

[50] A. Hewish, S. J. Bell, J. D. H. Pilkington, P. F. Scott, and R. A. Collins. "Observation of a Rapidly Pulsating Radio Source". In: Nature 217.5130 (Feb. 1968), pp. 709–713. DOI: 10.1038/217709a0.

[51] T. GOLD. "Rotating Neutron Stars as the Origin of the Pulsating Radio Sources". In: *Nature* 218.5143 (May 1968), pp. 731–732. ISSN: 1476-4687. DOI: 10.1038/218731a0. URL: https://doi.org/10.1038/218731a0.

[52] F. PACINI. "Rotating Neutron Stars, Pulsars and Supernova Remnants". In: *Nature* 219.5150 (July 1968), pp. 145–146. ISSN: 1476-4687. DOI: 10.1038/219145a0. URL: https://doi.org/10.1038/219145a0.

[53] R. N. Manchester. *Pulsar glitches and their impact on neutron-star astrophysics*. 2018. eprint: arXiv:1801.04332.

[54] M. Yu, R. N. Manchester, G. Hobbs, et al. "Detection of 107 glitches in 36 southern pulsars". In: MNRAS 429.1 (Feb. 2013), pp. 688–724. DOI: 10.1093/mnras/sts366. arXiv: 1211.2035 [astro-ph.HE].

[55] V. M. Kaspi, M. S. E. Roberts, and A. K. Harding. *Isolated Neutron Stars*. 2004. eprint: arXiv:astro-ph/0402136.

[56] D. A. S. et al. *The Third Fermi Large Area Telescope Catalog of Gamma-ray Pulsars*. 2023. arXiv: 2307.11132 [astro-ph.HE].

[57] H. Collaboration. "Measurement of the Crab Nebula Spectrum Past 100 TeV with HAWC". In: ApJ 881.2, 134 (Aug. 2019), p. 134. DOI: 10.3847/1538-4357/ab2f7d. arXiv: 1905.12518 [astro-ph.HE].

[58] H. E. S. S. Collaboration. "Resolving the Crab pulsar wind nebula at tera-electronvolt energies". In: *Nature Astronomy* 4 (Feb. 2020), pp. 167–173. DOI: 10.1038/s41550-019-0910-0. arXiv: 1909.09494 [astro-ph.HE].

[59] T. L. Collaboration. "Peta–electron volt gamma-ray emission from the Crab Nebula". In: *Science* 373.6553 (2021), pp. 425–430. DOI: 10.1126/science.abg5137. eprint: https://www.science.org/doi/pdf/10.1126/science.abg5137. URL: https://www.science.org/doi/abs/10.1126/science.abg5137.

[60] M. Collaboration. "MAGIC very large zenith angle observations of the Crab Nebula up to 100 TeV". In: *Astronomy amp; Astrophysics* 635 (Mar. 2020), A158. ISSN: 1432-0746. DOI: 10.1051/0004-6361/201936899. URL: http://dx.doi.org/10.1051/0004-6361/201936899.

[61] M. Collaboration. "Teraelectronvolt pulsed emission from the Crab Pulsar detected by MAGIC". In: A&A 585, A133 (Jan. 2016), A133. DOI: 10.1051/0004-6361/201526853. arXiv: 1510.07048 [astro-ph.HE].

[62] T. H. C. et. "Discovery of a radiation component from the Vela pulsar reaching 20 teraelectronvolts". In: *Nature Astronomy* 7.11 (Nov. 2023), pp. 1341–1350. ISSN: 2397-3366. DOI: 10.1038/s41550-023-02052-3. URL: https://doi.org/10.1038/s41550-023-02052-3.

[63] J. Kormendy and L. C. Ho. "Coevolution (Or Not) of Supermassive Black Holes and Host Galaxies". In: ARA&A 51.1 (Aug. 2013), pp. 511–653. DOI: 10.1146/annurev-astro-082708-101811. arXiv: 1304.7762 [astro-ph.CO].

[64] L. Ferrarese and D. Merritt. "A Fundamental Relation between Supermassive Black Holes and Their Host Galaxies". In: ApJ 539.1 (Aug. 2000), pp. L9–L12. DOI: 10.1086/312838. arXiv: astro-ph/0006053 [astro-ph].

[65] G. (Madejski and M. Sikora. "Gamma-Ray Observations of Active Galactic Nuclei". In: ARA&A 54 (Sept. 2016), pp. 725–760. DOI: 10.1146/annurev-astro-081913-040044.

[66] R. Blandford, D. Meier, and A. Readhead. "Relativistic Jets from Active Galactic Nuclei". In: *Annual Review of Astronomy and Astrophysics* 57.1 (2019), pp. 467–509. DOI: 10.1146/annurev-astro-081817-051948. eprint: https://doi.org/10.1146/annurev-astro-081817-051948. URL: https://doi.org/10.1146/annurev-astro-081817-051948.

[67] D. L. Meier, S. Koide, and Y. Uchida. "Magnetohydrodynamic Production of Relativistic Jets". In: *Science* 291.5501 (2001), pp. 84–92. DOI: 10.1126/science.291.5501.84. eprint: https://www.science.org/doi/pdf/10.1126/science.291.5501.84. URL: https://www.science.org/doi/abs/10.1126/science.291.5501.84.

[68] J.-H. Woo and C. M. Urry. "Active Galactic Nucleus Black Hole Masses and Bolometric Luminosities". In: *The Astrophysical Journal* 579.2 (Nov. 2002), pp. 530–544. ISSN: 1538-4357. DOI: 10.1086/342878. URL: http://dx.doi.org/10.1086/342878.

[69] W. Ishibashi and A. C. Fabian. "Active galactic nucleus feedback and triggering of star formation in galaxies". In: MNRAS 427.4 (Dec. 2012), pp. 2998–3005. DOI: 10.1111/j.1365-2966.2012.22074.x. arXiv: 1209.1480 [astro-ph.GA].

[70] N. J. McConnell and C.-P. Ma. "REVISITING THE SCALING RELATIONS OF BLACK HOLE MASSES AND HOST GALAXY PROPERTIES". In: *The Astrophysical Journal* 764.2 (Feb. 2013), p. 184. ISSN: 1538-4357. DOI: 10.1088/0004-637x/764/2/184. URL: http://dx.doi.org/10.1088/0004-637X/764/2/184.

[71] A. et al. "Daily Monitoring of TeV Gamma-Ray Emission from Mrk 421, Mrk 501, and the Crab Nebula with HAWC". In: ApJ 841.2, 100 (June 2017), p. 100. DOI: 10.3847/1538-4357/aa729e. arXiv: 1703.06968 [astro-ph.HE].

[72] H. Collaboration. "The 2014 TeV γ-Ray Flare of Mrk 501 Seen with H.E.S.S.: Temporal and Spectral Constraints on Lorentz Invariance Violation". In: ApJ 870.2, 93 (Jan. 2019), p. 93. DOI: 10.3847/1538-4357/aaf1c4. arXiv: 1901.05209 [astro-ph.HE].

[73] M. Collaboration. "Variable Very High Energy γ-Ray Emission from Markarian 501". In: ApJ 669.2 (Nov. 2007), pp. 862–883. DOI: 10.1086/521382. arXiv: astro-ph/0702008 [astro-ph].

[74] T. Piran. "The physics of gamma-ray bursts". In: *Reviews of Modern Physics* 76.4 (Oct. 2004), pp. 1143–1210. DOI: 10.1103/RevModPhys.76.1143. arXiv: astro-ph/0405503 [astro-ph].

[75] D. A. Frail, S. R. Kulkarni, R. Sari, et al. "Beaming in Gamma-Ray Bursts: Evidence for a Standard Energy Reservoir". In: *The Astrophysical Journal* 562.1 (Nov. 2001), p. L55. DOI: 10.1086/338119. URL: https://dx.doi.org/10.1086/338119.

[76] K. Z. Stanek, T. Matheson, P. M. Garnavich, et al. "Spectroscopic Discovery of the Supernova 2003dh Associated with GRB 030329". In: ApJ 591.1 (July 2003), pp. L17–L20. DOI: 10.1086/376976. arXiv: astro-ph/0304173 [astro-ph].

[77] A. Baktash, D. Horns, and M. Meyer. *Interpretation of multi-TeV photons from GRB221009A*. 2023. arXiv: 2210.07172 [astro-ph.HE].

[78] E. Burns, D. Svinkin, E. Fenimore, et al. "GRB 221009A: The Boat". In: ApJ 946.1, L31 (Mar. 2023), p. L31. DOI: 10.3847/2041-8213/acc39c. arXiv: 2302.14037 [astro-ph.HE].

[79] T. L. Collaboration. "Very high-energy gamma-ray emission beyond 10 TeV from GRB 221009A". In: *Science Advances* 9.46 (2023), eadj2778. DOI: 10.1126/sciadv.adj2778. eprint: https://www.science.org/doi/pdf/10.1126/sciadv.adj2778. URL: https://www.science.org/doi/abs/10.1126/sciadv.adj2778.

[80] L. Dirson and D. Horns. "Phenomenological modelling of the Crab Nebula's broad-band energy spectrum and its apparent extension". In: *arXiv e-prints*, arXiv:2203.11502 (Mar. 2022), arXiv:2203.11502. arXiv: 2203.11502 [astro-ph.HE].

[81] P. K. F. Grieder. *Extensive Air Showers: High Energy Phenomena and Astrophysical Aspects - A Tutorial, Reference Manual and Data Book*. 2010. DOI: 10.1007/978-3-540-76941-5.

[82] B. Rossi and K. Greisen. "Cosmic-Ray Theory". In: *Rev. Mod. Phys.* 13 (4 Oct. 1941), pp. 240–309. DOI: 10.1103/RevModPhys.13.240. URL: https://link.aps.org/doi/10.1103/RevModPhys.13.240.

[83] W. Heitler. *The Quantum Theory of Radiation*. Dover Books on Physics Series. Dover Publications, 1984. ISBN: 9780486645582. URL: https://books.google.de/books?id=8jVRAAAAMAAJ.

[84] F. Schmidt and J. Knapp. *CORSIKA Shower Images*. 2005. URL: https://www-zeuthen.desy.de/~jknapp/fs/showerimages.html.

[85] M. de Naurois and D. Mazin. "Ground-based detectors in very-high-energy gamma-ray astronomy". In: *Comptes Rendus Physique* 16.6 (2015). Gamma-ray astronomy / Astronomie des rayons gamma, pp. 610–627. ISSN: 1631-0705. DOI: https://doi.org/10.1016/j.crhy.2015.08.011. URL: https://www.sciencedirect.com/science/article/pii/S1631070515001462.

[86] S. Ohm. "Development of an advanced gamma/hadron separation technique and application to particular gamma-ray sources with H.E.S.S." In: (2010). DOI: 10.11588/HEIDOK.00010699. URL: http://archiv.ub.uni-heidelberg.de/volltextserver/id/eprint/10699.

[87] F. Arqueros, F. Blanco, and J. Rosado. "Analysis of the fluorescence emission from atmospheric nitrogen by electron excitation, and its application to fluorescence telescopes". In: *New Journal of Physics* 11.6 (June 2009), p. 065011. DOI:

10.1088/1367-2630/11/6/065011. URL: https://dx.doi.org/10.1088/1367-2630/11/6/065011.

[88] Y. Itikawa, M. Hayashi, A. Ichimura, et al. "Cross Sections for Collisions of Electrons and Photons with Nitrogen Molecules". In: *Journal of Physical and Chemical Reference Data* 15.3 (1986), pp. 985–1010. DOI: 10.1063/1.555762. eprint: https://doi.org/10.1063/1.555762. URL: https://doi.org/10.1063/1.555762.

[89] J. Rosado, F. Blanco, and F. Arqueros. "On the absolute value of the air-fluorescence yield". In: *Astroparticle Physics* 55 (2014), pp. 51–62. ISSN: 0927-6505. DOI: https://doi.org/10.1016/j.astropartphys.2014.02.003. URL: https://www.sciencedirect.com/science/article/pii/S0927650514000152.

[90] H. Collaboration. "Observations of the Crab nebula with HESS". In: *Astronomy &amp Astrophysics* 457.3 (Sept. 2006), pp. 899–915. DOI: 10.1051/0004-6361:20065351. URL: https://doi.org/10.1051%2F0004-6361%3A20065351.

[91] F. Aharonian, J. Buckley, T. Kifune, and G. Sinnis. "High energy astrophysics with ground-based gamma ray detectors". In: *Reports on Progress in Physics* 71.9 (Aug. 2008), p. 096901. DOI: 10.1088/0034-4885/71/9/096901. URL: https://dx.doi.org/10.1088/0034-4885/71/9/096901.

[92] J. M. Davies and E. S. Cotton. "Design of the quartermaster solar furnace". In: *Solar Energy* 1.2-3 (Apr. 1957), pp. 16–22. DOI: 10.1016/0038-092X(57)90116-0.

[93] A. D. et al. "First results on the performance of the HEGRA IACT array". In: *Astroparticle Physics* 8.1 (1997), pp. 1–11. ISSN: 0927-6505. DOI: https://doi.org/10.1016/S0927-6505(97)00031-5. URL: https://www.sciencedirect.com/science/article/pii/S0927650597000315.

[94] F. e. a. Aharonian. "Measurement of the flux, spectrum, and variability of TeV γ-rays from MKN 501 during a state of high activity." In: A&A 327 (Nov. 1997), pp. L5–L8. DOI: 10.48550/arXiv.astro-ph/9706019. arXiv: astro-ph/9706019 [astro-ph].

[95] J. Holder. *Atmospheric Cherenkov Gamma-ray Telescopes*. 2015. arXiv: 1510.05675 [astro-ph.IM].

[96] A. M. Hillas. "Cerenkov Light Images of EAS Produced by Primary Gamma Rays and by Nuclei". In: *19th International Cosmic Ray Conference (ICRC19), Volume 3*. Vol. 3. International Cosmic Ray Conference. Aug. 1985, p. 445.

[97] C.-L. Project. *Observations of the Crab Nebula and Pulsar with the Large-Sized Telescope Prototype of the Cherenkov Telescope Array*. 2023. arXiv: 2306.12960 [astro-ph.HE].

[98] M. de Naurois. "Blue light in the desert night". In: *Nature Astronomy* 2.7 (July 2018), pp. 593–593. ISSN: 2397-3366. DOI: 10.1038/s41550-018-0513-1. URL: https://doi.org/10.1038/s41550-018-0513-1.

[99] R. W. et al. "The Small-Sized Telescopes for the Southern Site of the Cherenkov Telescope Array". In: *Proceedings of 37th International Cosmic Ray Conference — PoS(ICRC2021)*. Sissa Medialab, July 2021. DOI: 10.22323/1.395.0728. URL: https://doi.org/10.22323%2F1.395.0728.

[100] L. et al. "First detection of the Crab Nebula at TeV energies with a Cherenkov telescope in a dual-mirror Schwarzschild-Couder configuration: the ASTRI-Horn telescope". In: *A&A* 634 (2020), A22. DOI: 10.1051/0004-6361/201936791. URL: https://doi.org/10.1051/0004-6361/201936791.

[101] T. Tavernier, J.-F. Glicenstein, and F. Brun. *Status and performance results from NectarCAM – a camera for CTA medium sized telescopes*. 2019. arXiv: 1909.01969 [astro-ph.IM].

[102] F. W. et al. "Performance verification of the FlashCam prototype camera for the Cherenkov Telescope Array". In: *Nuclear Instruments and Methods in Physics Research Section A: Accelerators, Spectrometers, Detectors and Associated Equipment* 876 (Dec. 2017), pp. 31–34. DOI: 10.1016/j.nima.2016.12.056. URL: https://doi.org/10.1016%2Fj.nima.2016.12.056.

[103] A. N. O. et al. *Development of a SiPM Camera for a Schwarzschild-Couder Cherenkov Telescope for the Cherenkov Telescope Array*. 2015. arXiv: 1509.02345 [astro-ph.IM].

[104] B. M. et al. "Detection of the Crab Nebula by the prototype Schwarzschild-Couder Telescope". In: *Proceedings of 37th International Cosmic Ray Conference — PoS(ICRC2021)*. Sissa Medialab, July 2021. DOI: 10.22323/1.395.0830. URL: https://doi.org/10.22323%2F1.395.0830.

[105] H. e. a. Abe. "Observations of the Crab Nebula and Pulsar with the Large-sized Telescope Prototype of the Cherenkov Telescope Array". In: ApJ 956.2, 80 (Oct. 2023), p. 80. DOI: 10.3847/1538-4357/ace89d. arXiv: 2306.12960 [astro-ph.HE].

[106] M. Holler, D. Berge, C. van Eldik, et al. *Observations of the Crab Nebula with H.E.S.S. Phase II*. 2015. arXiv: 1509.02902 [astro-ph.HE].

[107] A. Cao, Z. Aharonian, F.A. et al. "Ultrahigh-energy photons up to 1.4 peta-electronvolts from 12 γ-ray Galactic sources". In: *Nature* 594 (2021), pp. 33–36. DOI: https://doi.org/10.1038/s41586-021-03498-z. URL: https://www.nature.com/articles/s41586-021-03498-z.

[108] Z. C. et al. *The Large High Altitude Air Shower Observatory (LHAASO) Science Book (2021 Edition)*. 2022. arXiv: 1905.02773 [astro-ph.HE].

[109] M. Collaboration. "MAGIC very large zenith angle observations of the Crab Nebula up to 100 TeV". In: *Astronomy & Astrophysics* 635 (Mar. 2020), A158. DOI: 10.1051/0004-6361/201936899.

[110] D. Heck, J. Knapp, J. N. Capdevielle, G. Schatz, and T. Thouw. *CORSIKA: A Monte Carlo code to simulate extensive air showers*. Tech. rep. 51.02.03; LK 01; Wissenschaftliche Berichte, FZKA-6019 (Februar 98). 1998. DOI: 10.5445/IR/270043064.

[111] H. E. Dixon, J. C. Earnshaw, J. R. Hook, et al. "Computer Simulations of Cosmic-Ray Air Showers. I. Average Characteristics of Proton Initiated Showers". In: *Proceedings of the Royal Society of London Series A* 339.1617 (Aug. 1974), pp. 133–155. DOI: 10.1098/rspa.1974.0114.

[112] T. Pierog, I. Karpenko, J. M. Katzy, E. Yatsenko, and K. Werner. "EPOS LHC: Test of collective hadronization with data measured at the CERN Large Hadron Collider". In: *Phys. Rev. C* 92 (3 Sept. 2015), p. 034906. DOI: 10.1103/PhysRevC.92.034906. URL: https://link.aps.org/doi/10.1103/PhysRevC.92.034906.

[113] K. Bernlöhr. "Simulation of imaging atmospheric Cherenkov telescopes with CORSIKA and sim$_{t}$*elarray*". In: *Astroparticle Physics* 30.3 (Oct. 2008), pp. 149–158. ISSN: 0927-6505. DOI: 10.1016/j.astropartphys.2008.07.009. URL: http://dx.doi.org/10.1016/j.astropartphys.2008.07.009.

[114] T. P. D. Heck. *Extensive Air Shower Simulation with CORSIKA: A User's Guide, version 7.7410*. 2021. URL: https://web.iap.kit.edu/corsika/usersguide/usersguide.pdf (visited on 10/24/2022).

[115] N. Kalmykov, S. Ostapchenko, and A. Pavlov. "Quark-gluon-string model and EAS simulation problems at ultra-high energies". In: *Nuclear Physics B - Proceedings Supplements* 52.3 (1997), pp. 17–28. ISSN: 0920-5632. DOI: https://doi.org/10.1016/S0920-5632(96)00846-8. URL: https://www.sciencedirect.com/science/article/pii/S0920563296008468.

[116] H. Fesefeldt. *The Simulation of Hadronic Shower - Physics and Applications, PITHA-85/02, RWTH Aachen*. 1985. URL: http://cds.cern.ch/record/162911/files/CM-P00055931.pdf (visited on 11/10/2022).

[117] W. R. Nelson, H. Hirayama, and D. W. Rogers. "EGS4 code system". In: (Dec. 1985). URL: https://www.osti.gov/biblio/6137659.

[118] Q. e. a. An. "Measurement of the cosmic ray proton spectrum from 40 GeV to 100 TeV with the DAMPE satellite". In: *Science Advances* 5.9, eaax3793 (Sept. 2019), eaax3793. DOI: 10.1126/sciadv.aax3793. arXiv: 1909.12860 [astro-ph.HE].

[119] F. e. a. Alemanno. "Measurement of the Cosmic Ray Helium Energy Spectrum from 70 GeV to 80 TeV with the DAMPE Space Mission". In: Phys. Rev. Lett. 126.20, 201102 (May 2021), p. 201102. DOI: 10.1103/PhysRevLett.126.201102. arXiv: 2105.09073 [astro-ph.HE].

[120] O. G. et al. *scikit-learn/scikit-learn: scikit-learn 0.24.1*. Version 0.24.1. Jan. 2021. DOI: 10.5281/zenodo.4450597. URL: https://doi.org/10.5281/zenodo.4450597.

[121] F. Pedregosa, G. Varoquaux, A. Gramfort, et al. "Scikit-learn: Machine Learning in Python". In: *Journal of Machine Learning Research* 12 (2011), pp. 2825–2830.

[122] M. Blank. *Detection of the Crab Nebula with the first TAIGA IACT*. https://ediss.sub.uni-hamburg.de/handle/ediss/10436. [Accessed 28-11-2023]. 2023.

[123] T. .-. Li and Y. .-. Ma. "Analysis methods for results in gamma-ray astronomy." In: ApJ 272 (Sept. 1983), pp. 317–324. DOI: 10.1086/161295.

[124] R. Lessard, J. Buckley, V. Connaughton, and S. L. Bohec. "A new analysis method for reconstructing the arrival direction of TeV gamma rays using a single imaging atmospheric Cherenkov telescope". In: *Astroparticle Physics* 15.1 (Mar. 2001), pp. 1–18. DOI: 10.1016/s0927-6505(00)00133-x. URL: https://doi.org/10.1016%2Fs0927-6505%2800%2900133-x.

[125] W. Hofmann. "Comparison of techniques to reconstruct VHE gamma-ray showers from multiple stereoscopic Cherenkov images". In: *Astroparticle Physics* 12.3 (Nov. 1999), pp. 135–143. DOI: 10.1016/s0927-6505(99)00084-5. URL: https://doi.org/10.1016%2Fs0927-6505%2899%2900084-5.

[126] L. Collaboration. "A tera–electron volt afterglow from a narrow jet in an extremely bright gamma-ray burst". In: *Science* 380.6652 (2023), pp. 1390–1396. DOI: 10.1126/science.adg9328. eprint: https://www.science.org/doi/pdf/10.1126/science.adg9328. URL: https://www.science.org/doi/abs/10.1126/science.adg9328.

[127] F. A. et al. "Observation of the Crab Nebula with LHAASO-KM2A - a performance study ∗". In: *Chinese Physics C* 45.2 (Feb. 2021), p. 025002. DOI: 10.1088/1674-1137/abd01b. URL: https://doi.org/10.1088%2F1674-1137%2Fabd01b.

[128] C. et al. "The First LHAASO Catalog of Gamma-Ray Sources". In: *arXiv e-prints*, arXiv:2305.17030 (May 2023), arXiv:2305.17030. DOI: 10.48550/arXiv.2305.17030. arXiv: 2305.17030 [astro-ph.HE].

[129] A. Baktash and D. Horns. "EASpy: fast simulation of fluorescence and Cherenkov light from extended air showers at large zenith angles". In: *Journal of Instrumentation* 18.08 (Aug. 2023), P08018. DOI: 10.1088/1748-0221/18/08/P08018. URL: https://dx.doi.org/10.1088/1748-0221/18/08/P08018.

[130] V. de Souza, H. Barbosa, and C. Dobrigkeit. "A Monte Carlo method to generate fluorescence light in extensive air showers". In: *Astroparticle Physics* 22.3 (2004), pp. 263–273. ISSN: 0927-6505. DOI: https://doi.org/10.1016/j.astropartphys.2004.07.006. URL: https://www.sciencedirect.com/science/article/pii/S0927650504001306.

[131] D. Morcuende, J. Rosado, J. Contreras, and F. Arqueros. "Relevance of the fluorescence radiation in VHE gamma-ray observations with the Cherenkov technique". In: *Astroparticle Physics* 107 (Jan. 2019), pp. 26–34. DOI: 10.1016/j.astropartphys.2018.11.003. URL: https://doi.org/10.1016%2Fj.astropartphys.2018.11.003.

[132] K. Greisen. "Cosmic Ray Showers". In: *Annual Review of Nuclear and Particle Science* 10 (Jan. 1960), pp. 63–108. DOI: 10.1146/annurev.ns.10.120160.000431.

[133] T. K. Gaisser and A. M. Hillas. "Reliability of the Method of Constant Intensity Cuts for Reconstructing the Average Development of Vertical Showers". In: *International Cosmic Ray Conference*. Vol. 8. International Cosmic Ray Conference. Jan. 1977, p. 353.

[134] K. Kamata and J. Nishimura. "The Lateral and the Angular Structure Functions of Electron Showers". In: *Progress of Theoretical Physics Supplement* 6 (Jan. 1958), pp. 93–155. DOI: 10.1143/PTPS.6.93.

[135] F. Nerling, J. Blümer, R. Engel, and M. Risse. "Universality of electron distributions in high-energy air showers—Description of Cherenkov light production". In: *Astroparticle Physics* 24.6 (Jan. 2006), pp. 421–437. DOI: 10.1016/j.astropartphys.2005.09.002. URL: https://doi.org/10.1016%2Fj.astropartphys.2005.09.002.

[136] J. Rosado and D. Morcuende. *JaimeRosado/ShowerModel: v0.1.9*. Version v0.1.9. June 2022. DOI: 10.5281/zenodo.6773258. URL: https://doi.org/10.5281/zenodo.6773258.

[137] D. Morcuende and J. Rosado. "ShowerModel: A Python Package for Modelling Cosmic-ray Showers, Their Light Production and Their Detection". In: *ASP Conf. Ser.* 532 (2022), p. 155. arXiv: 2103.00578 [astro-ph.IM].

[138] F. K. et al. *The MODTRAN 2/3 Report and LOW-TRAN 7 Model*. Phillips Laboratory, Hanscom AFB, MA 01731, USA, 1996.

[139] S. Lafebre, R. Engel, H. Falcke, et al. "Universality of electron–positron distributions in extensive air showers". In: *Astroparticle Physics* 31.3 (2009), pp. 243–254. ISSN: 0927-6505. DOI: https://doi.org/10.1016/j.astropartphys.2009.02.002. URL: https://www.sciencedirect.com/science/article/pii/S0927650509000292.

[140] S. M. Seltzer and M. J. Berger. "Evaluation of the collision stopping power of elements and compounds for electrons and positrons". In: *The International Journal of Applied Radiation and Isotopes* 33.11 (1982), pp. 1189–1218. ISSN: 0020-708X. DOI: https://doi.org/10.1016/0020-708X(82)90244-7. URL: https://www.sciencedirect.com/science/article/pii/0020708X82902447.

[141] E. A. Uehling. "Penetration of Heavy Charged Particles in Matter". In: *Annual Review of Nuclear Science* 4.1 (1954), pp. 315–350. DOI: 10.1146/annurev.ns.04.120154.001531. eprint: https://doi.org/10.1146/annurev.ns.04.120154.001531. URL: https://doi.org/10.1146/annurev.ns.04.120154.001531.

[142] P. D. Group. *Particle Physics Booklet*. 2022. URL: https://pdg.lbl.gov/2022/download/db2022.pdf (visited on 10/24/2022).

[143] M. Ave, M. Bohacova, B. Buonomo, et al. "Measurement of the pressure dependence of air fluorescence emission induced by electrons". In: *Astroparticle Physics* 28.1 (Sept. 2007), pp. 41–57. DOI: 10.1016/j.astropartphys.2007.04.006. URL: https://doi.org/10.1016%2Fj.astropartphys.2007.04.006.

[144] M. Ave, M. Bohacova, B. Buonomo, et al. "Temperature and humidity dependence of air fluorescence yield measured by AIRFLY". In: *Nuclear Instruments and Methods in Physics Research Section A: Accelerators, Spectrometers, Detectors and Associated Equipment* 597.1 (Nov. 2008), pp. 50–54. DOI: 10.1016/j.nima.2008.08.050. URL: https://doi.org/10.1016%2Fj.nima.2008.08.050.

[145] J. Bolmont, P. Corona, P. Gauron, et al. "The camera of the fifth H.E.S.S. telescope. Part I: System description". In: *Nuclear Instruments and Methods in Physics Research Section A: Accelerators, Spectrometers, Detectors and Associated Equipment* 761 (Oct. 2014), pp. 46–57. DOI: 10.1016/j.nima.2014.05.093. URL: https://doi.org/10.1016%2Fj.nima.2014.05.093.

[146] K. Bernlöhr. "Simulation of imaging atmospheric Cherenkov telescopes with CORSIKA and sim_telarray". In: *Astroparticle Physics* 30.3 (Oct. 2008), pp. 149–158. DOI: 10.1016/j.astropartphys.2008.07.009. URL: https://doi.org/10.1016%2Fj.astropartphys.2008.07.009.

Acknowledgements

I would like to express my deepest gratitude to Dieter for your guidance and encouragement over the past 8 years. I am fortunate to have had such an exceptional mentor since my Bachelor studies - Thank you for your commitment to my academic and personal growth. A big chunk of my scientific knowledge and expertise is thanks to you.

I would also like to express my gratitude to Martin, LeHoang and Michael for their invaluable support, encouragement and shared experiences. The daily interactions and discussions in the office have created a positive and motivating work environment over the past years. At times, you guys managed to convince me that maybe I'm not as dumb as I sometimes think.

I want to express my heartfelt gratitude to Kathrin, Thomas, Andras, Henrik, Melli and Benny. I am truly fortunate to have friends like you by my side. You guys have never let me down, whether I was in a dark place or annoyingly in a good mood. I doubt that I would have finished this thesis without your support.

I extend my deepest gratitude to my parents and brothers for their support throughout my Ph.D. journey. A big thanks to my brother Omer for not breaking my arms when I asked him to while writing this thesis. You were (surprisingly) right - I actually finished it.

Eidesstattliche Versicherung

Declaration on oath

Hiermit erkläre ich an Eides statt, die vorliegende Dissertationsschrift selbst verfasst und keine anderen als die angegebenen Hilfsmittel und Quellen benutzt zu haben.

Hamburg den
01.12.2023
Unterschrift

Ali Baktash